# Material Characterization and Development of Simulant Phantoms for a Biofidelic Head Model

*Tristan Virgilio Tenio*

*A thesis submitted to the Faculty of Graduate Studies of*

*York University*

*in partial fulfillment of the requirements for the degree of*

**Master of Applied Science**

Graduate Program in the Department of Mechanical Engineering

Lassonde School of Engineering

York University

Toronto, Ontario, Canada

SEPTEMBER 2024

# *Abstract*

Traumatic Brain Injury (TBI) is a global health crisis, with concussions — classified as mild TBI — being particularly common in sports and daily activities. These non-penetrative injuries complicate diagnosis and analysis due to ethical and observational challenges. This thesis aims to develop a biofidelic head model for lab-based impact testing, bridging the gap of anatomical representation between computational models and physical validation.

This research focuses on characterizing materials that mimic the mechanical properties of human brain and skull tissues under impact conditions. These materials are tested for their ability to simulate the brain's compressive and shear responses and the skull's flexural strength, using advanced manufacturing techniques. The research, structured across five chapters, reviews existing head impact methods and current practices for simulant characterization, selects and tests brain and skull simulants, and designs a comprehensive methodology for creating a full-scale biofidelic head model, proposing advancements for more accurate TBI analysis and prevention.

# *Acknowledgements*

I want to begin my gratitude to my supervisor, Dr. Solomon Boakye-Yiadom, for the guidance he has provided throughout this thesis. Professor Solomon always concluded his supervisions with "you know how to contact me if you ever need help", and I knew I could rely on him if I ever needed it. Without his help throughout this project, it would not have been possible.

The gratefulness to my efforts extends to Dr. Garrett Melenka and his students for instilling a high standard of quality in all of their work, which I strived to attain while presenting my own research.

Thank you to all of my lab mates, both in the Processing-Structure-Property-Performance (PSPP) Lab and Melenka Lab groups. I give direct gratitude to Gurnek Tak, Calvin Bijl, Shauvik Pahari, and Thomas Barbuio for all of the hours of insight, consultation, proofreading, and yapping. Interestingly, this thanks extends to El Jefe Del Pollo for supplying our sustenance throughout the late nights in the lab. Also, thank you to Rhythm Reet for the weather.

Thanks to the M.E. Department techs: Armando Azevedo, Florin Alexandru, and Norman Nicholls for allowing me to momentarily steal equipment. Please let me know if any are still missing.

Thank you to Dr. Aleksander Czekanski and his students at IDEA-LAB, namely Usman Ali, Salman Chaudhry, and Dr. Burak Yenigun, for their in-depth knowledge in this related field and know-how towards the direction, methodology, and troubleshooting of both work and equipment.

Thank you to my family: my parents, aunt and uncle (my second parents), my Ama, my siblings, and my cousins for laying the foundation to bring me to this point. All of your hard work and nurturing has led to this and will only continue to show onwards.

A special gratitude goes towards Angela Huang for her emotional support, intellectual support, and because she always understood. You are what made these past years special, and I look forward to what the future will hold.

At first, I was unsure if I would be able to do this. Even while I am here, proving myself wrong, I firmly believe that the effort it took to get here was not without all of your unwavering support.

# *Dedication*

This one is for me.

*"Fly, you fools!" — Gandalf the Grey*

J.R.R. Tolkien, *The Fellowship of the Ring*

# TABLE OF CONTENTS

# LIST OF FIGURES

# LIST OF TABLES

# LIST OF EQUATIONS

# LIST OF ABBREVIATIONS

| Chapter 1 | |
|---|---|
| *TBI* | Traumatic Brain Injury |
| *GCS* | Glasgow Coma Scale |
| *AIS* | Abbreviated Injury Scale |
| *LOC* | Loss of Consciousness |
| *PTA* | Post-Traumatic Amnesia |
| *mTBI* | Mild Traumatic Brain Injury |
| *CTE* | Chronic Traumatic Encephalopathy |
| *HIMD* | Head-Impact Measurement Device |
| *ATD* | Anthropomorphic Test Dummy |
| *FEM* | Finite Element Model |
| *DMA* | Dynamic Mechanical Analysis |
| *AM* | Additive Manufacturing |
| *PLA* | Poly-lactic Acid |
| *PMMA* | Poly(methyl methacrylate) |
| **Chapter 2 — Repeats Omitted** | |
| *LA* | Linear Acceleration |
| *RA* | Rotational Acceleration |
| *NOCSAE* | National Operating Committee on Standards for Athletic Equipment |
| *UCDBTM* | University College Dublin Brain Trauma Model |
| *MPS* | Maximum Principal Strain |
| *HIC* | Head Injury Criterion |
| *SI* | Gadd Severity Index |
| *WSTC* | Wayne State Tolerance Curve |
| *HIP* | Head Impact Power |
| *GAMBIT* | Generalized Acceleration Model for Brain Injury Threshold |
| *CSDM* | Cumulative Strain Damage Measure |
| *VMS* | Von-Mises Strain |
| *SIMon* | Simulated Injury Monitor |

| | |
|---|---|
| *GHBMC* | Global Human Body Model Consortium |
| *NHTSA* | National Highway Traffic Safety Administration |
| *GHMBC M50* | Global Human Body Model Consortium Male 50$^{th}$ Percentile Model |
| *GHBMC F5* | Global Human Body Model Consortium Female 5$^{th}$ Percentile Model |
| *BTI* | Blast Traumatic Injury |
| *NFL* | National Football League |
| *ICP* | Intercranial Pressure |
| *NLV* | Non-Linear Viscoelasticity |
| *NVU* | Neurovascular Unit |
| *ECM* | Extracellular Matrix |
| *MRE* | Magnetic Resonance Elastography |
| *PDMS* | Polydimethylsiloxane |
| *GelMA* | Gelatin Methacrylate |
| $F_{max}$ | Maximum Force |
| *μCT/Micro-CT* | Micro-Computed Tomography |
| *TMD* | Tissue Mineral Density |
| *DIC* | Digital Image Correlation |
| *HB* | Hyperelastic Bone |
| *PGLA* | Poly(lactic-co-glycolic acid) |
| *PCL* | Polycaprolactone |
| *HA* | Hydroxyapatite |
| *PETG* | Polyethylene terephthalate glycol |
| *FDM* | Fused Deposition Modelling |
| *CNS* | Central Nervous System |
| *DM* | Dura Mater |
| *PAC* | Pia-Arachnoid Complex |
| *FC* | Falx Cerebri |
| *TC* | Tentorium Cerebelli |
| *SAS* | Sub-Arachnoid Space |
| *CSF* | Cerebrospinal Fluid |

| | |
|---|---|
| *OCT* | Optical Coherence Tomography |
| *TPU* | Thermoplastic Polyurethane |
| **Chapter 3 — Repeats Omitted** | |
| *DHR/HR-3* | Discovery Hybrid Rheometer Model HR-3 |
| *PBS* | Phosphate-Buffered Saline |
| *DAI* | Diffuse Axonal Injury |
| *G* | Initial Shear Moduli |
| *SD/S.D.* | Standard Deviation |
| *FFF* | Fused Filament Fabrication |
| **Chapter 4 — Repeats Omitted** | |
| *CAD* | Computer-Aided Design or Computer-Aided Drawing |
| *ABS* | Acrylonitrile Butadiene Styrene |
| *HXA-PMMA* | Hydroxyapatite-Coated Poly(methyl methacrylate) |
| $T_{trabecular}$ | Trabecular Thickness |
| $T_{outer}$ | Cortical Thickness Fraction |
| $T_{inner}$ | Trabecular Volume Fraction |
| *CTF* | Cortical Thickness Fraction |
| *TVF* | Trabecular Volume Fraction |
| *RP%* | Relative Performance |
| *CRP%* | Comparative Relative Performance |
| *CI* | Confidence Interval |
| *ANOVA* | Analysis of Variance |
| *MRI* | Magnetic Resonance Imaging |
| *NIH* | National Institute of Health |
| *STL* | Standard Triangle Language |
| | ***Alternatively:*** Stereolithographic Printing (STL Printing) |

# LIST OF THESIS PUBLICATIONS AND CONFERENCE PRESENTATIONS

**Refereed Journal Papers:**

1. **T. Tenio,** S. Boakye-Yiadom (2024), Characterization and Selection of a Skull Surrogate for the Development of a Biofidelic Head Model (Accepted to the *Journal of the Mechanical Behavior of Biomedical Materials, DOI: 10.1016/j.jmbbm.2024.106680*).
2. **T. Tenio,** S. Boakye-Yiadom (2024), Characterization and Selection of a Brain Simulant for the Development of a Biofidelic Head Model (*In preparation, to be submitted*).

**Non-Refereed Conference Presentations (Abstract Review):**

1. **T. Tenio,** S. Boakye-Yiadom (2024), Mechanical Characterization of Simulant Brain Surrogates in Developing a Biofidelic Head Model, *Canadian Society for Mechanical Engineering* (CSME 2024). Toronto, ON Canada, May 29, 2024.

**Selected Technical Presentations:**

1. **T. Tenio,** S. Boakye Yiadom (2024), Mechanical Characterization of Simulant Brain and Skull Surrogates in Developing a Biofidelic Head Model, *NSERC Alliance Program.*

# *Chapter 1 — Introduction, Motivation, and Background*

## 1.1 — Motivation

Traumatic Brain Injury (TBI) is a significant health concern globally and is defined as the structural or functional alteration of the human brain tissue [1], [2] due to external forces such as impact, penetration, or rapid relative movement of the skull [3], [4]. Neuropsychiatric burdens which occur in diagnosed patients from the survival of TBI often include cognitive, mood, and behavioural deficits. Affecting a minimum of 60 million global injuries and deaths annually [1], [3], [5], and a lifetime prevalence at a rate of up to 40% in all adults [3]. TBI is a "silent epidemic", such that there is no effective method for treatment of the disease and for characterization of kinematic signatures which lead to TBI events [1], [3], [5].

The severity of Traumatic Brain Injury is identified as a spectrum of injuries relevant to the human brain — as per the Glasgow Coma Scale (GCS) as well as the Abbreviated Injury Scale (AIS) — and is characterized by the clinical assessment of the patient's "level of consciousness", with assessment of parameters including the duration in loss of consciousness (LOC) and post-traumatic amnesia (PTA) [1], [3]. The GCS categorizes the degrees of severity for TBI into distinctions of mild, moderate, or severe [3].

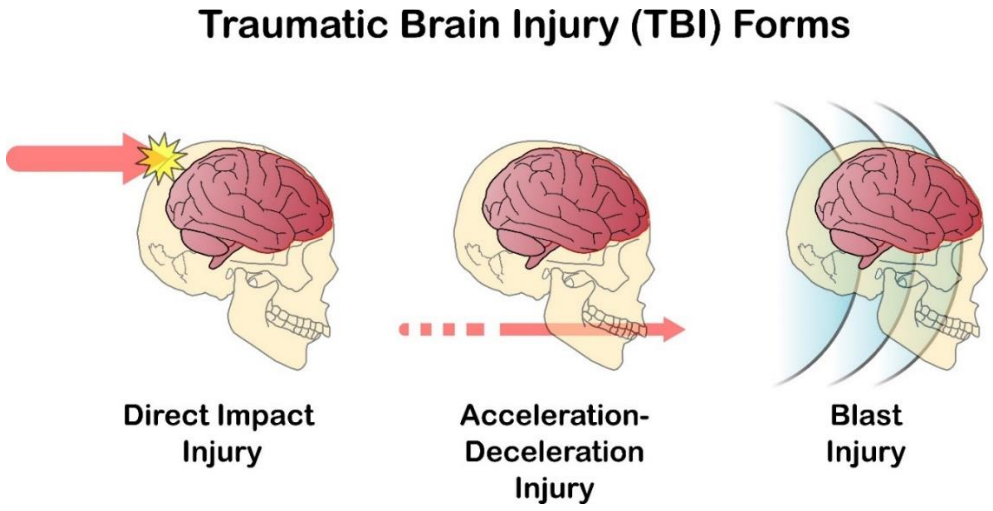


Figure 1.1 — Typical Forms of TBI Injury

Concussion, according to the GCS and AIS, is classified under the mild regime of the TBI spectrum (*mild Traumatic Brain Injury; mTBI)* and is the most prevalent form of TBI experienced, with an annual estimate of 42 million people affected globally [3], [6]. Commonly observed in sports impacts and falls, this categorization of TBI has begun to grow in concern due to its frequency in aspects of daily life [3], [7]–[9]. Of leading concern is in the implications of its consistent diagnoses in sports recreations such as American football, boxing, ice hockey, and other contact-based or combative sports [3], [8], [9]. In that, situations associated with repetitive concussive head impacts have observed progressive neurological decline and Chronic Traumatic Encephalopathy (CTE), a precursor to neurodegenerative syndromes such as Parkinson's disease, Alzheimer's disease, and dementia [3], [6], [8], [9]. Regardless of the common method, these concussive syndromes remain transient throughout all aspects of cause for mild head injury, and can result from accidents in mundane tasks, like falls, incoming blunt projectiles, and motor vehicle accidents, or more deliberately in incidents of assaults and homicide [3], [10].

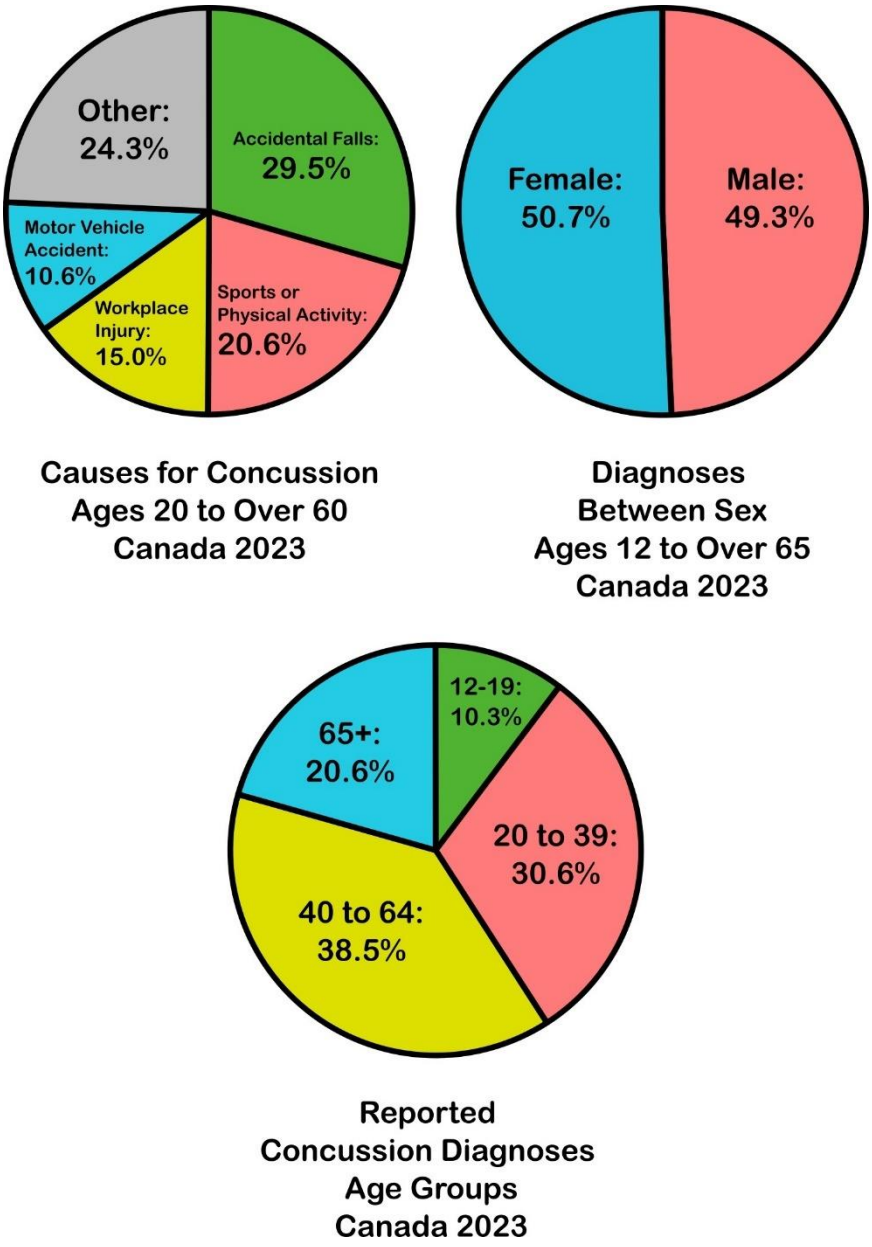


Figure 1.2 — Self-Reported Concussion Statistics (Canada 2023) [10]

Concussion is a type of non-missile or blunt force head impact, characterized by its inability to penetrate brain tissue, which presents significant challenges in both analysis and diagnosis [3]. The injury remains confined within the cranial vault, making direct observation of intracranial activity difficult. Additionally, ethical constraints prevent the use of living or cadaver human subjects for impact testing. As a result, the study of concussive kinematics has largely focused on monitoring head motions during impact. Common methodologies include the use of sensorized equipment or Head-Impact Measurement Devices (HIMDs) [11], [12], live video capture of head impacts [13],

and laboratory-based impact testing using Anthropomorphic Test Dummy (ATD) head forms [8], [9], [13]–[16].

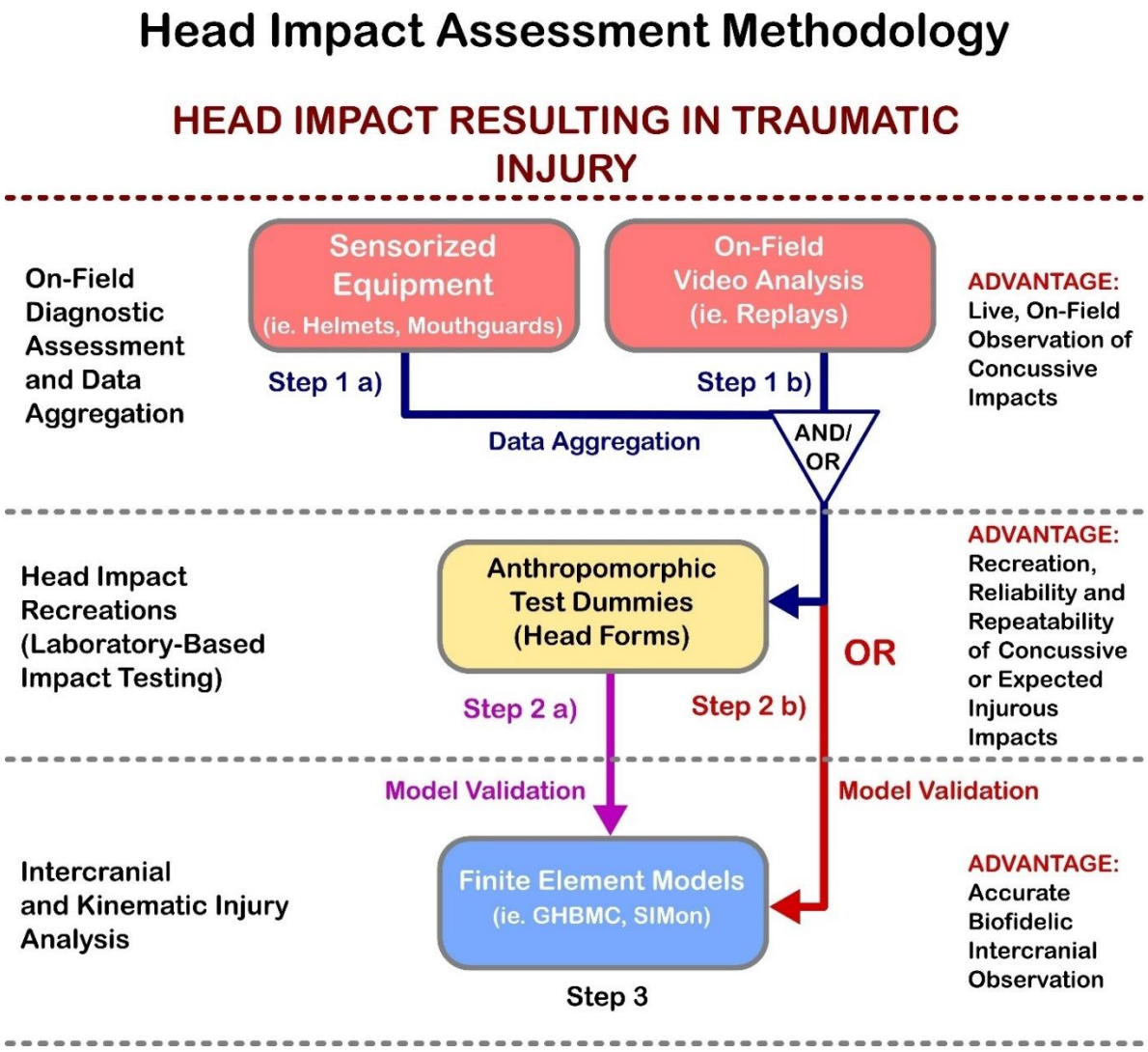


Figure 1.3 — Head Impact Assessment and Laboratory-Based Impact Assessment Methodology

Capturing head kinematic signatures provides essential data for the validation of intracranial analysis methods, most notably Finite Element Modelling (FEM) [17]–[21]. However, the use of these devices to validate FEM models presents discrepancies in the reported injury data. ATDs, favored for their reliability and repeatability, often produce varied results due to differences in the types of impacts tested, the head models used, and their degree of anthropomorphic accuracy [14], [15]. Moreover, the translation from a biofidelic computational model to a slightly anthropomorphic physical model can introduce confounding variables [8], [14], [15]. Therefore,

to accurately represent the intracranial kinematics of the human head during injurious impacts, it is crucial to bridge the gap between computational representations and their corresponding physical models.

## 1.2 — Objectives in Study

The objective of this thesis is to develop an improved iteration of a biofidelic head form for laboratory-based impact testing. This design aims to narrow the gap between computational models of the human head and the physical models used to validate these simulations.

To achieve this, the research will focus on conducting material characterization tests on readily available simulant materials and employing accessible manufacturing methods. The goal is to ensure that the new head form retains the reliability and repeatability of ATD head forms while improving biofidelity. Specifically, the studies presented in this thesis will address the material characteristics of brain tissue simulants (Chapter 3) and skull simulants (Chapter 4). These studies will establish materials that closely replicate the mechanical properties of their biological counterparts under conditions typical of head impacts. This will involve developing comprehensive testing criteria for both simulant structures, assessing their response under similar strain and loading rates.

The selection of an ideal simulant phantom is defined by their comparison to the material properties of their native structures under similar testing conditions. Identified from comprehensive literature surveys (See Chapter 2), the expected properties and characteristics of the native brain and skull can be observed in the Table 1.1.

*Table 1.1 — Expected Material Properties of Native Brain and Skull Specimens Determined from Literature Review*

| Tests | Reported Literature | Material Property and Expected Characteristics | |
|---|---|---|---|
| **Brain Tissue Characteristics** | | | |
| **Quasi-Static Compression ≤ 1 $s^{-1}$** | Navarro-Lozoya et al. (2019) [22], Singh et al. (2019) [23], Falland-Cheung et al. (2018) [24], Forte et al. (2017) [25] | **Non-linear, "Parabolic", Stress-Strain Behavior.** | |
| | | Early Strain Modulus **(< 10%)** | ~ 2-4 kPa |
| | | Moderate "Concussive" Strain Modulus **(10 < ε ≤ ~20%)** | ~ 5-10 kPa |
| DMA Frequency Sweep — **Compression** | Li et al. (2021) [26], Li et al. (2020) [27] | Concussive Storage Modulus Characteristics (**E'**) **(15 < *f* ≤ ~25 Hz)** | 5 < E' ≤ ~10 kPa |
| | | Concussive Loss Modulus Characteristics (**E"**) **(15 < *f* ≤ ~25 Hz)** | 1 < E" ≤ ~5 kPa |
| DMA Frequency Sweep — **Shear** | Forte et al. (2017) [25], Boudjema et al. (2017), Nicolle et al. (2004) [28], Bliston et al. (2001) [29] | Concussive Storage Modulus Characteristics (**G'**) **(15 < *f* ≤ ~25 Hz)** | ~ 50 kPa |
| | | Concussive Loss Modulus Characteristics (**G"**) **(15 < *f* ≤ ~25 Hz)** | ~ 10 kPa |
| **Skull Tissue Characteristics** | | | |
| **Flexural Tests** | Adanty et al. (2023)[1] [30], [31], Wu et al. (2021)[3] [32], Zhai et al. (2020)[2] [33], Ondruschka et al. (2019)[2] [34], Lee et al. (2019)[2] [35] | **Quasi-Elastic Loading Curve with Initial Load Dampening from Trabecular Region** | |
| | | **Distinct Strain Distribution following Compressive Strain on Outer Cortical and Tensile Strain on Inner Cortical Regions** | |
| | | **Flexural Modulus (MPa):** ~1700-2000 MPa **Ultimate Flexural Strength (MPa):** ~40-50 MPa | |

[1] Four-Point Bending Tests, [2] Three-Point Bending Tests, [3] Computationally Simulated Three-Point Bending Tests

The ultimate goal is to identify materials suitable for constructing a full-scale phantom that accurately represents a biofidelic head model. The research will also include the selection of materials for full-scale manufacturing and the development of the proposed head form using these methods.

## 1.3 — Thesis Outline

This thesis is divided into five chapters, each detailing the steps taken to complete this research. Chapter 2 presents a comprehensive literature review, providing the foundation for the work conducted. It explores the fundamentals and the current state of head impact assessment and biomechanical material simulants. Key topics include Anthropomorphic Test Devices (ATDs) and other Head Injury Measurement Devices (HIMDs), the validation and findings from Finite Element Modelling (FEM) of the human head, and the mechanical properties of critical head structures. The chapter begins with an overview of current devices used in head impact assessment and laboratory testing, followed by a discussion of computational modeling applications and their evolution. This leads into an examination of the mechanical properties of the brain, skull, and meningeal complex, along with notable simulant candidates. The chapter concludes with a review of previous attempts to develop biofidelic head models and suggestions for further advancements. The culmination of this review identifies key research gaps, laying the groundwork for the studies presented in this thesis.

Chapter 3 details the characterization and selection of a brain simulant for a biofidelic head model. Elastomers such as bovine and agar hydrogels, along with silicones of Shore Hardness 00-10, were chosen for their accessibility and potential to replicate critical brain structures. Material properties were assessed using protocols similar to those for native brain tissue, focusing on compressive and shear loading under conditions expected during concussions. Testing included quasi-static compression and oscillating deformations via Dynamic Mechanical Analysis (DMA). A detailed manufacturing methodology for developing a full-scale brain phantom using the selected simulant is also provided.

Chapter 4 focuses on the characterization and selection of a skull surrogate for the biofidelic head model. This study investigates the use of additive manufacturing (AM) techniques to develop biofidelic skull surrogates. Materials such as Polylactic Acid (PLA), a bone-simulant PLA variant,

and Hydroxyapatite-coated Poly(methyl methacrylate) (PMMA) were used to create models tested for flexural modulus and strength. Trabecular bone regions were simulated by varying infill densities (30%, 50%, 80%) and print raster directions, optimizing manufacturing parameters for biofidelic performance. A detailed methodology for manufacturing a full-scale skull phantom using the selected materials is provided.

Finally, Chapter 5 concludes the thesis, discussing the overall findings, limitations encountered in each chapter, and suggestions for future work to further refine and improve the proposed biofidelic head model.

## 1.4 — Thesis Contributions

From the works completed in this thesis, the main contributions identified include:

1. **Development of a Biofidelic Head Model**

   The work contributes to the development of a head model aimed at representing human cranial structures for lab-based impact testing, bridging the gap between computational models and physical validation systems. The proposed biofidelic head model can simulate brain and skull mechanics more realistically compared to existing head forms and is a significant step in improving the accuracy of concussion analysis and diagnosis. The proposal of a biofidelic head model designed specifically for the analysis of concussion and its kinematic markers further highlights the potential for improved design in safety equipment, such as contact sports helmets.

2. **Characterization of Simulant Materials for Brain and Skull**

   A comprehensive characterization criterion has been established for various materials intended to simulate the brain and skull. This includes quasi-static compression and dynamic compression and shear testing for brain simulants, and flexural strength tests for skull simulants, resulting in more accurate modeling of human tissue properties under impact conditions.

3. **Advanced Manufacturing Techniques for Skull Models**

The work introduces a novel approach to advanced fused filament fabrication additive manufacturing (FFF-AM) techniques, such as a designed trabecular region, to simulate the properties of skull bones with varying infill densities and print orientations. This method optimizes material properties to closely match those of native bone tissues and improves the reproducibility of simulant skull manufacturing.

4. **Addressing Gaps in Existing Headforms**

This work provides critical review of current Anthropomorphic Test Device (ATD) headforms and highlighted their limitations in accurately representing the human head during impact testing. By improving upon the biofidelity of these models, the work addresses a significant gap in head injury research, enabling better prediction and prevention of traumatic brain injuries.

# *Chapter 2 — Literature Review*

## 2.1 — Introduction

This chapter is regarding a review of the relevant literature considered in the construction and development of this thesis research. The objective of this literature review section is to provide an analysis of current methods assessing head impacts and intercranial kinematics and establish criteria towards the construction of native simulants and full-scaled head phantoms. As such, this chapter is divided into the following sections of study:

1. Head Impact Detection and Laboratory-Based Testing Methodologies
2. Concussion Mechanisms and mTBI-Predictive Parameters
3. Mechanical Properties and Characteristics of Native Human Head Structures, Objectives in Mechanical Simulation and Proposed Simulant Candidates
4. A Critical Review of Existing ATD Headforms and Implementations of Biofidelic Head Models

The relevant sections will be then aggregated to identify gaps in the current state of research. The established gaps will then be built upon by the fundamental studies of this proposed thesis.

## 2.2 — Head Impact Detection and Laboratory-Based Testing Methodologies

The presence of concussion as a mild Traumatic Brain Injury (mTBI) in diagnosed patients regards itself to non-missile or blunt force head impacts, where trauma on the brain tissue is resultant from impacts by objects or foreign bodies which do not penetrate the brain tissue [3]. This form of injury thus proves difficulty in the determination of the resulting method of impact and head kinematics associated to result in the concussive syndromes. Specifically, a challenge in concussion analysis persists such that in-vivo observations of intercranial mechanics are infeasible in the current state of the field [8]–[11]. This challenge is further bolstered by the ethical and sample procurement constraints regarding concussive impact recreations with living and cadaver human subjects [10]. As a result, the definition of kinematic parameters leading to concussion remain ambiguous in current practice, where diagnoses which lack on-site impact telemetry is relegated to scoring systems for the injured patient, based on neurocognitive questionnaires and external observations

[7], [12]. Regardless, recent studies have taken aim towards developing relevant kinematic signatures as potential precursors to concussive injuries. Research in this field regard the establishment of combined physical and computational simulative models to assess large-strain intracranial mechanics [8]–[10], [13]–[20]. The methodologies which follow are examples of current applications aimed to determine concussive thresholds in laboratory-based simulations.

### *2.2.1 — Head-Impact Measurement Devices (HIMDs) and On-Field Impact Detection*

An emerging and frequent application for the assessment of concussive injuries in sports and recreation include the implementation of embedded sensors in relevant equipment [11], [21]. Head-Impact Measurement Devices (HIMDs), such as the examples listed in the following studies, aim to alleviate the constraint in the lack of measurement systems identifying concussed athletes in on-field impacts. To establish the alleviation of this constraint, these devices attempt to observe head-impact biomechanics to which, traumatic events can be attuned to specific kinematic signatures. For example, if the head impact exceeds a defined threshold in measured kinematic signatures such as pressure gradients, strains, and accelerations, then, correlations can be made to assume that the patient or athlete has experienced a TBI.

O'Connor et al. [11] observed the current state-of-the-art regarding head impact measuring devices, including current implementations, and sensor methodologies. The study considers the main parameters of observation in head impact telemetry using these devices, specifically, those of resultant linear acceleration (LA) and resultant rotational acceleration (RA). The review further defines a limitation in this form of head impact detection methodology. That being, the inability to observe intercranial and tissue-level responses in head impacts. Due to this, the use of HIMDs can only be relegated to head accelerations with no method to observe inside the skull, including any relevant intercranial structures such as the brain tissue and meninges.

Wang et al. [21] further highlighted limitations regarding head impact sensors due to triggering biases. Aggregated from concussive impact telemetry data in American football and soccer from sensitized mouthguards, this study considered sensor effectiveness regarding triggering at the expected 10 – 30 G threshold range for common concussive impacts. This study further considered various triggering methodology, including the commonly observed per-axis and resultant linear

acceleration thresholds in sensitized equipment, as well as various directions of impact, such as the posterior, anterior, and lateral directions. It was observed that mouthguard sensors yielded a significant triggering bias in that they only triggered at a fraction of injurious impacts. Specifically, it was determined that the per-axis triggering method yielded a lower percentage of injury triggering. Sensor triggering biases were further observed in that sensor location heavily influenced which direction of impact resulted in threshold triggering, of which head accelerations at the lower end of the concussive threshold further exacerbated the reduction of triggering, down to a 27% trigger rate for per-axis thresholding, and 31% trigger rate for resultant thresholding at 10 G. Of the failed triggers were those of anterior impact locations, which are some of the more commonly observed forms of impacts in sports such as American football and soccer. The study defines a limitation in current mouthguard sensor methodologies, that being the use of an individual sensor in a specific head location can yield biases to certain concussive impacts, potentially generating false negatives in concussion triggering for diagnosed patients. It is recommended that ideal sensitization of the human head for on-field and laboratory-based impact telemetry should consider multiple sensor locations around the head, as well as considerations for rotational acceleration in impact thresholding.

### *2.2.2 — Laboratory-Based Impact Testing and Anthropomorphic Test Device (ATD) Headforms*

The utilization of Anthropomorphic Test Device (ATD) headforms in laboratory-based impact tests has been pivotal in advancing the understanding of biomechanics and injury mechanisms, particularly in contexts such as automotive safety, sports equipment design, military application, and industrial workplace safety [8], [9], [22], [22]–[25]. Application of ATD headforms alleviate the constraints given by sensitized equipment by observing impact telemetries throughout multiple points of the human head. The frontier study by Newman et al. [25] initially established the methodology of laboratory-based impact simulations using ATD headforms, achieved by conducting recreations of known concussive impacts — governed by on-field head acceleration telemetry of sensitized equipment and digital imaging — and applying the recorded impact energies and directions to dummy structures which simulate the human head and its kinematic traces.

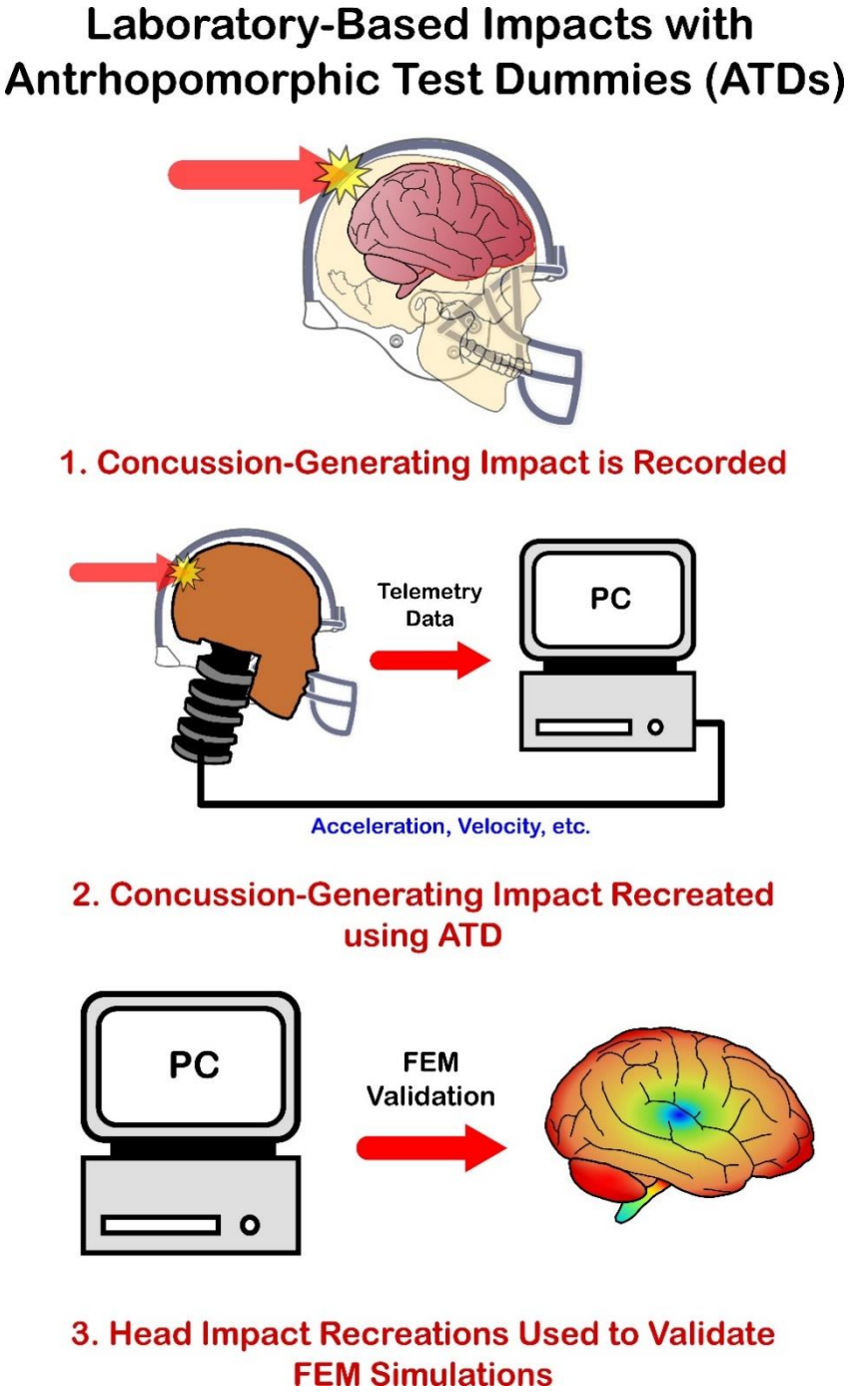


*Figure 2.1 — FEM Validation Process Using ATDs in Laboratory-Based Impact Tests*

One of the primary benefits of laboratory-based impact testing is the ability to establish controlled experimental conditions. In which, researchers can precisely manipulate variables such as impact velocity, angle, and force, ensuring consistency and reproducibility across experiments, and enhancing the reliability of results, facilitating accurate assessment of TBI risk factors and injury

mechanisms. Furthermore, the use of headforms in laboratory settings addresses ethical considerations associated with TBI research involving live and cadaver subjects. By eliminating the need for animal or human subjects, researchers can gather valuable biomechanical data without subjecting individuals or other living beings to potential harm.

Common devices applied as ATD headforms include — with increasing biofidelity — the EN 960, Hybrid-III, National Operating Committee on Standards for Athletic Equipment (NOCSAE), and Hodgson-WSU headforms, of which these devices are often present in use for safety in a multitude of industries in sports and recreation, automotive, and defense applications [8], [22], [24]–[26].

The Hybrid-III headform and neckform attachment are part of a full-body Hybrid-III ATD initially designed for automotive safety testing [25]. The full-body model consists of a cast aluminium frame, to which a removable vinyl skin is applied to the frame allowing for anthropomorphic likeness, such as the geometrical structure of the human head [22], [24], [25]. Furthermore, the headform structure is hollowed out to allow implanting of relevant instrumentation. As of date, the Hybrid-III headform is shown to be the most used device in relevant research, with its use in methodology ranging from impact tests regarding sports injuries and equipment, automotive safety, and military application [25]; as well as providing the availability for ranges of Hybrid-III models, such as the Male 50$^{th}$ Percentile and Female 5$^{th}$ Percentile models.

The NOCSAE headform is specifically designed for the assessment of helmeted impacts, and the full model only concerns the human head. The NOCSAE headform is once more a hollow shell headform which allows for sensor embedding, though is primarily designed for mounting on helmet drop tests and does not consider a design for a neckform. Due to this, mounting fabrications are often developed for its compatibility with the Hybrid-III neckform. Due to its designed purpose for helmeted impacts in sports and recreations, the NOCSAE headform serves as the testing standard for NOCSAE-approved helmets and equipment and established further anatomical accuracy through representation of the dummy head shape, which is more akin to a human head [24], [25].

With respect to the established properties of the Hybrid-III and NOCSAE headforms, the Hodgson-WSU further considers anatomical accuracy through the introduction of a glycerin bladder within the headform cavity to simulate the presence of the human brain. The glycerin bladder, as with any embedded instrumentation, are encased within a urethane skin. Like the NOCSAE headform, the

Hodgson-WSU requires a mounting fabrication onto the Hybrid-III neck to assess relevant impact tests [22].

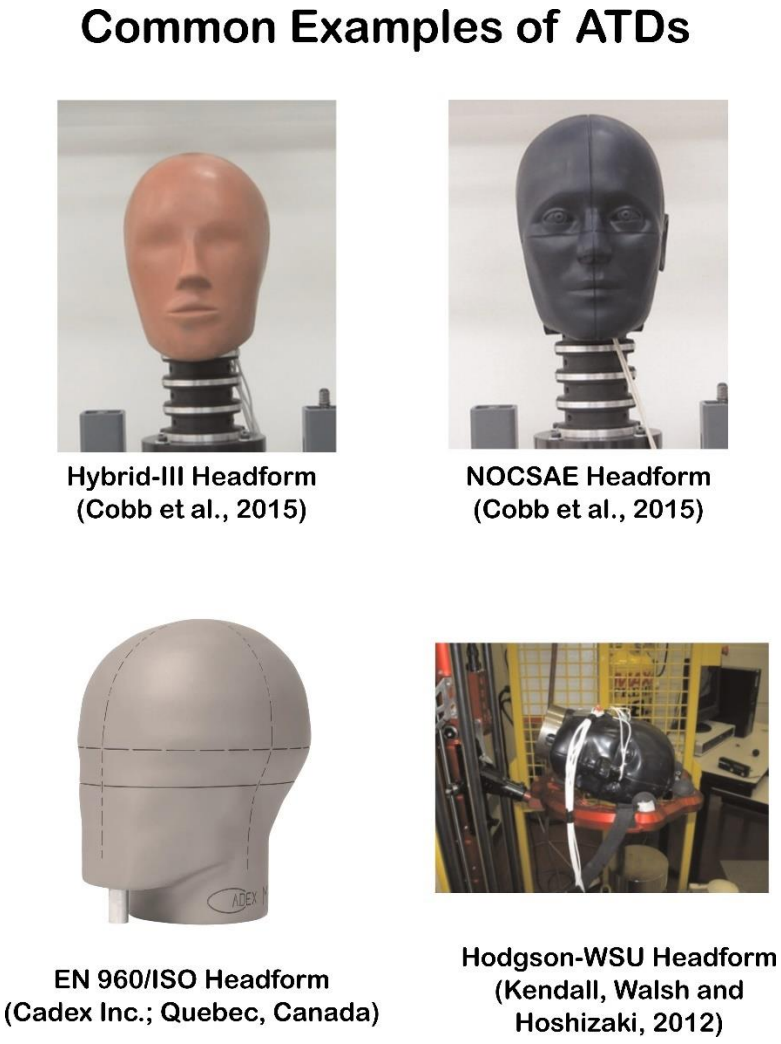


*Figure 2.2 — Common ATD Headforms Studied in Literature [24], [28]*



As such, studies have aimed to compare the performance of these commonly used headforms to observe and quantify their degree of accurate representation of the native human head. The earliest of these comparative analyses; Cobb et al. [24] measured the relative performance of the Hybrid-III and NOCSAE Male 50$^{th}$ Percentile headforms in laboratory-based impact tests. Major considerations between both headforms regard their spatial dimensions and mass. Pendulum

impact tests were conducted amongst both headforms fitted onto the Hybrid-III neck, impacting varying locations of the front, side, and rear of the helmeted headforms, while impactor velocities of 3.1, 4.9, and 6.4 m/s were considered to simulate concussive impacts. Linear and angular acceleration telemetries were observed and further metricized using the Head Injury Criterion (HIC) and Gadd Severity Index (SI) to associate accelerations with head injury. Amongst both headforms, similar response patterns were observed among the correlating impact conditions, though significant differences amongst both headforms were most prevalent amongst impact locations and velocities. The study concludes that the general morphology and design of the headforms yielded performance values with significant differences in helmeted impact testing, where the NOCSAE headforms demonstrated comparatively higher peak values in linear and angular accelerations. It was further established that the NOCSAE headform was the favorable option for impact testing protocols due to its closer anthropomorphic accuracy to the shape of the human head.

A similar comparative analysis was conducted by Koncan et al. [22] observing the Hybrid-III and Hodgson-WSU headforms. Impact tests were performed using a monorail drop rig at varied velocities of 2.5 and 3.5 m/s, from which the headforms impacted a 1” MEP padding in the occipital direction. No considerations were made for varied impact directions. To metricize the recorded impacts, Finite Element Modelling (FEM) utilizing the University College Dublin Brain Trauma Model (UCDBTM) was observed using the recorded impact telemetries as the impact variables, determining values of shear modulus and maximum principal strain (MPS) on the simulated brain model. The study highlighted the influence of ATD construction on the dynamic responses and simulation metrics, indicating that the Hybrid III headform typically generates lower response metrics compared to the Hodgson-WSU.

Both studies signify a challenge in the selection of ATD headform for impact testing, in that, noted differences between the ATDs emphasize the need for careful selection and consideration of headform properties in head injury research. In the conference study by Takhounts et al. [29], [30] to establish mathematical injury criterion models for laboratory-based impact testing, this challenge is further emphasized in that risk curve assessments for brain injuries showed high dependency on the given test dummies, displaying varying probabilities of injuries.

## 2.3 — Modelling Concussion Mechanisms, Computational mTBI-Predictive Thresholds and Scoring Systems

The ATDs presented are often used to validate models which numerically simulate the properties of critical head structures. These models address the need to define an ideal range to simulate native properties for impact. Numerical models assess cranial kinematics and characteristics of a full brain structure under impacts, which have since promoted the considerations for intercranial strain, and parameters not otherwise recognized without intercranial simulation. The following section observes the history of intercranial numerical head models, the current state of the art, and the novels findings of intercranial mechanics in concussion founded by the use of numerical simulations.

### *2.3.1 — Mathematical Injury Criterion Models and Traumatic Scoring Systems*

In conjunction with ATDs and sensitized equipment, mathematical models leverage computational simulations to predict the biomechanical responses of the human head to impacts, facilitating the development and refinement of injury criteria. While ATDs simulate human responses in controlled impact tests, these models provide crucial insights into the dynamics of intracranial head injuries and kinematics, which are otherwise given little-to-no representation in current ATD headforms [8], [9], [25]. Moreover, the integration of sensitized helmets and equipment, enhanced through technological advancements, allows for the calibration and validation of these models against real-world scenarios [13]. Such tools are instrumental in sports, military, and automotive industries, where understanding the mechanics of head impacts is essential for enhancing safety standards and preventing long-term neurological damage.

Of the most seen mathematical models involving laboratory-based and on-field impact testing include the Head Injury Criterion (HIC), developed in 1971 [25], [31]. The development of the HIC is based upon the Gadd Severity Index (SI), from which both are built upon the initially derived Wayne State Tolerance Curve (WSTC) [8], [9], [31].

$$HIC = \left[ (t_2 - t_1) \left\{ \frac{1}{(t_2 - t_1)} \int_{t_1}^{t_2} a(t)dt \right\} \right]_{max}$$

*Equation 2.1 — Head Injury Criterion (HIC) [24], [25], [31]*

$$SI = \int_0^T a(t)^{2.5} dt$$

*Equation 2.2 — Gadd Severity Index (SI) [24], [25], [31]*

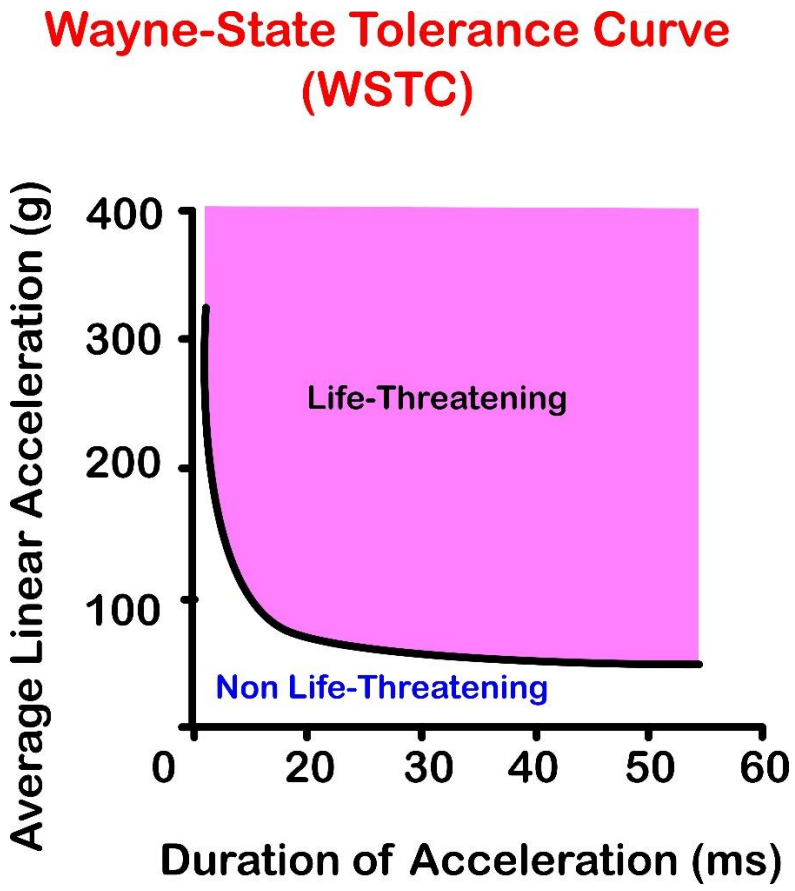


*Figure 2.3 — Wayne State Tolerance Curve (WSTC) for Concussion Detection [24], [25]*

These mathematical representations of traumatic injury evaluate linear acceleration of the head as a function of time. From which, it was determined that high-magnitude peak linear impact accelerations in prolonged impact durations yield life-threatening TBIs [31]. Initial postulation of linear acceleration as a motivator for TBI was regarded in the research to develop the WSTC, from which head impact tests were conducted on human cadaver subjects [25], [31]. These studies have since been applied onto ATDs to superimpose their kinematic signatures with the models determined from these tests [8], [24], [25].

Since then, mathematical injury models have evolved to consider a multitude of factors for injury outside of the limited assessments which strictly characterize TBIs by peak linear accelerations. Models such as the Head Impact Power (HIP) and Generalized Acceleration Model for Brain

Injury Threshold (GAMBIT) have been produced to correlate TBIs to rotational acceleration as a kinematic signature alongside linear accelerations [31]. Continuing studies of recent date, such as those by Hoshizaki et al. [8] and Sano et al. [32], have made attempts to consider evolutions of the foundational WSTC and SI models to consider current kinematic aspects such as rotational accelerations among varying aspects of injury.

### *2.3.2 — Computational Models Through Finite Element Modelling (FEM)*

Mathematical HICs have further extended past the strict observation of kinematic signatures, from which current research has correlated events of TBI to signatures of brain deformations. Metrics such as Cumulative Strain Damage Measure (CSDM), Von Mises Strain (VMS), and Maximum Principal Strain (MPS) have grown in prevalence as significant parameters for the assessment of TBI, following the use of Finite Element Modelling (FEM) to represent the brain tissue under impact scenarios [13], [30].

Popular FEM models such as the Simulated Injury Monitor (SIMon) and Global Human Body Model Consortium (GHBMC) have been considered in their use for recreations of impact scenarios akin to the methodologies found for ATDs [29], [30], [33]–[35]. Both the GHBMC and SIMon models were developed by the National Highway Traffic Safety Administration (NHTSA) through traumatic injury characterizations of mammalian subjects. Both models consider a FEM of the human brain and are initially designed to establish injury criteria for TBIs which are associated with Diffuse Axonal Injury (DAI) in automotive crash incidents [29], [30]. These models observe TBIs through metricizing parameters like CSDM and MPS throughout the human brain, with the GHBMC providing representation of the brain in 50$^{th}$ Percentile Male, and 5$^{th}$ Percentile Female models, among others [36]. Amongst both models, the GHBMC displays the closest biofidelic representation of the human head, with considerations for grey and white matter brain regions such as the corpus callosum, basal ganglia, thalamus, brain stem, and cerebellum. The GHBMC extends its biofidelity further as a part of a whole-body FEM representation with considerations for the skull, cerebrospinal fluid (CSF), and meningeal complex [29], [30], [36].

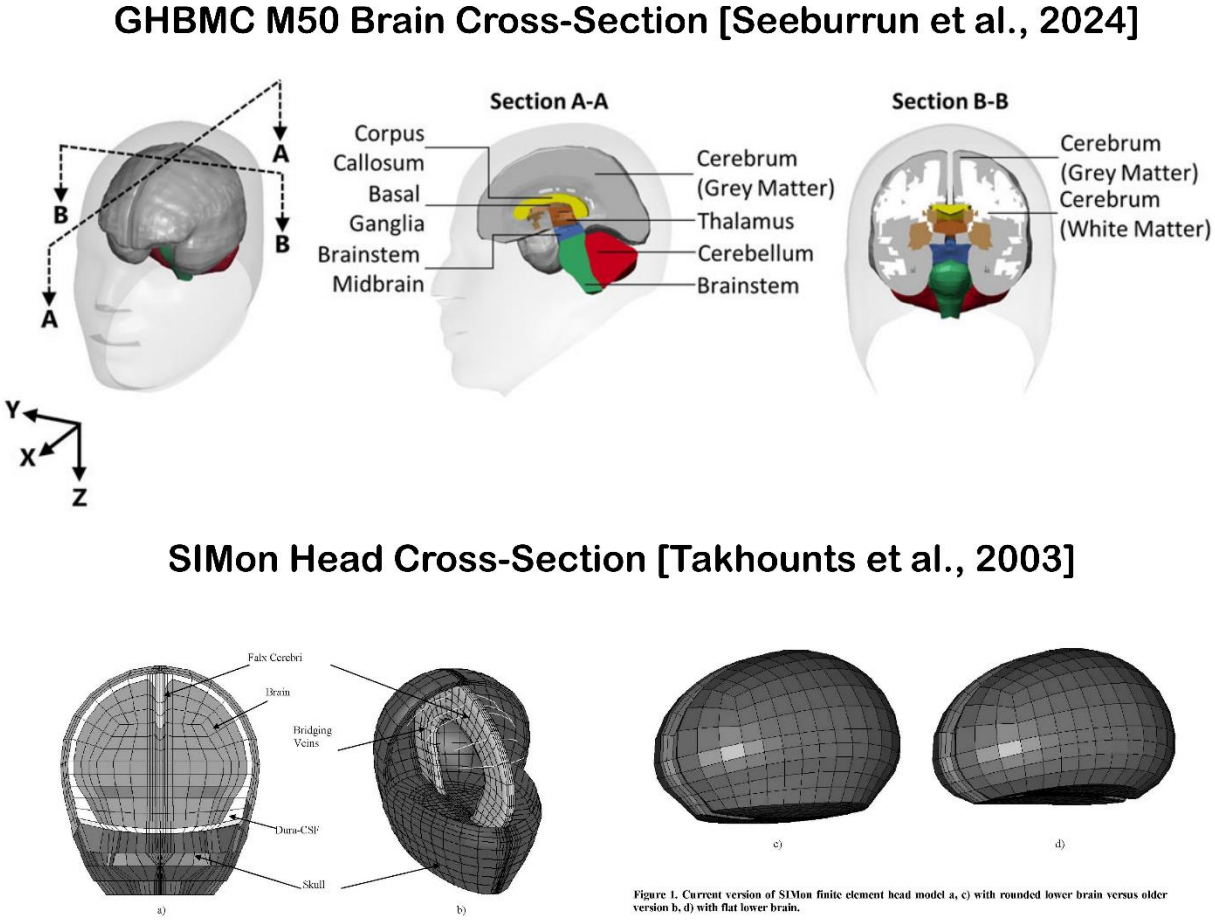


*Figure 2.4 — Cross-Sections for the GHBMC M50 and SIMon FEM Head Models [34], [178]*



Upon applying ATD and sensitized equipment impact data to these computational models, the SIMon and GHBMC models have shown that brain strains, specifically from rotational movements, correlate highly with concussion risks in CSDM and MPS [9], [29], [30]. As such, current computational modelling and simulation of the human head under injurious impact events

have shifted the consensus of injury-generating kinematic signatures to focus on rotational acceleration and cranial strain as the leading cause of concussive injuries.

### *2.3.3 — Expected Strain Ranges and Rates on Brain Tissue in Concussive Impacts*

A major challenge in the characterization and definition of concussion is found in the efforts to establish relevant thresholds for cranial strain and strain rate, to which, injury can be clearly outlined. A review in 2022 by MacManus and Ghajari [6] has been established to define a minimum threshold for TBI. In that, it was concluded in their review of aggregated studies that neural cells undergo significant cell death in-vitro under ranges of at least 20% strain, and at a 10 $s^{-1}$ rate.

The definition of this minimum threshold range for TBI correlates well with FEM recreations of known concussive impacts. Hosseini-Farid et al. [37] studied FEM simulated impacts of the brain, brain stem, dura, and skull. This study used real-world incident reports of golf ball head impacts to simulate impact speeds of 10, 15, and 20 m/s to a head model developed in-house, using MRI and CT scanned images, as well as characterizations of relevant tissues found in literature. Results determined a strain rate range of 14-182 $s^{-1}$ for TBI, though this study observed multiple FEM scenarios of golf ball collisions — simulating mTBI — and blast scenarios to the head — simulating significant Blast Traumatic Injury (BTI) — at varying speeds.

Elkin et al. in 2019 [20] further observed the effects of strain and strain rate dependency by the method of FEM simulation. On-field traumatic injury data was aggregated and recreated on a helmeted Hybrid-III ATD at varying speeds but held a constant impact energy. Impacts were then observed in FEM recreations on both SIMon and GHBMC models using the laboratory-based impacts. It was reported that mean peak strains from impact velocities at 5.5 m/s were ~20%, while strains were experienced at around 35% at ~10 m/s impact, within deviations of ~37%.

### *2.3.4 — Stress Concentrations on Brain Tissue in TBI Impacts*

Another aspect of this analysis is the distribution of cranial stresses under impact. Specific regions of the brain may be subject to greater strains under TBI-relevant impact energies and locations. In the Elkin et al. study [20], further emphasis was placed on head impact location, resulting in variance among peak strains recorded along specific sections of the brain. Regions like the crown and forehead consistently showed lower strains, while impacts to the rear and jaw pad resulted in

higher strains. The study quantified how much impact location contributed to variance in brain strain, finding it accounted for 33-37% of total variance — substantially more than variance from peak head kinematics alone. Thus, the study concluded that the impact location significantly influences brain strain and, by extension, potential concussion risk. Further emphasis was urged to be placed on concentrations of peak strain when considering specific impact locations. Of the peak strains reported in this research, MPS was distributed within the outer cortex of the brain, followed by inner strains of the cerebellum and brain stem.

Another similar study was made by Beckwith et al. in 2018 [19], where impact telemetry data of sensitized from the NFL was aggregated and reconstructed in FEM simulation using the SIMon and WHIM models. In this investigation, MPS, VMS, peak strain rates, and intercranial pressure occurred in the cerebrum (cortex), brain stem, corpus callosum, and cerebellum by order of magnitude. Once again, this study found impact locations to be a signifying aspect as to where peak strains occurred throughout the whole brain and resulted in variability in the aggregated impacts simulated. The study recommended that further validation of the FE models was necessary to establish deeper emphasis on impact locations and their correlations to concussive impacts.

In the case of these studies, peak strains that localized in the cortex were in close correspondence with the established thresholds for injury by MacManus and Ghajari [6], always exceeding the minimum threshold in their respective studies. These studies provide a good basis for the characterization of native and simulant samples and fall in line with each other in establishing a governing threshold for an injury criterion, though further emphasis can be employed for observation of the parameters which precipitate the cause of strain to the specific regions of the head. In this case, all literatures discussed highlighted the influence of impact location towards the regions of MPS on the brain.

### *2.3.5 — Common Concussive Loading Modes and Independent Variables Regarding Impact-Induced Cranial Strain*

In on-field impact scenarios and recorded impact data, cranial strain is regarded as a leading agent to cause brain injury on impact, with peak resultant rotational head acceleration as the correlating parameter on which strain has been reported to be dependent on in these collisions [6], [8], [9], [13], [19], [20], [37], [38]. Determining independent variables which would promote concussive

cranial strains can yield importance such that these kinematic signatures can determine simulative testing methodology for material characterization and ATD device validation.

In the review by Post and Blaine Hoshizaki in 2015 [9], direct correlations between rotational acceleration and cranial strain were established, observing studies of validated FE models through Hybrid-III ATD impact recreations of NFL injury data. While no correlation was made between linear acceleration and cranial strain, both linear and rotational accelerations are expected to increase with each other at the heightened magnitudes of impact energy, and it is suggested that a decrease of one variable will correlate to the reduction of the other. Furthermore, the interchangeability of resultant linear and rotational accelerations on the head during impact is also dependent on the location of impact, where impact vectors away from the head's center of gravity (CoG) are often seen to generate a greater rotational motion, while impacts directly towards the head CoG generate a greater linear motion [9], [13], [39]. This was further identified in the studies regarding head impact telemetries of sensitized equipment, such as the study by Wang et al. [21].

The research found in Bian and Mao [13] further establish a correlation between cranial strain and head kinematics by introducing the consideration of impact durations to FEM impact recreations. The observation of impact duration has been provided in the WSTC [31], however, Bian and Mao assess a novelty by correlating this kinematic signature to current impact parameters, such as cranial strain. Impact scenarios on the GHBMC Male $50^{th}$ Percentile FE model was observed in their average to exceed specific strain levels, and combinations of rotational and linear velocity magnitudes were induced at specific durations of 15, 20, 25, and 30 ms. Furthermore, stress modes of lateral bending, flexion, and extension were introduced. The investigation also introduced some kinematic signatures to consider in head impacts such as peak resultant rotational velocities as well as resultant decelerations. Rotational velocities yielded greater correlations to cranial strain across all ranges of impact while decelerating impacts at prolonged durations were seen to generate similar, if not, greater magnitudes of strain in comparison to accelerating impacts. Discoveries in this investigation align with the findings before; resultant rotational acceleration generates the highest production of strain. Axial rotation typically caused the highest brain strain, while flexion and extension stress modes were similarly matched, with its greatest influence affecting deep tissue brain strains in structures like the corpus callosum and the thalamus. Despite this observation, the linear acceleration of the head should not be left from consideration. Elkin et al. [20] observed a

direct correlation between an increase in intracranial pressure to linear acceleration, though the significance of ICP to traumatic brain injury is yet to be thoroughly established in the literature.

Conversely, some studies have shown that head accelerations which induce cranial strain may not be the only considerable parameter in the assessment of injury, and while the validation for a strain threshold has been established, one can still be made for validating strain rate. A study by Blaine Hoshizaki et al. in 2017 [8] provides validation of the WSTC to consider further kinematic aspects relevant to conditions relevant to sports impacts, such as rotational acceleration. In that, recorded injuries from numerous sports and accidents were once again recreated in Hybrid-III laboratory reconstruction. It was observed that similar impacts among the type of sport would congregate within a specific range within resultant head accelerations and impact duration (in ms). These findings were then correlated to establish an evolution of the foundational tolerance curve as the product of resultant head acceleration and impact duration. What resulted was a threshold curve of exponential decrease in acceleration as impact duration increases, akin to the WSTC. Specifically, lower impact energies can still result in injury depending on how prolonged the impact duration occurred. It was seen that these low-impact, long-duration impacts were often correlated with those found in mTBI-inducing collisions [8]. However, this study did note that the research identifies discrepancies between existing threshold curves and actual sports impact data. It shows that current models often underestimate the concussion risk associated with longer duration impacts that are typical in sports. The paper suggests that a new threshold curve is necessary to better reflect the dynamics of sports-related head impacts, one that would consider both the magnitude and duration of impact, as both rotational and linear accelerations, highlighting the need for different thresholds for different sports environments.

While the previous studies provide emphasis on the initial acceleration of brain tissue for concussive-generating impacts, another study proposed the observation of post-impact head motions and oscillations to signify potential concussive injury. Laksari et al. [18], explores oscillation frequencies of the head which could generate injury, and concludes that the brain and skull react to impact oscillations at a high resonance frequency of 15-25 Hz — an oscillation frequency found common in contact sports. The dynamic numerical model used to determine these results consists of the brain, described as a rigid body within a constraint medium of the skull, where the skull-brain was modeled as an under-damped system. The model was then fitted onto

MRI imaging of post-mortem human subjects under impact tests. The study postulates that at the defined frequency range, the natural frequency of the brain can be amplified by resonance with externally applied oscillations and can result in injurious effects. This resonance could be a possible mechanism for mTBI, as repetitive low-frequency impacts could lead to significant brain strain and injury. This high sensitivity was found to be most prevalent in impacts involving sagittal plane rotations of the head. The findings concludes that current helmet designs and safety standards should consider not only the magnitude of impacts but also their frequency content. Helmets should be optimized to mitigate the effects of low-frequency oscillations.

## 2.4 — Mechanical Properties and Characteristics of Native Human Head Structures, Objectives in Mechanical Simulation and Proposed Simulant Candidates

The parameterization of finite element models (FEM) for the human cranial vault has been achieved through extensive characterization of critical head structures. Significant research has focused on analyzing the material properties of the brain, skull, and interfacing soft tissues. However, a common challenge in these studies is the methodology for procuring specimens. Sample procurement from human cadavers poses ethical and handling constraints [15]. Additionally, recreating in-vivo conditions for native characterizations can introduce confounding variables, leading to a wide range of reported properties in the literature [15].

To address these challenges, research has developed simulant materials that mimic the mechanical, geometrical, and structural characteristics of their native counterparts. These studies serve various purposes, including surgical and educational practices [15], [40], biomedical and tissue regeneration applications [15], [41]–[44], and the development of anatomically accurate head models for FEM validation and intracranial observation [15]–[17], [39], [45]–[47].

The following section reviews current practices in the literature regarding the material properties and characteristics of native critical head structures such as the brain, skull, and meningeal complex. It also examines their microstructural compositions, which influence their mechanical, geometrical, and structural properties, and discusses reported material candidates that aim to replicate these relevant aspects.

## *2.4.1 — The Brain Tissue*

### ***2.4.1.1 — Mechanical Properties and Characterization of the Native Human Brain Tissue***

2.4.1.1.1 — Viscoelasticity, Strain-Rate Dependency and Non-Linear Stress Characteristics

Native brain tissue is shown to exhibit properties of viscoelasticity. Viscoelasticity of a material, in essence, is its ability to exhibit flow properties in an application of strain over time as expectant for a viscous substance, while — through properties of stress relaxation through amorphous polymer chaining — also being able to retain its original shape akin to that of an elastic substance [39], [44], [45], [47]–[51].

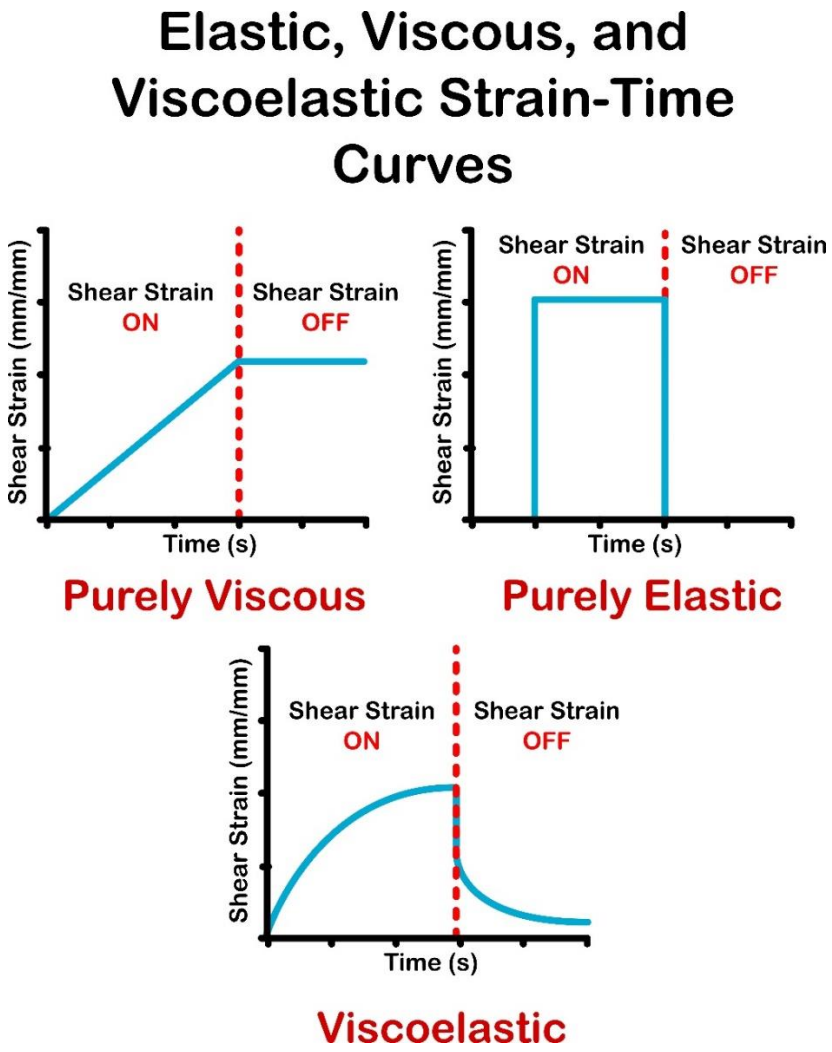


*Figure 2.5 — Stress-Time Curves for Pure Viscous, Pure Elastic, and Viscoelastic Materials*

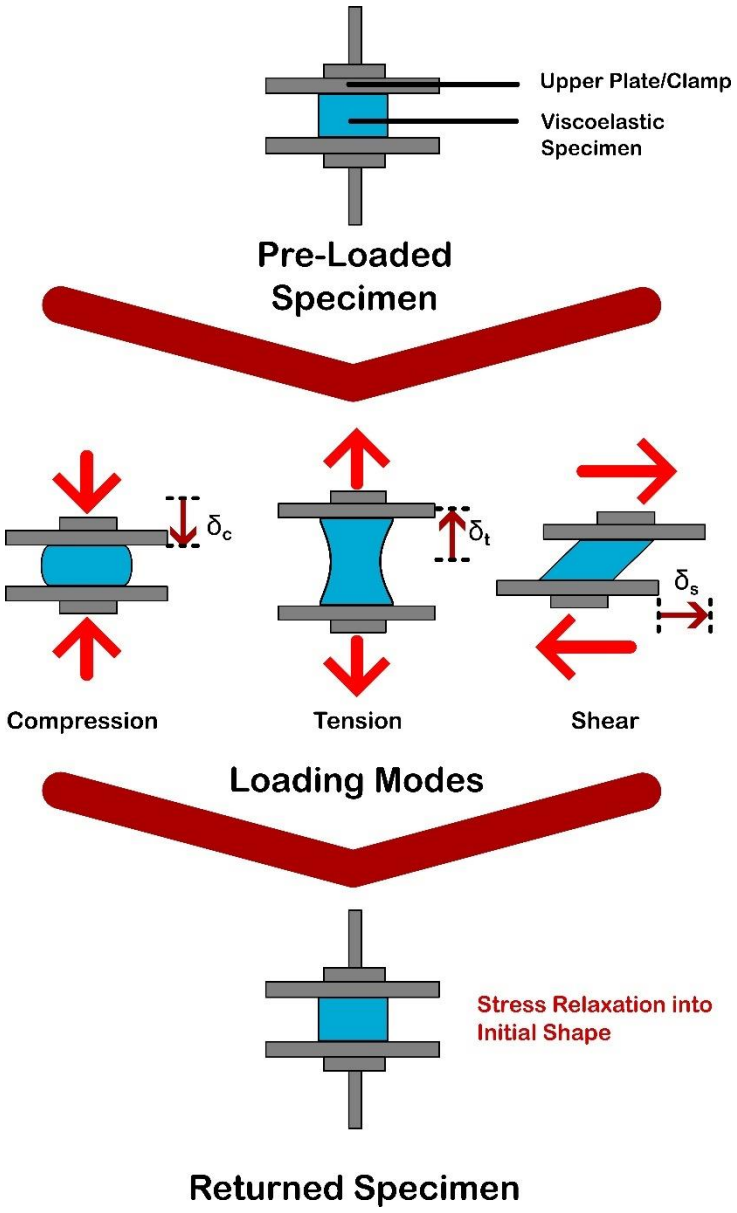


*Figure 2.6 — Physical Viscoelastic Response Observations*

As a result, a significant aspect of its mechanical response is in its non-linear, time-dependent strain characteristics. Meaning, the elastic response given by a loaded specimen of brain matter is wholly dependent on the strain and strain rate acting upon the material, where a combination of a given strain and rate at which it is applied defines the observed moduli and yield stress of the material [15], [39], [44], [45], [47]–[51]. Structurally, this time-dependant elastic behavior is in opposition to the elasticity found in crystallographic metals and semi-crystallographic polymers, imposed due to the stretching of intermolecular bonds [52], the stress relaxation and shape retainment of viscoelastic substances are resultant of the diffusion of molecules within an

amorphous polymer chaining which displace upon the induction of an external energy, and return to its preformed state at the release of that energy due to the intermolecular bonds which retain the initial polymer shape [52].

Furthermore, the viscoelastic nature of brain tissue observes one of a non-linear nature. In that, material properties are shown to change throughout its process deformation. The non-linear viscoelastic (NLV) behavior of brain tissue becomes apparent when observing its stress-strain response when under load. Tests such as quasi-static or stress-relaxation tests often observe a form of non-linear characteristics, which follow a retention of the material back to its pre-stressed state after loading [15], [39], [45]–[49], [51], [53]–[55].

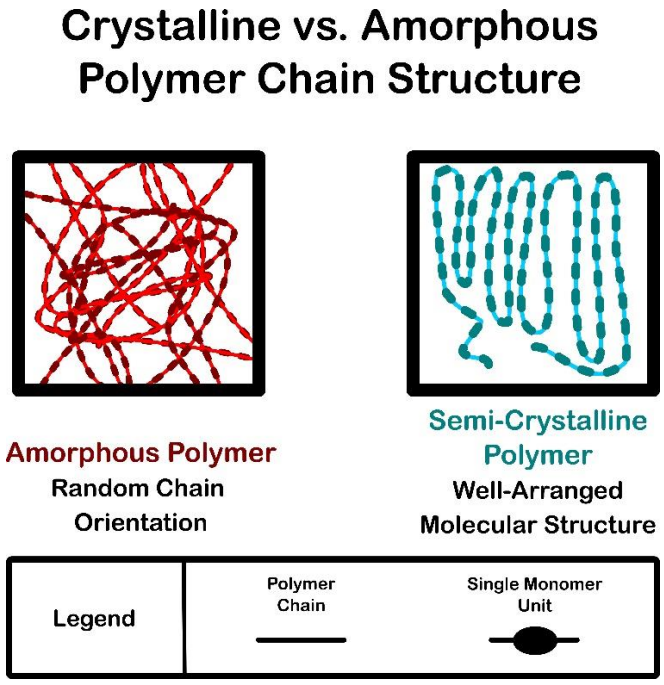


*Figure 2.7 — Amorphous vs. Semi-Crystalline Polymer Chain Structure*

2.4.1.1.2 — Heterogeneity and Anisotropies, and Macrostructural Regional Dependencies

The non-linear rate-dependent behaviour is further exacerbated by the anisotropic properties of brain tissue. The mechanical characterization of native human brain tissues under the stress-strain loading forms of compression, tension, and shear observed by Jin et al. have shown that brain tissue exhibits a strain-hardening behaviour under compression, a strain-softening behaviour in tension, and a relatively linear variation in shear [53]. The microstructural rate-dependent behaviour of brain tissue was more recently observed by Eksandri et al. [56] when conducting

stress-strain tests in tension and compression on native bovine white matter brain samples, of which compression-stiffening and tension-softening properties were proven. The anisotropic non-linear behaviour of brain tissue was hypothesized to be due to the change of cell densities of brain tissue while under loading, caused by glial cell bodies being condensed and acting against compressive forces, while these cell connections detach in tension. This hypothesis was further supported by histological observation of the macroscopic interactions of the glial cells before and after strain was introduced.

Furthermore, the heterogeneous composition of brain tissue is a major factor to consider within its overarching mechanical properties. Native brain tissue is a mixture of two functioning tissues: grey matter and white matter. While both tissue formations are necessary for the cognitive operation of the brain, grey and white matter can be differentiated by their specific functions in performing this overall role of cognitive activity. Chanda et al. describe the role of grey matter as the vehicle for cognitive stimuli in the human brain, while white matter serves its function through information transportation in response to stimuli [48]. In terms of the densities and distribution of these functioning components throughout the human brain, grey matter consists of 40% of the total brain while white matter consists of the remaining 60% [48]. Biologically, this is represented by an increased presence in glial cells in white matter, amongst a presence of other biological compositions of proteins and neuronal fibres specific to completing cognition, processing, and potential motor function [56], [57]. The variation of densities in functioning cells between both forms of brain tissue can be represented by a variety of mechanical properties which differ between characterized grey and white matter specimens. In that, literature has shown that native white matter samples observe to behave elastically stiffer than grey matter samples [6], [51], [53], [56], [58]–[60].

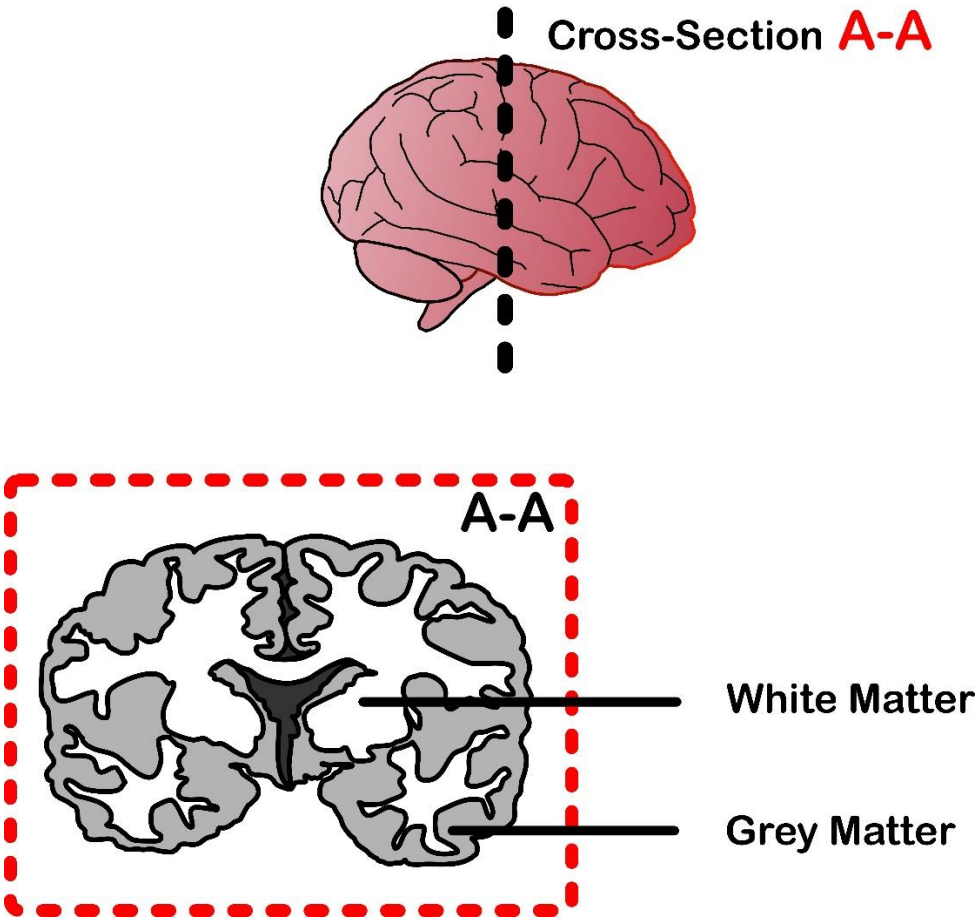


*Figure 2.8 — Cross-Section of the Brain Cerebrum Displaying Grey Matter and White Matter*

Despite many findings agreeing with this observation, some studies have observed several grey matter samples to portray stiffer stress-strain characterizations when compared to white matter [51], [61], [62]. Some limitations and considerations should be made for these studies, however. Firstly, the study from Christ et al. observes the characterization of the cerebellum samples from rat brain tissues, which may not be conducive to the overall characterizations of human or other mammalian brain tissues [50], [62]. Secondly, a major consideration from these studies also suggests a regional anisotropy of brain tissue, where specific functional areas of the bulk brain tissue will result in varying mechanical properties itself, due once again to the variations of cellular components amongst these regions of observation [50], [62].

In the case of this suggestion, other studies which do characterize white matter to be significantly stiffer than grey matter yield regional anisotropic values that agree with this hypothesis [6], [49], [50], [53], [60], [63]. Such considerations of this can be seen in the comprehensive study to

characterize native human brain tissue observed by Jin et al. [53]. This study characterizes human brain tissue across varying strain rates up to 50% strain in tension, compression, and shear and considers grey matter tissue samples extracted from the cortex and thalamus, and white matter tissue samples extracted from the corpus callosum and corona radiata. The stress-strain behaviour in compression from this study shows that grey matter thalamus samples exhibited a stiffer response than corona radiata white matter samples at strains exceeding 40% at medium (5 $s^{-1}$) and high (30 $s^{-1}$) strain rates [53].

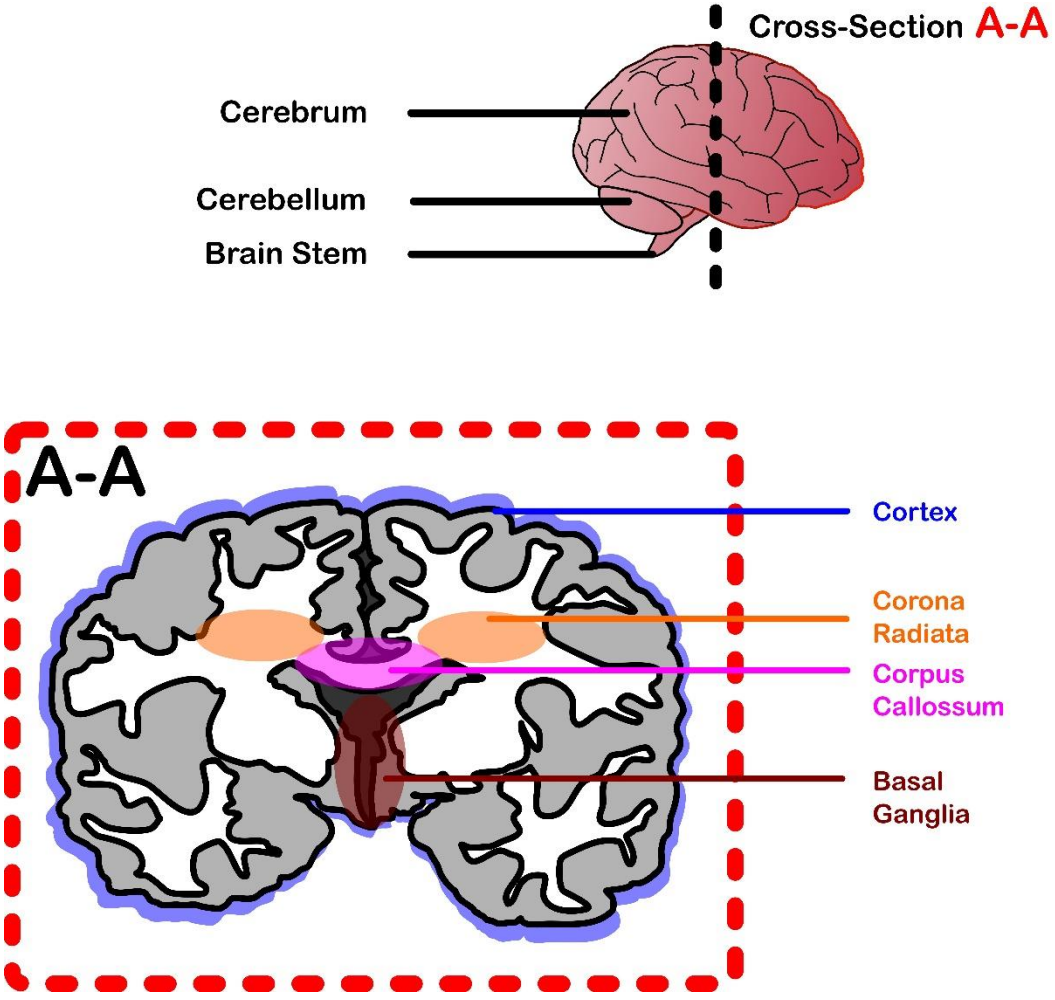


*Figure 2.9 — Cerebrum Cross-Section with Grey and White Matter Regions*

Moreover, a later study by Budday et. al conducted similar tests of human brain tissue in compression, tension, and shear. Samples in compression were loaded quasi-statically at a strain of up to 10% for a quasi-static rate of 0.0067 $s^{-1}$. Brain tissue samples were extracted from the cortex and basal ganglia (grey matter), and the corpus callosum and corona radiata (white matter)

[51]. Results found that the cortex was observed to provide the stiffest response, with the basal ganglia following closely. The corona radiata and corpus callosum exhibited softer responses. This study may not be indicative of cranial responses under impacts, however, in that the experiments observed only tested under slow, quasi-static strain and strain rates. In the study by Jin et. al, initial strains at low strain rates (0.5 $s^{-1}$) also observed that the cortex yielded stiffer responses than the corona radiata, though this observation changes once strains exceeded those found in the Budday et. al study (~15% strain) [53]. In concert with the observations found in Eksandri et al., these results can potentially point to the greater densities of functioning cellular components found in white matter tissues, where the increased presence of these cell bodies yield greater properties of strain stiffening at increased magnitudes of loading, hence the higher magnitudes of stress for white matter at specifically greater strains and loading rates [51], [53], [56].

The studies of Jin et al. in 2013 and Budday et al. in 2015 provide a comprehensive assessment of the characterization of human brain tissue and have served as the basis of a vast number of studies with similar aims [6], [15], [45], [47], [48], [50], [59], [60], [64], [65]. Though, the difference in testing methodologies amongst studies — specifically regarding the variations in specimen procurement, equipment, applied strain and loading rate — yield contrasting results which further magnify the challenges regarding the cause of providing an objective characterization to the brain tissue, proving difficulty in yielding a full spectrum of mechanical behavior for the brain. What can be argued amongst the vast numbers of literature, however, is that while magnitudes of material properties differ amongst studies, observations amongst the specific regions of the brain appear to be consistent, where white matter regions still display stiffer responses at increased loading modes due to their increased strain stiffening effects.

To further emphasize the complex regional anisotropies of the human brain, a more recent study found in Menichetti et al. [64] aimed to establish a comprehensive observation of human brain tissue. The strain rates and ranges established in the paper are in close agreement with values expected to simulate those in traumatic impact [6] — as with those in Jin et al. — testing at strains up to 35% at a rate of 10 $s^{-1}$. To assess the regional dependency of cortical grey matter on human brain tissue and assess the spatial distribution of neuronal cell bodies of the cortex, twelve regions of the brain were captured, which include a variation of grey and white matter areas, and samples from these regions were tested for viscoelasticity. While the findings of the study agreed with the

grey and white matter regional variations found in the papers previously discussed, the discovery found in this research is in the regional variation within the cortex of the brain. Previous papers have considered the cortex as a homogeneous structure throughout the outer perimeter of the human brain [15], [39], [44], [45], [48]–[51], [53], [56], [58], [61]–[63], [66]. This study, however, has proven that there are variations in initial shear moduli in specific areas of the cortex when observed under force-relaxation micro indentation tests [64]. What this study suggests is that while the variation between functional cranial regions still stands, regional variation of brain tissue may exceed current understanding. Thus, complete characterization and simulation of brain tissue may require a full observation of all sections of a brain tissue region, where a proposed candidate for biofidelic simulation may be suitable for a specific region of brain tissue, but not for others.

Furthermore, this hypothesis may extend past characterizations for the previously defined variations in grey and white matter and viscoelastic regions. An idealistic approach to a full simulation of brain tissue may not be defined by a single surrogate material, but rather by a combination of various materials coinciding with specific grey and white matter regions of the brain. These sections can then be assembled in such a way that they can achieve the biofidelity of an entire surrogate structure in comparison to a native human brain. It should also be noted that the papers discussed observe the characterization of brain tissues ex-vivo, where in-vivo characterization of living, functioning brain tissues may yield varying results [6], [64].

2.4.1.1.3 — Macro– and Microstructural Composition of Brain Tissue and its Effect on Material Characteristics

The cellular composition of brain tissue comprises of neuronal, glial, and endothelial cells [67], commonly referred to as the Neurovascular Unit (NVU) [68]. The critical cellular components of the NVU follow specific functions such that the neuronal cells specify in metabolic and sensory regulation throughout the central nervous system, glial cells serve as the physical interface amongst vasculature and cellular components, and endothelial cells specify in the protective lining of the blood-brain barrier [68]. Externally, the function and structural support of the functioning cells are regulated by the extracellular matrix (ECM) [69]. The connections amongst one another neuronal cells are what form the axon fiber microstructure transient throughout the brain tissue. It has been commonly observed that the micromechanical behaviour of cranial axons exhibits a response akin to that of viscoelastic solids [70]. The viscoelastic micromechanical behavior of the

axonal fibers is evident in their extent of property to the macrostructural behaviour of the bulk brain tissue [*See Section 2.4.1.1.2*].

Ahmadzadeh et al. [70] developed a microstructural model of the cranial axonal cytoskeleton microstructure for simulative loading. The basis for this research was branched from the observations of strain-rate dependency in cranial axonal fibres. Characterizations of cranial axonal fibers exhibited significant stretch tolerances up to double its pre-stretch length at quasi-static strain rates, while maintaining the ability to rebound into their pre-stretch state with no sign of damage. This contrasted with the results found of axonal fibers when experiencing dynamic loading rates more expectant for traumatic injury, where distortion of the axonal microtubule substructures observed were akin to those of the structure when under catastrophic depolymerization [6], [71]. It was observed through this study that the strain rate dependant nature of the neuronal axon is resultant of the tau proteins which serve as the crosslinker amongst axonal microtubules, which provide the viscoelastic behavior of amongst axonal structures. From their numerical simulations, high strain rate loading applications were met with mechanical failure of the axonal microtubules, while lesser, quasi-static strain rates observed the tau proteins to slide amongst microtubules, experiencing no damage.

The cellular rearrangement of cranial microstructure is a common observation amongst studies regarding the deformation mechanism of brain tissue. Reiter et al. aim to provide further evidence towards microstructural origin of brain tissue viscoelasticity [72]. To yield basis for numerical simulation, the study performed simultaneous compressive loadings on porcine brain tissue to observe the macroscopic deformation mechanisms with respect to cellular rearrangements. By histological observations of cellular rearrangements following loading, a stress relaxation time constant was able to be determined at which cells were observed to regress to their previous pre-stressed state. This provides further emphasis bridging between the cellular mechanism of brain tissue under deformation and the macroscopical viscoelasticity of bulk brain tissue, in that the stress relaxation behavior reinforces the non-linear, time dependent response of a viscoelastic substance.

Due to the relative infeasibility to yield a quantitative observation of brain tissue mechanical response within the microstructural scale, a considerable number of studies regarding this matter have observed characterizations by simulation or through qualitative histology. Histological

observations of brain tissue characterizations have provided in-depth insight on the cellular mechanisms when tissue specimens are loaded and deformed, allowing for the visualization of the viscoelasticity and anisotropies of the brain tissue at the cellular level. A notable example of this method is found in the study by Eksandri et al. [56]. Employing histological observations of bovine brain tissue under tension and compression, the effect of brain tissue anisotropy was determined through cellular rearrangement. It was seen that the tension-compression anisotropy was resultant of cellular rearrangement of glial cell bodies in which cells were condensed to withstand compressive forces, while these cell connections detach in tension. This observation aligns well with the non-linear stress-strain anisotropies of brain tissue under tension and compression, where the tissue exhibits a strain-stiffening exponential curve of stress-strain under compression, while a strain-softening logarithmic curve is experienced under tension [53], [56].

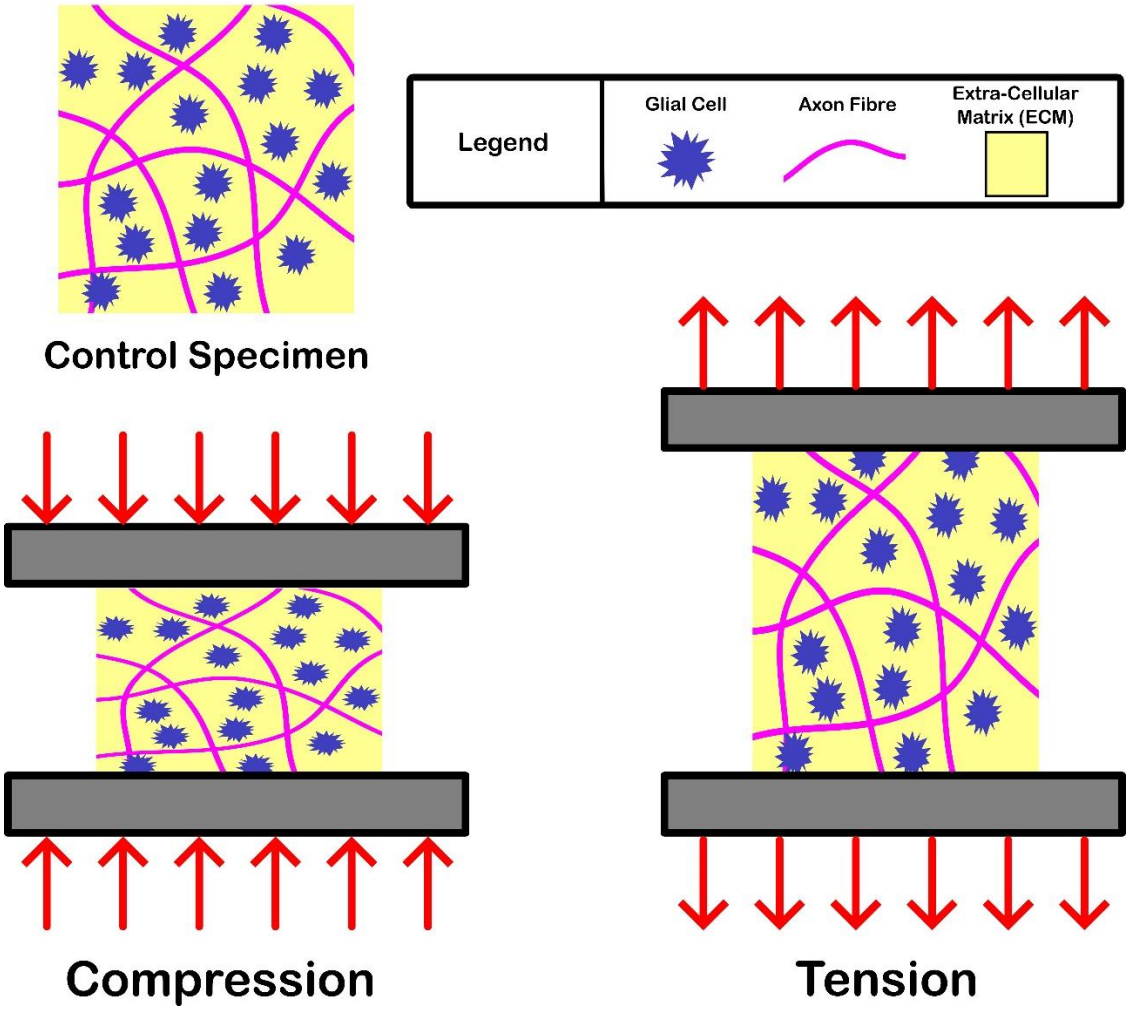


*Figure 2.10 — Brain Tissue Microstructure Exhibiting Tension-Compression Asymmetry*

Another consideration that can be made regarding the cellular influences on the bulk material property of brain tissue is in the regional heterogeneity of various functional sections of the brain. The study by Mota et al. [67] has shown volumetric observations of the relationship amongst cell interactions through method of isotropic fractionator. The observations have highlighted to exist that certain macrostructural regions of the brain tissue comprise of specific volumes and concentrations of neuronal cells to elicit their intended functions and performances. It was seen that the regions of the cerebral cortex and cerebellum amongst a suite of mammalian brain tissues, glial cell body mass fractions witness a consistent variation, the neuronal cell fractions comprising of the axonal fibres varied greatly amongst tissue regions. The increased presence of neuronal fibres in specific regions of the brain, in conjunction with their presence as a critical component in the mechanically influencing axon fibre structures, promotes the correlation to the regional dependencies in brain tissue. Specifically, stiffer responses in some regions of the brain — such as those of the white matter deep tissues [49], [53], [58] — are likely due to their neuron-dense compositions in structure.

The observations in review of the structural compositions of brain tissue have shown to directly point to the consistent macrostructural observations found in the dearth of studies characterizing the native brain tissue. Just so, simulation of critical components for the human skull-brain should consider the aspects which elicit the mechanical behaviors they aim to mimic in characterization and manufacturing. Understanding of these structural compositions and their influence on cranial mechanics can thus translate towards the reasonings to the portrayal of brain tissue found in the native characterizations, reviewed in the previous sections.

Specifically, the bulk structure of brain tissue as a viscoelastic substance appears akin to that of an amorphous polymer, such that its cellular chains are constructed and interlinked within a functional and structural medium [52], [67], [70], [73]. In this case, the assortment of NVUs and axon fibres comprise of the brain tissue's polymer chaining while these chains occur within the ECM as its structural medium [18], [67]. Formation of this manner in the guise of an amorphous polymer provides connection to its performance as an NLV substance, where artificial materials of similar structure can aim to yield similar performances in NLV and directional anisotropies. Furthermore, simulation of regional dependency can aim to mimic the regional dependencies of brain tissue by alteration of the density in cellular units within the amorphous polymer chain, as per the

observational studies conducted by Mota et al. [67]. This can be achieved by assessment in the alteration of concentrations involving the crosslinker components of simulant materials, depending on the materials studied.

2.4.1.1.4 — Methodological Considerations: Specimen Procurement, Species Dependency, Age and Sexual Dependency, and Ex-Vivo Testing

A common challenge in the characterization of human brain tissue is the process of procuring specimens for study. Characterization studies of brain tissue consistently emphasize the ethical and biosafety constraints associated with procurement, as well as the limited availability of human brain specimens [15], [45], [50], [74], [75]. Many experimental studies mitigate these issues by using various mammalian brain tissues, which avoid the handling and availability restrictions of human brain tissue [15], [44]–[47], [50], [74], [76], [77]. Budday et al. [15] reviewed characteristics differences from mammalian brains to human brains. From the studies reviewed, it was implied that a negative correlation between stiffness and total brain volume is present, suggesting that smaller brains tend to have a stiffer response. However, this hypothesis contradicts some shear relaxation experiments, where human brain tissue was found to be stiffer than porcine brain tissue. Despite this, the studies which have employed animal models to characterize brain tissues have argued that minimal significance to the human brain were observed [15], [44]–[47], [50], [74], [76], [77].

Further challenges involve the post-mortem extraction of specimen samples for ex-vivo testing. Degenerative effects begin immediately after death, requiring prompt commencement of post-mortem brain tissue testing [15]. This process includes procuring the brain, preparing sample specimens, setting up testing apparatus, and conducting tests, all with utmost efficiency to ensure behaviors akin to those in living subjects.

Ex-vivo testing of brain simulants must also simulate in-vivo environments to accurately capture native properties. Significant variations in properties occur due to differences in temperature [15], [45], [49] and hydration [49], [78]. Singh et al. [45] conducted ex-vivo quasi-static compression tests on porcine brain tissues, finding significantly stiffer elastic properties and increased initial shear modulus at body temperature (37°C) compared to room temperature (22°C). Similarly, DMA frequency sweep tests on human brain tissue by Forte et al. [49] showed increased stiffness

(Storage Modulus, G') with temperature increases, although humidity control was a factor in these changes.

Age also affects the reported properties of brain tissue. Budday et al. [15] found linear declines in whole-brain elasticity from ages 18 to 72. Sack et al. [79] investigated the effects of physiological aging and gender on brain viscoelastic properties using multifrequency magnetic resonance elastography (MRE). With a mean participant age of 49.35 ± 18.78 years, the study observed a 0.8% decline in elasticity and viscosity per year, with significant age-related changes noted.

MacManus et al. [65] studied the effects of age on multiple mammalian brain specimens, including mice, rats, and pigs, focusing on adolescent and young adult stages. Microindentation stress-relaxation tests showed decreased brain tissue stiffness with age, particularly during the transition from adolescence to young adulthood.

Takamura et al. [80] used MRE on 50 healthy individuals aged 20-69 years, balanced for sex, finding significant negative correlations between age and stiffness in most brain regions, except the cerebellum. The annual stiffness decline ranged from 0.0136 to 0.0049 kPa per year.

Arani et al. [81] also employed MRE to observe age and sex effects on brain tissue stiffness in 45 healthy volunteers aged 56-89 years. Significant linear correlations were found between age and stiffness in several brain regions, predicting an annual cerebrum stiffness decline of 0.011 ± 0.002 kPa.

Regarding sexual dependency, inconsistencies exist in the few reported studies. Sack et al. [79] found female brains to be approximately 9% more solid-like than male brains, making female brains appear mechanically younger by more than a decade ($p = 0.016$). Takamura et al. [80] observed no significant sex differences after adjusting for age, while Arani et al. [81] found stiffer brain tissue properties in females, particularly in the temporal and occipital lobes.

#### *2.4.1.2 — Mechanical Simulation of the Native Brain Tissue*

The previous section aimed to establish the characteristics necessary for the full simulation of the human brain, as well as yield some suggestions as to how surrogate materials can mimic brain tissue given the prescribed nature for injury. Here in this section, several studies which have proposed biofidelity to specific viscoelastic materials will be considered and evaluated. Adopting the findings from the previous sections, their research will be reviewed regarding the suggested

materials' ability to match the characteristics of brain tissue, as well as if the methods for testing can closely simulate the validated conditions for injury. Multiple papers have proposed a plethora of materials, though many are dependent on a specific application and only a selection of materials aims to consider simulation akin to mTBI [14], [39], [44], [45], [47]–[49], [82], [83]. In that respect, arguments made for biofidelity often vary in the literature [39], [40], [43]–[48], [82], [83].

2.4.1.2.1 — Non-Linear Viscoelastic (NLV) Simulation with Amorphous Polymers: Objectives in Simulation

The main goal commonly observed in material characterization of brain tissue simulants appear to be the attempt to capture the bulk NLV properties of brain tissue with an assortment of artificial polymers. In that, all the proposed materials appear to be elastomeric, with the leading assertion in emergence being the viscoelasticity of the material relative to the native brain tissue [39], [43]–[45], [47], [48], [48], [84], [85]. Amorphous viscoelastic polymers, or elastomers, have been the key basis of observation for tissue simulant characterizations and experiments, such that their material behaviour exhibits properties akin to those observed in natural soft tissue structures [43]. As such, these materials have been used in a suite of studies regarding the reconstruction and mimicking of human organs with these materials and methods [43].

A main consideration in their ability to recreate the non-linear, time-dependant strain nature in material characterization is in their compositional molecular structure, like those of the cellular compositions in native soft tissues (See Section 2.4.1.1.3). The microstructure of amorphous polymers gives in to the varied assortment of polymer chains which physically entangle and chemically bond amongst themselves to prove the form and structure of a viscoelastic substance. Which, to exhibit an elastic stress performance, these amorphous polymer chains must be covalently bonded amongst one another to form a network of polymer chains, a process called crosslinking [52].

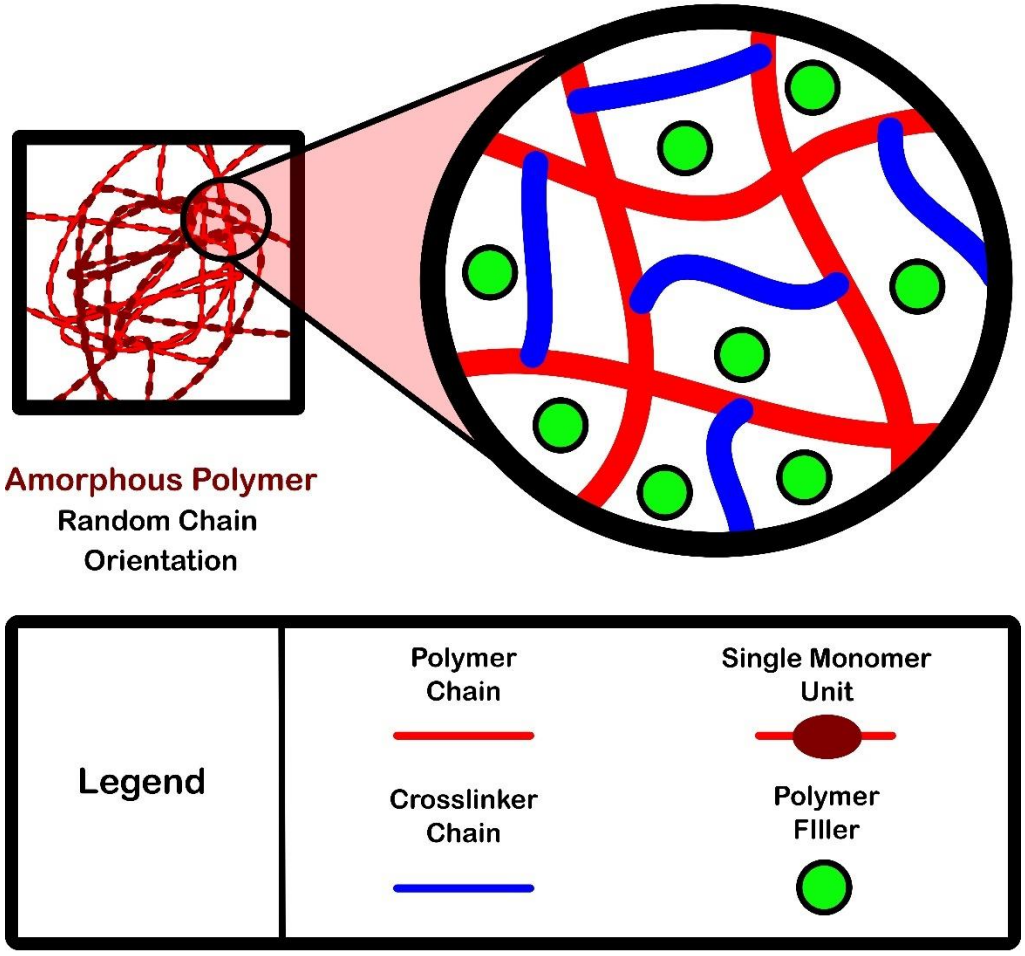


*Figure 2.11 — Amorphous Polymer Crosslinking*

The degree to which crosslinked elastomers experience uniaxial elastic stress is dependent and directly proportional to its concentration of crosslinked polymer network chains, as well as the degree of physical chain entanglements ("physical crosslinking") found within the closely packed polymer network structure [52], [86], [87]. The presence of physical chain entanglements is more prevalent amongst networks with longer polymer chains, which can promote greater opportunities for entanglement along the chain length. As such, the density of these parameters can significantly influence the elastic performance — or "stiffness" — of the material. The process of chemical crosslinking to produce an elastomer structure often involves the introduction of two-part viscous mixtures, denoted as parts A and B. For instance, part A would regard the polymer base which contains the necessary molecules and chains which comprise of the backbone of the amorphous

polymer network, while part B serves as the relevant crosslinking agents and fillers which conjoin and stiffen the polymer chains to transition the composition from a viscous substance to a viscoelastic solid [52], [87]. The formation of elastomeric materials under this method are most often witnessed amongst natural rubbers such as those comprised of silicone [16], [17], [45], [46], [48], [52], [87], or of the sulfur based vulcanized rubbers found in multiple engineering applications [52].

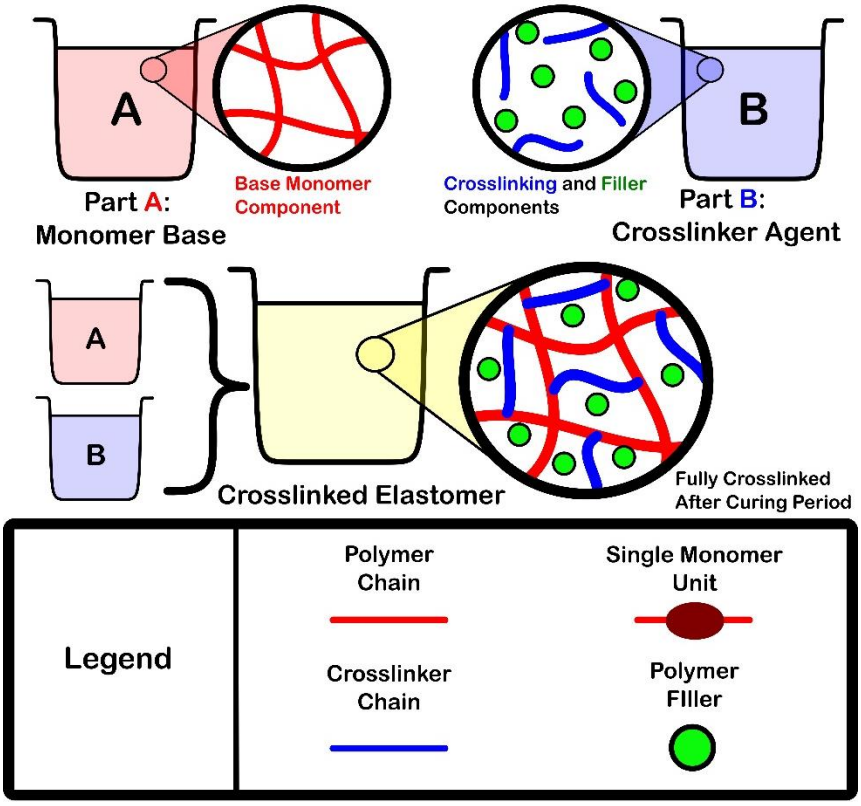


*Figure 2.12 — Crosslinking Elastomer (Rubbers) Formation Mechanism*

Alternatively, linear amorphous polymers can form crosslinked elastic structures through their introduction as a solvent into a homogeneous solution, a process called swelling [52]. In the formation of a swollen elastomer, the polymer solvent begins crosslinked as an inert polymer structure. When introduced into the solution at a defined concentration — either in volume or weight (v/v, w/v, w/w), the solute substance provides the framework from which the polymer network is filled by method of diffusion or osmosis of the given solute, therein forming an elastic substance once the solvent is completely dissolved and swelling reaches an equilibrium [52]. This process of formation is most seen amongst natural hydrogels which utilize the presence of water

as its swelling solute, such as the plant-based agar or alginate gels [43]–[47], [82], [83], or animal-based porcine and bovine gelatins [42], [45]–[47], [88]–[90].

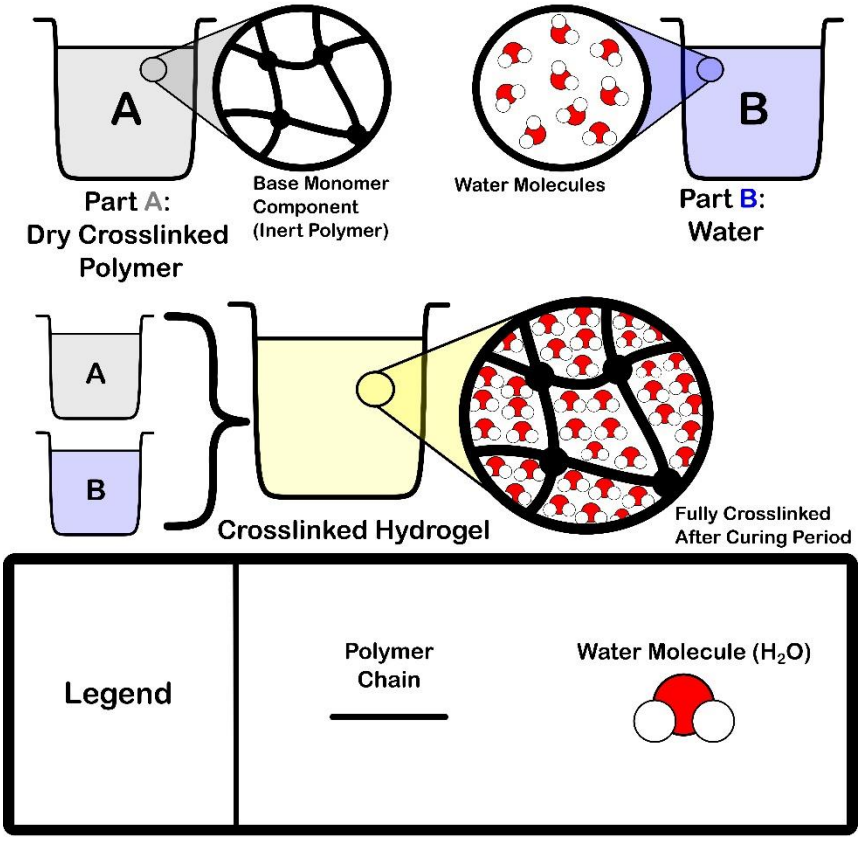


*Figure 2.13 — Hydrogel Crosslinking Mechanism*

Regarding their molecular representation akin to brain tissue, hydrogel swelling substances appear to display the closest structural resemblance to natural soft tissue formations, with both witnessing a polymer structure with an abundance of water to achieve its gel-like state [91]. Still, a challenge lies in the ability for an amorphous polymer structure to simulate the entire structural formations of natural tissues. That being, the form and function of living tissue are greatly intertwined, and thus, the mechanical characterization of natural tissue gives in to the hierarchal structure of its composition to successfully execute its intended functionalities (See Section 2.3.1.1.3).

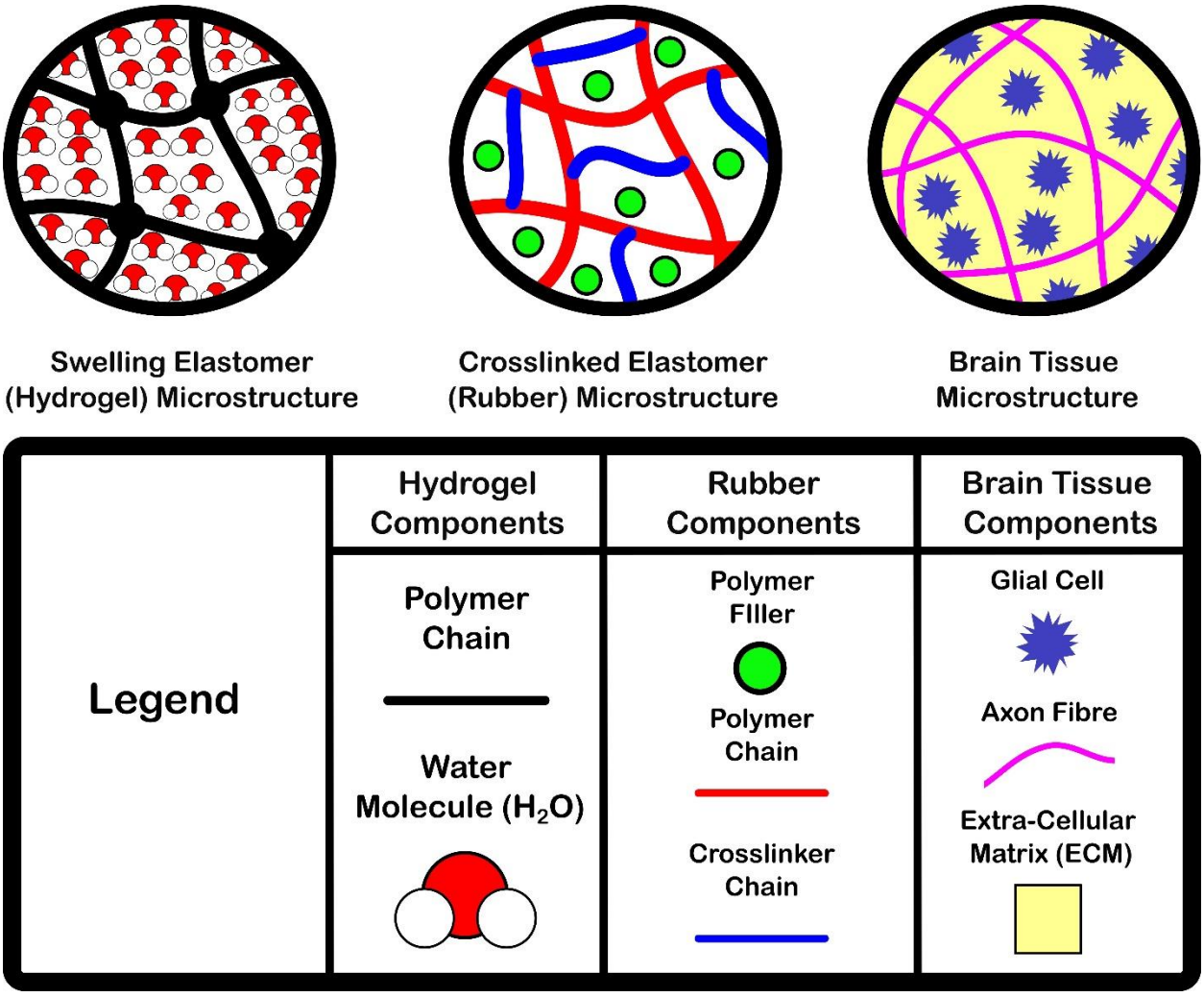


*Figure 2.14 — Microstructural Comparison Between Simulant Elastomers and Brain Tissue*

In consideration of this, characterization research of full-scale mechanical tissue simulants has often relegated their studies to the representation of bulk material properties in relation to soft tissues [42]–[47], [82], [83], [88], [89]. Regardless, accurate simulation of bulk material property still presents relevant use cases for its achievement in the matter. Most notably, phantom material bulk property representation of whole organ structures can give way to physical assessment of impact kinematics and injury thresholds at in-vivo levels of observation while mitigating the ethical and procurement concerns which entail the use of living beings or cadaver subjects (See Section 2.3.1.1.4, and 2.5.1). The following section observes proposed bulk property material simulants for the brain tissue, of which all reviewed studies consider some form of elastomeric

structure for the representation of brain tissue with varying methodologies and metrics of native representation.

2.4.1.2.2 — Proposed Simulant Candidates in Literature: Crosslinked Elastomers and Hydrogels

Wermer et al. [40] aimed to characterize brain tissue simulants for recreating blast-induced TBI. The study tested ballistic gelatin, gelatin derived from bovine bone and skin, and polyacrylamide (PAA) in 10%, 12%, and 15% volume in water weight (w/v) to generate respective elastic moduli in tension, compression, and density in shear. Each surrogate sample's material property was compared to grey and white matter characterizations found in literature, evaluated for biofidelity and ease of formation. The viscoelastic storage modulus (G'), loss modulus (G"), and density (ρ) in tension, compression, and shear were assessed using MTS testing of dog-bone formations in tension, flat-plate unconfined compression, and a rheometer for shear tests. PAA was identified as the most ideal candidate due to its ease of formation and tunability for specific mechanical properties. However, while all materials except ballistic gelatin exhibited compression-hardening and tension-softening behaviors, their magnitudes greatly exceeded the values found in literature. The strain rates tested (0.05 $s^{-1}$, 0.2 $s^{-1}$, and 0.5 $s^{-1}$) were significantly lower than the required 10 $s^{-1}$ threshold for simulating TBI, though strains tested were well above the defined threshold, reaching up to 50% [6], [40]. It is important to note that while PAA's tunability makes it an attractive candidate, acrylamide, a fundamental monomer used in its formation, is carcinogenic and neurotoxic [40], necessitating extensive caution.

Falland-Cheung et al. [47] examined the elastic behavior of gelatin, alginate, agar/glycerol, and agar/glycerol/water to simulate fresh porcine brain tissue. Compression tests at 0.25, 1, and 1.6 $s^{-1}$ were conducted on porcine and simulant samples, with strain ranges captured in steps of 0-20%, 20-40%, and 40-50%. The study found that while all candidates exhibited viscoelastic behavior at all strain ranges, their properties greatly exceeded those of porcine brain samples, particularly at medium (20-40%) and high (40-50%) strain steps. No specific material was identified as an ideal candidate, but the behavior of each material was considered. The strain rates tested did not correspond to those expected in blunt impact scenarios, highlighting a limitation of the study. Nonetheless, the study provides a direct comparison to brain tissue samples, primarily using porcine brain due to its similarity to human brain mechanical behavior and grey-to-white matter ratios [15], [45], [47].

Singh et al. [45] conducted a similar study comparing cranial simulants to porcine brain tissue, introducing viscoelastic testing using a Digital Mechanical Analyzer (DMA) in frequency sweep to record G' and G". The same materials from the previous study were used, with variations in (w/v) concentrations. No specific strain rate was established for the compression tests, but the tests were described as quasi-static. Strains were captured past 50%, and DMA oscillation frequencies were up to 200 Hz. The study fitted stress-strain behaviors to an Ogden hyperelastic model for all materials, capturing statistical variations compared to the control hyperelastic curve of porcine brain samples. Post-mortem effects on brain tissue characterization were also observed, with no significant changes noted after 24h and 48h post-mortem. Bovine gel at 3% and 5% wt. (w/v) closely matched porcine brain tissue in quasi-static compression, while agar gel aligned well during sinusoidal compression. This study validates mechanical analysis of brain tissue by considering post-mortem time effects but suffers from limited sample sizing. Brain tissue samples were a mix of grey and white matter, potentially biasing results.

Natural hydrogels, such as animal-based bovine and porcine gelatins or plant-based alginate and agar gelatins, are often proposed simulant candidates. While these materials exhibit some biofidelity, their manufacturing methods and material longevity present challenges for full-scale brain phantoms. Navarro-Lozoya et al. [46] assessed material degradation of swelling hydrogels and emulsion simulants in a full brain model, finding significant stiffening and weight loss after eight days. This highlights the need for short-term biofidelity consideration.

As an alternative, two-part silicone-based elastomers have shown promise due to their avoidance of water and ease of forming viscoelastic solids. The development of these silicone elastomers requires the composition of a Part A polymer base comprised of vinyl-terminated polydimethylsiloxane (PDMS) [89], [90]. PDMS requires an addition-cure system composing of a Part B cross-linking catalyst, in which the vinyl groups at the ends of the PDMS chains react with the silicon-hydride groups during the curing process, forming cross-links between the polymer chains. Common crosslinking catalysts observed include the addition of platinum for its relatively efficient curing times, as well as thermal and mechanical stability [89], [90].

Chanda et al. [48] tested variations of EcoFlex™ silicone, finding that altering (A) concentrations captured brain tissue behaviors at specific strain rates. Sylgard 527 PDMS dielectric gel, tested by Singh et al. and Kenry et al. [45], [86], showed significant performance in frequency sweep DMA

compared to porcine tissue, though handling issues were noted. Sylgard PDMS continues to show promise, with Zhang et al. [84] testing 1:10, 1:70, and 1:80 (A:B) concentrations of Sylgard 184 for unconfined compression simulations. Results indicated that reduced A polymer base concentrations matched porcine brain performance at non-shockwave strain rates.

In summary, various materials show potential as brain tissue simulants, with consistent biofidelity observed in elastomers formed through solution swelling or chemical crosslinking. Other elastomeric materials of alternative polymerization methods have been considered in study, such as the photo-crosslinking Gelatin Methacrylate (GelMA) [43], which has shown promising results in relative performance to human soft tissues in characterization. However, curation of this material, as well as the biohazard effects to aquatic life found in some common photoinitiator additives such as Irgacure 2959® [42], prove this material to be more challenging in sample procurement and repeatability in the scope of a full-scale model, and thus was not considered for bulk material analysis of simulant characterization.

#### *2.4.1.3 — Characterization and Analysis Methods for Native and Simulant Cranial Brain Tissue*

When reviewing the comparison methodology amongst simulant materials in relation to brain tissues, another commonality observed is such that characterization methods take after those used for native brain tissue studies (*See Section* 2.3.1.1). Due to the NLV nature of the brain tissue and simulant elastomers, further consideration must be taken place to assess material response outside of its stress-strain curve. Properties which pertain to its viscous and elastic parts, such as its energy storage, dissipation, strain stiffening/softening, and relaxation properties must be considered.

##### 2.4.1.3.1 — Uniaxial Testing and Stress Relaxation

A common application for the characterization of native brain tissue includes that of the uniaxial testing. This method is employed to assess bulk mechanical properties found in viscoelastic materials such as those of native brain tissue as well as its elastomer simulants. As such, these materials have been found in literature to be tested in uniaxial compression [45]–[47], [49], [54], [56], [56], [92]–[94], tension [48], [55], [56], [70], [82], [87], [95], [96], and shear [78], [97]–[99]. Characterization of these materials in all loading modes have thus further emphasized the significant regarding the anisotropic characteristics of brain tissue, with results often displaying varied viscoelastic loading curves among the tested axial directions. Characterization tests

comparing viscoelastic simulants to their native counterparts will often observe and compare the general loading curves of simulants relative to their native counterparts, or by comparing parameters yielded from constitutive modelling of both native and simulant experimental stress-strain data.

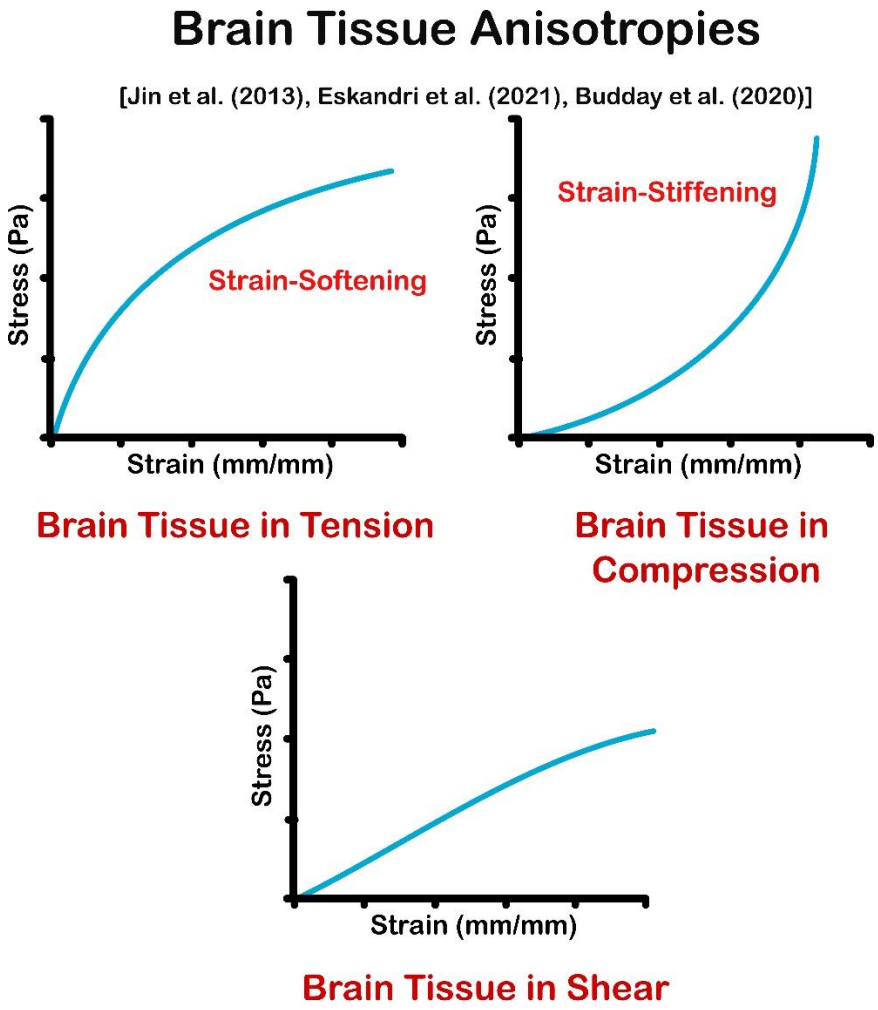


*Figure 2.15 — Tension, Compression, and Shear Stress-Strain Curves of Brain Tissue [15], [53], [56]*

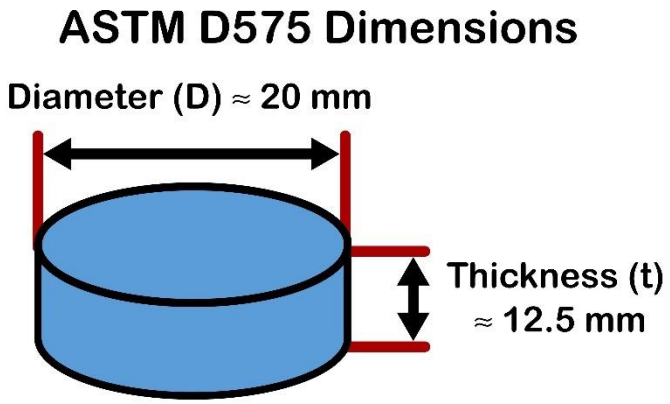


*Figure 2.16 — Common Testing Standard for Brain Tissue and Simulant Characterization: ASTM D575 Dimensions for Rubber Properties in Compression*

Alternatively, these uniaxial tests have been further employed to observe the viscoelastic properties of stress relaxation of the materials. From which, devices such as rheometers which are developed to capture the material properties of viscous and viscoelastic materials, can observe the degree to which viscoelastic solids relax to an equilibrium state following and holding a sequence of applied strain. In characterization tests of simulants comparing to their native counterparts, the observations of the NLV load curve are further supplemented with the equilibrium stress at which the material's relaxed state is held.

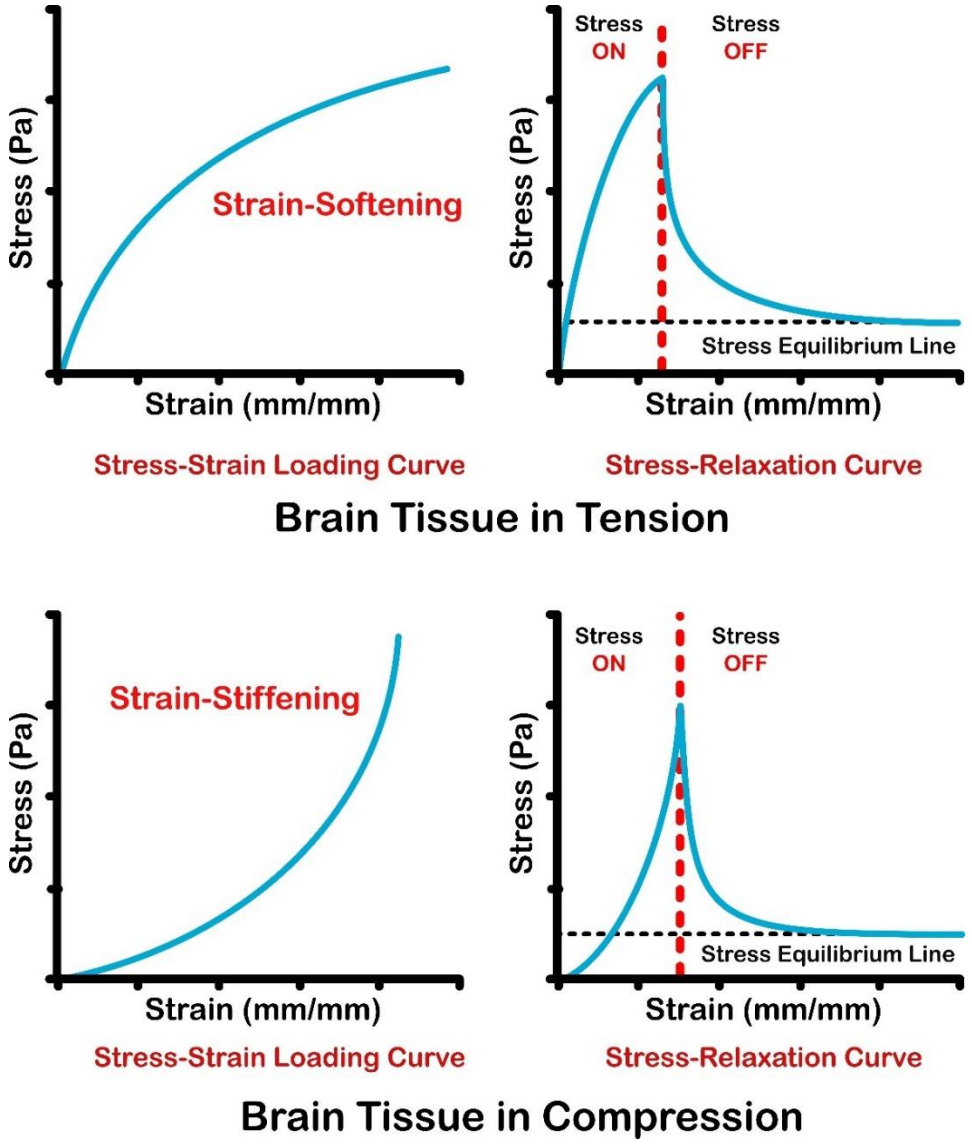


*Figure 2.17 — Stress-Relaxation Loading Curves for Tension and Compression*

2.4.1.3.2 — Hyperelastic Constitutive Modelling and Alternative NLV Characterization Methods

The observation of non-linear stress-strain behavior varies dependant on the elastomer, such that examination of a material's moduli characteristics requires intricate definition across its entire range of deformation. Considering characteristics of time-dependency and anisotropy in materials such as the brain tissue and simulant elastomers, full evaluation of a viscoelastic substance's stress-strain characteristics would be at the expense of time and computation. Thus, computational curve-fitting models have been extensively employed for the non-linear characteristics of these materials, such that the selection of a distinct curve-fitting model can accurately represent the anisotropic NLV of brain tissue and its simulant materials.

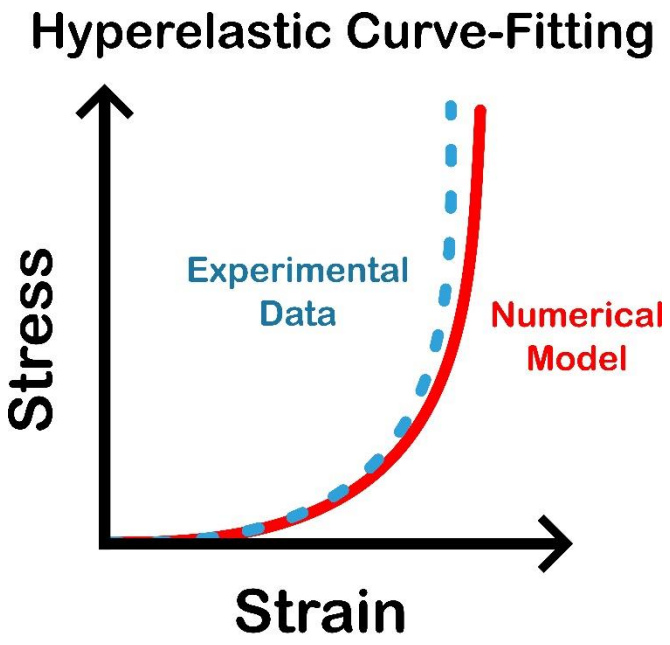


*Figure 2.18 — Hyperelastic Curve-Fitting Methodology*

Across early literature, a challenge in defining an accurate curve-fitting tool was presented. Research characterizing the brain tissue often displayed variability regarding the selection of phenomenological, isotropic strain-energy models [15]. The postulation of hyperelastic models assume that the given materials exhibit a strain energy function, or the amount of energy stored by the system or material within a given volume, relative to the amount of displacement applied to the system volume [100]. Variations of the strain energy function, such as the suite of hyperelastic models presented in material characterization, involve polynomial representations of the strain energy function, where differences occur in the number of defined terms for principal stretches, Of these models include those which have shown to depict properties of biological tissues with some accuracy, such as the neo-Hookean, Yeoh, Fung, Mooney-Rivlin, Gent, and Ogden constitutive curve-fitting modes [61], [100].

| **Ogden Model** | |
|---|---|
| $W(\lambda_1, \lambda_2, \lambda_3) = \sum_{i=1}^{n} \frac{\mu_i}{\alpha_i} ({\lambda_1}^{\alpha_i} + {\lambda_2}^{\alpha_i} + {\lambda_3}^{\alpha_i} - 3)$ | *Equation 2.3 — Ogden Hyperelastic Curve-Fitting Model (Strain Energy Function) [45], [64], [77], [96], [97], [100]–[104]* |

$$G = \frac{1}{2}\sum_{i=1}^{n}\mu_i\alpha_i$$

*Equation 2.4 — Initial Shear Modulus [45], [64], [77], [96], [97], [100]–[104]*

*Where **W** = Strain Energy Density*

*$\boldsymbol{\lambda_i}$ = Principal Stretch Ratios*

*n, μ, α = Material Constants*

***G** = Initial Shear Modulus*

**Mooney-Rivlin Model**

$$W = \sum_{i+j=1}^{N} C_{ij}(I_1 - 3)^i(I_2 - 3)^j$$

*Equation 2.5 — Mooney-Rivlin Model (Strain Energy Function) [64], [97], [98], [100], [105], [106]*

*Where $\boldsymbol{I_1}$ = Strain Energy Function:*

$$I_1 = \lambda_1^2 + \lambda_2^2 + \lambda_3^2$$

*$\boldsymbol{I_2}$ = Strain Energy Function:*

$$I_2 = \lambda_1^2\lambda_2^2 + \lambda_1^2\lambda_3^2 + \lambda_2^2\lambda_3^2$$

*$\boldsymbol{C_{ij}}$ = Material Constant*

**Neo-Hookean Model**

$$W = \frac{C_1}{2}(I_1 - 3)$$

*Equation 2.6 — Neo-Hookean Model, Strain Energy Function) [64], [100], [104], [107]*

*Where $\boldsymbol{C_1}$ = Material Constant*

---

**Yeoh Model**

$$W = \sum_{i=1}^{N} C_i(I_1 - 3)^i$$

*Equation 2.7 — Yeoh Model, Strain Energy Function [48], [100]*

**Fung-Demiray Model**

$$W = \frac{C_1}{2C_2}\left(e^{C_2(I_1-3)} - 1\right)$$

*Equation 2.8 — Fung-Demiray Model, Exponential Strain Energy Function [48], [100], [108]*

*Where* $C_1$ *= Infinitesimal Shear Modulus*

$C_2$ *= Stiffening Parameter*

**Gent Model**

$$W = \frac{\mu J_m}{2} ln\left(1 - \frac{I_1 - 3}{J_m}\right),$$

$$I_1 < J_m + 3$$

*Equation 2.9 — Gent Model, Micromechanical Strain Energy Function [5], [8], [49], [100], [109], [110]*

*Where* $\mu > 0$ *(Infinitesimal Shear Modulus)*

$J_m > 0$ *(Material Constant)*

Budday et al. [15], in their review of the current scientific advancements in brain tissue characterizations, compared the constitutive models of neo-Hookean, Mooney-Rivlin, Demiray, Gent, and Ogden to experimental data of the brain tissue cortex, basal ganglia, corona radiata, and corpus callosum stress-strain in simple shear, tension, and compression. Of the observed models, the Ogden One-Term model was the only constitutive model able to accurately represent the experimental data of all three loading modes ($R^2 \geq 0.995$) and was further able to provide a curve fit equation which could simultaneously define the brain tissue under all three given loading modes ($R^2 \geq 0.928$), denoting that the Ogden One-Term model was able to capture the material anisotropy of the brain tissue and its functional regions. The Ogden model has since then been used in the primary assessment which employ elastic analysis of brain tissue and relevant simulants [45], [64], [77], [96], [97], [100]–[104]

Alternatively, methods to characterize the non-linear viscoelastic stress strain curve include those of the strain-step approach. This method employees segmenting the entire stress strain graph of a viscoelastic materials' loading curve into steps of strain ranges. From there, a linear elastic modulus is determined within the relevant ranges of strain steps [46], [47], [54], [92].

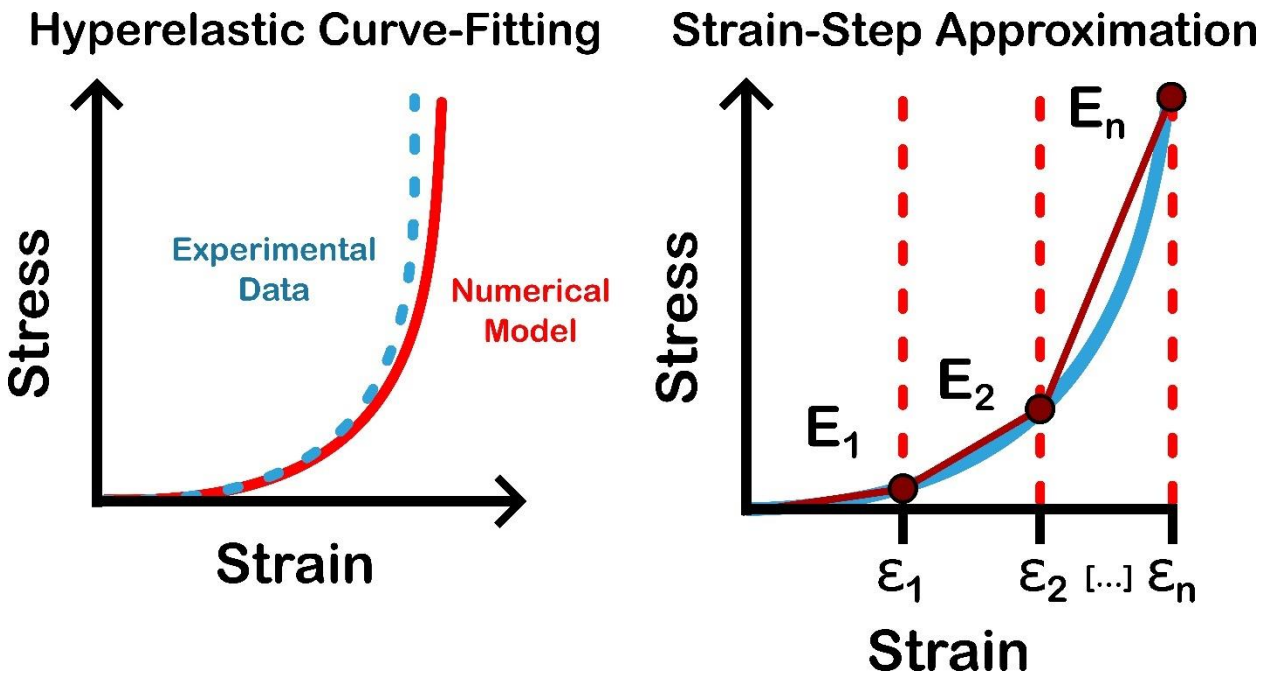


*Figure 2.19 — Comparison of Methodology Between Hyperelastic Curve-Fitting and Strain-Step Approximation*

2.4.1.3.3 — Viscoelastic Testing by Digital Mechanical Analysis (DMA)

Dynamic Mechanical Analysis (DMA) is a technique employed to characterize the viscoelastic properties of materials beyond stress-strain behavior. Most commonly, methods of DMA that can be most closely witnessed in the characterization of brain tissue and its simulants include stress relaxation tests [41], [60], [64], [77], [78], [97], [98] and, most notably, frequency sweep analyses [45], [49], [50], [59], [74]–[77], [111]. Devices such as rheometers are capable of DMA for the characterizations of liquids and viscoelastic solids

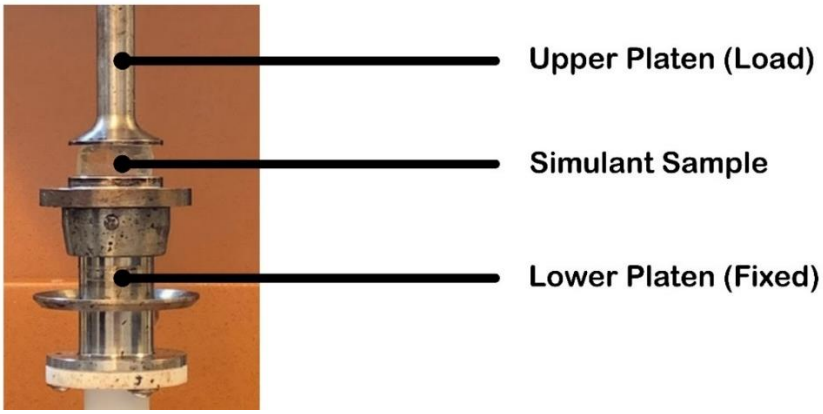


*Figure 2.20 — Specimen Sample Configuration for DMA Testing*

Frequency sweep analysis employs a range of frequency-dependent oscillations onto viscoelastic solids at a defined oscillation strain. The goal of this method is to determine the viscoelastic performance of a given material. Specifically, frequency sweep analysis allows for the quantitative observation of elastic and viscous components in a material's stress-response signal, and their variation under a change in frequency. The elastic and viscous portions are typically represented by the storage modulus (E′) and the loss modulus (E″), respectively. Both E' and E'' are representations of the applied sinusoidal strain and sinusoidal stress response in a dynamic regime [112]. The damping response of the viscoelastic material yields a sinusoidal stress and strain response with the same frequency, but different amplitudes. The damping response further applies a lag between the stress and strain response, known as the phase lag or phase angle (δ). The DMA stress and strain signals are represented by the following equations:

$$\sigma = \sigma_0 sin(t\omega + \delta)$$ *Equation 2.10 — DMA Stress Signal [112]*

$$\varepsilon = \varepsilon_0 sin(t\omega)$$ *Equation 2.11 — DMA Strain Signal [112]*

*Where* $\boldsymbol{\sigma_0}$ *= Stress Response*

$\boldsymbol{\varepsilon_0}$ *= Strain Response*

$\boldsymbol{\omega}$ *= 2πf (Angular Frequency)*

$\boldsymbol{\delta}$ *= Oscillatory Phase Angle or Phase Lag*

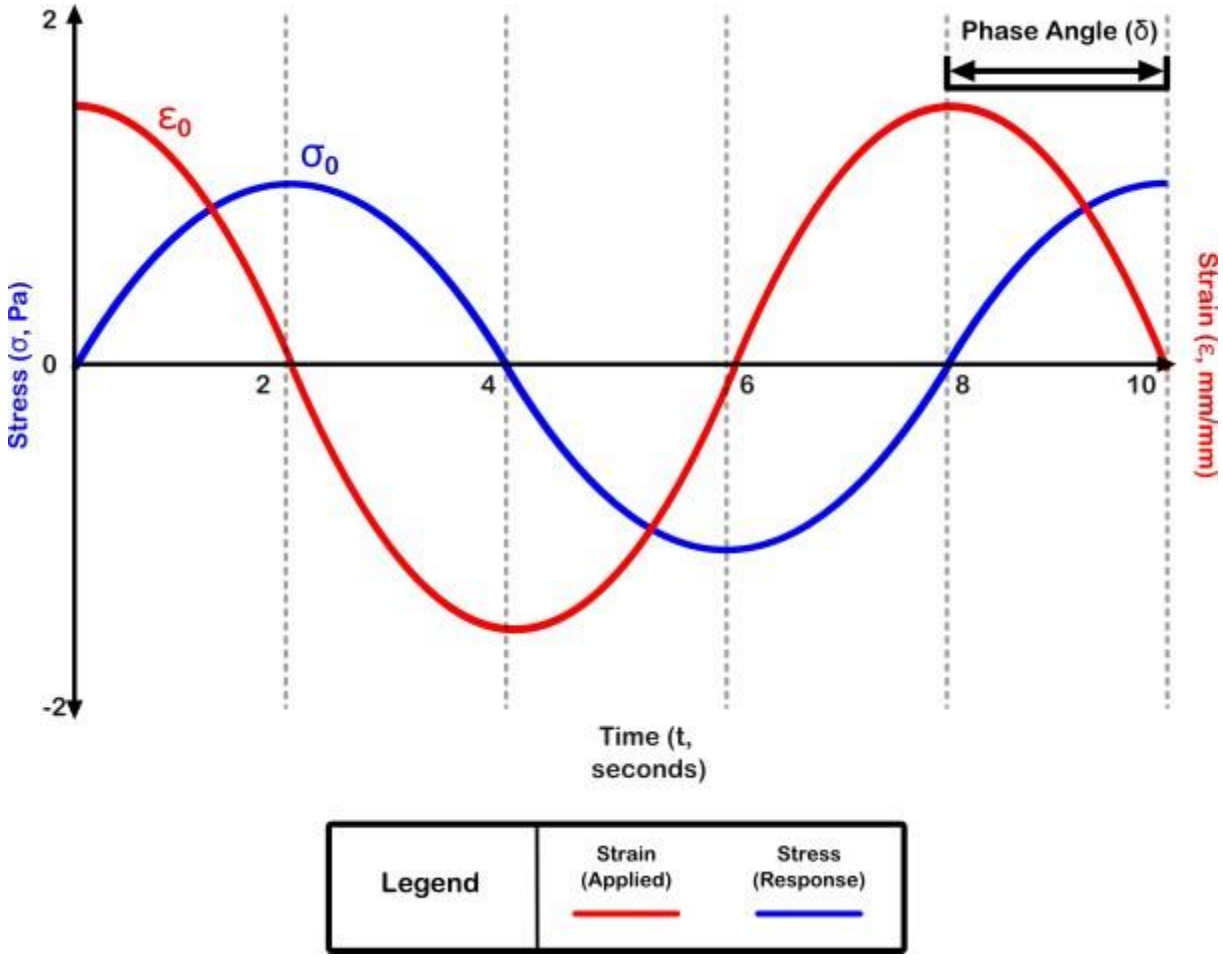


*Figure 2.21 — DMA Response Signals*

The storage modulus (E′) measures the energy stored in the material during deformation, which is a direct indicator of the material's stiffness. As the frequency of the oscillation increases, E′ can show how the material's ability to store energy changes, reflecting its elastic behavior at different dynamic conditions.

$$E' = \frac{\sigma_0}{\varepsilon_0}\cos\delta$$

*Equation 2.12 — Storage Modulus Equation [113]*

The loss modulus (E″), contrastingly, quantifies the energy dissipated as heat during deformation, which correlates with the material's damping ability. The variation of E″ with frequency provides insights into the material's internal friction and viscoelastic damping properties.

$$E'' = \frac{\sigma_0}{\varepsilon_0}\sin\delta$$

*Equation 2.13 — Loss Modulus Equation [113]*

Another important parameter obtained from frequency sweep analysis is the loss factor (tan δ), which is the ratio of the loss modulus to the storage modulus (E″/E'). This parameter represents the damping efficiency of the material. A high tan δ value indicates a high damping capacity, making the material effective in energy dissipation, while a low tan δ value suggests a predominantly elastic behavior.

Together, the storage and loss modulus components can both contribute to determine and overall viscoelastic complex modulus, which governs the entire viscoelastic behavior of a material. The complex modulus is governed by the root-sum-square of both loss and storage modulus components.

$$\tan\delta = \frac{E''}{E'}$$

*Equation 2.14 — Viscoelastic Loss Factor [113]*

$$E^* = E'\sin(\omega t) + E''\cos(\omega t), or$$
$$E^* = E' + iE''$$

*Equation 2.15 — Complex Modulus Equation [113]*

In the literature, characterization studies have employed the frequency sweep analysis to consider the elastic and viscous portions of the mammalian brain under dynamic loading effects [45], [59], [59], [74]–[77]. Characterizations of this manner has further been employed to consider resonant oscillations relevant in scenarios such as in oscillations experienced by the whole brain in daily function as well as during impact [18], [59], [74], [75].

### *2.4.2 — The Cranial Bone*

The representation of the human skull is a critical aspect to investigate in the development of a biofidelic head form and is a necessary consideration for the understanding of intercranial mechanisms of the head under impact and injury. In that, characteristics of bone can be broken down into the specific components of geometrical properties, material properties, and structural properties [114]. Furthermore, akin to the in-depth literature investigation employed upon the brain (See Section 2.5.1), the function of the microstructural components of the skull provides considerable influence and insight to the reported mechanical performance values found in the macrostructural bulk geometry, specifically in its characteristics of quasi-elasticity, heterogeneity and anisotropy, viscoelasticity, and regional dependency. The following section will govern these relevant aspects of the cranial bone to provide a further understanding in the methodology of developing and determining an ideal characterization and manufacturing process for the native

skull bone. Emphasis will further be placed on reported simulant candidates of cranial bone in the literature — both in methodology and characterization analysis — to identify a relevant research gap which this thesis will aim to address.

### *2.4.2.1 — Mechanical Properties and Characterization of the Native Human Skull Tissue*

2.4.2.1.1 — Quasi-Elastic Performance and Strain Rate Dependency

Quasi-elastic behavior in cranial bone is a critical aspect of their mechanical performance, particularly under varying strain rates. Characterization of the human skull's mechanical properties dates to the seminal studies by McElhaney et al. in the 1960s and 1970s [115]. These studies provided foundational insights into the density measurements and material characterizations of cortical and trabecular bone under different loading conditions—compression, tension, and shear. Notable takeaways regarding these studies included the influence of trabecular pore density and loading direction on mechanical performance of the skull bone.

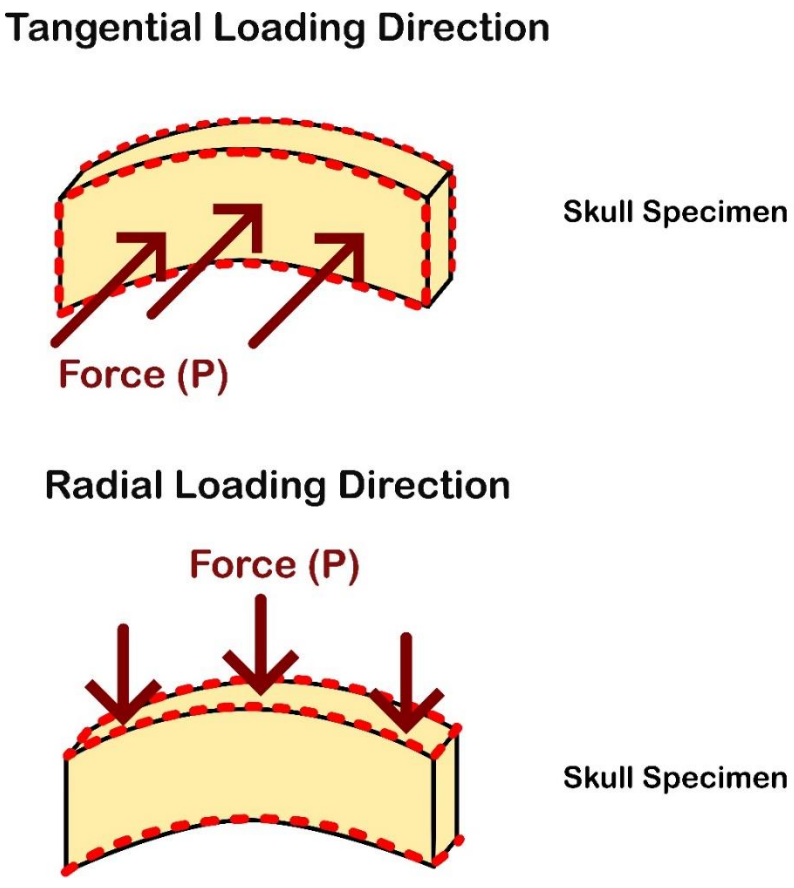


*Figure 2.22 — Anisotropic Loading Directions Tested on Skull Specimens in the Literature*

Advancements in Finite Element Modelling (see Section 2.3.2) have furthered the comprehension of cranial impact mechanics, emphasizing the importance of bending responses in head impacts. Since this shift in paradigm in the understanding of head impact kinematics, current characterization studies of the skull bone have underscored the structural geometry and energy absorption characteristics of the cranial vault in such scenarios [114], [116]–[119].

Experimental data on native bone specimens tested in bending have demonstrated a wide variation in elastic modulus and strength, attributed to the geometric variations across the skull. Nonetheless, these characterizations consistently display all three stages of the quasi-elastic regime, with the most pronounced quasi-elasticity observed in radial loading of the sandwich structure. This quasi-elastic loading curve is characterized by an initial non-linear toe regime, a linear elastic portion representing the material's elastic modulus, and a non-linear creep regime indicating plastic deformation before fracture. The toe-regime can be attributed to the initial stressing of the cancellous diploë, which provides the intended function of initial stress absorption.

The sandwich composition of cranial bone promotes a quasi-elastic performance most evident in loading directions perpendicular to the radial cortical-cancellous-cortical structure. This three-stage stress-strain characteristic is crucial for understanding the cranial bone's mechanical behavior and its implications for impact resistance and energy absorption in head injuries.

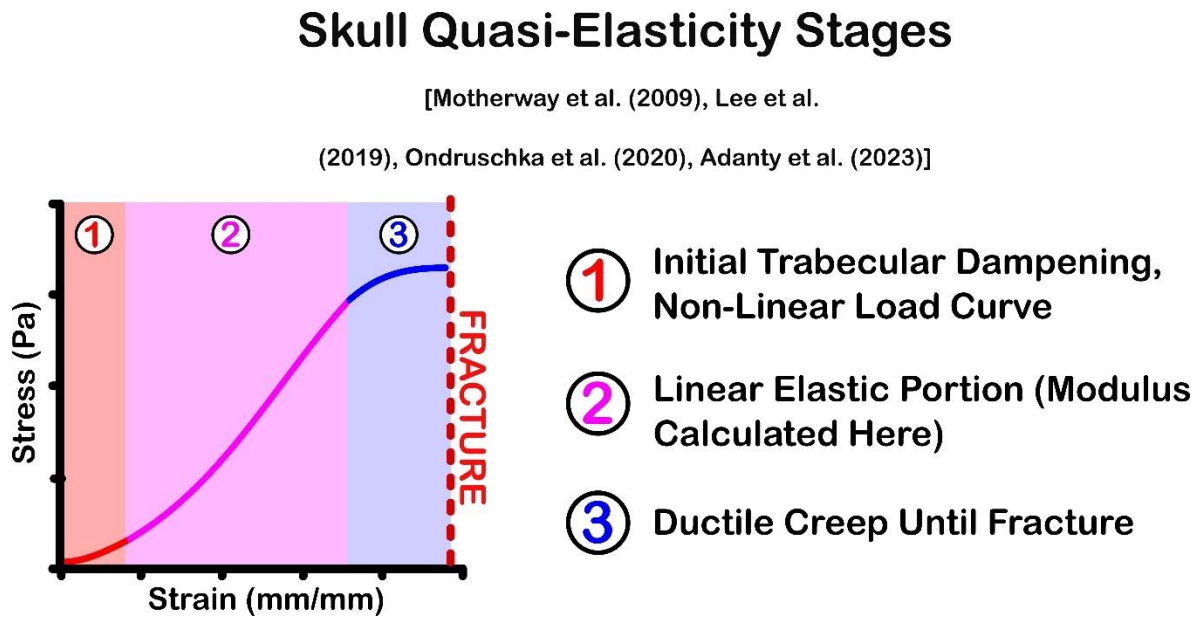


*Figure 2.23 — Quasi-Elastic Stress-Strain Stages of Skull Specimens in Flexion [114], [116], [119]–[122]*

Extending the investigation beyond the quasi-elastic performance of the human skull, the influence of strain rate on the material properties of cranial bone holds significant prominence. Motherway et al. [114] conducted an in-depth investigation into the effects of loading rate and cranial sampling position on the mechanical properties of cranial bone using three-point bending tests. Their findings revealed that the elastic modulus, maximum force to failure, and maximum bending stress were significantly higher at increased testing speeds, signifying the viscoelastic nature of cranial bone.

Adanty et al. [120], [121] most recently observed four-point bending characterizations of the parietal and frontal lobe specimens of 23 human calvaria, both male and female. Testing was conducted at an intermediate strain rate — 2–3 $s^{-1}$ — and material performance was compared to known quasi-static values. This research observed reductions in surface fracture strains when compared to quasi-static bending results, while compared quasi-static values displayed reduced bending moment values. When compared to other reported values in the literature conducting tests at intermediate strain rates [114], [123], Adanty et al. reported comparable results.

Further exploration by Zhai et al. [122] focused on the effects of loading direction and strain rate on cranial bone's mechanical behavior. Their research demonstrated that cranial bone becomes increasingly brittle as the strain rate increases, exhibiting a transition from ductile to brittle behavior. The elastic modulus and ultimate strength of cranial bone were found to vary significantly with different strain rates, emphasizing the material's dependency on the rate of loading.

These studies collectively illustrate that the cranial bone's mechanical response is highly sensitive to strain rate, with higher rates leading to increased brittleness and higher mechanical properties such as elastic modulus and ultimate strength. Understanding this strain rate dependency is crucial for applications involving dynamic loading conditions, such as impacts and trauma, providing insights into the cranial bone's performance under different stress scenarios.

2.4.2.1.2 — Micro- and Macrostructural Composition and its Effect on Material Characteristics

The microstructural composition of cranial bone, encompassing cellular and extracellular matrix components, plays a pivotal role in determining its overall mechanical performance and functional characteristics. The formation of bone microstructure gives rise to the osseous tissue forming the

bone matrix, a composite material consisting of a tensile-resistant organic component primarily comprised of Collagen Type-1 fibers and a compression-resistant inorganic component primarily made of calcium-hydroxyapatite crystals [124]–[127].

Calcium-hydroxyapatite crystals, $Ca_{10}(PO_4)_6(OH)_2$, are embedded within the collagen matrix through osteoblast activity, providing hardness and structural integrity within the osseous tissue. This enhances the compressive strength and stiffness of the bone, allowing it to resist deformation and fracture under high loads [124].

Osteoblasts promote the formation of hydroxyapatite through deposition of Type-1 Collagen fibers, which develop the scaffold for the osseous matrix and serve as the medium for mineral deposition, eventually synthesizing into hydroxyapatite [124], [127]. Collagen fibers contribute to the tensile strength and toughness of the bone, enabling it to absorb and dissipate energy from impacts. The orientation and density of collagen fibers within the cortical and cancellous layers influence the bone's ability to withstand tensile and shear forces.

The synthesis of collagen fibers into hydroxyapatite mineralization contribute to the development of lamellar bone, observed in the osteoblast transportation of the collagen matrix into layered sheets, or lamellae. These layers are oriented such that inter-layer fibers run parallel to one another, while between layers, fiber orientations are angled against neighboring lamellae. These oblique contrasting fibril angles enhance bone strength and its anisotropic characteristics [127], (See Section 2.4.2.1.3).

In the bulk structure of bone, lamellae synthesize into two structural formations. The first observes the formation of annular layers around circulatory arteries, ventricles, capillaries, and nerves, creating osteons, which serve as singular units in forming compact cortical bone [124], [127]–[129]. This arrangement ensures the compact cortical region remains dense and stiff compared to cancellous bone.

Conversely, lamellae in cancellous bone organize into parallel sheets, forming trabeculae [127]–[129]. These sheets develop into a three-dimensional lattice that composes the cancellous bone region, exhibiting greater porosity due to the lack of need to facilitate circulatory transport, and elasticity, though with a significantly lower Young's modulus.

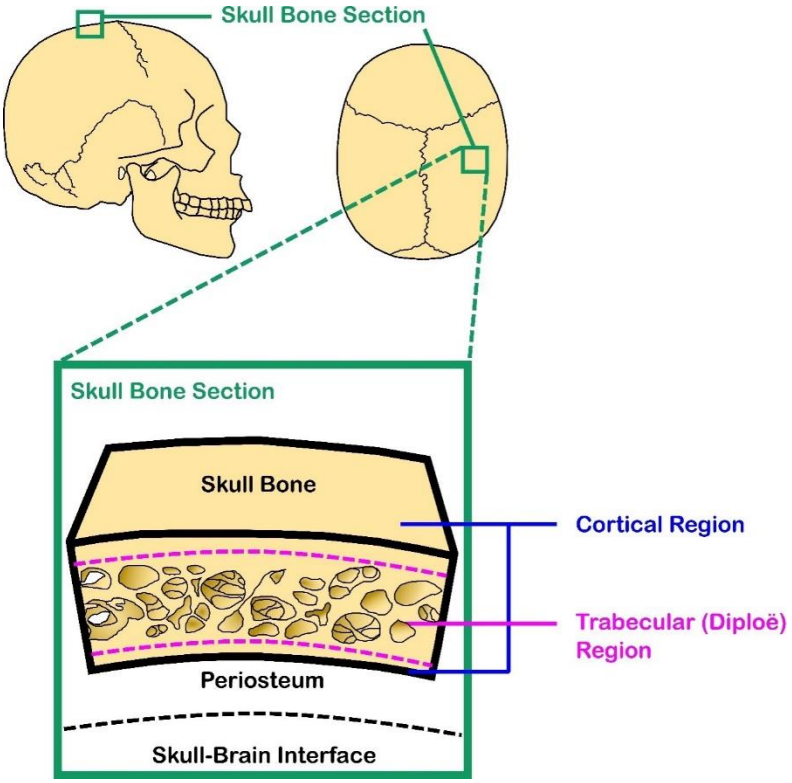


*Figure 2.24 — Cortical and Cancellous Regions of the Human Skull Bone*

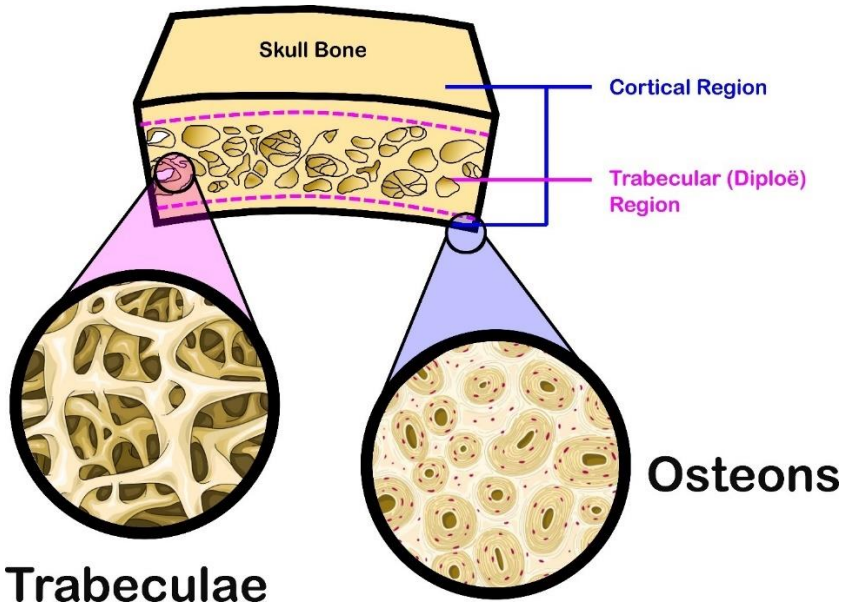


*Figure 2.25 — Cortical and Cancellous Regions and Microstructural Osteons and Trabeculae*

The greater density and distribution of hydroxyapatite crystals in the compact osteon of cortical bone contribute to the cranial bone's overall strength and durability, while the porous, sponge-like structure of the lamellae sheets in cancellous bone allows for pronounced elasticity and impact absorption [114], [117], [124].

Examination of the macrostructural features, such as cortical and trabecular bone regions, reveals their significant impact on the mechanical properties and overall performance of cranial bone. Studies have shown how variations in composition influence strength, toughness, and elasticity.

The cranial calvarium, classified as a flat bone, serves to provide points of attachment for surrounding muscles while protecting internal organs, such as the brain [126], [127]. Flat bones exhibit a larger surface area and thin cross-sections, similar to the pelvis and scapula.

The cranial bone's macrostructure is a three-part composite structure with two dense cortical tables (inner and outer) and a middle layer of spongy cancellous bone (diploe). This layered structure affects the mechanical properties, providing both strength and flexibility. The outer and inner cortical layers, composed of high-density compact bone, contribute significantly to the skull's strength and stiffness, enabling it to withstand high loads and resist bending and fracture.

Wu et al. [117] developed a theoretical model predicting cranial bone failure mechanisms under three-point bending, identifying three primary failure modes: tensile yield of the inner cortical bone, shear of cancellous bone, and compressive wrinkling of the outer cortical bone. This study highlighted the significant impact of cranial bone curvature and composite structure on mechanical properties under bending loads. Experimental observations by Adanty et al. [120], [121] have validated this behavior through strain gauge measurements of both inner and outer cortical layers.

Further characterization investigations revealed the significant influence of the diploë structure on mechanical responses. Variations in porous densities and structural arrangements within the diploë were shown to affect compressive and torsional strength, modulus, energy absorption, ultimate strain, and shear strength. Subsequent studies explored additional aspects such as trabecular volume ratios, cortical thicknesses, and total bone thicknesses [116], [119], [130]–[132].

Characterization studies by Motherway et al. [114] and Ondruschka et al. [119] demonstrated that cortical layers have a higher elastic modulus and bending strength compared to the cancellous core. For instance, Ondruschka et al. noted bending moduli of up to 3330 MPa for periosteum-

attached cortical bone. The cancellous diploë, less dense and more porous than the cortical tables, plays a crucial role in energy absorption, helping to dissipate forces during impacts. The diploë's mechanical properties, such as its lower modulus and higher energy absorption capacity, allow it to act as a cushion, reducing the likelihood of fractures.

Studies like those by Wu et al. [117] indicate that the cancellous bone's structure significantly influences failure mechanisms under bending loads, with shear in the cancellous layer and tensile yield in the cortical layers being critical factors. Morphological characteristics, such as the thickness and density of the cortical layers and the porosity of the cancellous diploë, play a significant role in determining the mechanical properties. Motherway et al. [114] highlighted that variations in these morphological parameters could lead to differences in the mechanical response of the cranial bone under dynamic loading conditions.

The prominence of porous density and its influence on the material properties of the bone has been recognized since the fundamental studies by McElhaney et al. [115]. Understanding these micro- and macrostructural compositions and their effects on material characteristics is crucial for accurately modeling and predicting the mechanical behavior of cranial bone under various loading conditions.

2.4.2.1.3 — Heterogeneity and Anisotropies

A key characteristic of cranial bone, noted across multiple points in the literature, is its anisotropic properties. Due to the complex composite structure of the bone, its mechanical properties vary depending on the direction of the load. Cranial cortical bone has randomly oriented osteons, unlike load-bearing bones such as the femur where osteons are aligned in the direction of primary loading [124], [127]–[129]. This random orientation results in cranial cortical bone exhibiting transverse isotropy rather than true anisotropy [130]–[132].

McElhaney et al. [115] highlighted the variability in mechanical responses based on loading directions, with cranial bones exhibiting greater strength and stiffness when loaded tangentially rather than radially. Tangential loading resulted in higher ultimate strength and modulus in compression, while radial loading demonstrated superior energy absorption capabilities. Motherway et al. [114] further observed anisotropic behavior, showing that mechanical properties

such as elastic modulus, maximum force to failure, and maximum bending stress were significantly influenced by the loading direction and cranial sampling position.

Zhai et al. [122] extended the understanding of radial and tangential anisotropic loading seen in McElhaney et al. Their anisotropic characterization of the native cranial bone included three-point bending tests on curved specimens of the human frontal bone. Across quasi-static, intermediate, and high strain rates, tangentially loaded specimens displayed increased flexural modulus and ultimate flexural strength, whereas radially loaded specimens exhibited greater toughness. This anisotropic behavior aligns well with the formation mechanism of cortical and cancellous bone regions, in that the parallel lamellae syntheses found in cancellous bone are shown to align along axes of mechanical stress [127].

The spatial variation in mechanical properties within different regions of the skull is also significant. Differences between the frontal, parietal, occipital, and temporal bones affect their mechanical behavior. The upper regions of the calvaria, including the frontal, parietal, and occipital bones [133], have been the focus of many characterization tests. These studies have reported variations in properties depending on the region sampled [114]–[116], [119], [130]–[132], [134], [135].

Geometrically, spatial variations around the skull calvaria include differences in cortical and total thicknesses, trabecular densities, and overall shape, all of which affect mechanical behavior. Motherway et al. [114] highlighted variations within the frontal and parietal regions, showing that frontal bone samples exhibited higher strength and greater energy absorption before failure compared to parietal bone samples. Similarly, Lee et al. [116] conducted quasi-static three-point bending tests on specimens from the frontal, occipital, and parietal regions. They found that sample thickness, a parameter variable throughout the calvarium, had the most significant statistical correlations with flexural modulus and strength.

Ondruschka et al. [119] and Zwirner et al. [123] conducted similar three-point bending tests, confirming the influence of thickness on mechanical properties. The studies also included the temporal bone in their studies, with Zwirner et al. noting that it has a lower quantity of diploë and is generally thinner, leading to lower maximum force ($F_{max}$) values compared to other regions. Frontal and occipital bones exhibited higher resistance to failure forces, with the occipital bone being the most robust under impact conditions. The frontal bone was found to be the most elastic,

while the temporal bone was the least elastic, with the parietal and occipital bones falling in between these extremes.

Most recently, Adanty et al. [120], [121] aimed to identify how morphometric and geometric properties of the human calvarium influence its mechanical response, focusing on differences between the frontal and parietal bones. Using Micro-Computed Tomography (μCT) scanning of human cadaver frontal and parietal skull specimens, they found that frontal bones exhibited higher trabecular connectivity, thicker trabeculae and cortical regions, higher second moment of inertia, and tissue mineral density compared to parietal bones. Parietal bones showed higher porosity, indicating a less dense structure.

In conclusion, spatial variations in the skull calvarium, including differences in geometry, structure, and material composition, significantly influence the mechanical performance of cranial bone. Specimen thickness is a consistent variable with a significant effect on material performance, and this parameter varies across different regions of the calvarium. For accurate characterization and simulation of cranial bone, it is crucial to account for these spatial variations to achieve biofidelic representation of material, structural, and geometrical compositions.

2.4.2.1.4 — Additional Mechanical Influences: Soft Tissues, Age, and Sex

The detailed research sections above focus on the general material properties of bone, yet they highlight limitations and considerations regarding additional external parameters that significantly affect recorded material properties.

Foremost, the literature underscores the significance of surrounding soft tissues, such as the dura mater and the periosteum, in influencing the mechanical properties of cranial bone. Studies by Lee et al. [116] and Ondruschka et al. [119] supplemented bare bone flexion tests with specimens retaining their periosteum. Ondruschka et al. observed that the bending modulus of periosteum-attached skull bone was 3330 MPa, compared to 1979 MPa for periosteum-removed bone. Lee et al. similarly found a statistically significant increase in both bending modulus and strength when soft tissues were attached. Motherway et al. [114] emphasized the role of soft tissues in distributing mechanical loads across the skull during impacts, arguing that these tissues absorb and dissipate impact energy, reducing fracture risk.

Age is another critical factor influencing the characterization of human bone. Studies such as those by McElhaney et al. [115] (56-73 years old), Adanty et al. [121] (83.6 ± 9.0 years for males, 88.4 ± 9.0 years for females), and Zwirner et al. [123] (3 weeks to 94 years) provided age data for the cadavers used. These studies found that age significantly impacts the mechanical properties of the human skull. McElhaney et al. noted that cranial bones become more brittle with age, reducing their ability to withstand dynamic loads. Zwirner et al. reported a negative correlation between age and mechanical properties such as bending strength and modulus, with older specimens generally showing decreased strength. Adanty et al. highlighted that older bones tend to have lower tissue mineral density (TMD) and higher porosity, which leads to reduced mechanical strength. Age-related changes in cortical thickness and trabecular structure also affect the mechanical response of cranial bones, as noted by McElhaney et al.

Sex appears to have the least significant influence among the external factors studied. Lee et al. [116] reported minor differences in mechanical properties between male and female cranial bones, attributing these differences to variations in cortical thickness and density, with female bones generally being less dense but more flexible. Zwirner et al. [123] observed some differences in mechanical properties between sexes, though these were less pronounced compared to age and regional variations. Female samples showed higher bending strength at certain impact velocities, suggesting sex-specific variations in bone density and structure. Adanty et al. [121] noted that male cranial bones tend to have higher TMD, and cortical thickness compared to female bones, which affects their mechanical response to impacts. These differences are important for developing sex-specific models for head injury prevention.

Overall, while the general mechanical properties of cranial bone are well-studied, additional factors such as surrounding soft tissues, age, and sex significantly influence these properties. Soft tissues like the periosteum enhance the mechanical strength and load distribution of the skull, emphasizing the importance of including these tissues in mechanical analyses. Age-related changes, including increased brittleness and decreased bending strength, highlight the need for age-specific considerations in biomechanical studies. Although sex differences are less pronounced, they still affect the mechanical response and should be accounted for in developing accurate and reliable head injury prevention models. Integrating these factors into future research

will improve the understanding and simulation of cranial bone behavior, leading to improved predictive models and accurate material simulation.

#### *2.4.2.2 — Objectives in Mechanical, Geometrical, and Structural Simulation of the Native Skull Bone*

Mechanical simulation plays a crucial role in understanding cranial bone behavior, with significant implications for injury mechanics, protective equipment design, and biofidelic head form design. By simulating the mechanical properties of the skull, researchers aim to establish an outline of expected performances for various investigated simulant materials. Ideally, these materials should display similar quasi-elastic capabilities to their native counterparts. Synthesizing multiple influences — such as structural, geometrical, and material properties [114], [115] — can help simulant materials achieve comparable results to native bone by incorporating the composite cortical-trabecular-cortical sandwich structure.

Quantitative performance metrics, including material modulus, ultimate strength, and energy absorption capacity, should be considered when comparing simulant materials to native bone. These parameters have been extensively evaluated in the literature [114], [114]–[117], [119]–[123], [130]–[132], [134]–[138]. However, constructing these complex structures presents challenges, particularly due to the entropic heterogeneity of the cancellous core. Macroscopic measurements, such as trabecular volume ratios [116], [130]–[132], reveal highly randomized trabecular pore diameters, counts, and shapes, which vary among individuals and hinder repeatability in characterization and simulation [139]–[142]. Some researchers, like Lee et al. [116] and Ondruschka et al. [119], have assumed trabecular pore patterns as homogeneous structures, noting that these differences have no statistical significance on material properties. Studies by Smith et al. [142] and Rajapakse et al. [141] found mean trabecular pore diameters around 102 μm with spherical and ellipsoid shapes.

In skull bone simulation, many homogeneous materials focus on material performance rather than geometrical and structural representations. Additionally, literature characterizations show variability in skull thickness across different regions (frontal, occipital, and parietal), which further varies among individuals [114], [116], [119], [122]. These thickness variations significantly influence material properties, complicating sample procurement, especially for tests like three-point bending. While polymer structures might use ISO 20795-1 standards for three-point bending

tests [143], the skull's geometry complicates manufacturing native specimens, often requiring curved specimen tests. Thus, developing simulant samples with standardized testing must consider these natural geometrical representations to ensure test repeatability.

2.4.2.2.1 — Quasi-Elastic Characterization and Analysis Methods for Native and Simulant Cranial Bone

Quasi-elastic analysis is crucial for understanding cranial bone behavior, focusing on the material's ability to deform and recover under load. This analysis is relevant to cranial bone simulation as it helps predict how the skull will react to different forces. These methods provide detailed insights into material performance under various conditions.

Case studies often use quasi-elastic analysis to simulate skull bone behavior. The most common metric in literature is the quantification of relative material performance, particularly in terms of modulus, strength, and stress-strain relationships. Characterization tests of surrogate materials frequently compare these parameters to human calvaria bone [119], [143]–[145]. Material characterization spans the spectrum of strain-rate classifications, including quasi-static [119], [136], [143], [144], intermediate, and high strain rates [136], [145].

Comparison studies vary across loading modes, such as tension [143], compression [136], [146], and flexion [119], [143]–[145]. Insights from quasi-elastic simulations include understanding skull deformation and stress distribution, which are essential for developing protective equipment and improving injury mechanics knowledge.

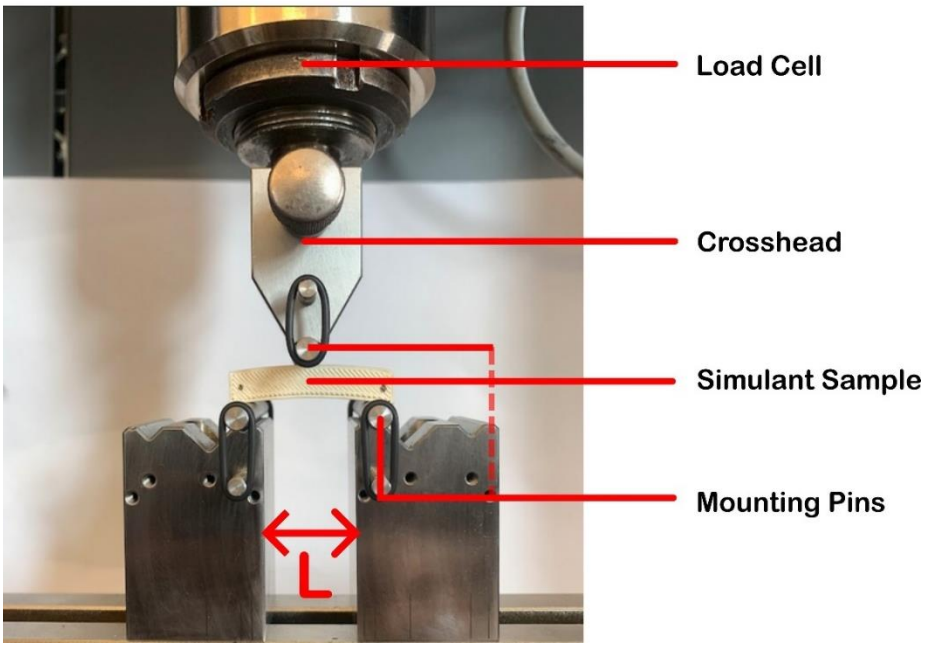


*Figure 2.26 — Three-Point Bending Configuration for a Skull Simulant Specimen*

2.4.2.2.2 — Digital Image Correlation (DIC)

A significant challenge in the mechanical analysis of the native skull is the process of specimen procurement. Characterization studies often require testing specimens that adhere to the natural geometry of the skull [114], [116], [119]–[121], [130]–[132]. This often results in irregularly shaped specimens, with geometrical variations throughout different regions of the skull leading to variability in reported results or a significantly reduced sample size. This challenge is particularly prevalent in flexural tests, where bending samples must adhere to the skull's curvature to characterize the cortical-cancellous composite structure of native bone.

Flexion tests on the skull are complex due to the multiple loading modes involved: compressive strain on the outer cortical table, tensile strain on the inner cortical table, and shearing strain on the cancellous region [121]. Studies like Adanty et al. [121] have used strain gauges in these discrete locations, but this method poses risks to accuracy, as factors such as the invasive contact of strain gauges and position of discrete gauge locations can affect the reported strain properties of tested specimens [147]–[153]. Comprehensive strain analysis must consider these factors to observe the skull's complex loading characteristics in bending.

Simulant sample construction for comparative characteristics also faces these challenges. Simulant tests often adhere to standardized testing parameters, such as ISO 20795-1 for polymer structures

in flexion [143]. However, comparisons to native bone can be yield confounding variables due to differences in sample size and shape, as native bone properties are highly susceptible to structural variations (see Section 2.5.2.1.3). Some simulants have been developed to better capture the curved nature of skull specimens [119], [144], but challenges in strain analysis of native curved structures remain present.

Digital Image Correlation (DIC) is a proposed method for comprehensive strain analysis in both simulant and native skull structures. DIC is a non-contact, non-invasive optical method that measures full-field displacement and strain on the surface of an object. It captures images of the specimen's surface before and after deformation and compares these images to determine changes [147]–[155]. This method is useful in biological applications for accurately observing material heterogeneities, anisotropies, and non-linear strain characteristics, such as in bone [156].

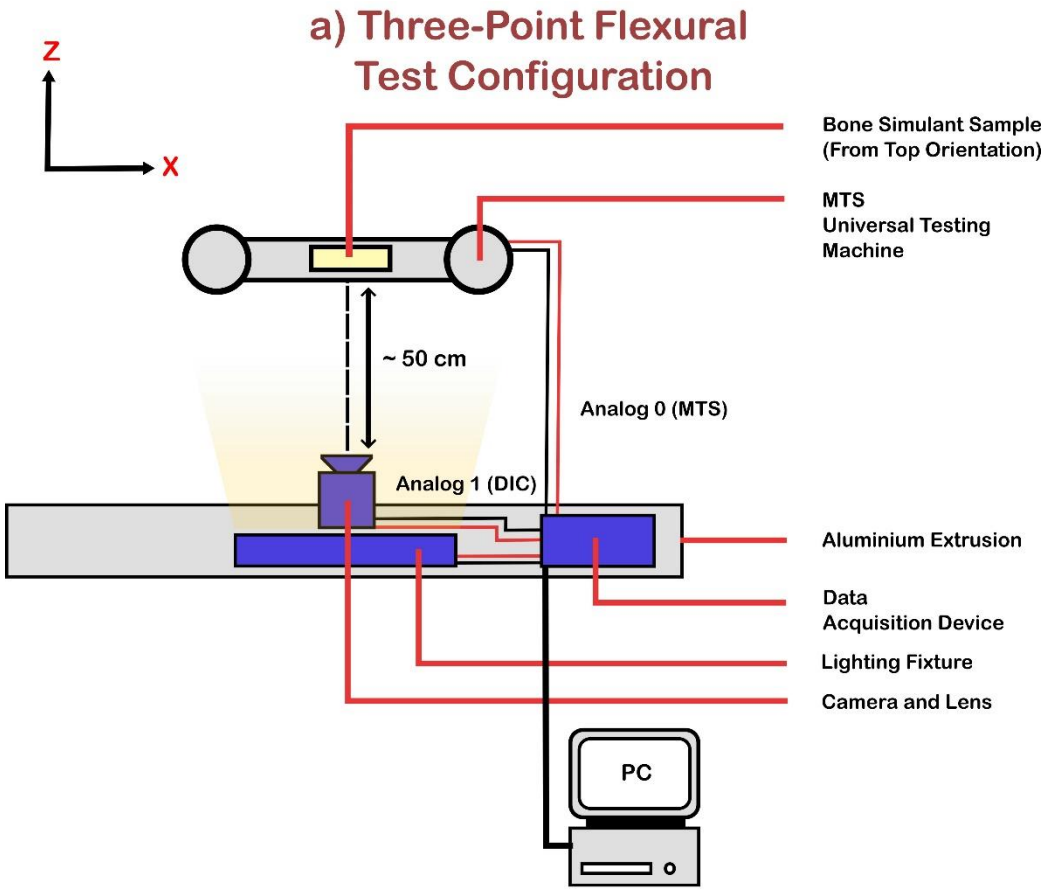


*Figure 2.27 — Two-Dimensional DIC Testing Configuration for Skull Simulant Testing*

Specimen surfaces are speckled with a random pattern to enhance feature recognition. The images are divided into small subsets (facets), and the position of each subset is tracked between the reference (undeformed) and deformed images. Correlation algorithms obtain the displacement field by correlating the subsets, from which strain is derived by calculating the gradient [147]–[157].

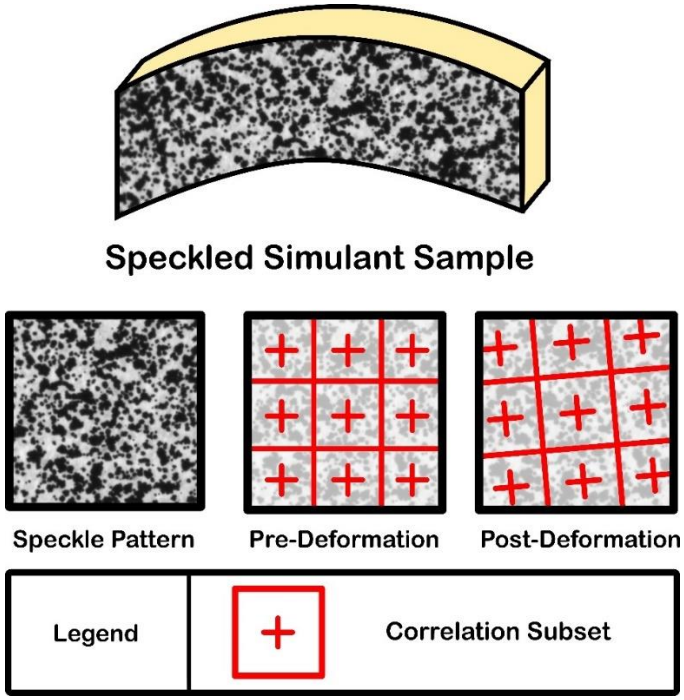


*Figure 2.28 — DIC Methodology: Speckle Pattern and Post-Processing Speckle Correlation*

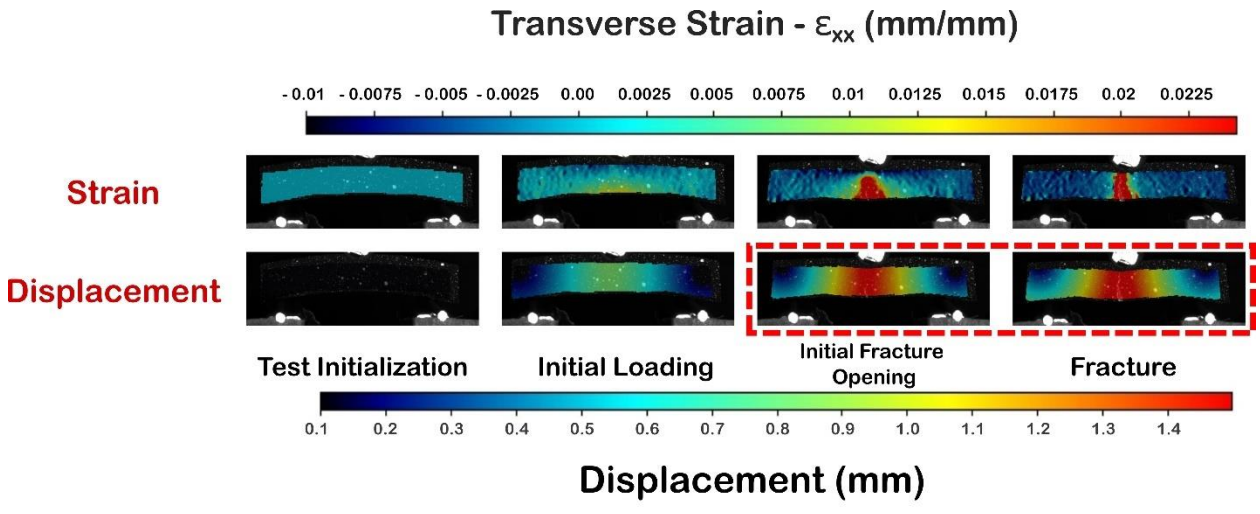


*Figure 2.29 — Strain and Displacement Field Correlations from Skull Simulant Testing*

Studies employing DIC for the analysis of native and simulant tissues include Ondruschka et al. [119] and Gunnarsson et al. [138] for strain analysis of skull specimens in flexion, the former incorporating skull simulants; Alexander et al. and Sztefek et al. [134], [156] for similar tests in compression; Monaheng et al. [157] for the numerical validation of mandible implants; and Brown et al. [137] for shear-punching analysis of skull specimens. Zwirner et al. [96] also utilized DIC for strain analysis of the human dura mater in tension.

#### *2.4.2.3 — Proposed Simulant Candidates in Literature and Relevant Applications*

Simulants are essential for replicating the mechanical properties of cranial bone, enabling accurate biomechanical testing and research. The literature proposes various materials and methods for creating skull simulants, each with specific criteria for selection. These criteria include mechanical properties, ease of fabrication, and similarity to native bone.

##### 2.4.2.3.1 — Resin Simulants

Resin-based materials are frequently used as simulants for cranial bone due to their favorable mechanical properties. Epoxy resin is a common candidate, often mold-casted to form the desired shape. The development process involves mixing a polymer base with a hardening agent, which cures into a solid state.

Resin simulants are extensively used in mechanical testing and medical training due to their ability to mimic the mechanical behavior of human cranial bone accurately. Studies such as those by Ondruschka et al. [119] evaluate different materials, including epoxy resin, for simulating human skull bone under biomechanical testing. Epoxy resin has been found to possess mechanical properties closely matching human calvarium bone, making it suitable for biomechanical studies. Key properties like flexural modulus, $F_{max}$, and strain are comparable to native bone, although flexural strength tends to be lower.

Further research by Falland-Cheung et al. [143] tested both epoxy resin and fiber-filled epoxy resin composites for tensile and flexural properties. Epoxy resin is preferred for lower impact forces due to its similar elastic modulus and flexural strength to human bone. Both epoxy resin and fiber-filled epoxy resin exhibit tensile elastic moduli ranging from 5.49 to 8.33 GPa. In flexural tests, fiber-filled epoxy resin showed the highest flexural modulus (17.96 GPa) and strength, significantly higher than other materials. Epoxy resin's flexural properties are the closest to human

cranial bone, and differences in mechanical properties between uniaxial loading modes highlight the anisotropic properties of the resins, further establishing their bone-like characteristics.

2.4.2.3.2 — Additive-Manufactured (AM) Polymer Simulants

Additive manufacturing (AM), commonly known as 3D printing, has been increasingly used to create skull simulants due to its ability to fabricate complex geometries and patient-specific structures. AM techniques have shown promise in prosthesis and implantation applications, providing both economic viability and anatomical accuracy.

Lal et al. [158] introduced a cost-effective method for fabricating patient-specific cranial implants using Fused Deposition Modelling Additive Manufacturing (FDM-AM). This method involves creating FDM-AM negative molds from CT data and using compression-moulded PMMA (polymethyl methacrylate) to produce the final implant. These implants accurately match the patient's anatomy and are compared to traditional materials like titanium and PEEK, highlighting the benefits of AM in terms of cost and anatomical precision.

Jakus et al. [146] further explored AM materials for surgical implantation, introducing a new biomaterial called Hyperelastic Bone (HB), developed for bone regeneration. This material, synthesized using poly(lactic-co-glycolic acid) (PLGA) or polycaprolactone (PCL) combined with hydroxyapatite (HA), was printed into scaffolds using a 3D bioprinter. Compression tests showed that HB constructs had suitable elasticity and mechanical strength for bone applications. Biocompatibility studies revealed successful osteogenic cell proliferation and tissue integration in mice.

Case studies demonstrate the effectiveness of 3D-printed skull simulants. Various materials used in AM, such as PLA (poly-lactic acid) and PETG (polyethylene terephthalate glycol), have been compared to native skull bone. Falland-Cheung et al. [143] tested PLA and PETG simulants against epoxy resin simulants in quasi-static flexural and tensile tests. While PETG and self-cure acrylic had lower tensile moduli (1.47-2.64 GPa), PLA exhibited a tensile modulus of 2.89-3.69 GPa, closer to the lower range of native skull properties. PLA showed closer ultimate strength values in tension and flexion, suggesting its potential for achieving biofidelity in impact-relevant strain rates.

Mantecón et al. [144] extended the analysis of PLA as a material simulant to native bone by developing simulants resembling curved specimens from skull studies [114], [116], [119]–[121]. Two case studies included three-point bending for AM bone sections and lateral compression and frontal point-loading for full skull phantoms. Flexion results indicated that printing orientation had minimal effect on mechanical properties due to high infill percentage, but sample geometry significantly influenced flexural properties. PLA samples' flexural modulus and strength varied compared to natural bone but were within the same order of magnitude, confirming PLA's potential as a mechanical simulant. The study highlighted the need to replicate natural bone microstructure for improved accuracy and explore alternative 3D printing approaches.

Prospects in additive manufacturing for cranial bone simulants include further advancements in replicating the natural bone microstructure and exploring new 3D printing techniques to enhance the biofidelity of simulants for better mechanical and anatomical accuracy.

2.4.2.3.3 — Composite Structured Simulants

Composite materials have significant potential as skull simulants due to their ability to closely mimic the mechanical properties of cranial bone. The literature proposes various composite materials, emphasizing their structural and mechanical characterization, and evaluates their effectiveness in replicating human skull behavior.

Additive manufacturing (AM) of composite materials combines intricate structural design with tailored mechanical properties, enhancing their use in biomedical applications. Han et al. [159] reviewed the use of hydroxyapatite (HA) and HA-based nanocomposites in hard tissue engineering. HA, due to its compositional similarity to bioapatite, provides excellent biocompatibility and bioactivity. However, traditional fabrication techniques limit HA's application in bone, cartilage, and dental fields. AM methods offer new possibilities for tissue engineering, emphasizing the need for multi-material deposition to mimic tissue heterogeneity and optimize AM for accuracy and processing time.

Similarly, Zhang et al. [160] investigated 3D printed scaffolds made from polylactic acid (PLA) and HA for bone tissue regeneration in cranioplasty. These scaffolds, fabricated using FDM printing, exhibited notable mechanical properties, improved degradation behavior, and high bioactivity, making them suitable for personalized bone repair applications. The compressive

strength of the composite scaffolds was significantly higher than HA porous ceramics and comparable to the upper range of human cancellous bone.

Composite materials have also been employed in commercial bone simulants outside of scaffolding and AM. Brown et al. [136] evaluated the mechanical properties of three commercially available bone simulants — Synbone, Sawbone, and Bonesim — under quasi-static and dynamic loading conditions. Synbone, a polyurethane-based foam, and Bonesim, a composite of ground-up bovine cortical bone and cyanoacrylate adhesive, showed mechanical properties within the range of human cranial bone under quasi-static conditions. Bonesim Y, a higher density variation, was identified as the most suitable simulant for cranial bone based on mechanical properties and microstructural analysis. In material characterization tests, Synbone and Bonesim displayed mechanical properties closely matching those of human cranial bone. Synbone exhibited significant elastic recovery after dynamic loading, while Bonesim showed complete fragmentation, indicating that none of the synthetic materials closely replicated the dynamic mechanical response of human cranial bone.

The composite material structures closely resemble the stress-strain response of human calvaria due to their success in mimicking the cortical-cancellous structure of natural bone. However, no research has yet constructed these relevant regions using AM simulant materials. Composite structures highlight the importance of additives in fine-tuning mechanical properties for tissue mimicking of native bone. Further investigation into these materials is warranted to determine an ideal simulant structure that accurately replicates the human skull's mechanical behavior, while considering the mechanical, geometrical, and structural characteristics critical to the material behaviour of the native skull.

### *2.4.3 — The Meninges*

The meningeal complex, or meninges, consists of membranous tissues that encase the Central Nervous System (CNS). The meninges play a critical role in maintaining CNS homeostasis by providing mechanical, immunological, and vascular support to the brain. While concussion studies have predominantly focused on brain deformation (see Section 2.3), recent research has increasingly examined the role of the meninges in TBI. Experimental and computational studies have demonstrated that the meninges serve a protective function during impacts. For instance, Gu

et al. [161] observed significant dampening effects from the meninges in computational models of TBI-related traumas.

Clinical observations also highlight the importance of the meninges in TBI cases, with damage to these tissues often observed in injured patients [162]. These findings underscore the need to consider the mechanical properties and protective roles of the meninges in studies of head injuries and their prevention.

#### *2.4.3.1 — Mechanical Properties, Composition, and Characterization of the Meninges*

The meninges consist of three primary layers: the dura mater (DM), the arachnoid mater, and the pia mater. The pia and arachnoid mater membranes are intimately connected via arachnoid trabeculae and are collectively referred to as the pia-arachnoid complex (PAC) [162]–[164]. Each layer of the meninges provides specific functions relevant to their location in the cranial vault, resulting in varying mechanical, compositional, and geometrical properties.

Being a soft tissue, the meninges exhibit NLV properties (See Section 2.4.1.1.1). In contrast to the simulating loading modes for brain tissue, properties such as ultimate tensile strain and strength, and strain to failure have shown to represent injurious loading conditions for these regions [162]–[164].

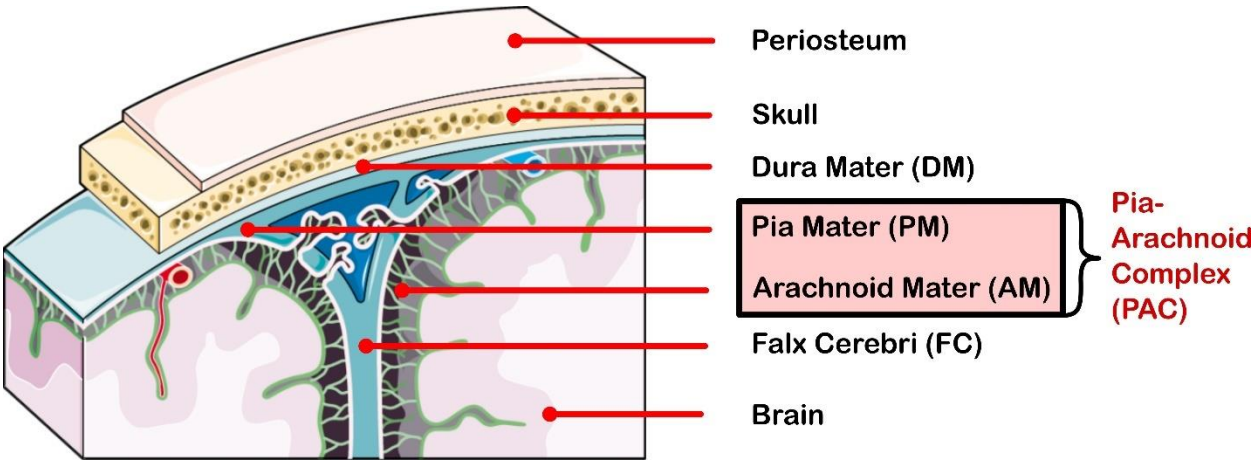


*Figure 2.30 — Cross-Section of the Cranial Vault*

2.4.3.1.1 — The Dura Mater (DM), Falx Cerebri (FC), and Tentorium Cerebelli (TC)

The dura mater (DM), also known as the pachymeninx, is the outermost layer of the meninges, serving as the densest and most protective membrane covering the brain and spinal cord. It functions as a connective tissue membrane attached to the periosteum of the skull [96], [162]–[164]. The DM is composed of a dense Collagen Type-1 and Type-3 architecture, essential for its load-bearing capacity, providing significant mechanical stiffness and strength. Additionally, the DM contains a network of vasculature responsible for transporting cranial immune cells.

Zwirner et al. [96] provided comprehensive tensile data on the mechanical properties of the human DM. They obtained 126 human dura mater samples from the temporal bones of 75 cadavers (50 male, 25 female), ranging from 2 to 94 years old. Dog bone-shaped samples were prepared according to ISO 527-2 for polymers in tension, and uniaxial tensile tests were conducted using DIC to measure strain. Engineering stress-strain curves were captured, and Scanning Electron Microscopy analyzed collagen fiber alignment in the DM. The tensile tests reported mean values of $70 \pm 44$ MPa in elastic modulus, $7 \pm 4$ MPa in tensile strength, and $11 \pm 3\%$ for maximum strain. Significant variability in material properties was observed between individuals, with no notable differences between DM regions and sex. However, there were negative correlations between age and material properties.

The large mechanical variability of the DM is attributed to its complex collagen fiber architecture, which displays regional variations throughout the cranial vault. Walsh et al. [164] conducted research on the regional mechanical and biochemical properties of porcine DM. Uniaxial tensile tests on porcine DM samples from the temporal, frontal, parietal, and occipital lobes, as well as the superior sagittal sinus, revealed significant regional anisotropic behavior. The study found substantial differences in stiffness between regions, with the superior sagittal sinus being the stiffest. Compositionally, stiffness correlations related to collagen Type-1 and elastin protein densities, with collagen-I and elastin being abundant in the superior sagittal sinus and frontal regions.

Geometrically, the DM extends to partition relevant brain sections. These extensions include the Falx Cerebri (FC) and the Tentorium Cerebelli (TC). The FC partitions the left and right hemispheres of the brain, constraining brain displacement and rotation within the cranial vault. The TC separates the cerebellum from the cerebral hemispheres and supports the weight of the

cerebral hemispheres [163]. Despite their potential role in providing mechanical stability in the cranial vault, no current study has provided mechanical analysis of these dural extensions [162].

2.4.3.1.2 — The Pia-Arachnoid Complex (PAC)

The Pia-Arachnoid Complex (PAC), also known as the leptomeninges, consists of the pia mater and the arachnoid mater, which are connected by the arachnoid trabeculae and subarachnoid vasculature. The Subarachnoid Space (SAS) between these layers is filled with cerebrospinal fluid (CSF), serving as a shock absorber and cushioning the brain [162].

The arachnoid mater, situated between the dura mater and the pia mater, aiding in the distribution of CSF, acts as a cushion which helps absorb shock to the brain [162]. The pia mater, the innermost layer, is a delicate membrane closely adhering to the brain's surface, providing a protective barrier and supporting the brain's vascular system [162].

Regarding previous studies which aimed to assess the material properties of the human PAC, little reports have been provided. Some studies are present, however, in the characterization of other mammalian specimens. Jin et al. [165] investigated the biomechanical properties of the bovine pia-arachnoid complex under tensile loading at varying strain rates. Bovine PAC samples were shaped into dog-bone specimens for uniaxial testing. These tests, conducted at strain rates ranging from 0.01 $s^{-1}$ to 100 $s^{-1}$ using a high-rate tensile testing machine, recorded mechanical properties such as ultimate tensile strength, elastic modulus, and failure strain. The bovine PAC exhibited an elastic modulus of 0.3 to 1.8 MPa and an ultimate tensile strength of 0.5 to 3.0 MPa, with strain to failure negatively correlated with increased strain rates.

Recently, Benko et al. [166] extended PAC characterization studies to human subjects. Using five post-mortem human subjects (ages 32-86), they determined the traction modulus by inserting a gauge needle into the arachnoid membrane and increasing pressure by pumping saline solution into the PAC membrane with a manometer. Starting at physiological intracranial pressure (ICP) (10 ± 1.5 mmHg), the pressure was linearly increased to 30 mmHg. Strain measurements were conducted qualitatively using post-hoc Optical Coherence Tomography (OCT) to image the PAC during inflation, tracking membrane displacement. The mean normal traction modulus was found to be 12.6 ± 4.8 kPa. Regional anisotropy was observed, with the superior and occipital regions exhibiting greater modulus and stiffness values compared to inferior regions.

#### *2.4.3.2 — Challenges and Objectives in Mechanical Characterization and Simulation of the Meninges, and Examples of Simulation in Literature*

The greatest challenge in characterizing the bulk material properties of the meninges lies in the geometrical constraints related to sample procurement. Walsh et al. [162] review these limitations, noting that replication of in-vivo conditions, tissue extraction, specimen geometry measurements, testing conditions, and strain measurements all contribute to confounding variables in the mechanical assessment of the meninges.

These challenges are further exacerbated when creating artificial simulant structures that represent the meninges. Simulant materials must be produced with dimensions and methodologies similar to their native counterparts, considering the nonlinear viscoelastic (NLV) properties of these soft tissues while also recreating the geometrical and compositional structure of the dura mater (DM) and the pia-arachnoid complex (PAC).

The thickness of the dura mater ranges from 0.35 mm [167] to 1.11 mm [168], while the falx cerebri (FC) measures approximately 0.45 ± 0.16 mm [169]. In characterization methodologies, these dimensions were considered suitable in specimen procurement for bulk material characterization [96].

Singh et al. [170] examined the roles of the FC and the TC by developing an anatomical head model. They created surrogates for the FC and TC using thermoplastic polyurethane (TPU). The elastic modulus of the TPU dural simulants was recorded to be 20 MPa, less than the reported deviations found in Zwirner et al. [96]. Still, the implementation of these tissue phantoms showed that they effectively redistributed strains in the brain surrogate, resulting in statistically significant reductions in maximum principal strain (MPS).

The surrogate representation of the PAC proves more challenging due to its extremely thin dimensions, often on the order of tenths of a micron [166]. To address this, some studies have explored alternative methods of sample procurement [165] and characterization techniques [166].

Efforts to represent the bulk material properties of the PAC include work by Petrone et al. [16], [17], who used a composite structure of nonwoven polyester sheets attached to Platsil Gel 00-20 Silicone. This approach yielded comparable properties in tension relative to native PAC properties

found in Jin et al. [165], although further details on specimen construction and geometrical accuracy in simulation were not provided.

Altogether, the mechanical characterization and simulation of the meninges face significant challenges, primarily due to geometrical constraints and the complexity of accurately replicating in-vivo conditions. These difficulties extend to the creation of simulant structures that must mimic the intricate properties of the DM and PAC. Despite these challenges, studies continue to explore innovative methods for sample procurement and characterization, striving to develop accurate and functional simulants. Advancements in this area are crucial for improving the understanding of meningeal mechanics and enhancing the accuracy of biomechanical models used in medical research and injury prevention. Future iterations of simulant construction should consider bulk material analysis of simulant materials which can recreate these material properties of the DM and PAC, which would then be carried over to their influence on the role of the full-scale structure, as per the study by Singh et al. [170].

## 2.5 — A Critical Review of Existing ATD Headforms and Considerations for Biofidelic Head Models

The validated FEM models have further extended the potential kinematic parameters in concussion, with definitions for cranial strain, rotational kinematics, and oscillations. These intercranial parameters establish the current forefront of concussion detectors in head impacts, extending past the previously reported linear head acceleration as the motive for concussion and TBI-related injuries found in initial mathematical models. The relatively comprehensive simulative models of the brain, such as those in the GHBMC and SIMon models, provide biofidelic observation of the human head's intercranial kinematics. In which, these models consider regions such as the cortex, thalamus, corpus callosum, basal ganglia, brain stem, and cerebellum; each with their own specific definition of material property. Furthermore, these models provide characterizations of the other components of the cranial vault, such as the skull and dura mater. Still, a research gap remains present such that the physical ATD head models used to validate these computations are not adequate with the given biofidelic representations of the human head, thus having been shown to result in some discrepancies in impact characterizations [8], [9], [22], [24].

It has been made apparent that the selection of an ATD headform for laboratory-based impact testing — despite its favorable traits of high repeatability and reliability — yields variability regarding the selection of which ATD is used in impact testing [22], [24]. Such that, careful consideration must be given to the properties of the headform utilized in head injury research and can significantly influence the outcome of the biomechanical impact assessment; no one device can properly portray the performance of the human head at any or all sequences of head impact.

Mathematical validation studies, such as the one found by Hoshizaki et al. [8], [9], have shown that impact recreations with the Hybrid-III ATD yield increased magnitude of kinematic signatures compared to the WSTC for injury, calling for improved mathematical models extending past the assumption of the human skull-brain as a singular rigid body. Furthermore, it was found in the previously defined comparative studies of ATD head models that increased biofidelity in geometrical representations of the human head [24], as well as the introduction of brain surrogates in ATD headforms [22], resulted in higher peak kinematic magnitudes compared to the Hybrid-III model, the least biofidelic of those compared in research, and the one used in the aforementioned validation study. From the studies regarding the performance of established ATDs (*Section 2.2.2)*, it appears that devices which favor anatomical accuracies generate significant differences in kinematic parameters when validated under FEM, such as MPS, and linear and rotational accelerations.

As FEM simulations of head impact continue to focus on intercranial mechanisms in their influence on TBI and the spectrum of TBI-related injuries (*See Section 2.3*), the demand for validation of through devices which observe kinematics within the cranial vault is further emphasized. Currently established ATD devices still only yield a mere representation of the human head in shape and mass, though considerations for the intercranial components like their computational counterparts are neglected, or — like the Hodgson-WSU — desire further anthropomorphic accuracy [22].

### *2.5.1 — Improved ATD Headforms and Biofidelic Head Models*

Several studies have focused on developing biofidelic head models with the goal of creating devices that accurately mimic the kinematic behavior of the human head and its critical structures. These head models serve various purposes, including improving the anatomical accuracy of ATDs

[16], [17], [171], [172], assessing the mechanical function of critical structures [39], [90], [144], [170], [173]–[177], and facilitating surgical practice [14], [39].

Petrone et al. [16], [17] developed an ATD head model with anatomical geometric accuracy and material properties designed to provide reliable and repeatable data for the experimental validation of finite element (FE) models and the evaluation of helmets designed for multidirectional impact protection. This ATD features a biofidelic head model mounted on a Hybrid-III neck stand, with brain and skin surrogates made from PlatsilGel 00-20 (brain) and 25 (skin) silicone-based A+B crosslinking gel, and a 3D-printed ABS skull. Silicone oil serves as the surrogate for cerebrospinal fluid (CSF). The head model includes linear and rotational accelerometers, strain gauges, and pressure gauges to capture impact kinematic signatures. Validation tests showed that the head model could replicate pressure curve patterns from cadaver studies and accurately recreate intracranial kinematics during impact.

Freitas et al. [171] developed biofidelic head models to simulate Behind Head Blunt Trauma (BHBT) events, bridging the gap between high-biofidelity post-mortem human subject (PMHS) testing and low-biofidelity commercial ballistic headforms. Their brain surrogate, made from Perma-gel mixed with iron powder to achieve a nominal brain mass, and rehydrated post-mortem human craniums for the skull surrogate, validated the effectiveness of combat helmet components in reducing injury thresholds and kinematic magnitudes.

Singh et al. [170] included representations of the falx cerebri (FC) and tentorium cerebelli (TC) within a brain simulant to observe their influence on kinematic stability within the cranial vault. Their biofidelic head model, featuring an AM PLA skull simulant, a gelatin brain simulant, and an AM TPU dural simulant, demonstrated the importance of these structures in redistributing strains in the brain surrogate during concussive impacts.

Falland-Cheung et al. [90] developed an anatomical head model to measure the transfer of impact forces through various head layers. Using an epoxy-resin half-skull, polyvinyl siloxane scalp, and an agar/glycerol gel brain, they simulated CSF with a modified intravenous fluid. Accelerometers placed throughout the head model captured data from impacts, demonstrating significant force transfer and displacement through the head layers, with the highest impact forces observed at the skin surface.

These studies highlight the potential for biofidelic head models to accurately capture intracranial kinematics and mechanical responses, facilitating improved testing for mechanical characteristics of brain tissue and their simulants. However, achieving greater accuracy requires comprehensive characterization studies of simulants, similar to those presented in Sections 2.4.1.2, 2.4.2.3, and 2.5.3.2.

Testing for biofidelic simulation should involve inducing combinations of strain-inducing rotational impacts and coup pressure-inducing linear impacts, with impact durations reflecting the specific traumatic injury (e.g., mTBI or blast). Characterizations can extend to injurious head oscillations, utilizing dynamic mechanical analysis (DMA) to define ideal simulant candidates within the scope of these oscillations. Some studies, like the DMA frequency sweep analyses by Li et al. [50], [74], [75], have used similar ranges to determine brain tissue properties within the given oscillations.

Furthermore, impact data suggest that anisotropy of brain structures can be simplified to simulate regions expected to experience peak strain, such as the cerebral cortex [13], [19], [20], [37]. However, thorough analysis of deep tissue strain to white matter regions, such as the corona radiata, and various cortical regions is recommended for future studies [64]. Accurate compositional representations also extend to the skull, with no reported simulant structures yet addressing the recreation of cancellous regions, trabecular pore geometries, and BVFs in full-scale representations. Characterization studies of native counterparts have shown the significance of these structures in mechanical dampening and stress-strain behavior (Section 2.4.2.1.2).

An additional challenge lies in the lack of characterization studies for the meningeal complex, the DM, and the PAC. Despite sample procurement constraints, some studies have attempted simulations with comparable results [16], [17], [170]. Future iterations of these simulants should aim for comprehensive characterization studies akin to native studies in the literature [96], [106], [162]–[166], if native structure procurement for testing is infeasible.

## 2.6 — Gaps in Literature

The previous sections have outlined current practices in mechanical testing and simulation of critical human head structures: the brain, skull, and meninges. The primary goal of this thesis is to assess and establish solutions to improve current ATDs used for laboratory-based head impact

evaluation and FEM validation of simulated head impacts. This literature review has identified key gaps that will guide the methodology and proposed study of this thesis.

**Intracranial Mechanics Observation:**

- There is a lack of feasible methods for in-vivo observation of intracranial mechanics during head impacts (Section 2.2).

**Sensor Effectiveness:**

- Current HIMDs and sensor placements may not provide comprehensive data, potentially leading to false negatives in concussion detection (Section 2.2.1).

**Standardization of ATD Headforms:**

- Significant differences in performance metrics among ATD headforms suggest a need for standardized selection criteria and usage protocols in research (Section 2.2.2).
- Statistically significant kinematic differences among various ATD head models indicate that those with more anatomical accuracy display greater magnitudes of kinematic signatures related to concussive injuries.

**Comparisons of ATDs as Validators for FEM Models:**

- Computational FEM models of the human head are becoming increasingly biofidelic in representing critical head structures, with intracranial brain deformations due to excessive rotational accelerations being a key focus (Section 2.3).
- Current ATD head models used to validate these simulations do not accurately depict intracranial head components such as the brain, skull, and meninges complex (Section 2.5).

**Identification of Material Property Gaps in Current Models:**

- Simulant materials for the human brain and skull have been established, but their implementation as full-scale structures (e.g., biofidelic ATD head models) needs further exploration. Loading conditions relevant to those tested on ATDs, such as concussions, should be investigated more deeply.

- Improved ATD head forms and simulant structures have been developed with brain-like properties, but the vast reported properties of brain tissue in the literature make establishing a comprehensive brain simulant challenging (Section 2.4.1.3). Further assessment can be achieved through comprehensive testing criteria considering viscoelasticity of simulant structures in both uniaxial loading and oscillation frequency tests. Current biofidelic head models have yet to consider aspects such as oscillation frequencies in accurately representing brain tissue (Section 2.5.1).
- There is a need for improved simulation of critical structures, particularly the skull. Current bone simulants proposed in the literature behave like bone in material properties but do not consider the trabecular structure's kinetic dampening and loading effects (Section 2.4.2.3). Further iteration of bone simulants should consider these cancellous structures in both testing specimens and full-size constructions.
- Representation of the meninges remains a greater challenge due to the lack of comprehensive characterization studies on both native and simulant meningeal structures. Specifically, there is a lack of mechanical characterization of the FC and TC extensions of the DM (Section 2.4.3.1.1). Further studies are needed to understand the regional anisotropy and mechanical properties of the PAC in humans. Developing accurate meningeal simulants requires a deeper understanding of the material properties and structural composition of the meninges (Section 2.4.3.2). Current simulant materials need refinement to replicate the thin dimensions and complex mechanical behavior of native tissues accurately.

This literature review has identified significant gaps in the mechanical testing and simulation of critical human head structures, specifically in the areas of intracranial mechanics observation, sensor effectiveness, standardization of ATD headforms, and material property gaps in current models. Addressing these gaps is crucial for developing more accurate and reliable ATD head models and FEM simulations, ultimately leading to better protection and understanding of head injuries. The findings from this review will guide the methodology and proposed study of this thesis, aiming to contribute to the advancement of biofidelic head models and improved head impact evaluation techniques.

## 2.7 — Proposed Study

Addressing the gaps identified in the literature, the following chapters will outline research aimed at filling these gaps. Specifically, these chapters will consider characterization tests of simulants designed to mimic the mechanical, geometrical, and structural properties of critical head structures.

**Chapter Three: Characterization and Selection of a Brain Simulant for the Development of a Biofidelic Head Model**

This chapter focuses on selecting and characterizing brain simulants for developing a biofidelic head model. Elastomers such as bovine and agar hydrogels and silicones with Shore Hardness 00-10 are chosen for their accessibility and potential to replicate critical native structures. The material properties of these simulants will be determined using testing protocols similar to those used for native brain tissue characterization. These tests will simulate loading modes expected in concussion scenarios through compressive and shear loading in the brain, both in quasi-static and oscillating deformations using Dynamic Mechanical Analysis (DMA). Comparative values for quasi-static compression will be derived from the elastic modulus at defined strain ranges and the Ogden hyperelastic curve-fitting model. Frequency sweep moduli will be compared at specific points of frequencies.

**Chapter Four: Characterization and Selection of a Skull Surrogate for the Development of a Biofidelic Head Model**

This chapter investigates the use of additive manufacturing (AM) techniques to develop biofidelic skull surrogates. Materials such as Polylactic Acid (PLA), a bone-simulant PLA variant, and Hydroxyapatite-coated Poly(methyl methacrylate) (PMMA) will be used to create models tested for their flexural modulus and strength. The trabecular bone regions will be simulated by adjusting infill densities and print raster directions, optimizing manufacturing parameters for biofidelic performance. Additionally, this study will introduce Digital Image Correlation (DIC) to observe comparable strain fields and biofidelic failure mechanisms during testing. DIC will allow for accurate capturing of strain flow for irregular specimen geometry, choosing a skull-mimicking curved structure over a standardized testing specimen. This research aims to establish an ideal cranial bone simulant using these materials and manufacturing techniques, comparing material performance and failure mechanisms relative to native values and observations.

**Full-Scale Phantom Construction**

Each chapter will culminate in the construction of the proposed ideal simulants into a full-scale phantom. The development of these structures aims to address the relevant research gaps and realize the potential of constructing anatomically correct, biofidelic headforms for comprehensive impact testing and validation.

# *Chapter 3 — Characterization and Selection of a Brain Simulant for the Development of a Biofidelic Head Model*

## 3.1 — Introduction and Background

Efforts to understand Mild Traumatic Brain Injury (mTBI; concussion) — often called a 'silent epidemic' — are crucial due to its significant impact, particularly on young adults in sports [1]–[4]. mTBI results from concussive impacts that involve varying loading modes and impact rates, potentially leading to long-term cognitive deficits and mood disorders [1], [3], [5]–[11]. Consequently, the study of physical models simulating the human skull-brain complex is a rapidly evolving field aimed at improving the understanding of TBIs and enhancing safety measures, especially in sports [6], [7], [12]–[31].

Researchers have employed laboratory-based impact testing using Anthropomorphic Test Dummies (ATDs) such as the Hybrid-III, NOCSAE, and Hodgson-WSU models to simulate concussive scenarios and establish injury thresholds [6]–[11], [32]–[35]. Additionally, Finite Element Method (FEM) simulations of the human skull-brain under impact have proven relevant in depicting intracranial kinematics during concussive impacts [6]–[11], [36]–[38]. These simulations underscore the need for ATD head forms in validating head impact recreations, using extracted kinematic data as initial parameters. However, current ATD models lack biofidelic accuracy, limiting their effectiveness in predicting injury outcomes. Variations in kinematic signatures among ATD models due to differing representations of the human head have highlighted the need for improved validation and accurate injury thresholds [35], [39].

Improved head forms have been investigated in relevant studies [12], [32]–[34]. To develop a full-scale surrogate for testing kinematic events, it is essential to consider the material properties of brain tissue under blunt force impacts [12], [18], [25], [32], [33], [40]. Recent literature has focused on the mechanical characterization of native and simulant human head structures [3], [5]–[10], [12]–[14], [16], [18], [31], [36], [41]–[55]. Identifying suitable simulant materials that replicate the viscoelastic behavior of native brain tissue remains a challenge. Existing studies highlight the

complexities of brain tissue behavior, including its viscoelastic properties, regional variations, and environmental effects [12]–[14], [16], [18], [30], [31], [49], [56]. Various materials have been proposed as simulant candidates, but consensus on an ideal material for representing brain tissue in concussion scenarios is still needed.

This research addresses the gap in brain simulant characterization by providing a comprehensive testing criterion for all potential loading modes leading to concussion (Figure 3.1, Figure 3.2). By aggregating data from existing studies and defining key parameters for simulant evaluation [5]–[11], [36], [57], this study aims to identify an ideal surrogate material that closely mimics the mechanical response of native brain tissue under concussive blunt force impacts. Previous studies have suggested tissue simulants based on their performance relative to brain tissue. For instance, Singh et al. reported that bovine gelatins at 3% and 5% (wt%) closely match mixed grey and white porcine brain tissue in uniaxial compression, with 0.4% (wt%) agar gels performing similarly in viscoelastic frequency sweeps [14]. Falland-Cheung et al. and Navarro-Lozoya et al. further characterized agar and mammalian gelatin tissue simulants, with variations of mixed (A:B) compositions showing promising biofidelic results [15], [16]. These studies demonstrated that varying compositions of bovine gel and agar gel (wt%) closely represent brain tissue at specific uniaxial compression strain rates [15]. Alternatively, variations of silicone elastomers have been considered for simulation. Singh et al. observed that Sylgard 527 PDMS closely represents brain tissue in viscoelastic frequency sweeps, despite manufacturing challenges [14]. However, all tested 1:1 silicone elastomer compositions exhibited significantly stiffer responses than brain tissues [14], [15]. Chanda et al. suggested that variations of (A:B) silicone elastomer compositions can provide a closer depiction of brain tissue responses, as demonstrated through uniaxial tensile tests of developed dog-bone simulants [13].

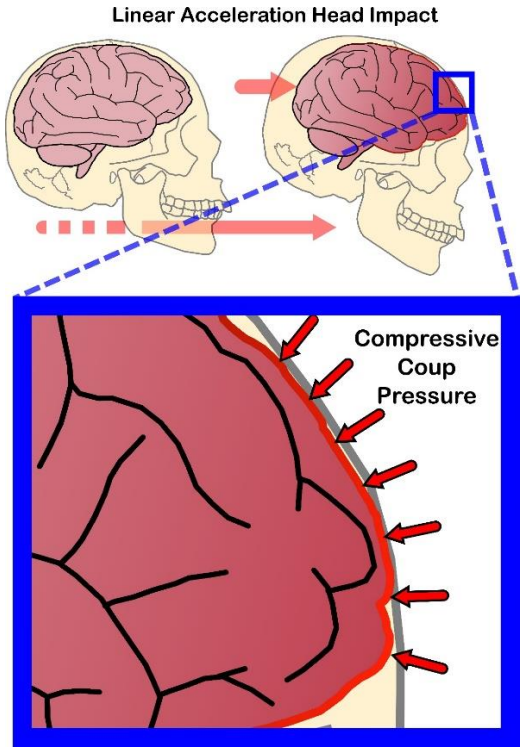


*Figure 3.1 — Linear Acceleration Head Impact Loading Modes*

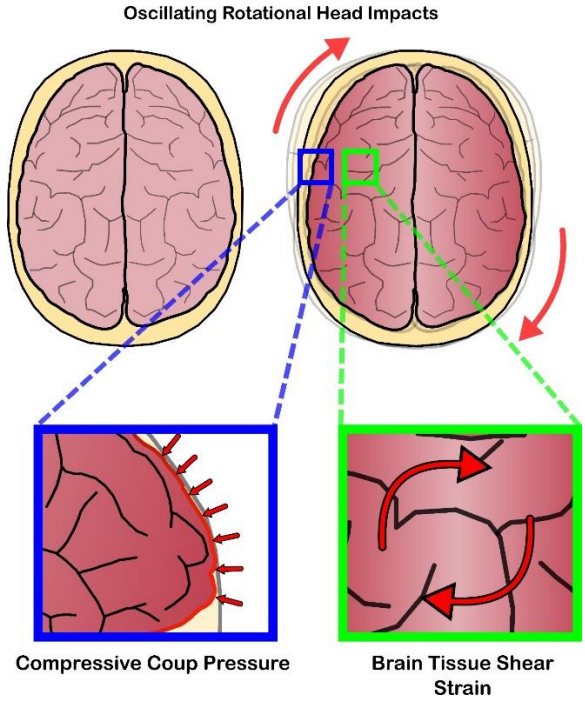


*Figure 3.2 — Rotational Oscillation Impact Loading Modes*

In brief, while numerous studies have proposed ideal simulant candidates, the variation in testing protocols and methodologies has prevented the selection of an objective candidate. Additionally,

the need to consider multiple aspects of concussive loading modes, such as oscillating stresses in compression and shear, remains. Studies on the oscillation characteristics of the human brain suggest the potential for amplifying resonant frequencies, resulting in excessive cranial strain and concussive symptoms [36], [58], [59]. This study aims to aggregate common approaches in brain tissue simulant tests, establish a comprehensive testing protocol for brain tissue under concussive scenarios, and propose a material that best mimics brain tissue. Advancements in skull-brain modeling will contribute to improved understanding and prevention of mTBI, enhancing safety measures in sports and beyond.

## 3.2 — Materials and Methods

### *3.2.1 — Brain Surrogate Characterization Protocol*

#### ***3.2.1.1 — Biofidelic Representation of the Native Human Brain***

Four specific simulant candidates were selected for material testing: bovine gelatin (Product No. G9391; Sigma-Aldrich, Merck KGaA; Darmstadt, Germany), agarose (agar) gelatin, a composite bovine/agar gel mixture, and varying concentrations of silicone elastomers. These materials and their specific concentrations were chosen based on their performances reported in previous literature [13]–[15], [20], [27], [50]. Each sample was prepared using the appropriate methods for mixing and gelation and then molded into cylindrical shapes with dimensions of 12.5 mm thickness and 20 mm diameter, following the ASTM D575-91 standard for rubber properties in compression [60]. Detailed observations of sample dimensions are shown in Figure 3.2.

3.2.1.1.1 — Preparation of Swelling Hydrogel Elastomers

The selected bovine gelatin concentrations for this experiment were 3% and 5% (wt%), while the agar gelatin concentration was 0.4% (wt%). Additionally, a combination of 4% bovine gelatin and 0.4% agar gelatin mixed at a 1:3 weight distribution was tested. These concentrations were chosen based on their elastic performance, which is comparable to porcine brain tissue [14]–[16].

To prepare the samples, distilled water was heated and stirred to around 80°C to maintain uniform consistency and prevent water evaporation. The prescribed weight of gelatin powder was then measured and dissolved in the heated water to achieve the desired weight concentrations. Using magnetic hot plates, the mixture was stirred for 20-30 minutes until fully melted. The mixture was

then carefully extracted and injected into enclosed polycarbonate molds lined with wax paper to prevent adhesion. These molds conformed to the ASTM D575-91 standard for rubber properties in compression. The filled molds were sealed in plastic bags to retain moisture and prevent material loss during gelation. After at least 24 hours of solidification, the samples were ready for testing.

3.2.1.1.2 — Preparation of Two-Part Crosslinking Silicone Elastomers

Silicone elastomers have been considered as simulant candidates due to their biofidelic responses and tunable concentrations, which allow them to mimic mechanical responses across various strain rates [13], [14], [17], [20]. This study will observe varied concentrations of silicone elastomers using proposed methods for testing biofidelity. Silicone elastomers of Shore Hardness 00-10 (EcoFlex™ series; Smooth-On Inc.; Macungie, Pennsylvania) were developed in concentrations of 1:1 (50% A, 50% B), 1:9 (10% A, 90% B), and 1:19 (5% A, 95% B) by weight.

The required weight distributions were measured using an electronic mass scale to ensure precise mass concentrations for samples within the polycarbonate ASTM D575 molds. Parts A and B were then combined and stirred thoroughly and slowly to minimize the formation of large bubbles. The viscous pre-formed samples were placed in a vacuum chamber for approximately 15 minutes, or until all possible bubbles were removed, respecting the 30-minute pot life of the silicone.

Once bubble-free, the pre-crosslinked viscous mixture was incorporated into the polycarbonate molds. The crosslinking times of the silicone elastomers varied according to their compositions: 4 hours for the 1:1 mixture, at least 12 hours for the 1:9 mixture, and up to 36 hours for the 1:19 mixture, as per the manufacturer's guidelines. Once fully formed, the samples were extracted from the molds and underwent similar test preparation procedures as the natural hydrogel specimens.

### *3.2.1.2 — Material Characterization Testing*

The brain tissue simulants were subjected to Dynamic Mechanical Analysis (DMA) using the Discovery Hybrid Rheometer (Model HR-3; TA Instruments; New Castle, Delaware) to characterize their mechanical properties. This analysis included quasi-static compression properties and dynamic viscoelastic properties, evaluated through frequency sweep tests for both compression and shear. All tests were conducted at room temperature, and the results were compared with brain tissue data from similar conditions in previous studies [14]–[16], [18], [45],

[58], [59], [61], [62]. Table 3.1 lists the testing conditions for native mammalian brain tissues used for comparison.

*Table 3.1 — Literature Review Testing Conditions for the Characterization of Native Mammalian Brain Tissues*

| Study | Brain Tissue | Testing | Test Conditions |
|---|---|---|---|
| Li et al. (2021) [45] | Bovine (**Grey Matter:** Cortex, Basal Ganglia; **White Matter:** Corona Radiata, Corpus Callosum) | DMA Compression (Frequency Sweep) | 0.5 to 35 Hz; Mean Displacement: 20% Strain |
| Li et al. (2020) [58] | Porcine (Mixed Grey and White Matter) | DMA Compression (Frequency Sweep) | 0 to 35 Hz; 10 to 20% Strain |
| Navarro-Lozoya et al. (2019) [15] | Porcine (Mixed Grey and White Matter) | Quasi-static Compression (Strain Step) | 0.1 $s^{-1}$, 1 $s^{-1}$; Up to 50% Strain, Strain Steps of 10% |
| Singh et al. (2019) [14] | Porcine (Mixed Grey and White Matter) | DMA Compression (Frequency Sweep) | 0-200 Hz; 0.2 to 0.37% Strain |
| | | Quasi-static Compression | 0.01 $s^{-1}$ ; 60% Strain |
| Falland-Cheung et al. (2018) [16] | Porcine (Mixed Grey and White Matter) | Quasi-static Compression (Strain Step) | 0.25 $s^{-1}$; Up to 50% Strain, Strain Steps of 20% |
| Boudjema et al. (2017) [61] | Lamb and Bovine (**Grey Matter:** Thalamus; **White Matter:** Corona | DMA Compression (Frequency Sweep) | 0 to ~20 Hz and 0 to ~100 Hz; 1% Strain, 50% Strain |

| | | | |
|---|---|---|---|
| | Radiata, Corpus Callosum) | | |
| Forte et al. (2017) [18] | Human (Parietal Lobe; Grey and White Matter) | DMA Shear (Frequency Sweep) | 0.01 to 25 Hz; 1% Strain |
| | | Quasi-Static Compression (From Compression Relaxation Tests) | 1, $1 \times 10^{-2}$ and $1 \times 10^{-4}$ $s^{-1}$; 35.6% True Strain |
| Nicolle et al. (2004) [62] | Human (Grey and White Matter) and Porcine (White Matter) | DMA Shear (Frequency Sweep) | 0.1 to 10000 Hz; 0.01% to 0.1% Strain |
| Bliston et al. (2001) [110] | Bovine (Mixed Grey and White Matter) | DMA Shear (Frequency Sweep) | 0.01 to 20 Hz; 0.1% Strain |

The applied strain, strain rate, and oscillations were selected based on the values experienced by cranial tissue during human head impacts [5]–[11], [36]. The characterization experiments followed a testing matrix (Table 3.2) designed to simulate the material characteristics of native brain tissues under these loading conditions, aiming to accurately represent brain tissue through artificial simulants during injurious events.

*Table 3.2 — Testing Matrix for Brain Tissue Simulants and Testing Sequences*

| Materials | Sample Size (n) | | | | | | Concentration Total |
|---|---|---|---|---|---|---|---|
| | Test Sequence / Concentration (wt. %) or (A:B wt.) | Quasi-Static Compression | DMA Frequency Sweep (Compression) 0.2% Strain | DMA Frequency Sweep (Shear) Strains (%) | | | |
| | | | | 1 | 10 | 20 | |
| Bovine Gel | 3% | 5 | 5 | 5 | 5 | 5 | 25 |
| | 5% | 5 | 5 | 5 | 5 | 5 | 25 |
| | Total per Test | 10 | 10 | 10 | 10 | 10 | |
| | | | | 30 | | | |
| | Material Total | 50 | | | | | |
| Bovine Gel and Agar Gel Mixture | 4% Bovine, 0.4% Agar (1:3) | 5 | 5 | 5 | 5 | 5 | 25 |
| | Total per Test | 5 | 5 | 5 | 5 | 5 | |
| | | | | 15 | | | |
| | Material Total | 25 | | | | | |
| Agar Gel | 0.4% | 5 | --* | --* | | | 5 |
| | Total per Test | 5 (*DMA not tested) | | | | | |
| | Material Total | 5 | | | | | |
| EcoFlex Silicone 00-10 | (1:1) | 5 | 5 | 5 | 5 | 5 | 25 |
| | (1:9) | 5 | 5 | 5 | 5 | 5 | 25 |
| | (1:19) | 5 | 5 | 5 | 5 | 5 | 25 |
| | Total per Test | 15 | 15 | 15 | 15 | 15 | Grand Total (n) |
| | | | | 45 | | | 155 |
| | Material Total | 75 | | | | | |

3.2.1.2.1 — Quasi-Static Compression Tests

For the quasi-static compression tests, samples were compressed using the HR-3 rheometer with 25 mm ETC steel parallel plate attachments at a constant strain rate of 1 mm/s (0.1 $s^{-1}$). Configuration of simulant specimens can be observed in Figure 3.3. The strain was incrementally increased to 60% of the samples' initial thickness, replicating the maximum strain experienced by native brain tissue when significant axonal nerve cell destruction occurs [5].

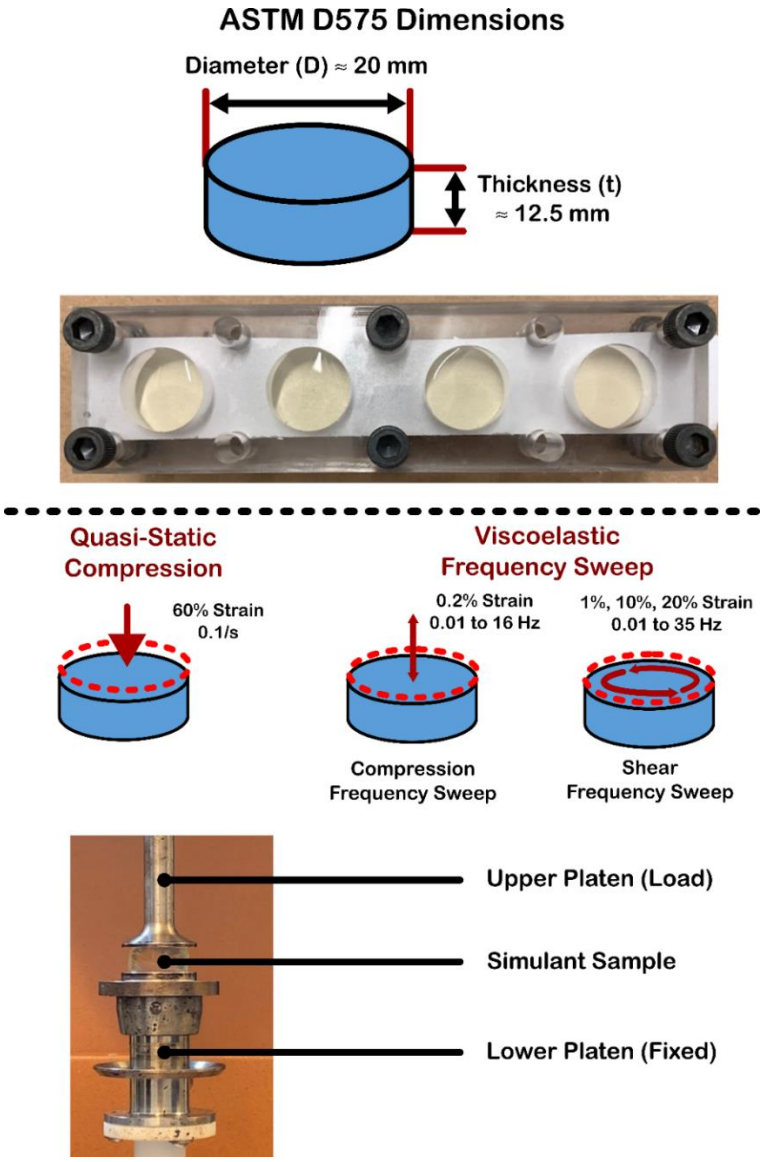


*Figure 3.3 — Brain Simulant Dimension Specifications (Top), and Test Configurations (Bottom)*

To ensure secure positioning and hydration of the samples during testing, Gaffer Friction Tape (Product No. GPB30; Gaffer Power Inc.; Vancouver, British Columbia) supported by a phosphate-

buffered saline (PBS) coating was applied to the rheometer's parallel plate attachments. The device was calibrated to its zero gap with the tape in place, and the crosshead axial force was zeroed before each test to reduce noise. The testing gap was set slightly above the sample thickness to minimize preloading and ensure accurate strain application, accommodating up to 50% strain, sufficient for simulating significant brain tissue injury and comparison to brain tissue characterizations in literature. Stress-strain data were captured using the TA Instruments TRIOS Data Acquisition Software for subsequent analysis.

Given the non-linear nature of the viscoelastic samples' stress-strain performance, the data required translation to a hyperelastic curve-fitting model to obtain accurate moduli and elasticity parameters for comparison to brain tissue and surrogate alternatives [14], [47], [63], [64]. Two methods were employed: a strain-step linear fitment method for assessing non-linear viscoelastic stress-strain behavior, and a hyperelastic curve-fitting model to determine viscoelastic parameters (Figure 3.4).

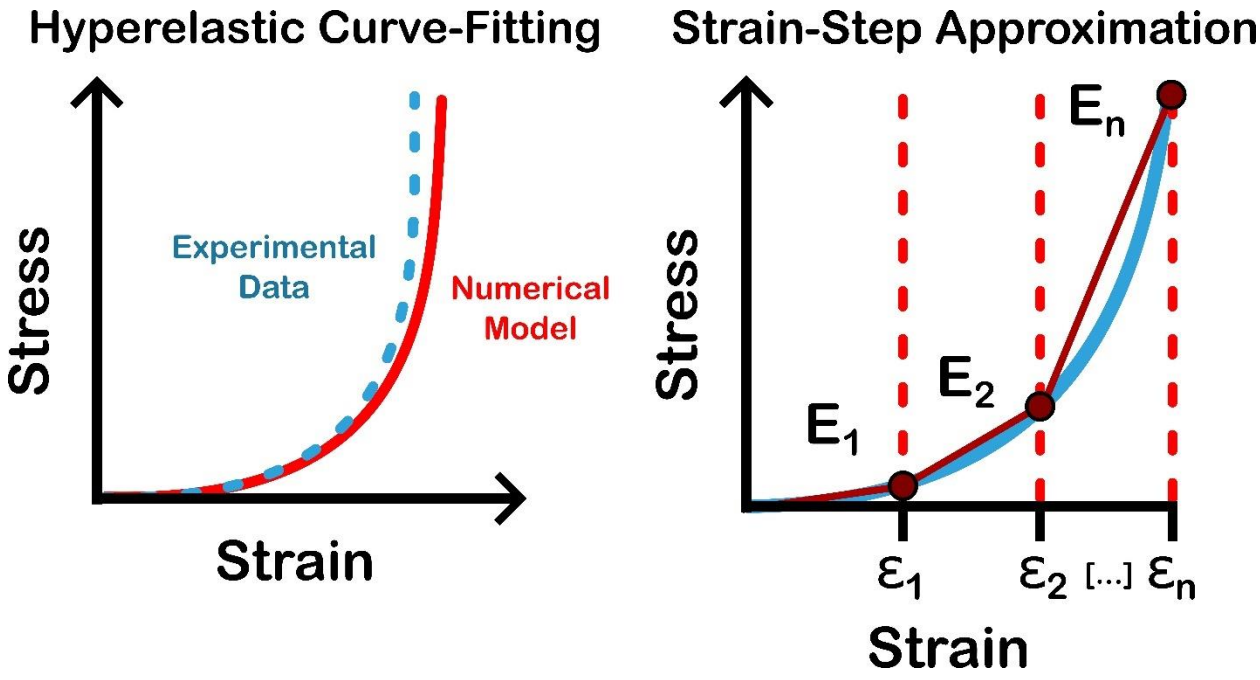


*Figure 3.4 — Non-Linear Modulus Calculation Methodologies*

The strain-step approach involves fitting critical strain regions (strain steps) into distinct intervals (e.g., 0-10%, 10-20%), characterizing the corresponding elastic modulus within each step. This methodology allows comprehensive characterization of the material's mechanical response. For this study, strain steps were adopted from Falland-Cheung et al., Navarro-Lozoya et al., and

Tamura et al. [15], [16], [65]. A three-moduli strain-step approach was applied at regions of 0-20%, 20-40%, and 40-50% [16], followed by a five-moduli strain-step approach at regions of 0-10%, 10-20%, 20-30%, 30-40%, and 40-50% [15], [65]. The moduli for these regions were compared to similar studies and other quasi-static characterizations of native brain tissues with open-access data.

The Ogden hyperelastic model was chosen for hyperelastic curve fitting, as it has been shown to capture the anisotropies of brain tissue's stress behavior in tension and compression loading modes [47], [63]. Experimental stress-strain data from the tested simulant samples were input into MATLAB 2023b software (The MathWorks, Inc., Natick, Massachusetts) for curve fitting using the Ogden model. The initial shear moduli of each surrogate candidate were then compared against each alternative.

$$W(\lambda_1, \lambda_2, \lambda_3) = \sum_{i=1}^{n} \frac{\mu_i}{\alpha_i} ({\lambda_1}^{\alpha_i} + {\lambda_2}^{\alpha_i} + {\lambda_3}^{\alpha_i} - 3)$$

*Equation 3.1 — Ogden Hyperelastic Curve-Fitting Model [14]*

$$G = \frac{1}{2} \sum_{i=1}^{n} \mu_i \alpha_i$$

*Equation 3.2 — Initial Shear Modulus [14]*

*Where **W** = Strain Energy Density; $\boldsymbol{\lambda_i}$ = Principal Stretch Ratios; **n, μ, α** = Material Constants; **G** = Initial Shear Modulus*

Parameters were evaluated using a p-value comparison from a two-tailed t-test, where the null hypothesis claimed that the proposed materials display biofidelic representation of native tissue. P-values below 0.05 rejected the null hypothesis, indicating that the proposed material did not have biofidelic material properties.

3.2.1.2.2 — Viscoelastic Frequency Sweep Tests Using Dynamic Mechanical Analysis (DMA)

Viscoelastic frequency sweep tests are crucial for evaluating the biofidelic performance of simulant candidates under head impact scenarios. These tests simulate strains and oscillations on the candidate materials relative to the expected strains and strain rates experienced by cranial tissue during traumatic impacts.

The viscoelastic properties of the selected surrogate candidates were assessed using a TA HR-3 rheometer, leveraging its frequency sweep capabilities in both compression and shear. Frequency sweep tests involved subjecting the specimens to oscillating shear or compressive deformation at predetermined frequencies and strains. In this experiment, shear strains of 1%, 10%, and 20%, and a compressive strain of 0.2%, were applied to the specimens. Oscillation frequencies ranged from 0.01 to 35 Hz in shear, corresponding to expected frequencies in injurious head impacts [5]–[11], [36]. These oscillations correlated with strain rates of 0.35 $s^{-1}$ (1% strain), 3.5 $s^{-1}$ (10% strain), and 7 $s^{-1}$ (20% strain). Compressive DMA was conducted with oscillations from 0.01 to 16 Hz (0.07 $s^{-1}$), within the maximum capabilities of the HR-3 device.

The selected strains were chosen to observe notable behaviors found in brain tissue. A 1% shear strain and 0.2% compressive strain denote the region of viscoelastic linearity, where the dynamic modulus is linearly dependent on the frequency applied to the material [14], [67]. A 10% strain corresponds to the maximum principal strain at which brain tissue begins to show evidence of Diffuse Axonal Injury (DAI) due to excess tensile strain on axonal fibers under rapid shear stress [5], [66]. Finally, a 20% strain defines the minimum threshold at which Traumatic Brain Injury (TBI) is found to occur in head impacts [5].

Following frequency sweep testing, viscoelastic parameters, including storage modulus, loss modulus, and their respective complex moduli, were determined for subsequent analysis. The storage and loss moduli represent the real and imaginary parts of the material's viscoelastic performance, indicating the elastic (storage) and viscous (loss) components, respectively [14]. The complex modulus, the root squared sum of the storage and loss moduli, serves as the key parameter for material performance, reflecting the overall viscoelastic properties derived from DMA testing.

During testing, the samples were securely positioned and loaded into the HR-3 device. The device's crosshead was adjusted to apply a slight pre-load of approximately 0.05 N, ensuring proper contact for dynamic loading. Once the pre-load was established, the specified strains and a range of frequencies were applied to facilitate the experimentation. Gaffer friction tape was applied to the testing geometry to prevent slippage during dynamic testing.

## 3.3 — Results

### *3.3.1 — Brain Simulant Characteristics*

#### ***3.3.1.1 — Uniaxial Unconfined Quasi-Static Compression Testing***

Quasi-static compression results were generated from the developed testing specimens (*n = 35; n = 5 per material and concentration tested*). The mechanical properties of the tested samples are summarized in Tables 3.3 to 3.5. From the observed values in testing (Figure 3.5), all specimens except agar gel demonstrated loading mechanisms similar to those of brain tissue up to the recorded 50% strain. The varying elastomers exhibited stiffer responses than the natural-based hydrogels, with silicone elastomers generating the stiffest response. Among the elastomers, higher concentrations of the B-component resulted in stiffer responses. Consequently, EcoFlex™ 00-10 (1:1) was omitted from Figure 3.3 due to its excessively stiff loading response compared to the other materials. Stiffer responses were indicated by a greater rate of increase in the non-linear stress-strain curve. Agar gel experienced the stiffest response at around 30% strain but failed before reaching the full 50% strain range.

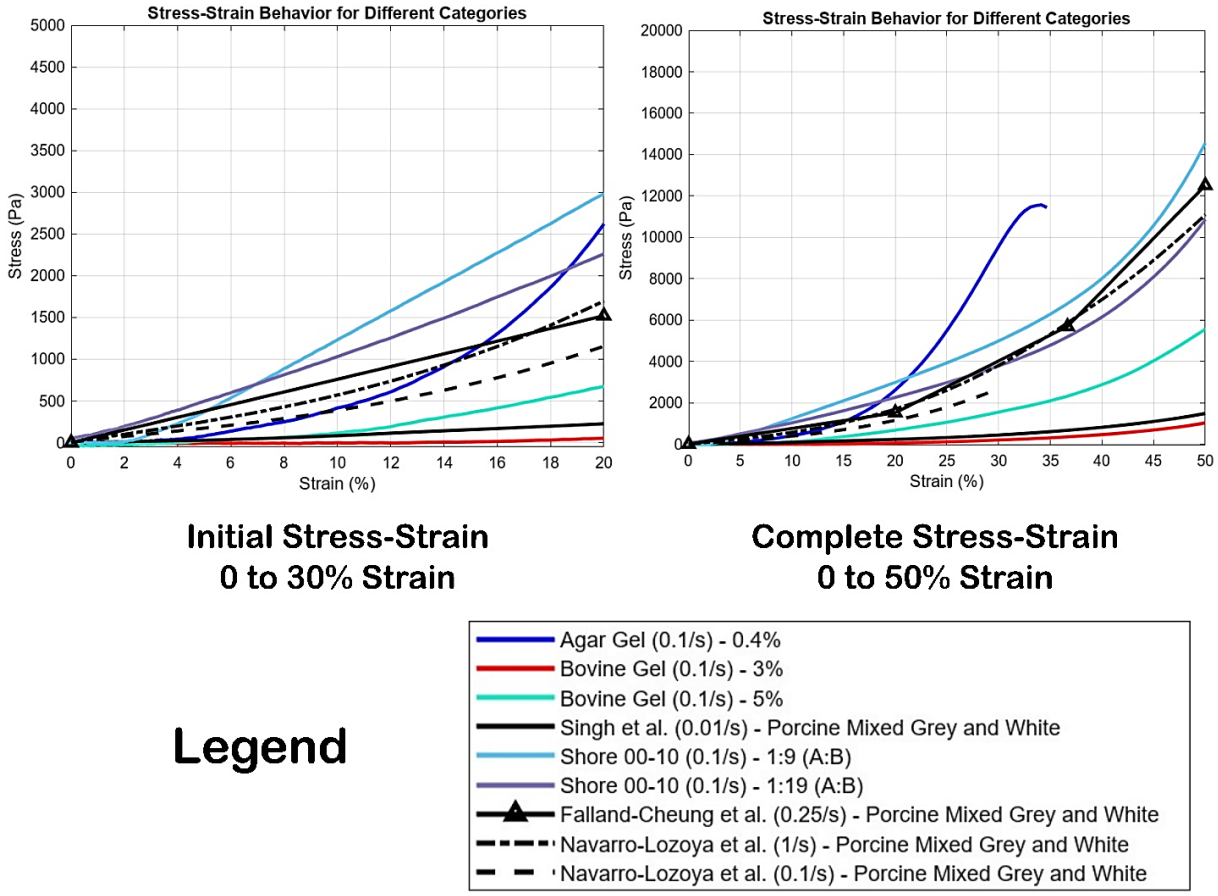


*Figure 3.5 — Mean Stress-Strain Behaviour of Simulant Candidates Compared to Room Temperature Brain Tissue in Literature [14]–[16]*

3.3.1.1.1 — Strain Step Approach for Hyperelastic Curve Fitment

To compare the compression results with those found in the literature, elastic moduli determined from the stress-strain data for each tested material were fitted into a strain-step approximation for strain ranges of 0 to 10% (E1), 10 to 20% (E2), 20 to 30% (E3), 30 to 40% (E4), and 40 to 50% (E5) for the five-moduli strain-step approach, and 0 to 20% (E1), 20 to 40% (E2), 40 to 50% (E3) for the three-moduli approach [15], [16], [65]. For materials that failed before reaching the defined strain ranges—such as agar gel at 0.4% concentration—elastic moduli were calculated only up to their ultimate strength. Studies characterizing native brain tissue without employing the strain-step approach were approximated for strain-step analysis in this study [14].

*Table 3.3 — Five Moduli Strain-Step Elastic Modulus Approximations for Tested Samples in Comparison to Native Mammalian Brain Tissues Found in Literature [14], [15]*

| **Study** | **Material** | **Elastic Modulus (Assuming Strain Step Technique) [kPa]** | | **95th Percentile Confidence Interval** | **p-Value** | |
|---|---|---|---|---|---|---|
| | | | | | **Singh et al. (2019) [3]** | **Navarro-Lozoya et al. (2019) [4]** |
| **Current Study** | Agar Gel, 0.4% Mean Value **0.1 $s^{-1}$** | $E_1$ | 9.27 ± 1.6 | [8.14, 10.4] | Incompatible for Comparison | Incompatible for Comparison |
| | | $E_2$ | 43.66 ± 8.9 | [37.71, 49.61] | | |
| | | $E_3$ | 72.97 ± 9.4 | [66.43, 79.52] | | |
| | | $E_4$* | -109.43 ± 5.1 | [-112.98, -105.88] | | |
| | | $E_5$* | -3.39 ± 1.9 | [-4.73, -2.06] | | |
| | Shore 00-10 1:1 (50% A; 50% B) Mean Value **0.1 $s^{-1}$** | $E_1$ | 36.26 ± 2.63 | [33.28, 29.24] | 0.0154 | 0.0162 |
| | | $E_2$ | 52.63 ± 4.14 | [47.95, 57.31] | | |
| | | $E_3$ | 61.57 ± 2.59 | [58.64, 64.49] | | |
| | | $E_4$ | 82.95 ± 3.39 | [78.55, 87.35] | | |
| | | $E_5$ | 147.51 ± 7.58 | [138.93, 156.09] | | |
| | Shore 00-10 1:9 (10% A; 90% B) Mean Value **0.1 $s^{-1}$** | $E_1$ | 10.62 ± 1.06 | [9.43, 11.82] | 0.0138 | 0.220 |
| | | $E_2$ | 17.52 ± 1.08 | [15.94, 18.38] | | |
| | | $E_3$ | 19.34 ± 1.31 | [17.84, 20.85] | | |
| | | $E_4$ | 27.83 ± 1.76 | [25.83, 29.82] | | |
| | | $E_5$ | 54.34 ± 2.71 | [51.28, 57.41] | | |
| | Shore 00-10 1:19 (5% A; 95% B) Mean Value **0.1 $s^{-1}$** | $E_1$ | 10.49 ± 0.19 | [10.28, 10.71] | 0.008 | 0.276 |
| | | $E_2$ | 12.66 ± 0.38 | [12.22, 13.10] | | |
| | | $E_3$ | 13.94 ± 0.19 | [13.72, 14.16] | | |
| | | $E_4$ | 18.94 ± 0.58 | [18.28, 19.60] | | |
| | | $E_5$ | 34.97 ± 0.40 | [34.52, 35.42] | | |
| | Bovine Gel 4% and Agar Gel 0.4%, Mixed Mean Value **0.1 $s^{-1}$** | $E_1$ | 2.47 ± 0.37 | [2.18, 2.77] | 0.0278 | 0.088 |
| | | $E_2$ | 3.67 ± 0.71 | [3.10, 4.23] | | |
| | | $E_3$ | 6.32 ± 1.07 | [5.47, 7.18] | | |
| | | $E_4$ | 11.00 ± 1.72 | [9.62, 12.38] | | |
| | | $E_5$ | 13.46 ± 1.68 | [12.12, 14.81] | | |
| | Bovine Gel, 3% Mean Value **0.1 $s^{-1}$** | $E_1$ | 1.19 ± 0.29 | [0.98, 1.41] | 0.178 | 0.019 |
| | | $E_2$ | 1.69 ± 0.23 | [1.52, 1.87] | | |
| | | $E_3$ | 2.77 ± 0.28 | [2.56, 2.98] | | |
| | | $E_4$ | 5.88 ± 1.11 | [5.06, 6.70] | | |

| | | | | | | |
|---|---|---|---|---|---|---|
| | | $E_5$ | 10.90 ± 2.37 | [11.47, 14.98] | | |
| | Bovine Gel, 5%<br>Mean Value<br>**0.1 $s^{-1}$** | $E_1$ | 6.04 ± 2.00 | [4.55, 7.52] | 0.070 | 0.549 |
| | | $E_2$ | 8.68 ± 2.61 | [6.75, 10.62] | | |
| | | $E_3$ | 12.46 ± 3.75 | [9.68, 15.24] | | |
| | | $E_4$ | 22.10 ± 8.77 | [15.61, 28.60] | | |
| | | $E_5$ | 50.31 ± 24.31 | [32.32, 68.34] | | |
| **Singh et al. (2019) [3]** | **Porcine Brain**<br>(Mixed Grey and White Matter)<br>Room Temperature<br>**0.01 $s^{-1}$**<br>**(Approximation from Stress-Strain Data)** | **$E_1$** | **0.78** | | | |
| | | **$E_2$** | **1.41** | | | |
| | | **$E_3$** | **2.12** | | | |
| | | **$E_4$** | **3.72** | | | |
| | | **$E_5$** | **6.61** | | | |
| **Navarro-Lozoya et al. (2019) [4]** | **Porcine Brain**<br>(Mixed Grey and White Matter)<br>**1 $s^{-1}$**<br>**Room Temperature** | **$E_1$** | **5.70** | | | |
| | | **$E_2$** | **11.26** | | | |
| | | **$E_3$** | **21.16** | | | |
| | | **$E_4$** | **31.76** | | | |
| | | **$E_5$** | **41.00** | | | |

***** Elastic Moduli for Agar gel after 30% not recorded due to material failure prior to defined strains.

*Table 3.4 — Three-Strain Step Elastic Modulus Approximations for Tested Samples in Comparison to Native Mammalian Brain Tissues Found in Literature [14]–[16]*

| **Study** | **Material** | **Elastic Modulus (Assuming Strain Step Technique) [kPa]** | | **95th Percentile Confidence Interval** | **p-Value** | | |
|---|---|---|---|---|---|---|---|
| | | | | | **Singh et al. (2019) [3]** | **Navarro-Lozoya et al. (2019) [4]** | **Falland-Cheung et al. (2019) [5]** |
| **Current Study** | Agar Gel, 0.4%<br>Mean Value<br>**0.1 $s^{-1}$** | $E_1$ | 26.1 ± 4.99 | [22.63, 29.55] | Incompatible for Comparison | Incompatible for Comparison | Incompatible for Comparison |
| | | $E_2$ | -18.31 ± 6.28 | [-22.67, -13.96] | | | |
| | | $E_3$* | -3.39 ± 1.93 | [-4.23, -2.06] | | | |

| | | | | | | | |
|---|---|---|---|---|---|---|---|
| | Shore 00-10 1:1 (50% A; 50% B) Mean Value **0.1 $s^{-1}$** | $E_1$ | 41.58 ± 2.78 | [38.43, 44.72] | 0.107 | 0.111 | 0.095 |
| | | $E_2$ | 72.39 ± 3.12 | [68.86, 75.93] | | | |
| | | $E_3$ | 147.51 ± 7.58 | [138.93, 156.09] | | | |
| | Shore 00-10 1:9 (10% A; 90% B) Mean Value **0.1 $s^{-1}$** | $E_1$ | 17.42 ± 1.10 | [16.18, 18.66] | 0.103 | 0.325 | 0.064 |
| | | $E_2$ | 23.40 ± 1.51 | [21.70, 25.11] | | | |
| | | $E_3$ | 54.35 ± 2.71 | [51.28, 57.41] | | | |
| | Shore 00-10 1:19 (5% A; 95% B) Mean Value **0.1 $s^{-1}$** | $E_1$ | 10.99 ± 0.11 | [10.86, 11.11] | 0.092 | 0.376 | 0.017 |
| | | $E_2$ | 16.36 ± 0.40 | [15.91, 16.81] | | | |
| | | $E_3$ | 34.97 ± 0.40 | [34.52, 35.42] | | | |
| | Bovine Gel 4% and Agar Gel 0.4%, Mixed Mean Value **0.1 $s^{-1}$** | $E_1$ | 2.92 ± 0.40 | [2.57, 3.24] | 0.088 | 0.122 | 0.364 |
| | | $E_2$ | 8.36 ± 1.46 | [7.19, 9.54] | | | |
| | | $E_3$ | 13.59 ± 1.53 | [12.37, 14.81] | | | |
| | Bovine Gel, 3% Mean Value **0.1 $s^{-1}$** | $E_1$ | 1.30 ± 0.23 | [1.13, 1.48] | 0.297 | 0.097 | 0.178 |
| | | $E_2$ | 4.25 ± 0.59 | [3.82, 4.69] | | | |
| | | $E_3$ | 13.22 ± 2.37 | [11.47, 14.98] | | | |
| | Bovine Gel, 5% Mean Value **0.1 $s^{-1}$** | $E_1$ | 6.92 ± 2.10 | [5.37, 8.48] | 0.204 | 0.948 | 0.201 |
| | | $E_2$ | 17.25 ± 6.06 | [12.76, 21.74] | | | |
| | | $E_3$ | 50.33 ± 24.31 | [32.32, 68.34] | | | |

| | | | | |
|---|---|---|---|---|
| **Singh et al. (2019) [3]** | **Porcine Brain** (Mixed Grey and White Matter) Room Temperature **0.01 $s^{-1}$ (Approximation from Stress-Strain Data)** | **$E_1$** | 1.05 | |
| | | **$E_2$** | 2.88 | |
| | | **$E_3$** | 6.61 | |
| **Navarro-Lozoya et al. (2019) [4]** | **Porcine Brain** (Mixed Grey and White Matter) **1 $s^{-1}$ Room Temperature** | **$E_1$** | 7.93 | |
| | | **$E_2$** | 26.71 | |
| | | **$E_3$** | 41.07 | |
| **Falland-Cheung et al. (2018) [5]** | **Porcine Brain** (Mixed Grey and White Matter) **0.25 $s^{-1}$ Room Temperature** | **$E_1$** | **2.44** | |
| | | **$E_2$** | **10.18** | |
| | | **$E_3$** | **25.02** | |

* Elastic Moduli for Agar gel after 30% not recorded due to material failure prior to defined strains.

Observing the moduli step comparisons for both the five-step (Table 3.3) and three-step (Table 3.4) approaches, the results from the three-step approach showed that all materials, except for bovine gel at 3% and 5% concentrations, behaved similarly to tested brain tissue with minimal statistical difference (p-value > 0.05). When using the five-step approach, the number of biofidelic simulants decreased, with Shore 00-10 (1:9) and (1:19), bovine gel 5%, and the bovine gel and agar gel combination (4% bovine; 0.4% agar) demonstrating biofidelic responses with no statistically significant differences compared to specific brain tissue results found in the literature.

3.3.1.1.2 — Ogden Hyperelastic Curve Fitting

The stress-strain curves were alternatively approximated using the Ogden hyperelastic curve-fitting model to determine parameters for initial shear moduli (Figure 3.6). Studies that did not employ a curve-fitting method were subsequently curve-fitted for comparison if compatible. The Ogden One-Term (1st Order) Model best portrayed the non-linear nature of the viscoelastic stress-strain curves observed in experiments. Parameters for this model are tabulated in Table 3.5, which

also specifies any material requiring expanded terms for the Ogden Hyperelastic Model. The study by Falland-Cheung et al., which used the strain-step approach, was excluded from hyperelastic curve fitting due to insufficient data points for an accurate fit [5].

*Table 3.5 — Ogden Hyperelastic Parameters for Tested Simulant Materials and Native Mammalian Brain Tissue Specimens Found in Literature [14], [15], [18]*

| **Study** | **Material** | **Ogden Hyperelastic Parameters** | | **p-Value** | | | | |
|---|---|---|---|---|---|---|---|---|
| | | | | ***Singh et al. [3] (0.01 $s^{-1}$)*** | ***Navarro-Lozoya et al. [4]*** | | ***Forte et al. (0.01 $s^{-1}$) [7]*** | |
| | | | | | ***1 $s^{-1}$*** | ***0.1 $s^{-1}$*** | ***GM*** | ***WM*** |
| **Current Study** | Agar Gel, 0.4% Mean Value **0.1 $s^{-1}$** | ***G** (Initial Shear Moduli, kPa)* | 9.23 ± 4.3 | 0.04 | 0.10 | 0.626 | 0.136 | 0.003 |
| | | *$95^{th}$ Percentile Confidence Interval (kPa)* | [6.47, 14.0] | | | | | |
| | | ***$R^2$ Value*** | 0.987 | | | | | |
| | Shore 00-10 1:1 (50% A; 50% B) Mean Value **0.1 $s^{-1}$** | ***G** (Initial Shear Moduli, kPa)* | 22.61 ± 1.60 | 7.38 x $10^{-5}$ | 9.53 x $10^{-5}$ | 1.25 x $10^{-4}$ | 1.40 x $10^{-4}$ | 2.51 x $10^{-4}$ |
| | | *$95^{th}$ Percentile Confidence Interval (kPa)* | [21.2, 24.0] | | | | | |
| | | ***$R^2$ Value*** | 0.997 | | | | | |
| | Shore 00-10 1:9 (10% A; 90% B) Mean Value **0.1 $s^{-1}$** | ***G** (Initial Shear Moduli, kPa)* | 7.65 ± 0.85 | 0.0014 | 0.010 | 0.0032 | 0.0051 | 0.20 |
| | | *$95^{th}$ Percentile Confidence Interval (kPa)* | [6.83, 8.32] | | | | | |
| | | ***$R^2$ Value*** | 0.993 | | | | | |
| | Shore 00-10 1:19 (5% A; 95% B) | ***G** (Initial Shear Moduli, kPa)* | 5.79 ± 2.68 | 5.19 x $10^{-5}$ | 6.66 x $10^{-4}$ | 1.53 x $10^{-4}$ | 3.06 x $10^{-4}$ | 0.0544 |

| | | | | | | | | |
|---|---|---|---|---|---|---|---|---|
| | Mean Value **0.1 $s^{-1}$** | *95th Percentile Confidence Interval (kPa)* | [3.72, 8.43] | | | | | |
| | | ***$R^2$ Value*** | 0.995 | | | | | |
| | Bovine Gel 4% and Agar Gel 0.4%, Mixed Mean Value **0.1 $s^{-1}$** | ***G** (Initial Shear Moduli, kPa)* | 1.12 ± 0.29 | 0.010 | 6.10 x $10^{-4}$ | 0.0020 | 5.91 x $10^{-4}$ | 3.85 x $10^{-5}$ |
| | | *95th Percentile Confidence Interval (kPa)* | [0.91, 1.43] | | | | | |
| | | ***$R^2$ Value*** | 0.993 | | | | | |
| | Bovine Gel, 3% Mean Value **0.1 $s^{-1}$** | ***G** (Initial Shear Moduli, kPa)* | 1.07 ± 0.09 | 0.12 | 4.78 x $10^{-5}$ | 1.31 x $10^{-4}$ | 5.34 x $10^{-5}$ | 5.32 x $10^{-6}$ |
| | | *95th Percentile Confidence Interval (kPa)* | [0.99, 1.14] | | | | | |
| | | ***$R^2$ Value*** | 0.999 | | | | | |
| | Bovine Gel, 5% Mean Value **0.1 $s^{-1}$** | ***G** (Initial Shear Moduli, kPa)* | 3.43 ± 0.73 | 0.039 | 0.10 | 0.623 | 0.14 | 0.0033 |
| | | *95th Percentile Confidence Interval (kPa)* | [2.58, 3.86] | | | | | |
| | | ***$R^2$ Value*** | 0.997 | | | | | |
| **Singh et al. (2019) [3]** | **Porcine Brain Room Temperature** Mean Value (Mixed Grey and White Matter) **0.01 $s^{-1}$** | ***G** (Initial Shear Moduli, kPa)* | **0.69684** | | | | | |

| | | | | |
|---|---|---|---|---|
| **Navarro-Lozoya et al. (2019) [4]** | **Porcine Brain Room Temperature** Mean Value (Mixed Grey and White Matter) **1 $s^{-1}$ (Approximation from Stress-Strain Data)** | | ***G*** *(Initial Shear Moduli, kPa)* | **5.9277** |
| | **Room Temperature** Mean Value (Mixed Grey and White Matter) **0.1 $s^{-1}$ (Approximation from Stress-Strain Data)** | | ***G*** *(Initial Shear Moduli, kPa)* | **4.0575** |
| **Forte et al. (2017) [7]** | Human (Parietal Lobe; Grey and White Matter) **1 $s^{-1}$** | GM | $\mu_1$ *(kPa)* | **0.520** |
| | | | $\alpha_1$ | **4.4** |
| | | | ***G*** *(Initial Shear Moduli, kPa)* | **1.144** |
| | | WM | $\mu_1$ *(kPa)* | **1.030** |
| | | | $\alpha_1$ | **4.3** |
| | | | ***G*** *(Initial Shear Moduli, kPa)* | **2.21450** |

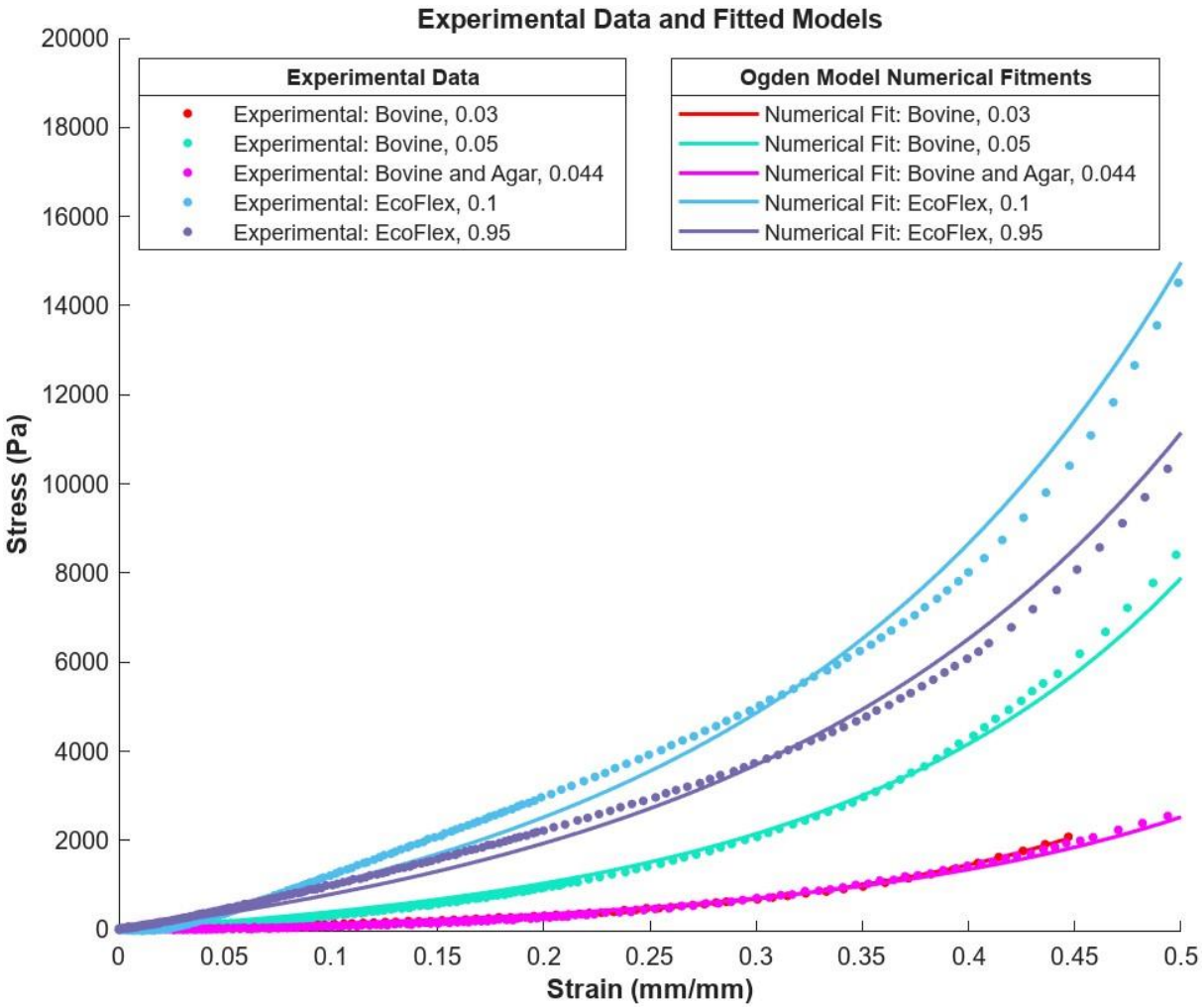


*Figure 3.6 — Ogden Numerical Curve Fitting for Simulant Materials ($R^2 > 0.99$)*

The results indicate that the Ogden model provided a more rigorous analysis approach. Among the proposed simulants, agar gel at 0.4%, Shore 00-10 at (1:9) and (1:19) compositions, and all bovine gel variations exhibited responses similar to brain tissue characterizations in the literature, with little statistical significance (p-value > 0.05). Bovine gel at 5% demonstrated the most biofidelic response compared to brain tissue values from the literature, aligning closely with results from Navarro-Lozoya et al. on mixed porcine brain tissue (for 1 $s^{-1}$ and 0.1 $s^{-1}$ strain rates) and Forte et al. on human grey matter [4], [7]. Agar gel at 0.4% also showed a biofidelic response regarding its initial shear modulus, closely resembling the mixed porcine brain study by Singh et al. and the grey matter study by Forte et al. [3], [7]. However, beyond the initial strain response, the stress-strain behavior of agar gel did not accurately mimic that of brain tissue (Figure 3.3).

The observed results and parameters are detailed in Table 3.5, highlighting the effectiveness of the Ogden model in capturing the viscoelastic properties of the simulants compared to native brain tissue.

#### *3.3.1.2 — DMA Through Viscoelastic Frequency Sweep Tests*

DMA frequency sweep results were obtained from the testing specimens (*n = 120; n = 5 per material and concentration tested, n = 5 per applied shear strain, n = 5 per specimen for compression frequency sweeps*). The mechanical properties of the tested samples in shear and compression are shown in Figures 3.7 to 3.13. Viscoelastic behaviors were derived from the crosshead data generated by the TA Discovery HR-3 during compressive and shear oscillation testing. For shear frequency sweep tests, strains of 1%, 10%, and 20% were applied. For compression tests, a strain of 0.2% was used due to the HR-3 device limitations and to observe the linear viscoelastic limit of the materials. Agar gel was excluded from viscoelastic analysis due to its insufficient biofidelic performance in quasi-static compression tests.

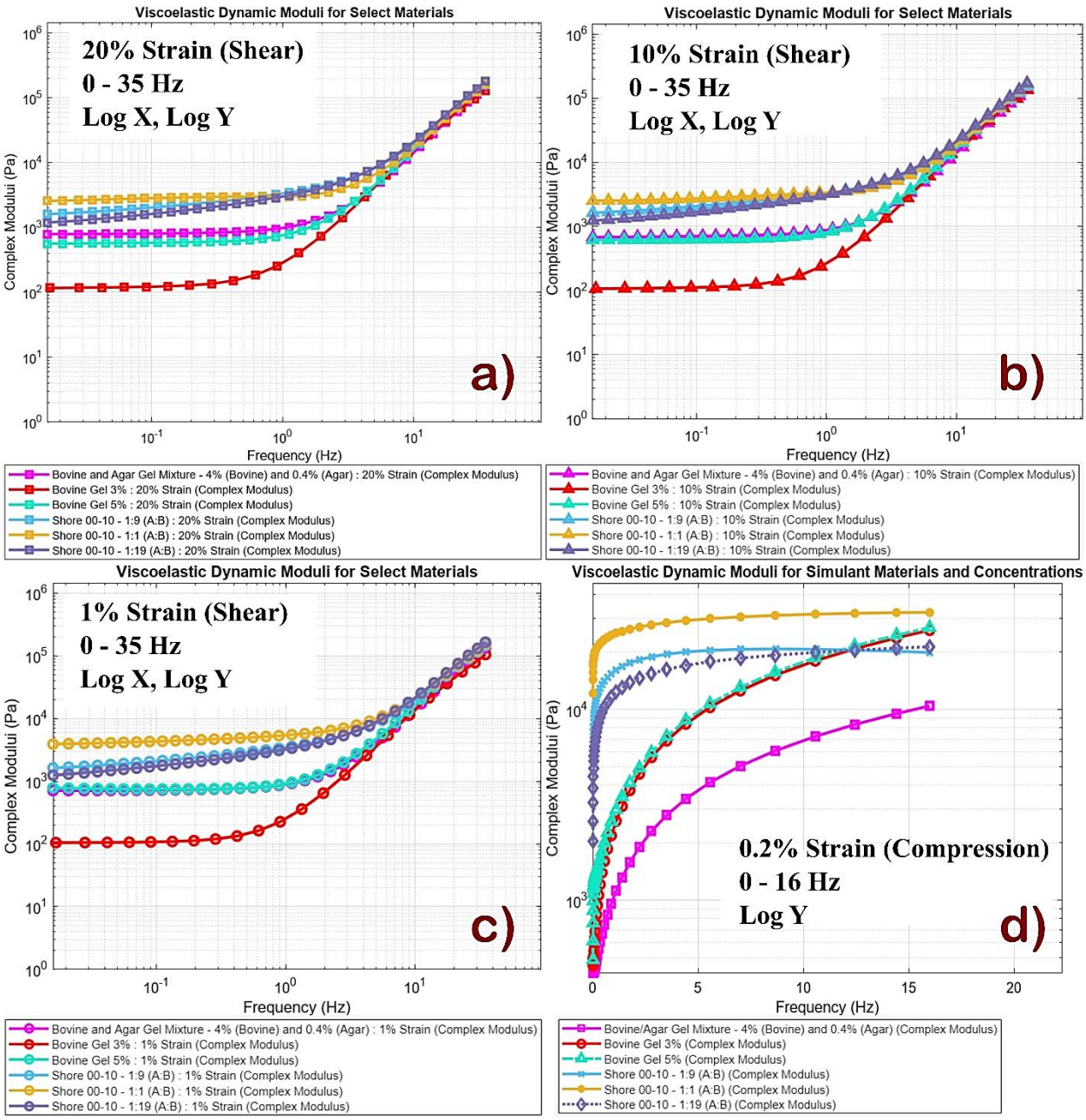


*Figure 3.7 — Complex Moduli of Tested Simulants in Shear Frequency Sweep: (a) Shear DMA, 1% Strain; (b) Shear DMA, 10% Strain; (c) Shear DMA, 20% Strain; (d) Compression DMA*

3.3.1.2.1 — Shear Viscoelastic Testing

Frequency sweep tests revealed an exponential increase in storage modulus with a linear increase in frequency, indicating strain-rate dependency in shear, with materials behaving more elastically at higher strain rates. Strain dependency was also observed, with all simulants displaying increased elasticity as strain increased. When comparing the performance to native brain tissues for shear

frequency sweep, the proposed materials closely matched mammalian brain tissues at lower frequencies (Figure 3.11). Brain tissue demonstrated a linear-logarithmic increase in dynamic moduli with increasing frequency, a behavior consistent with findings from various studies [18], [45], [58], [59], [61], [62], [67], [68].

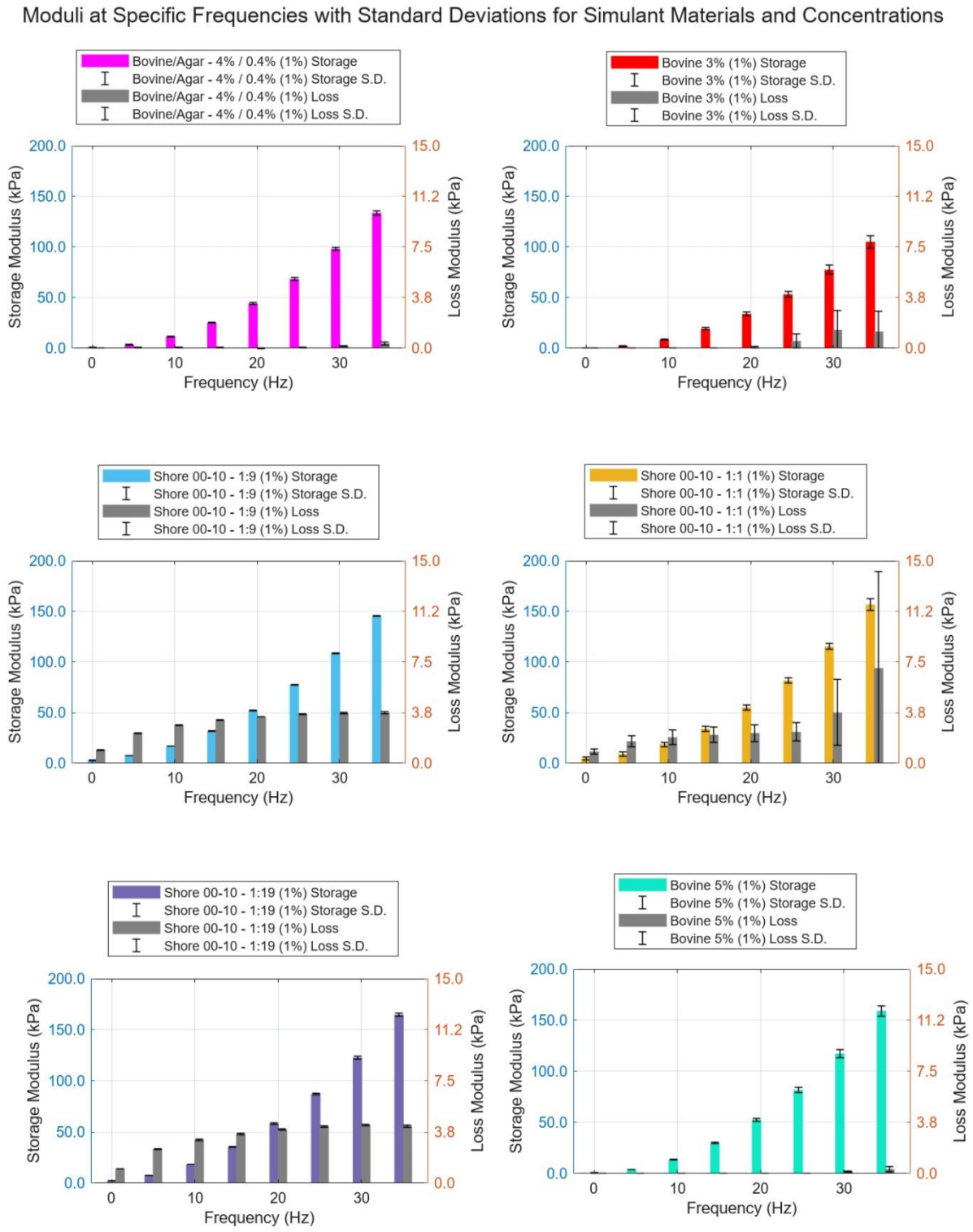


*Figure 3.8 — Dynamic Moduli at Specific Frequency Points for Shear (1% Strain)*

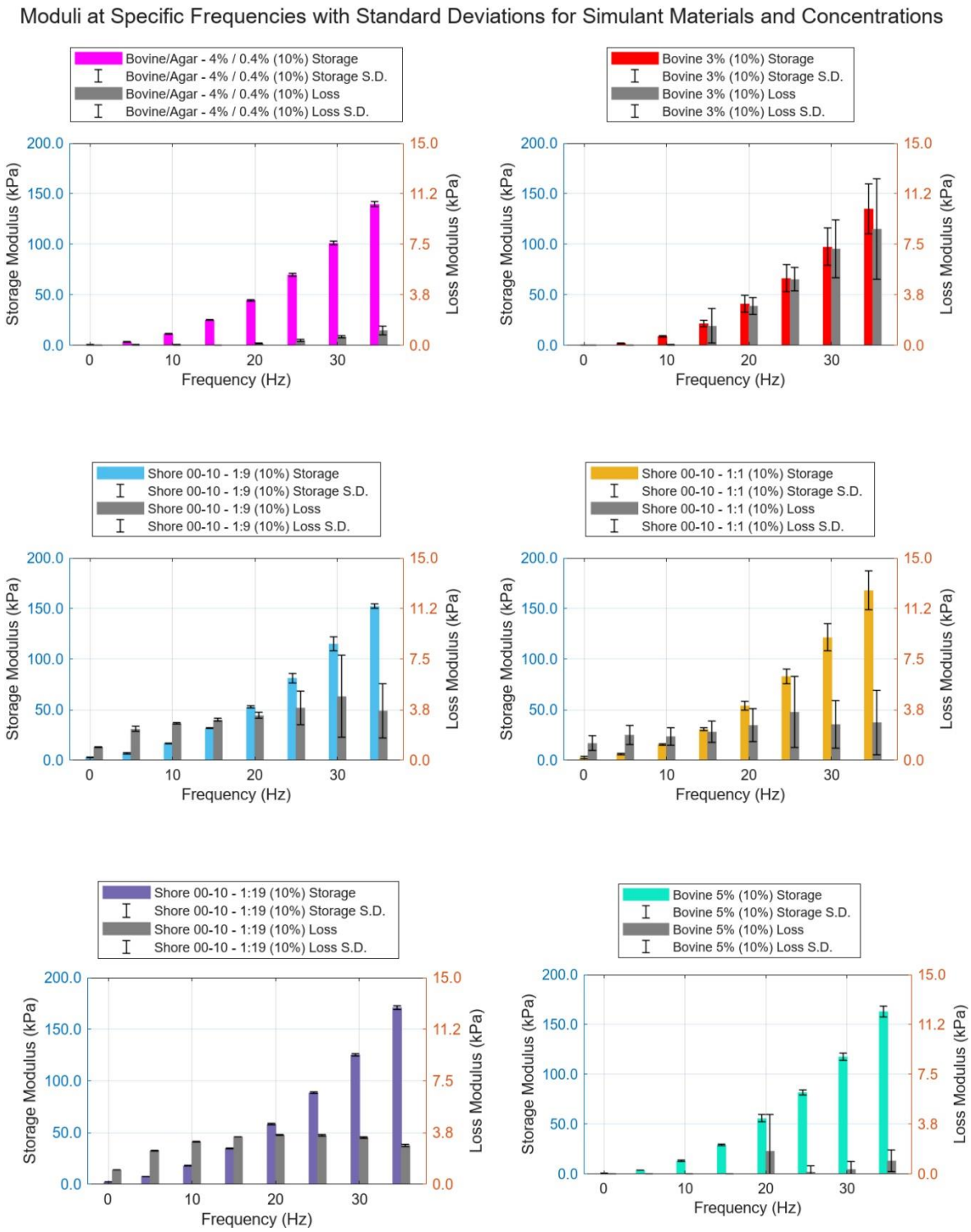


*Figure 3.9 — Dynamic Moduli at Specific Frequency Points for Shear (10% Strain)*

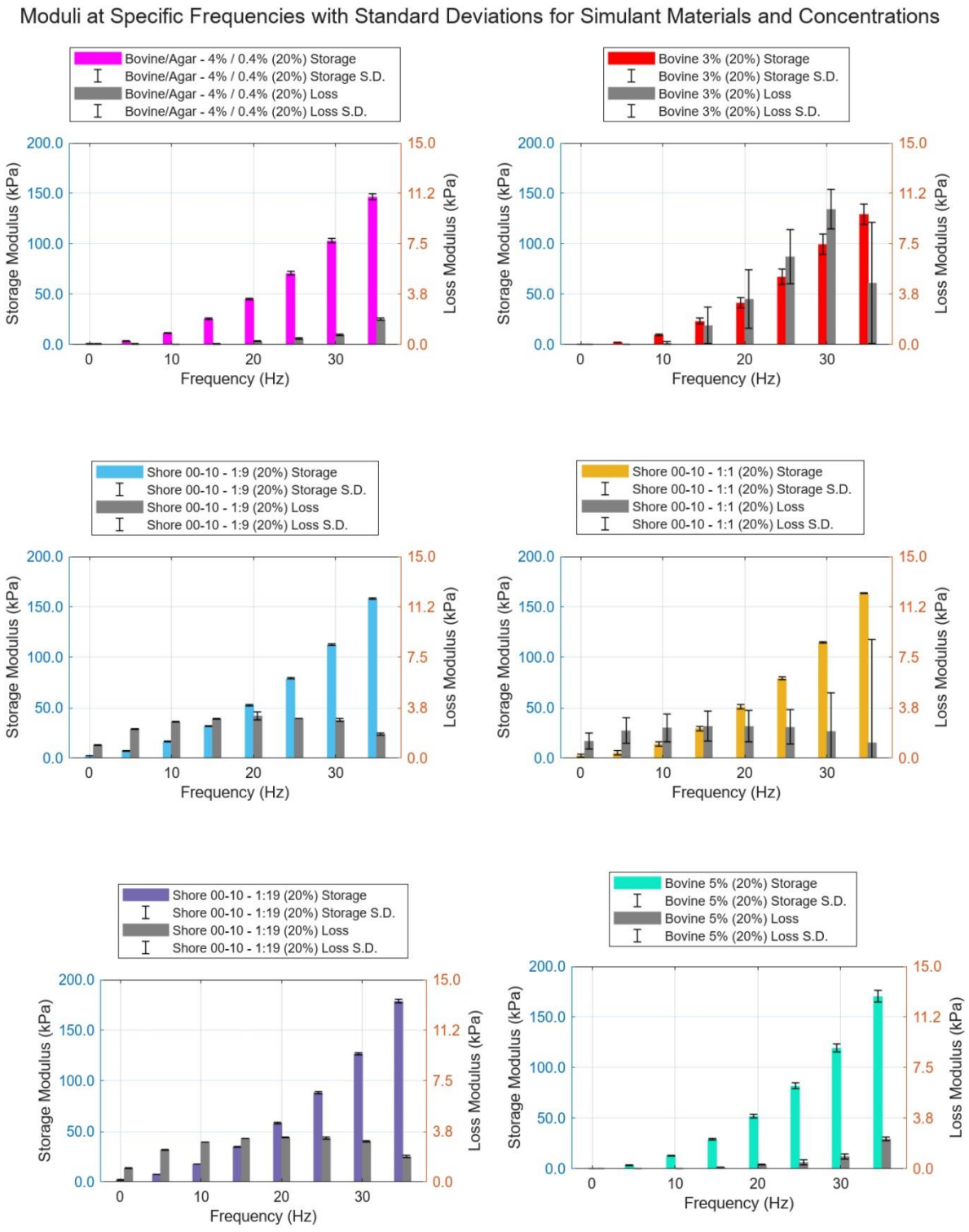


*Figure 3.10 — Dynamic Moduli at Specific Frequency Points for Shear (20% Strain)*

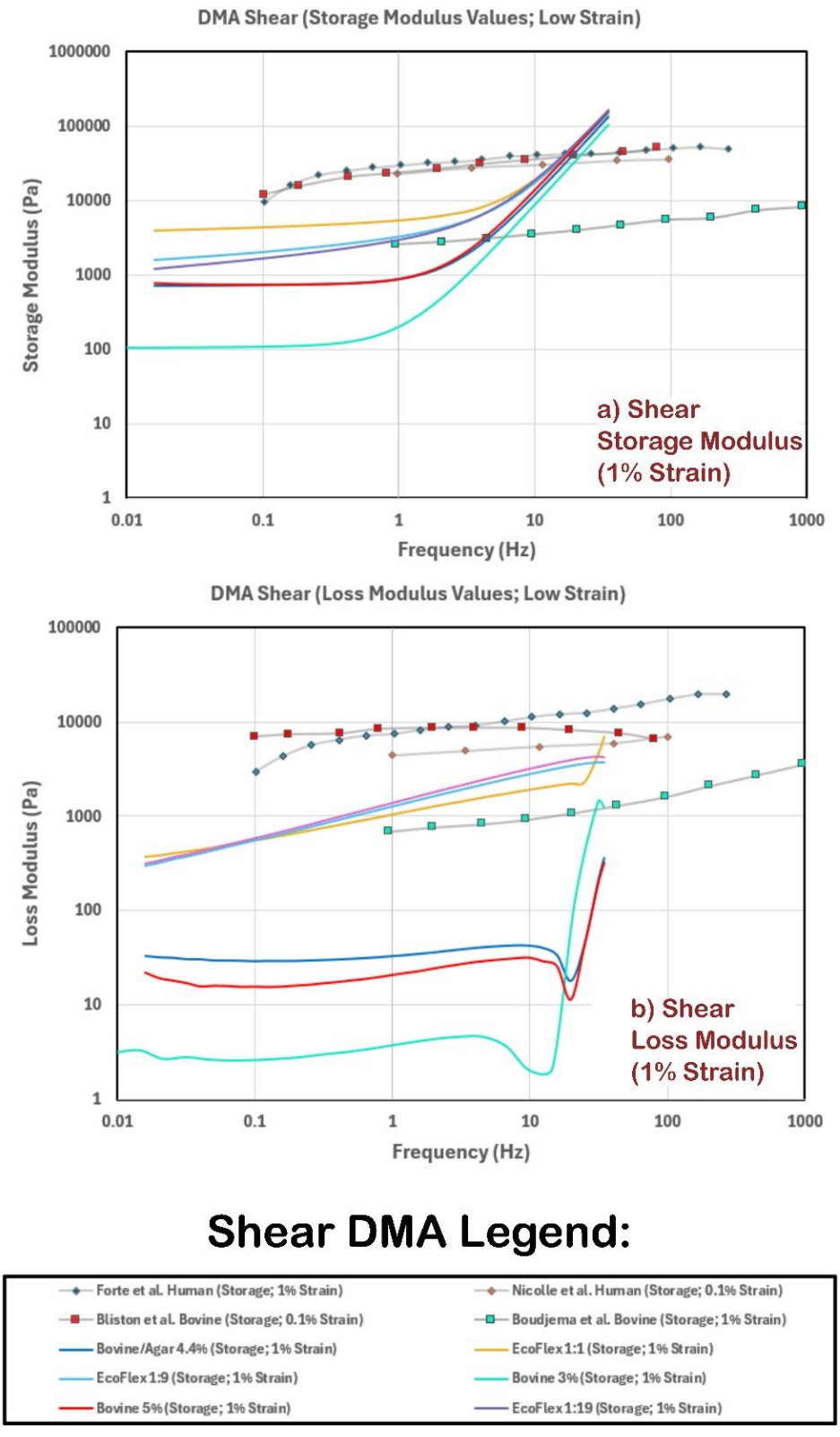


*Figure 3.11 — Sheat DMA Simulant Comparisons to Literature Review; a) Storage Modulus; b) Loss Modulus [29], [30], [32], [39], [90], [110]*

Simulant materials showed a similar linear-logarithmic increase at lower frequencies (0.01 Hz to 5 Hz), with a significant increase beyond ~10 Hz. Some materials, such as Shore 00-10 silicone elastomers, maintained a steady linear rate until reaching higher frequencies, indicating biofidelic performance at these specific frequencies. Silicone elastomers maintained biofidelity for an extended frequency range, exhibiting performance between non-human mammalian and human brain tissues. Increased strain in shear oscillation tests resulted in an increased response in loss modulus. Hydrogels exhibited an exponential increase in loss modulus with increased strain, while silicone elastomers showed a logarithmic increase, reaching a limit at 10-30 Hz, followed by a slight decrease. This behavior aligned with brain tissue loss modulus values, with silicone elastomers capturing these values more accurately.

Although all materials behaved similarly across the frequency range, moduli magnitudes varied at different frequency points. Natural hydrogels exhibited lower storage moduli than silicone elastomers, with simulants comparing more closely to non-human mammalian brain tissue values from literature (Figure 3.11), ranging from 126.21 Pa at 0.05 Hz to 86935.45 Pa at 25 Hz (at 20% strain) [18], [45], [58], [59], [61], [62], [67], [68]. Higher concentrations in hydrogels increased elasticity in viscoelastic parameters, with storage moduli rising per hardening composition. Conversely, higher hardener concentrations reduced the viscous portion of viscoelasticity, decreasing loss moduli. Hydrogels showed an exponential increase in both viscoelastic moduli with increased frequency and strain, correlating with brain tissue behaviors. Silicone elastomers, on the other hand, displayed viscoelastic magnitudes closer to human brain tissue found in literature, with storage moduli ranging from 2207.05 Pa at 0.05 Hz to 90056.50 Pa at 25 Hz (20% strain) [18], [62].

3.3.1.2.2 — Compression Viscoelastic Testing

Compression DMA tests provided the greatest distinction among materials when evaluating viscoelastic properties under two loading modes. Two characteristic behaviors emerged: natural hydrogels exhibited a consistent exponential increase in modulus with rising frequency (Figure 3.12), while silicone elastomers showed an initial increase in elasticity, plateauing in storage modulus between 5-15 Hz. Bovine gel concentrations did not significantly differ in storage modulus magnitude, but dynamic modulus varied, with Bovine/Agar displaying the least elastic performance and Shore 00-10 at (1:1) composition showing the highest elastic response. Shore 00-

10 silicone compositions showed variations in storage modulus, where higher A component polymer base concentrations correlated with greater elastic responses.

Variations in loss moduli were also observed. Bovine gel specimens exhibited similar behaviors across concentrations, but recorded loss moduli varied among materials. Hydrogel samples showed a consistent increase in magnitude across the frequency range, while silicone specimens experienced an initial decrease in magnitude followed by increases. This "inflection point" in the viscous response varied with (A:B) concentrations, with reductions in the A-part hardener generally delaying the inflection point. All silicone specimens showed an inflection point between 5-10 Hz in loss modulus magnitude. After this point, loss modulus values increased and aligned well with mammalian brain tissue values at similar frequency ranges (Figure 3.13).

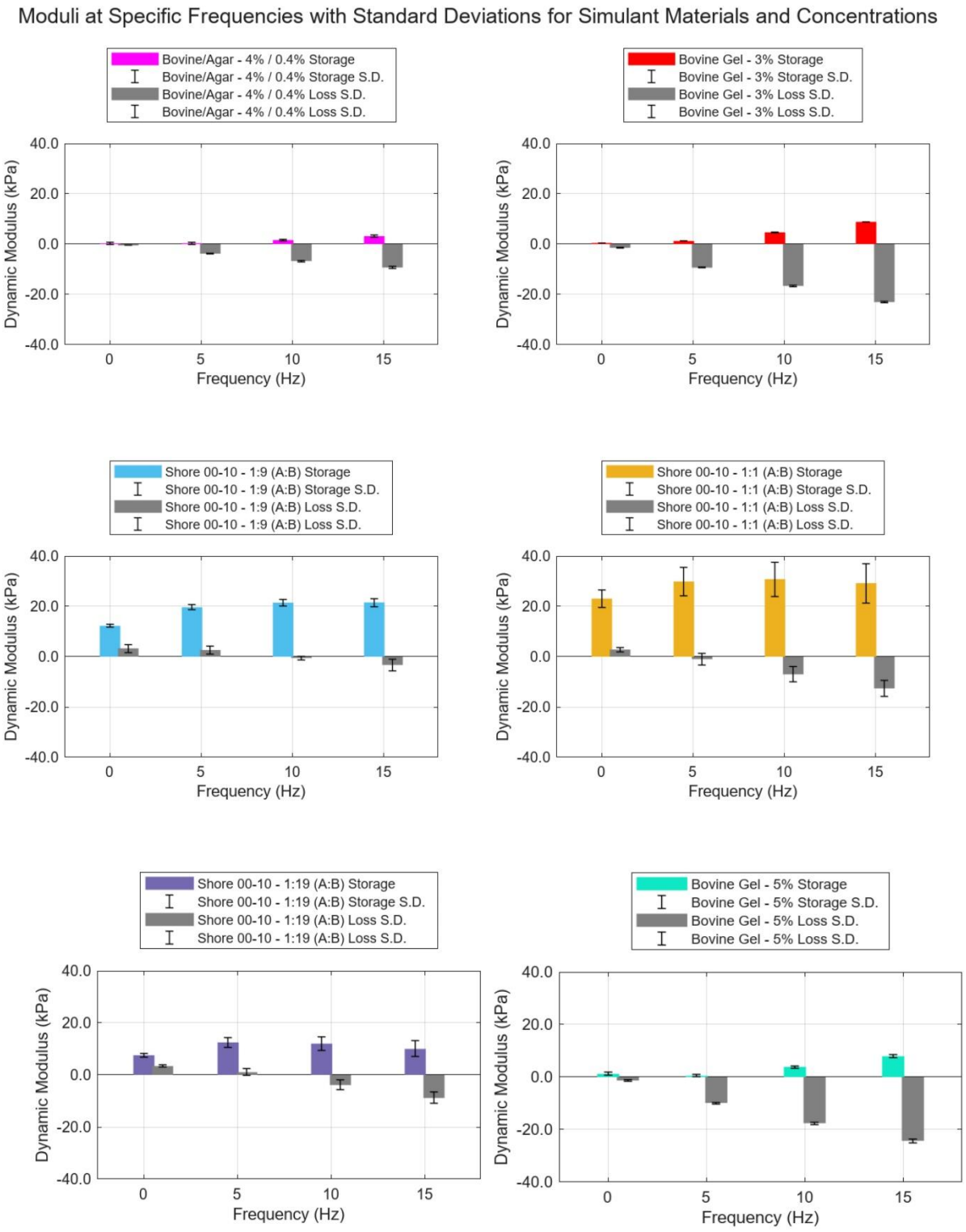


*Figure 3.12 — Dynamic Moduli at Specific Frequency Points for Compression*

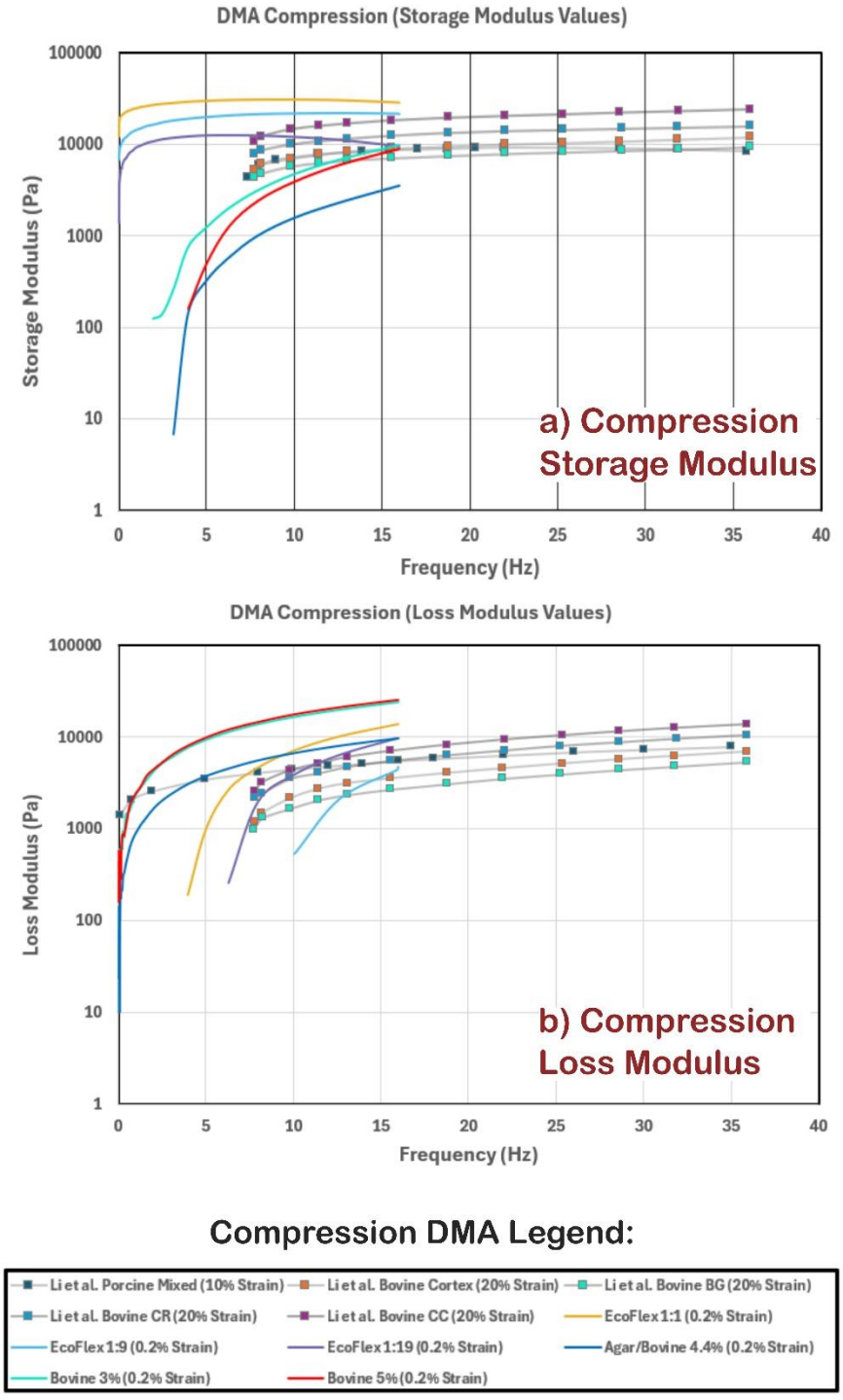


*Figure 3.13 — Compression DMA Simulant Comparisons to Literature Review; a) Storage Modulus; b) Loss Modulus [29], [30], [32], [39], [90], [110]*

## 3.4 — Discussions

This research aims to establish a series of methods for characterizing and selecting potential material candidates and manufacturing techniques to create an artificial device capable of accurately simulating the behavior of the human head under concussive impacts. This objective was achieved by reviewing known studies on the mechanical characterization of biological structures critical to the form and function of the human head, such as brain tissue [14]–[16], [18], [41]–[45], [47], [57], [58], [61]–[65], [67]–[69], and by recreating these tests using similarly behaving simulant materials. Additionally, simulant parameters were adjusted and observed regarding their effects on material performance and behavior in these recreations. Adjusted parameters included varying concentrations of the same material, such as in hydrogel brain simulant candidates and (A:B) compositions of silicone elastomers. The results of these defined tests are categorized based on their respective methodologies below.

### *3.4.1 — Brain Simulant Characteristics from Quasi-Static Compression and Viscoelastic Frequency Sweep Tests*

The purpose of this study is to evaluate the elastic performance of viscoelastic simulant candidates relative to the characterizations of native brain tissue structures found in the literature. A quasi-static strain rate approach was employed to comprehensively evaluate the material bulk modulus in its elastic state. Materials were tested up to 50% strain, as failure in the microstructural compositions of brain tissues, such as the axonal fibers responsible for neural transport, occurs within these ranges [5].

All tested simulant samples were subjected to a general quasi-static strain rate that utilized the full capacity of the Discovery HR-3 rheometer for the given strain range while also considering the general strain rates observed in quasi-static compression tests. This approach accounts for the numerous reported properties of brain tissues, each with variations in testing parameters and strain rates.

The study highlights the importance of simulating the elastic performances of brain tissues through quasi-static compression and viscoelastic frequency sweep tests. These tests help in understanding how well the simulant materials mimic the mechanical behavior of brain tissue, which is crucial for developing biofidelic models for studying concussive impacts and improving safety measures.

#### *3.4.1.1 — Quasi-Static Compression*

In the strain-step approach, the analysis involved breaking down the stress-strain curve into segments to assess the non-linear behavior of viscoelastic samples. Different studies on brain tissue used variations of this approach, such as the five-step methods found in Navarro-Lozoya et al. and Tamura et al. [15], [65], and the three-strain step analyses for porcine brain found in Falland-Cheung et al. and Rashid et al. [16], [70]. This method allowed for calculating elastic moduli values for defined strain ranges (steps of 10% strain in the five-step and 20% strain in the three-step). Comparisons with native studies revealed varying biofidelity among simulant materials. While most materials showed biofidelity in the three-step approach, fewer exhibited this quality in the more finely segmented five-step method.

The hyperelastic curve-fitting approach employed the Ogden model for comprehensive fitting of stress-strain curves. Known for capturing strain-stiffening and softening effects [42], [47], [71], this model was used to determine the materials' Initial Shear Modulus (G). Despite these efforts, no simulant materials fully matched the characteristics of brain tissue across all studies. However, certain materials displayed greater biofidelity for specific characteristics, with 5% Bovine Gel being particularly noteworthy for its consistency across multiple literature sources [14]–[16], [49], [72]–[74].

Discrepancies in strain rates between the tests conducted and reported values for brain tissue could potentially influence material performance, as simulants were compared to literature values throughout the quasi-static range (0.01 $s^{-1}$ to 1 $s^{-1}$). The strain rate dependency observed in brain tissue and viscoelastic materials highlighted that higher strain rate specimens were associated with stiffer responses [14]–[16], [18], [72]. Therefore, simulant tests should consider strain rate application when comparing brain tissue literature values.

While strain rate dependency is significant in tissue-mimicking viscoelastic materials, simulants with tunable compositions may be more favorable for capturing varying loading rates and heterogeneities. For instance, silicone elastomers exhibited less strain rate dependency compared to hydrogels, indicating potential adjustments to mimic specific strain rate performances (Appendix A, Figure A1). Adjusting silicone concentrations could better replicate brain tissue responses under concussive impacts. Further research in this area is warranted, as suggested by Chanda et al. [13], where EcoFlex™ silicone with Shore Hardness 00-10 of varying (A:B)

concentrations was tested akin to brain tissue specimens in quasi-static and intermediate strain rate tension. It was observed that varying (A:B) concentrations captured the brain tissue tested at specific strain rates, proving that the tunability of this material could promote the representation of brain tissue under defined loading scenarios.

#### *3.4.1.2 — Viscoelastic Frequency Sweep Testing of Simulant Samples*

The viscoelastic properties of the simulant candidates were evaluated in both shear and compression to comprehensively assess their performance under various loading modes and magnitudes expected in concussive impacts [6], [7], [11], [36]. Key frequency points were identified to observe the viscoelastic performance of each material in terms of storage modulus, loss modulus, and the root-sum-square value of these parameters, the viscoelastic complex modulus. These metrics offer a comprehensive understanding of the elastic and viscous contributions to the elastomeric material under stress, facilitating comparison with the behavior of brain tissues.

The establishment of an ideal simulant candidate with biofidelic viscoelastic properties is critical for accurately representing the dynamic behavior of brain tissue during concussive impacts. Mild traumatic brain injuries (mTBIs) are often associated with rotational accelerations that generate oscillating stresses within the skull-brain interface [6], [7], [11], [36]. Therefore, the ability of a material to mimic these oscillatory stresses is crucial for developing effective simulants.

The tests simulated concussive oscillations under varying loading modes, strains, and strain rates to observe and correlate the viscoelastic performance of the materials. This approach provided a broad range of comparison points with native brain tissue data from the literature. Similar points of moduli at increasing frequencies were tabulated and observed, or identified within their frequency sweep graphs [18], [45], [58], [59], [61], [62]. The dynamic moduli points and their analyses are presented in Figures 3.8 to 3.13, with further details available in the Appendix A.

By analyzing these viscoelastic properties, this study aimed to identify the most biofidelic materials for representing brain tissue under concussive loading conditions. The results offer valuable insights into the suitability of different simulant candidates for mimicking the complex mechanical behavior of brain tissue, thereby contributing to the development of more accurate and reliable models for studying mTBI.

3.4.1.2.1 — Frequency Sweep Testing in Shear

Regarding the relative magnitudes of the material moduli, Forte et al. observed that grey matter dynamic moduli performed at magnitudes between $10^2$ to $10^3$ Pa across 0.01 Hz to 25 Hz for both storage and loss values, while white matter ranged from $10^3$ to $10^4$ Pa for the same frequency range, consistent with other literature [18], [45], [58], [59], [61], [62]. Generally, loss moduli displayed magnitudes of approximately $10^1$ Pa less than storage moduli but increased at a similar linear-logarithmic rate. In comparison to the simulants tested in this study, all materials behaved similarly until higher frequency ranges where the linear-logarithmic rate increased, with storage moduli values rising to a magnitude of $10^5$ Pa.

An interesting observation is that both the minimum and maximum storage moduli were exhibited by the silicone elastomers with the lowest concentration of silicone crosslinker: 1:19, or 5% A (silicone base) and 95% B (crosslinker). Variations in crosslinker concentrations resulted in decreased initial frequency moduli for lower concentrations but increased moduli at higher frequencies. Additionally, lower crosslinker concentrations displayed heightened responses to strain dependency and loss moduli. This may be due to differences in material compositions and structural formation, with silicone elastomers utilizing a Part A composition to crosslink a Part B silicone functional group, while hydrogels use swollen polymer networks in water to form their viscoelastic shape [56], [75]–[77]. Although hydrogels structurally resemble natural formations in soft tissue, they often do not retain a similar degree of elasticity, with their viscous portions more prevalent at lower concentrations.

In contrast, silicone elastomers consistently increased loss modulus throughout the frequency range but reached a plateau at certain frequencies, especially when higher strains were introduced. This behavior is expected as silicone elastomers, which require no water input, generally display greater elastic responses due to stronger crosslinked polymer chaining [56], [76], [77]. Slight increases in loss moduli with reduced crosslinker concentrations potentially indicate stress softening due to fillers in the silicone polymer structure. Liao et al. confirmed that fillers are introduced in forming EcoFlex™ silicone rubber, with varying concentrations of polymer filler correlating to material effects of strain softening [78]. This could explain the higher magnitudes at greater frequencies regarding crosslink densities, where lower crosslink densities promote a greater frequency range for energy dissipation and storage, reducing elasticity at smaller

frequencies while enhancing storage moduli at higher frequencies. These observations suggest that while hydrogels require higher concentrations to achieve greater elastic performance, they may sacrifice relative performance to brain tissue in quasi-static compression. Silicone elastomers, with their tunable crosslinker concentrations, offer a promising alternative for replicating the viscoelastic behavior of brain tissue under shear loading conditions.

3.4.1.2.2 — Frequency Sweep Testing in Compression

In compression frequency sweep tests, the contributions of elastic and viscous components to the viscoelastic behavior of each material type were notable. The primary distinction between hydrogel specimens and silicone elastomer specimens is that silicone elastomers displayed predominantly elastic performance, whereas hydrogels exhibited predominantly viscous performance.

Hydrogel candidates yielded negative loss modulus values at all frequency points, continuing a linear downward trend as frequency increased. The loss modulus governs the imaginary component of the viscoelastic complex modulus, indicating the degree of energy dissipation in loaded forces [79], [80]. A negatively trending loss modulus suggests negatively dissipative forces, where the material does not fully dissipate previously loaded energy before more energy is introduced. As loading frequency increases, insufficient time is given for the material to relax back to its pre-strained state, resulting in superimposed excess energy on the next loading cycle. This superimposition amplifies with frequency, leading to increased loss modulus values.

The hydrogels consistently decreased in loss modulus throughout the frequency range, while silicone elastomers successfully dissipated stored energies up to approximately 5-10 Hz, where negative loss modulus values began to occur. This behavior emphasizes the stress softening observed in shear testing, where loss modulus magnitudes for hydrogels significantly exceeded storage modulus, indicating predominantly viscous behavior.

For silicone values, the inflection from positive to negative loss modulus values occurred after approximately 5 Hz. This aligned well with the tested loss moduli results for brain tissue (Figure 3.13) [45], [58], [59]. Stress softening claims found in shear testing explain this performance, as similar traits were observed [56], [76], [77]. The silicone elastomers experienced greater

magnitudes, while the hydrogels showed closely related values, except for the Bovine/Agar Gel Mixture, possibly due to Agar Gel concentrations.

While complex moduli values displayed a positive magnitude, the storage and loss modulus values for brain tissue in the literature demonstrated elastic behavior at increased frequencies, with viscoelastic moduli parameters remaining positive throughout frequency sweep testing in compression [18], [45], [58], [59], [61], [62]. Th silicone-based elastomers maintained elasticity at higher frequency ranges. In determining the optimal biofidelic material compared to human brain tissue, researchers must prioritize selection criteria. This study concludes that select hydrogel materials closely resemble native materials in quasi-static compression and structure, while silicone elastomers better mimic brain tissues in viscoelastic performance. Similar observations were made in shear testing comparisons, where silicone elastomers performed closer to human brain tissues, and hydrogels performed closer to non-human mammalian brain tissues [18], [45], [58], [59], [61], [62]. Among the silicone elastomers, the 1:19 (A:B) concentration exhibited optimal performance.

3.4.1.2.2 — Considerations for Manufacturability and Employment of Brain Simulants in a Full-Scale Brain Phantom

When creating a human head phantom device, it is essential to consider the feasibility of implementing potential materials as mimicking components for a true-to-scale human brain. Priority must be given to the device and its constituent materials regarding their longevity, repeatability in head impact testing, and ease of manufacturing a full-scale brain phantom.

Observations during the creation of material samples highlighted important considerations for their potential applications and handling in full-scale manufacturing. Notably, hydrogel samples showed significant degradation after a minimum of 36 hours from creation, losing shape and mechanical properties, unlike the silicone elastomer samples. Navarro-Lozoya et al. observed similar degradation effects in full-scale hydrogel phantom structures, with clear signs of degradation after three weeks of refrigeration, including material stiffening and loss of mass due to shrinkage [15]. Therefore, using hydrogel materials in a head phantom device may necessitate refrigeration and interchangeability between head phantoms. Repeated use of the same structure could result in varied performance due to degenerative properties, and replacing a head phantom for each test

would require meticulous attention to maintaining correct concentrations and manufacturing standards to ensure repeatable performance.

Another aspect of hydrogel materials is the incorporation of water to create samples and phantom structures. If sensors are to be applied to portray intracranial mechanisms during head impacts, ensuring that sensors embedded inside the brain phantom are waterproofed is crucial to avoid electrical short-circuiting.

While hydrogels exhibit accuracy in material structure and elastic performance compared to native brain tissues, additional measures are necessary to make these materials feasible for use in a full-scale, repeatable brain phantom. In contrast, silicone elastomers, though lacking structural and quasi-static biofidelity, possess accurate viscoelastic properties and tunable capabilities, allowing for cranial stress responses over a defined range of strain and rate due to their diminished response in strain rate dependency. Moreover, silicone elastomers do not suffer from material degradation and do not require water incorporation, facilitating repeatable testing applications and sensor embedding.

Despite no distinct material providing true-to-property characteristics across the entire range of strain, strain rate, and impact scenarios for the human brain, the results from testing confirm that a brain phantom suitable for strictly observing the simulation of concussive impacts can be achieved. Silicone elastomers, with their specific strengths, offer a suitable material to govern the behavior of brain tissue under these conditions.

#### *3.4.1.3 — Development of a Full-Scale Biofidelic Brain Phantom*

This section outlines the creation of a life-sized brain phantom based on the methodologies defined in this study. The brain model was sourced from the National Institute of Health (NIH) 3D Model database (NIH 3D National Institute of Health; Bethesda, Maryland), which provided patient-specific MRI scans of a coupled skull and brain. To ensure accuracy, the model's dimensions were adjusted according to the GHBMC M50 specifications [81]. The brain phantom was manufactured with EcoFlex 00-10 Silicone in 1:19 (A:B) composition. The 3D brain model was developed out of Poly-lactic Acid (PLA) using a Bambu Carbon X1 Fused Filament Fabrication (FFF) printer (Bambu Lab Ltd.; Hong Kong). The printed model served as the negative for the mould used to develop the silicone phantom.

First, the printed negative was bolted by the brain stem and secured into a container box to maintain a fixed position during the molding process (Figure 3.14). Modelling clay of a minimum thickness of ~20 mm was positioned at the base of the container box to ensure that the entirety of the brain geometry was covered by the mold (Figure 3.15). The negative was then completely coated with silicone mold release (Smooth-On Universal ™ Mold Release; Smooth-On Inc.; Macungie, Pennsylvania), from which the mould release was left to dry for a minimum of 5 minutes. This process was repeated for a minimum of three times.

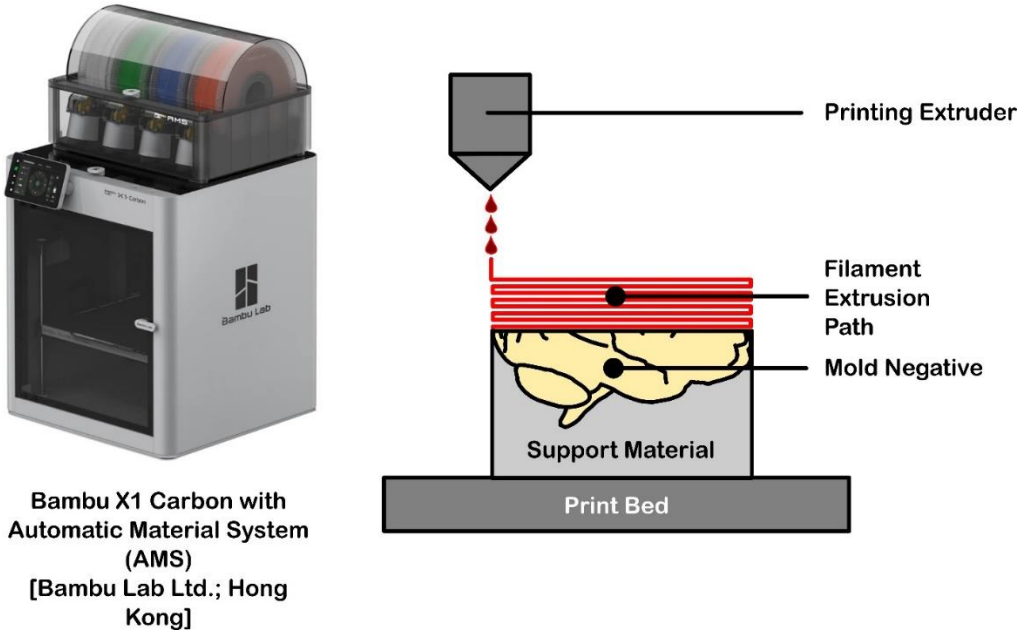


*Figure 3.14 — Bambu X1 Carbon with Negative Mold Volume Printing Methodology*

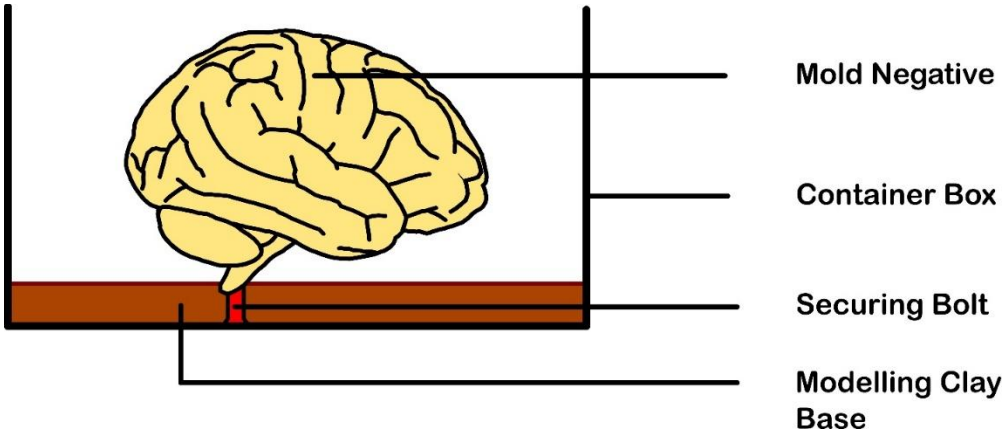


*Figure 3.15 — Brain Phantom Negative Mold Diagram*

Mixed EcoFlex 00-10 Silicone at (1:1) composition served as the mold volume. To retain the complex shape of the brain, as well as to consider overhangs in the model, the mold is partitioned at the brain volume's center of gravity to form a two-part mold. This partition further served to allow for the potential embedment of sensors in the brain. The first half of the two-part mold volume was poured into the container box with the negative volume secured. This first part encased the bottom of the brain stem up to the brain center of gravity, at around halfway up the cerebrum. FFF-printed PLA alignment keys were positioned around the corners of the mould to ensure alignment between both mold halves. The bottom half was then left to cure for at least 24 hours. Following the curing process, mold release coating process was repeated for the bottom half of the two-part mold. Once the mold release coatings dried, viscous silicone was poured to fill the remainder of the container box and was left to cure for another 24 hours. At the completion of the mold construction, both halves of the mold were separated from the container box and the printed negative was removed. A step-by-step process of the mold creation can be seen in Figure 3.16, while the physical mold and negative volume is represented in Figure 3.17.

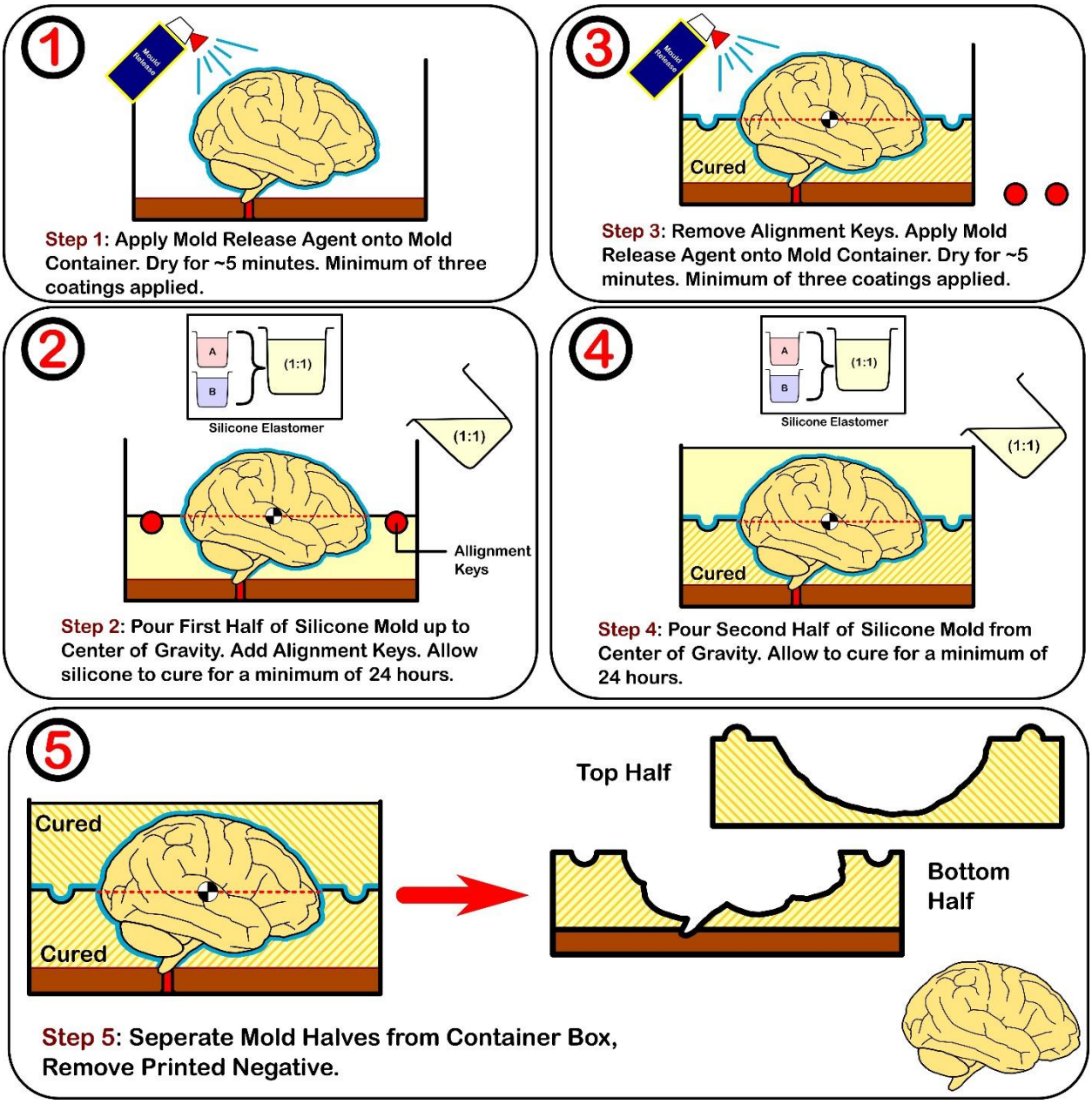


*Figure 3.16 — Brain Phantom Mold Creation Process*

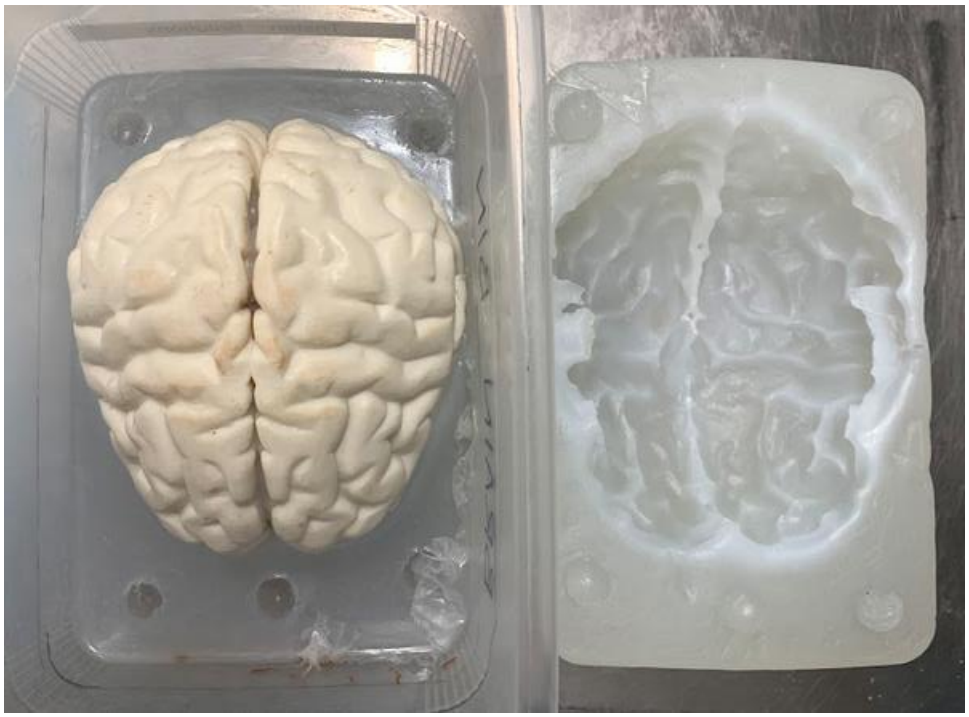

*Figure 3.17 — Top and Bottom Silicone Mold Cavities with FFF-Printed Negative Volume Model*

To create the phantom, the silicone at (1:19) composition was poured into the negative halves. The mold negatives were coated with the release agent as per the process in creating the mold. Once dried, A and B compositions were mixed and degassed as per the manufacturing process defined in Section 3.2.1.1.2. The silicone at its viscous state was poured into the mold volumes and were cured for a minimum of 36 hours. At the completion of the curing process, both halves of the brain phantom were assembled. Further exploration of the brain phantom making process can be observed in Figure 3.18. Meanwhile, the completed brain phantom is presented in Figure 3.19.

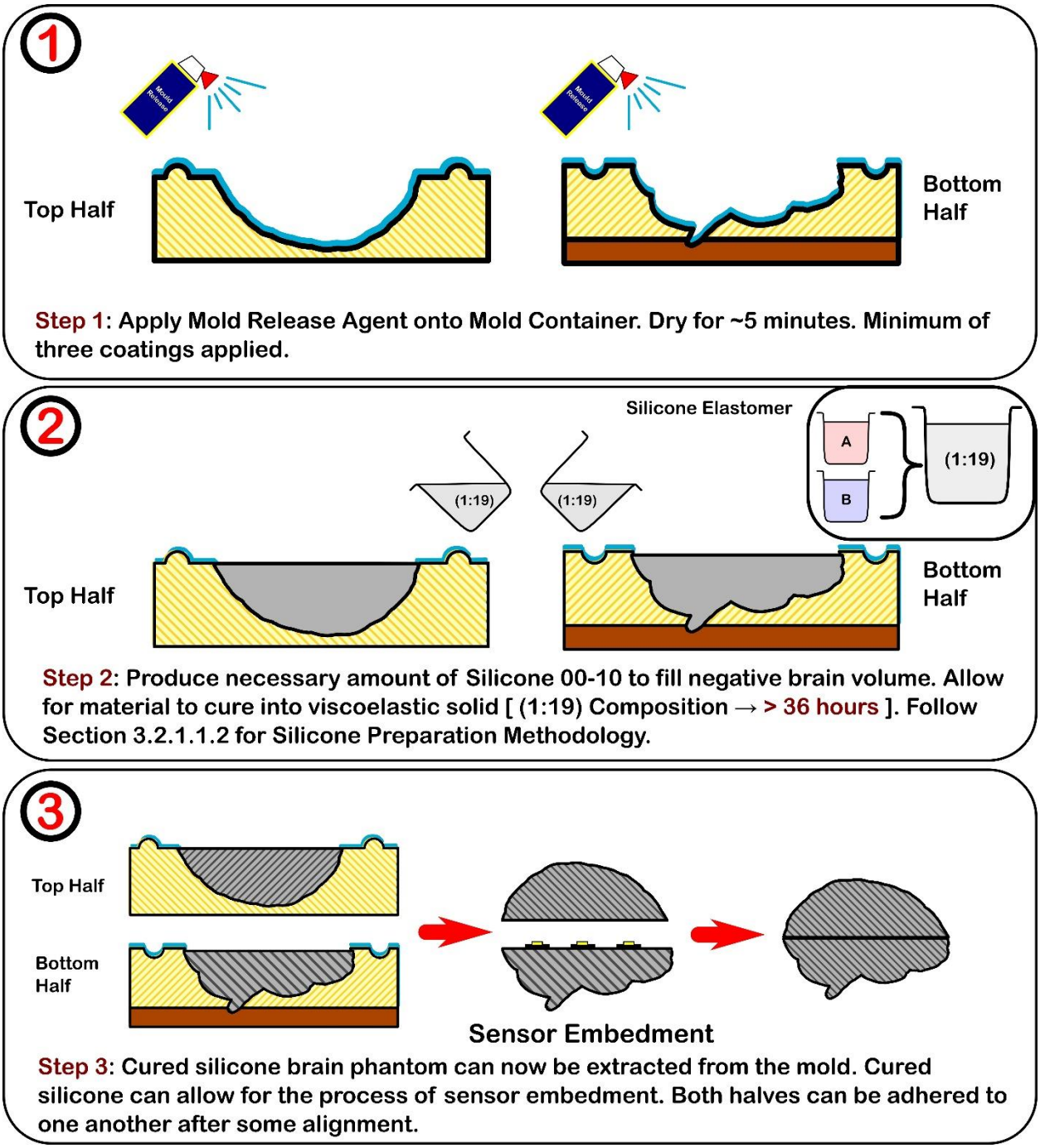


*Figure 3.18 — Brain Phantom Construction Process with Silicone Molding Technique*

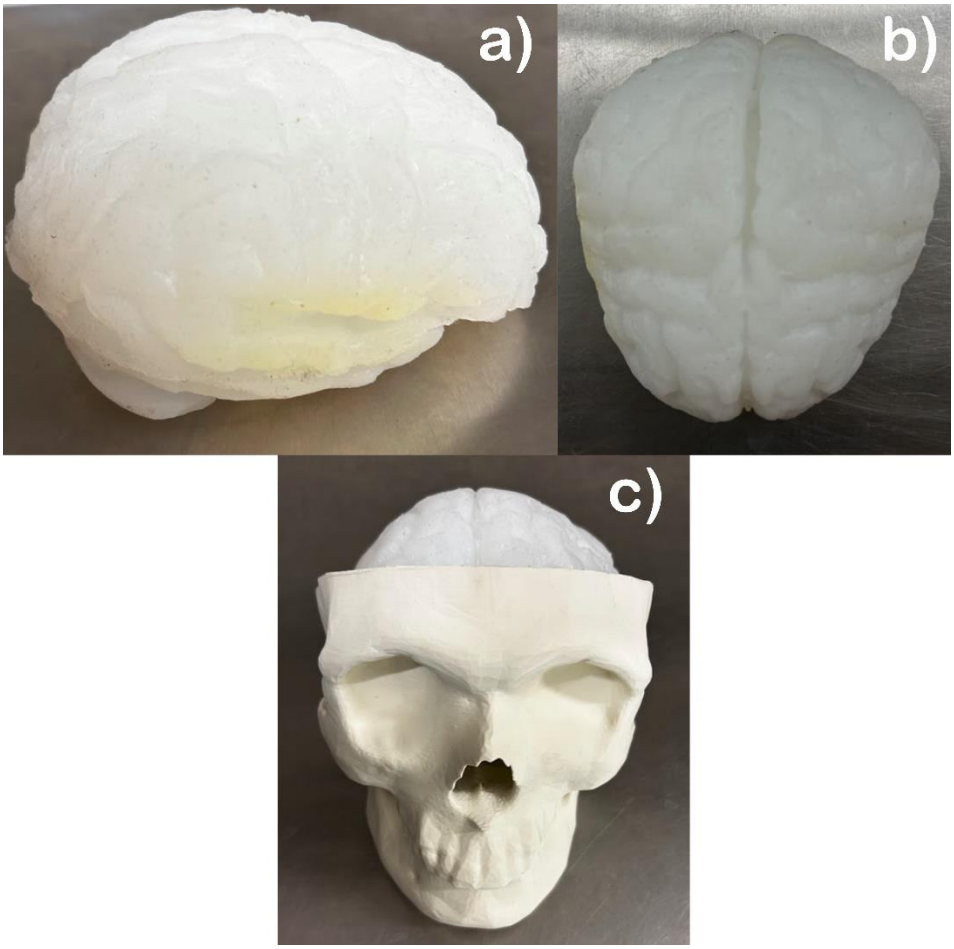


*Figure 3.19 — Developed Silicone 00-10 Brain Phantom a) Sagittal Plane and b) Transverse Plane, c) Coupled Biofidelic Brain and Skull Model*

*Table 3.6 — Comparative Properties of Brain Phantom and Native Full-Brain (GHBMC)*

| **Brain Phantom Characteristics** | |
|---|---|
| *Volume, V ($cm^3$)* | 883.150 |
| *Mass (g) [with EcoFlex 00-10]* | 918.476 |
| *Density (g/cc) [EcoFlex 00-10]* | 1.04 |
| **Native Brain Characteristics (GHBMC M50) [81]** | |
| *Average Volume ($cm^3$) [83]-[86]* | ~ 1300 to 1450 |
| *Average Mass (g) [83]-[86]* | ~ 1370 |
| *Average Density (g/cc) [82]* | 1.06 |

The current iteration of the brain simulant phantom observes its partition into two halves of the brain, split evenly by its center of gravity. This is to ensure ease of maintenance and experimentation in the event of sensor embedment applications, such as implementations of accelerometers and gyroscopes for kinematic analysis. Further iterations of this developed brain phantom should consider complete encasement of the silicone mold after sensor embedment. Changes in the manufacturing process should remain the same to the one described. However, further considerations should include an injection inlet for silicone pouring as well as an exhaust spout to expel any trapped gasses in the closed-mould process. Similar studies such as Petrone et al. [32], [33] have conducted similar techniques in the construction of a simulant brain phantom. Differences in these molding techniques can be observed in Figure 3.20.

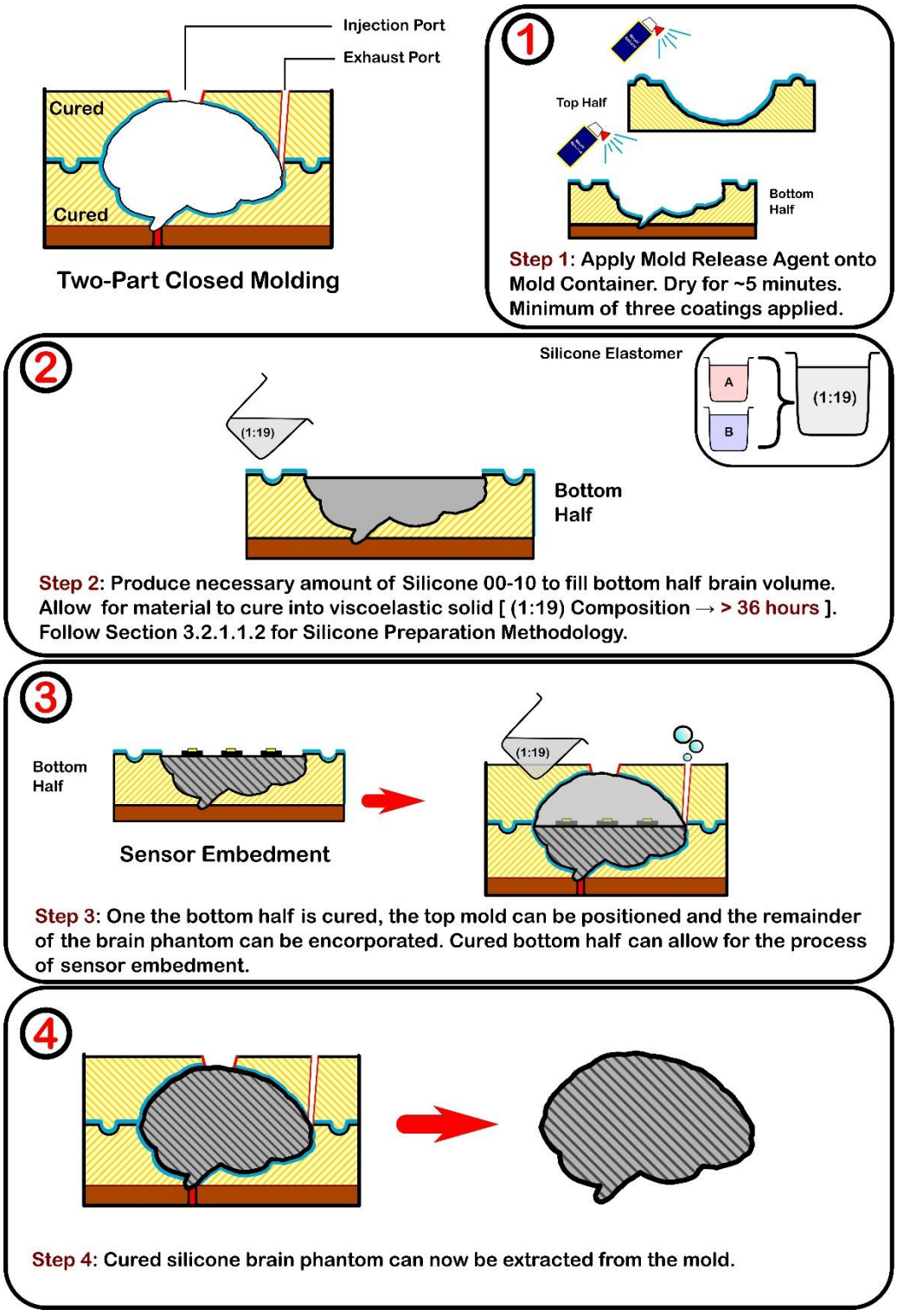


*Figure 3.20 — Brain Phantom Construction Process with Closed-Mold Silicone Molding Technique*

## 3.5 — Future Works and Conclusions

This study sought to identify and propose artificial materials that can simulate critical structures within the human head, specifically the human brain. The following sections outline future work and considerations related to the respective tests conducted. From the testing, it was clear that no single simulant provided optimal biofidelity across all testing aspects. Bovine Gel at 5% concentration emerged as the most promising in uniaxial quasi-static compression tests. In viscoelastic testing, Shore 00-10 Silicone at 1:19 (5% A, 95% B; wt%) concentration demonstrated notably accurate biofidelic results to human brain tissues in both compressive and shear oscillation DMA tests at lower oscillations, although it displayed significantly greater stress values in quasi-static compression. While Bovine Gel-based concentrations showed more biofidelic accuracy relative to bovine and non-human mammalian brain tissues, Bovine Gel at 5% exhibited results comparable to brain tissue at similar strain rates. All simulants demonstrated relative viscoelastic accuracy at lower frequency ranges between 0.01 to 15 Hz, although their moduli values increased significantly, surpassing biofidelic performance at higher frequencies.

Considering manufacturability, the Shore 00-10 Silicone series appears to be the most feasible approach for implementing a full-scale brain phantom, primarily due to the degradation effects observed in hydrogel samples, which lost shape and mechanical elasticity after 24 hours. However, these materials can only maintain biofidelity within a specific range of applications due to their lack of strain rate dependency, as tested among strain rates. Although no material could maintain biofidelity across all aspects of brain tissue impacts and stresses, the tunable properties of silicone elastomers in crosslinking concentration allow them to be tailored to mimic specific impact scenarios. As future work to develop a human head phantom for concussion simulation, the defined material is sufficient to provide a full-scale brain mimic for this application.

The HR-3 rheometer exhibited limitations in characterizing the viscoelastic capabilities of the tested simulant candidates due to its maximum linear speed of 10 mm/s, restricting observations to quasi-static strain rates. Additionally, compressive frequency sweep tests were limited to a 0.2% oscillation strain and a maximum frequency of 16 Hz. Despite these limitations, the observations provided sufficient characterization within linear viscoelastic limits and considered frequencies relevant to injurious head impacts [36]. This study aimed to capture biofidelity in loading modes

expected in concussive scenarios, acknowledging that the selected materials might not fully replicate all aspects of natural brain tissue behavior.

Future studies should extend characterizations to the heterogeneous regions of the brain and explore the development of simulant structures replicating microstructural features to enhance biofidelity. Research has shown that mammalian brain tissues exhibit varying properties depending on grey matter and white matter regions. For instance, Jin et al. [69] observed that grey matter thalamus samples exhibited a stiffer response than corona radiata white matter samples at strains exceeding 40% at medium (5 $s^{-1}$) and high (30 $s^{-1}$) strain rates. Similarly, Budday et al. [41] found that the cortex provided the stiffest response, with the basal ganglia following closely, while the corona radiata and corpus callosum exhibited softer responses. Further emphasizing the complex regional anisotropies of the human brain, Menichetti et al. [54] observed variations in initial shear moduli within specific cortex areas during force-relaxation micro-indentation tests.

In contrast, the simulants characterized in this research were compared to mixed grey and white matter and separated grey and white matter brain tissue specimens reported in the literature. Despite this, the study identified notable differences in material properties among various materials and concentrations. Future evaluations could involve comparing these materials to defined brain tissue regions reported in the literature. Additionally, constructing a comprehensive brain phantom might involve using multiple regions composed of varying materials and compositions.

This approach has the potential to more accurately reproduce the material performances observed in human brain tissue, advancing the understanding of brain injury biomechanics. The characterization of simulants in this study has established a potential candidate for a brain phantom specifically designed to mimic the bulk material behavior of brain tissue in concussion injury and relevant concussive loading modes.

# *Chapter 4 — Characterization and Selection of a Skull Surrogate for the Development of a Biofidelic Head Model*

This chapter is adapted from the study *Characterization and Selection of a Skull Surrogate for the Development of a Biofidelic Head Model* by Tenio and Boakye-Yiadom (2024) in the *Journal of the Mechanical Behaviour of Biomedical Materials* [DOI: 10.1016/j.jmbbm.2024.106680].

## 4.1 — Introduction and Background

The field of physical models simulating the human skull-brain is rapidly evolving, aiming to mimic native geometrical, mechanical, and biochemical properties [1]–[20]. However, the complex nature of the skull-brain remains a challenge [1], [5], [21]–[50], with current models often representing specific properties rather than providing a complete simulation [51]–[60]. These studies focus on understanding the mechanical characteristics of human head tissues during Traumatic Brain Injury (TBI), a global concern affecting millions annually [35], [61]–[63]. TBI, resulting from excessive cranial strain due to linear and rotational acceleration, primarily impacts young adults and older individuals, leading to hospitalizations and deaths [2], [63], [64]. Moderate or mild TBI (mTBI, concussion), common in sports-related injuries and falls, can cause cognitive deficits and mood disorders [34], [65]. Additionally, repetitive concussive head impacts can lead to progressive neurological decline and Chronic Traumatic Encephalopathy (CTE), a precursor to neurodegenerative conditions like Parkinson's disease, Alzheimer's disease, and dementia [34], [66]–[68].

Concussion results from non-missile or blunt force head impacts where trauma to the brain tissue occurs without penetration [66]. Due to this, examining the mechanisms causing concussive syndromes in this type of injury is complex. Specifically, the analysis of concussion is challenging due to the infeasibility of in-vivo observations of intracranial mechanics with current technology [41], [67]–[69]. Ethical and sample procurement constraints regarding concussive impact recreations with living and cadaver human subjects further complicate this issue [41]. Consequently, defining the kinematic parameters leading to concussion remains ambiguous.

Diagnoses without on-site impact telemetry rely on scoring systems based on neurocognitive questionnaires and external observations [70], [71].

To address the challenges of in-vivo impact assessments, researchers have simulated impact scenarios using laboratory-based impact testing with head forms like Hybrid-III, NOCSAE, and Hodgson-WSU. These head forms help establish relevant thresholds for head accelerations [51], [52], [54], [60]–[64], [67], [68], [72]–[75]. However, current head forms could be more biofidelic, closely matching human morphology and providing observations of intracranial concussion assessments beyond head accelerations [51], [52], [60], [71]–[76]. Comparisons between Hybrid-III, NOCSAE, and Hodgson-WSU head forms reveal performance discrepancies, with the former of the three showing reduced impact sensitivity, crucial for accurate concussion detection [60], [77]. In response, recent studies aim to develop biofidelic head forms using materials and manufacturing techniques to mimic human head structures [51]–[56], [78]. Falland-Cheung et al., Petrone et al., and Freitas et al. [51], [52], [54], [79] aimed to develop head forms for anatomical geometric accuracy through developed skull-brain head models with similar performance. These models allow for the observation of head impact characteristics not physically observable in laboratory-based tests, such as intracranial pressure (ICP). The head form developed by Falland-Cheung et al. further demonstrated the propagation of stress throughout simulated critical structures of the intracranial vault on impact.

Similarly, research has focused on material biofidelity in full-scale head models. Forte et al. developed brain phantoms characterized in comparison to native brain tissues [8]. Mantecón et al. [15] created full-scale skull phantoms through additive manufacturing to assess compressive fracture characteristics, comparing them to expected results in native human skulls. Additionally, Hanna et al. [78] characterized half-skull surrogates to observe and recreate head deformations from blunt force impacts.

Considering the progress made on these fronts, material biofidelity can be further enhanced. Previous studies have advanced this area with established testing methods, but the specimens used could better represent the geometry and structure of human cadaver skull specimens. Current biofidelic skull surrogates in research have yet to account for the complex sandwich-like layered composition of cranial bone, which includes the compact and brittle outer cortical (tabula) regions and the porous and ductile inner trabecular (diploë) regions (*Figure 4.1*). Native studies show that

these morphological regions affect the material behavior of human skull bone, with the bulk structure displaying a quasi-elastic response and some non-linear ductile creep before brittle fracture [13], [43], [47], [48], [80], [81].

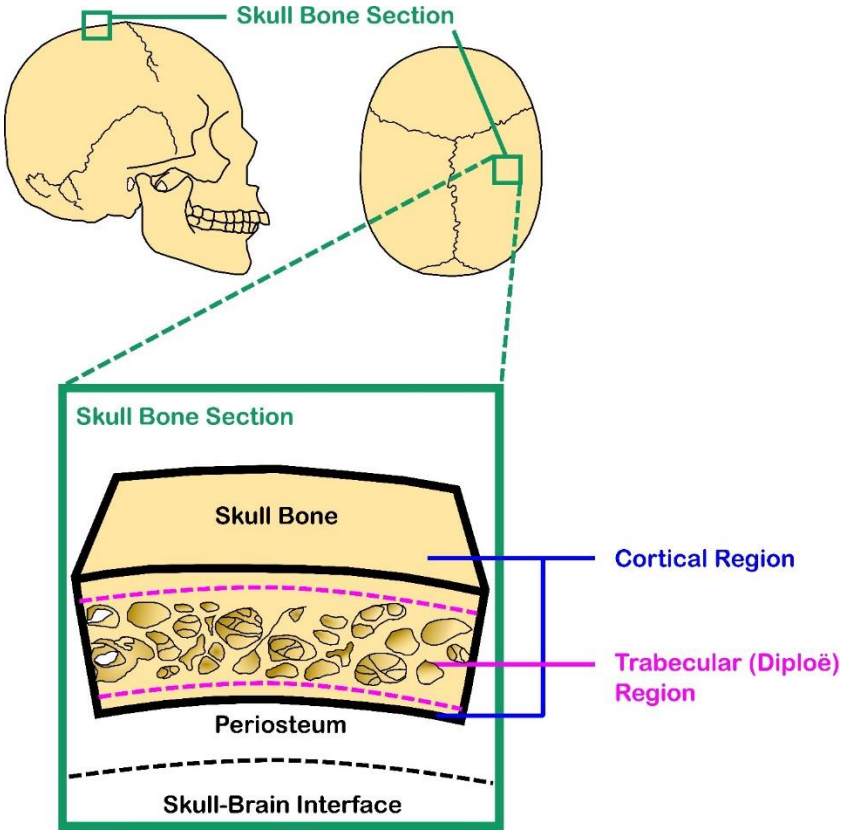


*Figure 4.1 — Structural Composition of Cranial Bone Showing the Cortical and Trabecular (Diploë) Bone Regions*

To achieve morphological accuracy of these native structures, evolving Additive Manufacturing (AM) techniques offer low-cost, repeatable, and sustainable rapid prototyping methods capable of constructing complex geometries, unlike traditional manufacturing alternatives. This study uses various materials produced with AM, employing the Fused Filament Fabrication (FFF) technique, aiming for greater anatomical correctness in proposed simulants. The research aims to establish FFF to represent the skull bone's diploë-tabula complex by adjusting infill density and printing direction. Materials such as PLA [5], [15], as well as PMMA, used in prosthesis and dental industries [82]–[84], will be studied to compare their performance to the bone characteristics found in the literature. Additionally, this study will introduce Digital Image Correlation (DIC) to observe comparable strain fields and biofidelic failure mechanisms during testing. DIC will allow for the

accurate capturing of strain flow for an otherwise irregular specimen geometry, choosing a skull-mimicking curved structure over a standardized testing specimen. This research aims to establish an ideal cranial bone simulant using these materials and manufacturing techniques, comparing material performance and failure mechanisms relative to native values and observations. Onwards, the simulant structure may be employed in a full-scale geometrically and materialistically accurate biofidelic model of the human skull.

## 4.2 — Materials and Methods

### *4.2.1 — Bone Surrogate Characterization Protocol*

#### ***4.2.1.1 — Additive Manufacturing (AM) Using FFF Printers***

Simulant samples were created using Fused Filament Fabrication (FFF) [87]–[92]. FFF is an additive manufacturing process where material is deposited layer-by-layer to generate a three-dimensional object. This method involves heating a polymer to a defined melting temperature, allowing the filament to reach a viscous molten state. The filament is then extruded through a heated nozzle and deposited onto a build platform, where it begins to rapidly cool and solidify (*Figure 4.2*) [85].

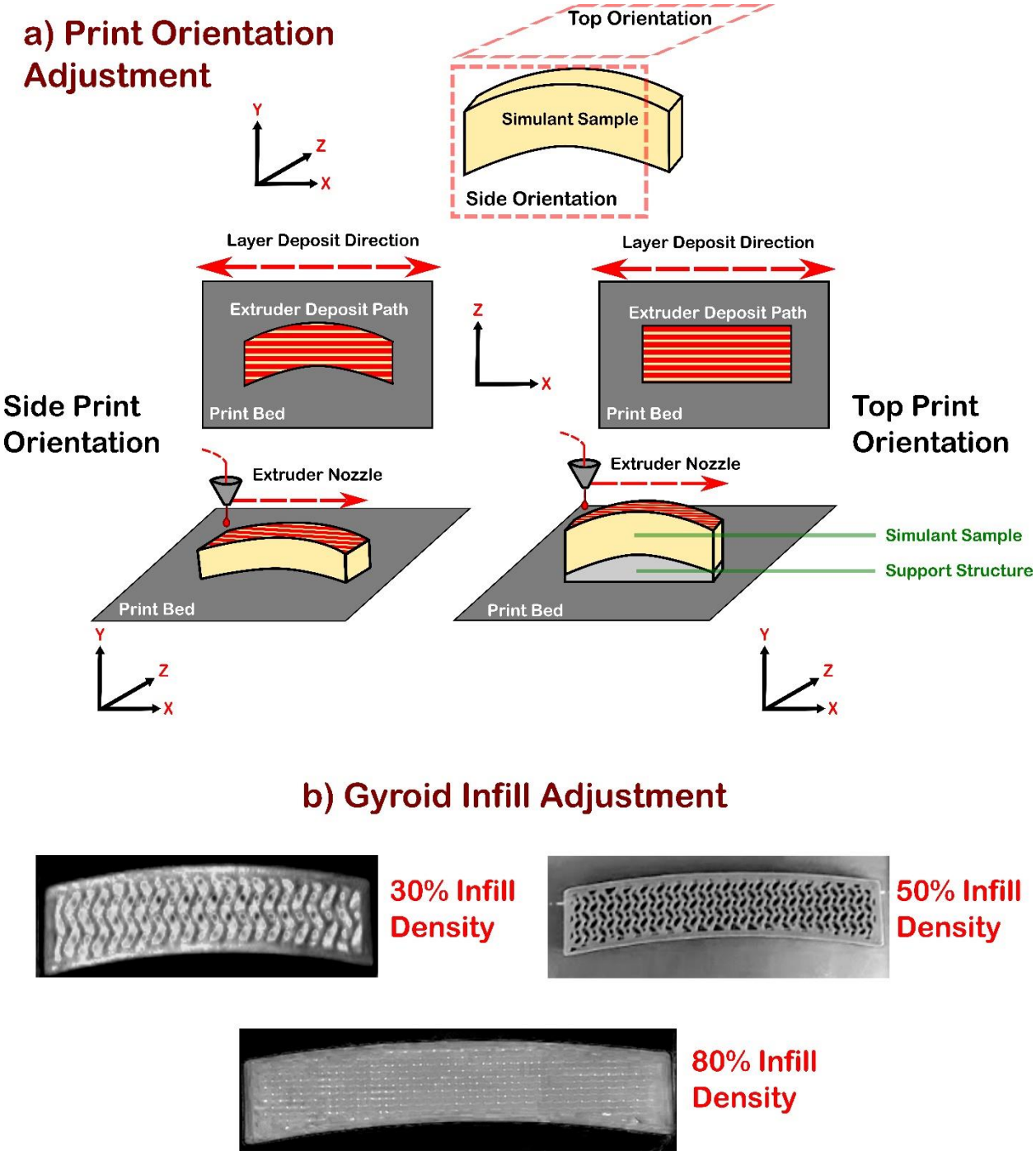


*Figure 4.2 — (a) Print Orientation and (b) Infill Densities of Manufactured Bone-Simulant Structures*

The printer nozzle or print bed moves along a defined path based on a three-dimensional model designed with CAD software and imported into slicing software, which optimizes the printer's path for AM. The nozzle traces the x- and y-directions relative to the build platform to form a single

layer. After completing a layer, the nozzle head or build platform adjusts in the z-direction for the next layer, allowing for the construction of a three-dimensional object. The printing path and other processing parameters can be adjusted to optimize print quality, material strength, and visual appearance. For this study, the infill pattern and density were adjusted to simulate the inner cancellous (diploë) region of human cortical bone [46]–[48].

All samples for this study were produced using a *Bambu X1 Carbon* printer (Bambu Lab Ltd.; Hong Kong). This nozzle-driven FFF printer controls toolpath direction by modulating the nozzle head in the x- and y-directions, while the print bed modulates in the z-direction for layer height control. Certain materials, such as Hydroxyapatite-coated PMMA, required an ambient enclosure to ensure optimal print quality, a feature offered in the Bambu X1 Carbon. The 3D solid models (.STL files) were imported to the printer's *Bambu Studio* slicing software for printing. The printing parameters for each material are provided in Table 4.1.

*Table 4.1 — FDM Printing Parameters for Simulant Samples*

| **Material** | **Layer Height (mm)** | **Nozzle Diameter (mm)** | **Nozzle Temperature (°C)** | **Build Platform Temperature (°C)** | **Nozzle Speed (mm/s)** |
|---|---|---|---|---|---|
| *PLA* | 0.2 | 0.2 | 220 | 35 | 50 |
| *Bone-Simulating PLA* | | | 245 | 60 | 50 |
| *HXA-PMMA** | | | 250 | 110 | 40 |

***Special Attention:** For quality prints, significant drying must be done for HXA-PMMA filament prior to use. *~18 hours of drying at 80°C* was done *prior to and during printing*. For bed adhesion, a brim, raft, and skirt (*~ 1.6 mm skirt height*) were printed alongside samples. Printer should provide some ambient enclosure. Ensure no significant humidity in surrounding laboratory or room.

#### *4.2.1.2 — Bone Simulant Selection and Manufacturing Materials*

##### 4.2.1.2.1 — PLA and Bone-Simulating PLA

Polylactic Acid (PLA) has become a predominant material in FFF due to its exceptional properties [86]. PLA has a relatively low melting temperature (180ºC and 210ºC) reducing its thermal gradient and thus minimizing any thermal stresses to promote material warping. This ease of printing and production has led to its widespread use [86]. Additionally, PLA is biodegradable and sustainable, making it an environmentally conscious alternative for thermoplastics. It is sourced from organic materials such as corn starch and sugar cane [11], [18], [85], [86], allowing its use in biomedical applications like implants and scaffolds [11], [14], [18]. One such application includes its potential as a stimulant for native human bone in creating biofidelic structures like the human skull [5], [15]. Falland-Cheung et al. [5] investigated the performance of several polymers in the simulation of the human skull, observing their elastic modulus relative to native skull structures in tension, compression, and flexion. They found that PLA exhibits suitable mechanical behavior for simulating cranial bone under higher strain rates and blunt force impacts in tensile and flexural modes.

Given PLA's performance as a bone simulant, it was selected for characterization tests in this study. The materials chosen are two forms of PLA: *Generic PLA* (3DPrintingCanada©; Hamilton, Ontario; Product No. 8000003030112) and *SimuBone™ Bone-Modeling PLA* (3DXTECH®; Grand Rapids, Michigan; Product No. BON2010750WT2). *SimuBone™* introduces additives to PLA aiming to simulate the look and feel of native bone.

##### 4.2.1.2.2 — PMMA and Hydroxyapatite Coating

Poly(methyl methacrylate) (PMMA), commonly known as acrylic, offers distinct characteristics when utilized as a thermoplastic polymer filament in additive manufacturing [16], [18]. However, it lacks some features present in popular alternatives like PLA and ABS, making it a less conventional choice for FFF printing. PMMA is more challenging to print due to its brittleness, significant shrinkage, and warpage during printing, necessitating a heated bed and an enclosed environment to maintain consistent ambient temperatures. Additionally, unlike PLA, PMMA is non-biodegradable and does not support eco-friendly production and recycling processes [16], [18]. Despite these challenges, PMMA has historically been used in the medical industry for dental

fillings, replacements, and orthodontic devices due to its biocompatibility and thermal stability within body temperature ranges [18], [87].

Like PLA, PMMA can be modified with additives to achieve specific properties tailored to its intended application, including enhanced mechanical properties [88], and biocompatibility [87]. For this study, the focus was on *Bonelecule™ Hydroxyapatite-coated PMMA* (OssFila©; Hong Kong; Product Code: OSF-FLB-HS). This medical-grade, bioactive filament simulates bone by incorporating hydroxyapatite additives into PMMA, imparting bone-like mechanical characteristics and promoting better adhesion during bone implantation. The integration of hydroxyapatite coatings in bone implants has been shown to enhance the mechanical strength of scaffold materials while accelerating bone regeneration, making it highly beneficial for AM applications in implants, scaffolding, and prosthetics [16], [18], [87], [88].

#### *4.2.1.3 — Adjustment of Infill Density for Simulation of Diploë*

The infill densities of the bending samples were adjusted to simulate the elastic behavior of the porous inner trabecular region in native bone. Studies by Chacón et al. and Melenka et al. [86], [89] concluded that increasing the infill percentage in AM samples significantly increases the elastic modulus and ultimate strength of PLA-printed tensile samples.

Infill densities were adjusted to match the elastic properties and trabecular volume ratios observed in the human skull. Observations by Lee et al. indicated that inner trabecular volume ratios in the human skull range between 50% and 90% [47], while Boruah et al. [46] observed median trabecular bone volume fractions of 0.47. Each surrogate candidate was printed with 30%, 50%, and 80% infill densities to observe the effects on material elasticity and generate characterizations to determine the optimal infill density that best simulates native bone. The selected infill pattern aimed to closely resemble the natural morphology of native diploë [44]–[46]. In this study, the gyroid infill pattern available in the *Bambu Studio* printing software was used to simulate the natural porous structure of diploë.

#### *4.2.1.4 — Adjustment of Print Raster Direction as a Parameter for Elasticity and Strength*

The printing orientation of an additively manufactured part, which refers to the arrangement of the part's layers during its manufacturing process, can significantly influence its strength, durability, and elasticity [87]–[92]. Anisotropy due to the direction of material deposition must be considered

in the material characteristics of AM samples. Ramezani Dana et al. [92] observed that the printing orientation relative to the direction of loading affects the strength of the material, with mechanical stiffness favoring adjacently layered surfaces over parallel-deposited layers. This is attributed to greater adhesion forces among adjacently printed layers and the direction of loading concerning printing direction.

Considering this, simulant structures were further optimized by varying the printing orientation. Along with changes to infill density and material selection, each set of material samples was printed in two configurations of print orientation: filament deposition was directed on the tangential (side) face of the testing samples and along the radial (top) face of the samples. Further depiction of printing orientation can be observed in Figure 4.2.

#### *4.2.1.5 — Skull Bone Surrogate Flexural Specimens*

The samples produced for the relevant experiments were generated to simulate tests to determine the flexural modulus and strength of native human cortical bone [13], [47]. Tests conducted by Lee et al. and Ondruschka et al. retrieved cranial samples from donated cadavers for material characterization. Flexural specimens of a fixed span and width were extracted along the skull's frontal, parietal, temporal, and occipital regions from two cadavers. Variations in specimen thickness were found due to the differing thicknesses of the skull along these regions [13], [47]. The effect of the periosteum and dura mater soft tissues on the mechanical properties of the human skull was also established [13], [47]. The presence of the periosteum affected thickness measurements when determining the dimensional properties of the samples. The dimensional parameters and other relevant properties affecting the mechanical properties in these tests are listed in Table 4.2 and Figure 4.4. Figure 4.3 presents the variation in Case One and Case Two simulant specimens, which is elaborated further below in *Sections 2.1.5.1* and *2.1.5.2*, respectively.

For the current study, AM samples were printed considering the dimensional parameters listed above. To evaluate the accurate representation of skull curvature for the flexural performance of the specimens, the curvature applied to the specimens was determined from the Global Human Body Model Consortium Male 50th Percentile Model (GHBMC M50) [93]. The prescribed dimensions for the prepared samples, as well as cortical and cancellous thicknesses, are listed in Table 4.2.

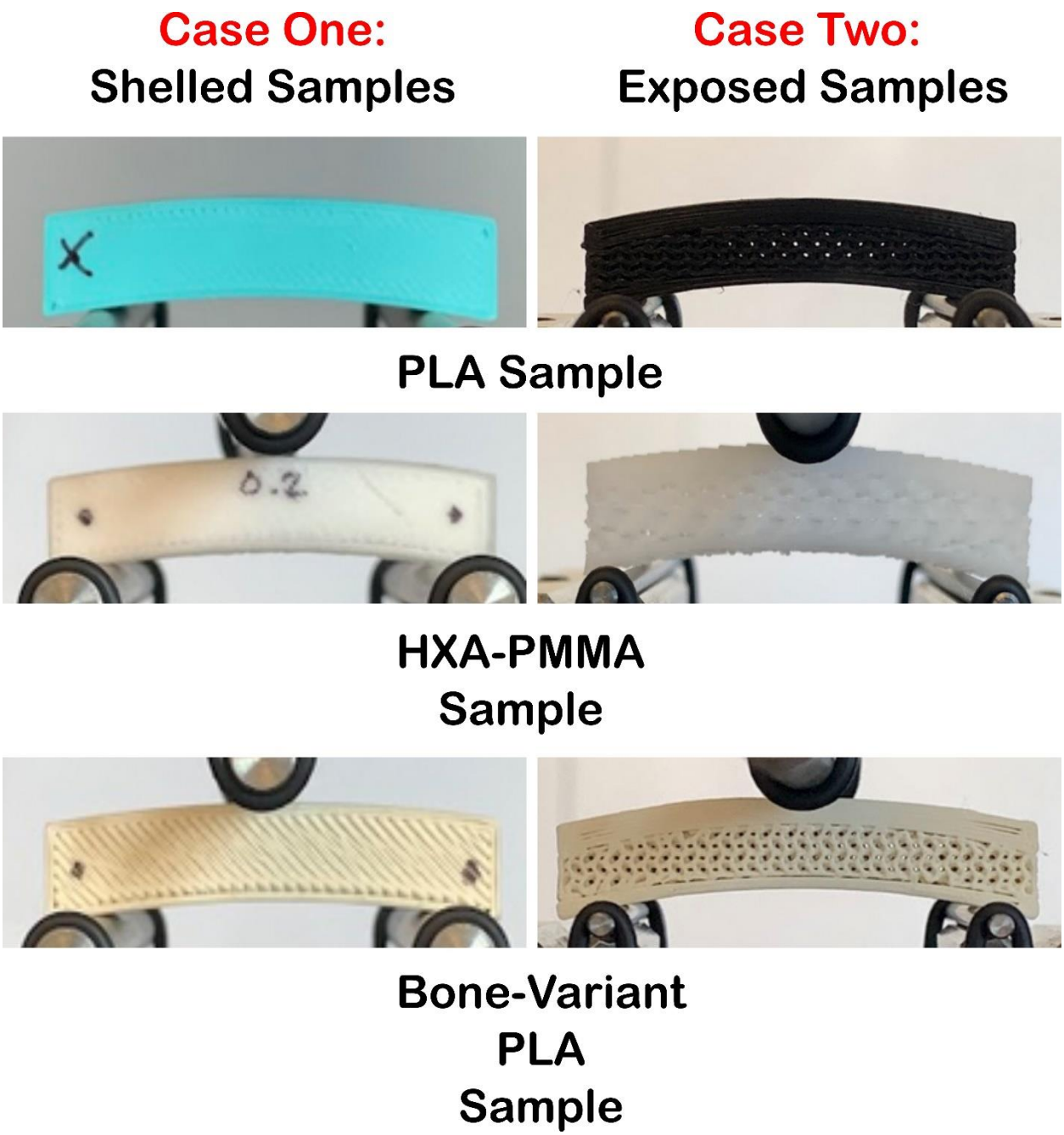


*Figure 4.3 — Mounted Simulant Samples Based on Filament Materials*

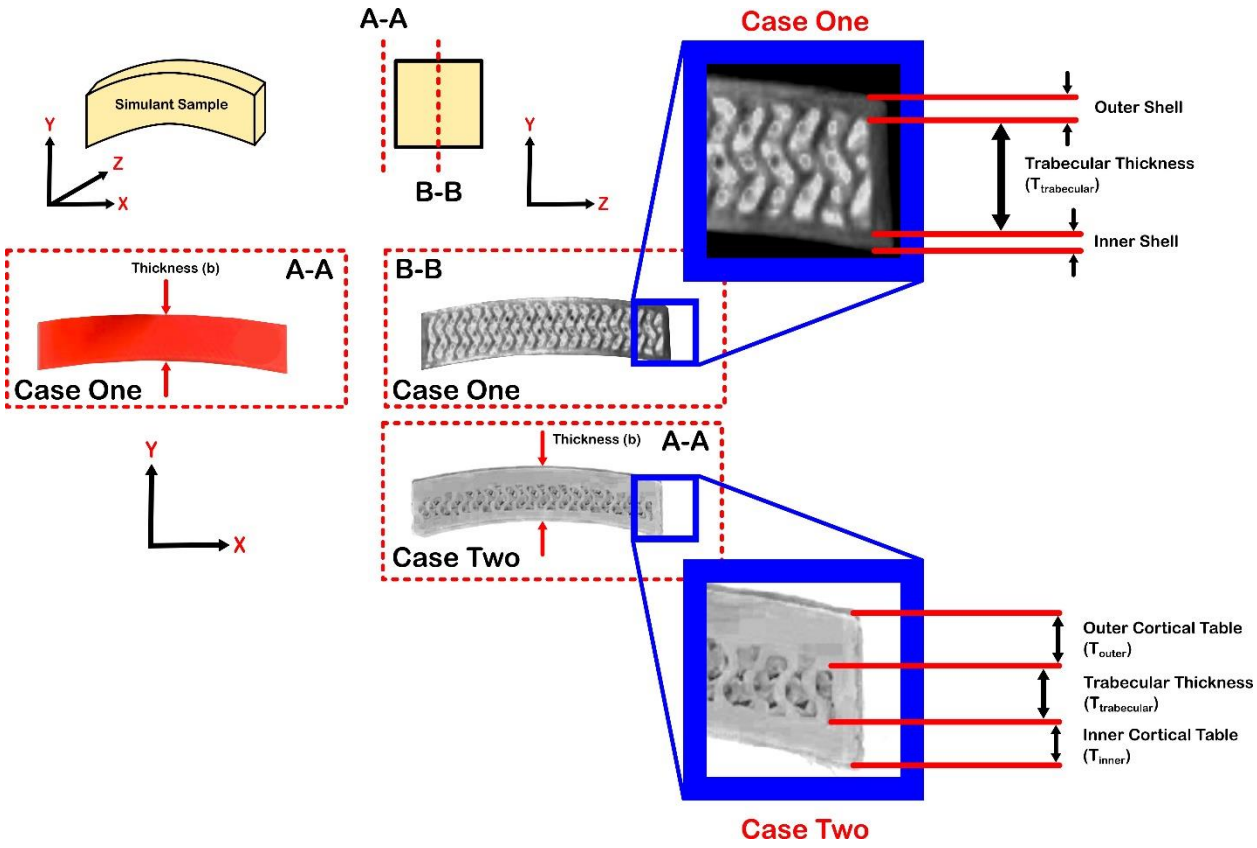


*Figure 4.4 — Specimen Thickness Measurements (PLA; 30% Infill, Side-Printed); Shell Thickness, and Cortical and Trabecular Tables*

*Table 4.2 — Dimensional Parameters for Native and Simulant Human Skull Specimens [13], [47]*

| **Material** | **Skull 1** | | | **Skull 2** | | |
|---|---|---|---|---|---|---|
| | **Thickness (mm)** | **Width (mm)** | **Trabecular Volume Ratio** | **Thickness (mm)** | **Width (mm)** | **Trabecular Volume Ratio** |
| ***Lee et al. (2019)*** | **Bare Bone** | | | | | |
| | 7.32 ± 1.87 | 10.12 ± 0.21 | 0.71 ± 0.11 | 7.83 ± 1.63 | 10.46 ± 0.23 | 0.84 ± 0.08 |
| | **Soft Tissue Attached** | | | | | |
| | 5.75 ± 1.84 | 10.08 ± 0.32 | 0.64 ± 0.11 | 8.40 ± 1.96 | 10.09 ± 0.32 | 0.89 ± 0.05 |
| ***Ondruschka et al. (2019)*** | **Bare Bone** | | | | | |
| | N/A | 10 ± 0.25 | N/A | N/A | 10 ± 0.25 | N/A |
| | **Soft Tissue Attached** | | | | | |
| | N/A | 10 ± 0.25 | N/A | N/A | 10 ± 0.25 | N/A |
| ***Current Study*** | **Simulant Materials (Bare Bone Simulation)** | | | | | |
| | **Mean Width (b):** 9.52 ± 1.03 mm | | | **Mean Thickness (d):** 7.96 ± 0.15 mm | | |
| | **Skull Circumference (GHBMC M50) [88]:** 89.13 mm | | | | | |
| | ***Case Study 2:*** **Cortical and Trabecular Table Measurements** | | | | | |
| | **Outer Cortical Thickness ($T_{outer}$):** 2.21 ± 0.27 mm | | | **Inner Cortical Thickness ($T_{inner}$):** 1.42 ± 0.19 mm | | |
| | **Cortical Thickness Fraction (CTF):** 1.57 ± 0.17 | | | | | |
| | **Trabecular Volume Fraction (TVF):** 0.59 ± 0.05 | | | | | |

4.2.1.5.1 — Case One: Adjustment of Infill Density Within Solid-Walled Specimens

The first case in this study explores the impact of infill density and print raster orientation on a solid-walled structure. Building upon the simulant characterization studies by Falland-Cheung et al. [5] and Mantecón et al. [15], where FFF-printed PLA bone simulants were created with a 100% solid infill density and compared to skull bone tests from existing literature, this study modifies these parameters to examine their mechanical effects. Specimens with similar configurations were produced, maintaining solid shell walls approximately 1 mm thick around the outer perimeter (*Figure 4.4*). Infill densities of 30%, 50%, and 80% were tested to assess their influence on the mechanical properties of the simulants.

4.2.1.5.2 — Case Two: Adjustment of Infill Density Within a Defined Cortical-Trabecular Sandwich Structure

The second case study considers the design of bending specimens to observe the three-tiered sandwich structure seen in native bone. Printed simulant samples were designed to replicate the structure of native bone samples, particularly from the frontal skull, for mechanical testing [13], [47], [81]. This required careful consideration of the specific volumetric geometries of the cortical and cancellous regions. Average thicknesses of the cortical-cancellous regions were derived from several studies [46]–[48] to govern the 3D design of the simulant structure. Outer and inner cortical tables vary across the human skull. However, Boruah et al. [46] determined a mean thickness ratio of approximately 1.6, favoring the outer cortical region. This thickness ratio was applied to the printed simulants, considering the dimensions of the specimens characterized in the first case study and the native bone specimens in Lee et al. [47] and Ondruschka et al. [13] (*Figure 4.4*). Cortical tables were printed with 100% infill and a monotonic line path to simulate their dense structure. While a trabecular volume ratio is prescribed in these specimens, the adjustment of infill densities among Case Two conditions remains to observe the effects on elastic properties.

### *4.2.1.6 — Three-Point Bending Tests and Digital Image Correlation (DIC)*

Three-point bending tests were conducted on the developed specimens to obtain material flexion results. Full evaluation of the printing parameters and conditions tested can be found in Table 4.3. Characterization testing was performed on an *MTS© Criterion™ Model 43* (Illinois Tool Works Inc.; Glenview, Illinois) universal testing machine with three-point bending fixtures to mount specimens (*Figure 4.5*). A 10 kN load cell was used to apply the necessary force for specimen

fracture, with the load applied at a rate of 10 mm/min (equivalent to ~0.01 $s^{-1}$). Specimens were placed on mounting pins with a radius of 2 mm, with the bottom resting pins positioned at a 30 mm span. The loading pin was situated at the apex of the sample's curvature. Samples were carefully placed using positional markings on the device and specimen to ensure consistent positioning and performance for each test subject. A diagram of the testing configuration and specimen mounting is shown in Figure 4.5. Similar parameters were used for native characterization in the studies by Lee et al. and Ondruschka et al. [13], [47]. To obtain comparable results for the performance of the simulant materials, this study adopted similar calculations of flexural stress and strain for beams with rectangular cross-sections.

$$\sigma = \frac{3Fc}{2bd^2}$$

*Equation 4.1 — Flexural Stress*

*[13], [47]*

**Where:**

*F — Applied Force (N)*

*c — Span (30 mm)*

*b — Width (mm)*

*d — Thickness (mm)*

$$\varepsilon = \frac{6Yd}{c^2}$$

*Equation 4.2 — Flexural Strain*

*[13], [47]*

**Where:**

*Y — Applied Deflection (mm)*

*Table 4.3 — Testing Matrix Configuration for Three-Point Bending Tests*

| Material | Sample Size (n) | | |
|---|---|---|---|
| | Print Orientation / Infill Density (%) | Top-Print Orientation | Side-Print Orientation |
| ***PLA*** | *30* | *5* | *5* |
| | *50* | *5* | *5* |
| | *80* | *5* | *5* |
| | ***Orientation Total*** | ***15*** | ***15*** |
| | ***Material Total*** | | ***30*** |
| ***HXA-PMMA*** | *30* | *5* | *5* |
| | *50* | *5* | *5* |
| | *80* | *5* | *5* |
| | ***Orientation Total*** | ***15*** | ***15*** |
| | ***Material Total*** | | ***30*** |
| ***Bone-Like PLA*** | *30* | *5* | *5* |
| | *50* | *5* | *5* |
| | *80* | *5* | *5* |
| | ***Orientation Total*** | ***15*** | ***15*** |
| | ***Material Total*** | | ***30*** |
| ***Testing Total (per Print Orientation)*** | | ***45*** | ***45*** |
| ***Total with Shelled Samples ($n_{shelled}$)*** | | | ***90*** |
| ***Total with Exposed Cortical and Trabecular Regions ($n_{exposed}$)*** | | | ***90*** |
| ***Grand Total (n)*** | | | ***180*** |

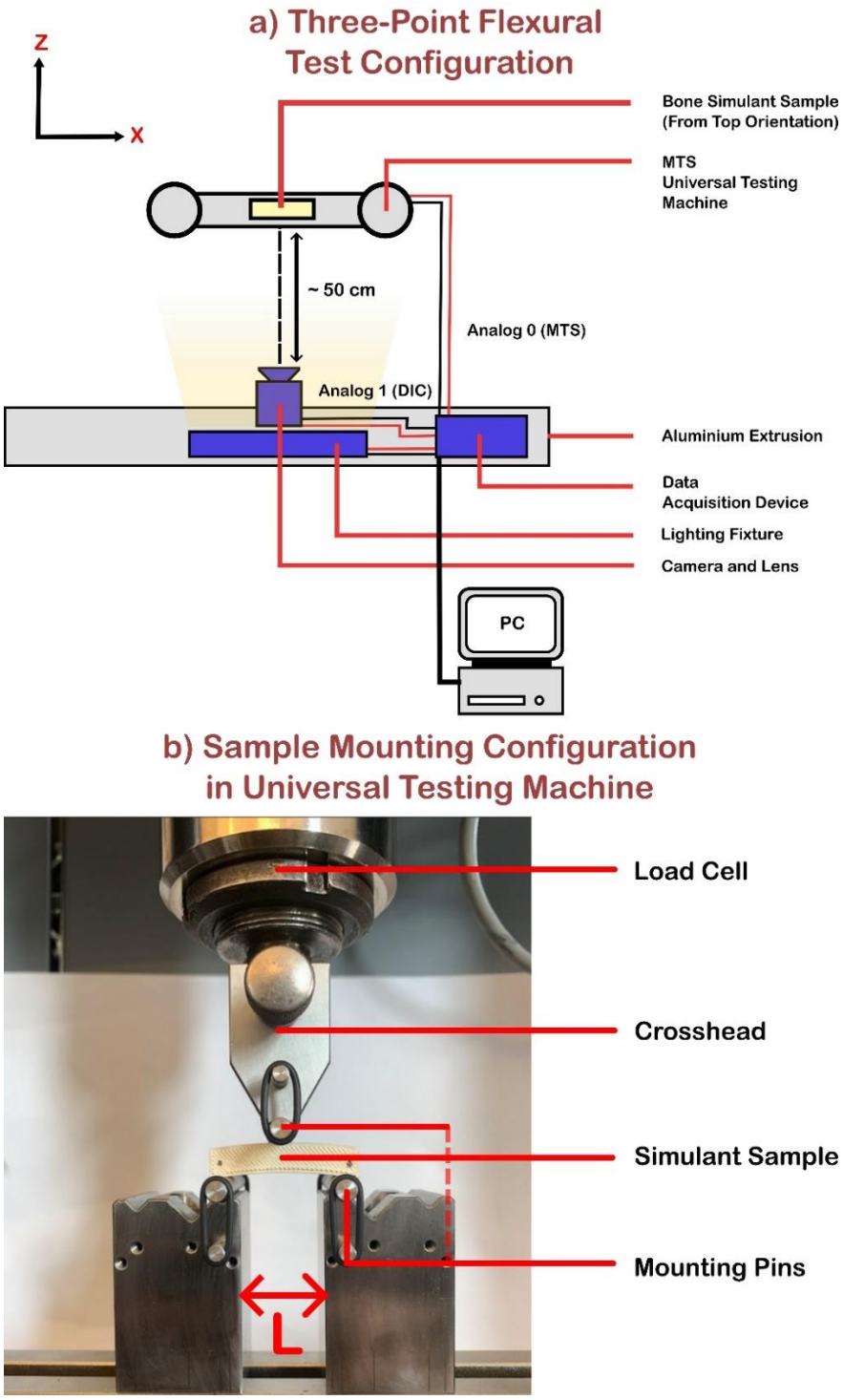


*Figure 4.5 — Digital Image Correlation (DIC) Configuration and Three-Point Bending Test Setup*

Additionally, Digital Imaging Correlation (DIC) was performed alongside three-point bending tests to visualize the strain fields of the tested specimens. This was necessary due to the irregular

shaping of the testing samples, aiming to match and recreate the performance of extracted human skull samples in similar tests [13], [47], as opposed to conventional standards for assessing the bending performance of polymers, such as the ISO 20795-1 standard [5]. DIC was conducted using *the LaVision StrainMaster Portable*™, (LaVision GmbH; Göttingen, Germany) while image processing was conducted using the *LaVision DaVis*™ *Version 10.0.3* Data Analysis Software (LaVision GmbH; Göttingen, Germany). Full specifications of imaging parameters and equipment can be observed in Table 4.4. A single camera observed the strain field on the specimen's tangential (side) face using 2D DIC. Optimal image contrast was achieved by positioning lighting appropriately, while additional background curtains and opaque tape were added to reflective surfaces of the testing equipment to ensure speckle contrast and image quality (*Table 4.4, Figure 4.6*). For this part of the study, the specimens from the first case study were investigated with DIC due to the solid outer shell, which allowed for sample speckling.

During testing, the specimens were placed within the testing apparatus and loaded until visible fracture occurred or the device's load or displacement threshold was exceeded. Data was recorded from the initialization of loading until the crosshead detected fracture due to a significant drop in load or by manual termination of loading once the operator deemed a material failure. Digital imaging was manually triggered to begin before the loading process and ended after global fracture was determined or when the device's fracture thresholds were triggered. Load/displacement data from the universal testing machine was captured and tabulated, while images from the loading process were recorded using the camera and data acquisition device (*Figure 4.5*). These images were then used to develop data correlations for material strain and displacement fields during loading.

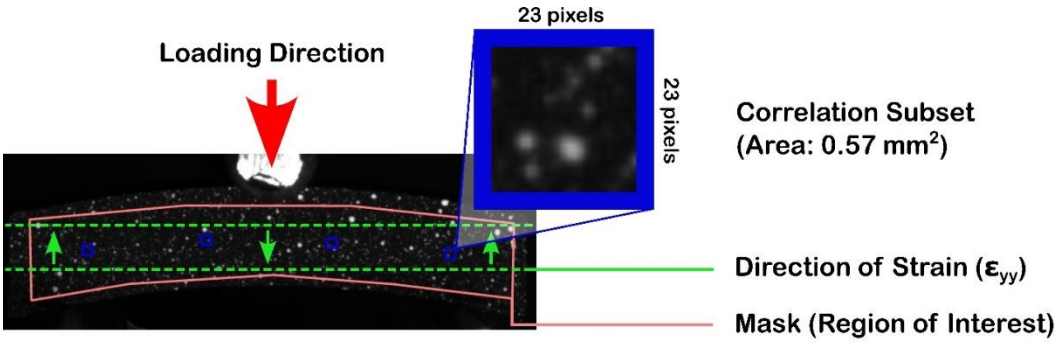


Figure 4.6 — Digital Image Correlation (DIC) Calibration and Post-Processing Parameters

*Table 4.4 — Digital Image Correlation (DIC): Imaging Equipment and Parameters*

| **Components and Hardware** | **Model Number** | **Specifications** |
|---|---|---|
| ***Camera*** | *Imager M-Lite 5M CMOS Camera (Model: 1101503)* | **Resolution:** *2464* x *2056* pixel<br>**Pixel Size:** *3.45* µm x *3.45* µm |
| ***Data Acquisition Hardware*** | *LaVision GmbH StrainMaster Portable™ (Model: 1104218)* | -- |
| ***Lens*** | *Model: FL-CC3516-2M* | **Size:** *35* mm<br>**Aperture Value:** *f / 1.6* |
| ***Lighting Fixtures*** | *LED Illumination Set (Model: 1103348)* | Linear Unit<br>**Length:** *30* cm<br>**White Light Output:** *6500* K<br>**Blue Light Output:** *45* nm |
| ***Calibration Tool*** | *058-5-SSDP Plate Model* | **Dimensions:** *58* mm x *58* mm |
| ***Data Analysis Software*** | *LaVision GmbH DaVis™ Version 10.0.3* | -- |
| **Image Correlation Parameters** | | |
| ***Field of View*** | *150* x *180* $mm^2$ | |
| ***Capture Rate*** | *10* Hz | |
| ***Correlation Subset Size*** | *23* pixels | |
| ***Subset Step Size*** | *8* pixels | |
| ***Subset Scale Factor*** | *30.46* pixels/mm | |
| ***Correlation Mode*** | Relative to First | |

## 4.3 — Results

### *4.3.1 — Bone Simulant Characteristics from Three-Point Bending Tests*

Material characteristics were obtained from the specimens (*n = 180; n = 5 for each material and parameter for infill density and print orientation; n = 90 for each case study*). Ten samples (*n = 10; PLA at 30% Infill, Side Orientation, and PLA at 50% Infill, Top Orientation*) were incompatible with or insufficient for DIC correlation due to poor image quality. The mechanical properties of select specimens are provided in Tables 4.5 and 4.6. A complete representation of all tested candidates is provided in *Appendix B, Table B1*. Comparisons to natural cranial bone were supplemented by results found in Lee et al. and Ondruschka et al. for cranial bone without soft tissue [13], [47] (*Table 4.5, Table 4.6*). Statistical significances of the effect of infill density on simulant material modulus and strength are further provided in Figures 4.8 and 4.9 and Tables 4.7 to 12. Detailed observation of the mean stress-strain behaviors of each material and specimen condition can be found in *Appendix B, Figures B3 to B14.* Stress-strain graphs with standard deviations can be found beginning on *Appendix B, Figure B6*.

The stress-strain behaviors were tabulated to assess each material's properties in terms of flexural modulus, flexural strength, and their compiled mean characteristics. The mean characteristics closely matching those of cranial bone with deviation are tabulated in Table 4.5 for simulants of the first case study and Table 4.6 for the second case study. To compare performances with those found in the literature, Tables 4.5 and 4.6 provide a relative performance metric, which is the percent ratio between the mean simulant modulus and strength compared to the respective mean properties for native bone (*Equation 4.3*).

The specimen conditions presented in their respective tables display condition sets that observe relative performance (RP%) metrics greater than the comparative relative performance (CRP %). CRP% regards the ratio between reported mean values and their standard deviations in either flexural modulus, or strength properties. If the RP% values of a simulant are greater than their respective CRP% value, it suggests that the performance of the simulant falls within the deviations in the reported properties of native bone. The selected specimen conditions for display observe RP % > CRP % in at least two categories between reported properties of flexural modulus and strength among both native bone characterizations found in the literature [13], [47]. The reported mean

properties of all simulant conditions, as well as their relative performances to the literature, can be found in *Appendix B, Tables B2* for Case One specimens, and *B3* for Case Two specimens.

$$RP\ (\%) = 100\% \times \left| \frac{(E\ or\ F)|_{Simulant\ Mean}}{(E\ or\ F)|_{Literature\ Mean}} \right|$$

*Equation 4.3 — Relative Performance (RP) Equation*

$$CRP\ (\%) = 100\% \times \left| \frac{(E\ or\ F)|_{Literature\ (Literature\ Mean\ \pm\ Standard\ Deviation)}}{(E\ or\ F)|_{Literature\ Mean}} \right|$$

*Equation 4.4 — Comparative Relative Performance (CRP) Equation Using Standard Deviations from the Literature*

**Where:** *E — Flexural Modulus (MPa)*

*F — Flexural Strength (MPa)*

*Table 4.5 — Case One: Mean Mechanical Performance of Comparable Shelled Bone Simulant Candidates (n = 5 for Each Statistic)*

| ***Material*** | **Infill Density (%) [*Sample Size*]** | **Print Orientation** | **Flexural Modulus (MPa)* [95% CI]** | **Relative Performance (%)** | | **Flexural Strength (MPa)* [95% CI]** | **Relative Performance (%)** | |
|---|---|---|---|---|---|---|---|---|
| *PLA* | 50 [*n = 5*] | Side | ***1415.8 ± 108.1 [1324.7, 1495.3]*** | **83.0** | *71.2* | ***52.8 ± 0.5 [52.3, 53.5]*** | **74.1** | *96.5* |
| | 80 [*n = 5*] | Side | ***1732.1 ± 28.9 [1708.7, 1754.7]*** | **98.2** | *87.3* | *66.1 ± 0.2 [65.9, 66.3]* | **42.6** | *79.4* |
| | 80 [*n = 5*] | Top | ***1330.4 ± 55.3 [1255.9, 1412.9]*** | **78.5** | *67.4* | *69.6 ± 1.6 [67.8, 71.5]* | **34.2** | *72.9* |
| *HXA-PMMA* | 80 [*n = 5*] | Side | ***1397.4 ± 56.1 [1316.0, 1438.9]*** | **81.1** | *69.6* | *62.3 ± 0.7 [61.6, 63.2]* | **51.5** | *86.2* |
| *Bone-Like PLA* | 50 [*n = 5*] | Side | ***1534.3 ± 57.5 [1457.7, 1588.0]*** | **89.6** | *76.9* | ***45.5 ± 0.8 [48.2, 48.8]*** | **84.4** | *88.5* |
| | 80 [*n = 5*] | Side | ***1921.1 ± 42.5 [1873.0, 1969.2]*** | **86.9** | *97.0* | *62.5 ± 0.6 [61.9, 63.2]* | **51.1** | *85.9* |
| | 80 [*n = 5*] | Top | ***1303.3 ± 135.5*** | **76.7** | *65.8* | *59.6 ± 1.2 [58.2, 61.0]* | **58.1** | *91.2* |
| **Human Bone (Lee et al.) [13]** | -- | -- | **1699 ± 712** | **Comparative Relative Performance: Modulus (CRP%)** | | **42 ± 14** | **Comparative Relative Performance: Strength (CRP%)** | |
| | | | | **58.1** | | | **66.7** | |
| *Human Bone (Ondruschka et al.) [47]* | -- | -- | *1979.7 ± 815.1* | *Comparative Relative Performance: Modulus (CRP%)* | | *54.8 ± 18.9* | *Comparative Relative Performance: Strength (CRP%)* | |
| | | | | *58.8* | | | *65.5* | |

***Bolded** values indicate properties that fall within the deviation ranges of cranial bone properties in Lee et al; *Italicized* values indicate properties that fall within the deviation ranges of cranial bone properties in Ondruschka et al.

*Table 4.6 — Case Two: Mean Mechanical Performance of Comparable Exposed Bone Simulant Candidates (n = 5 for Each Statistic)*

| ***Material*** | **Infill Density (%)** [***Sample Size***] | **Print Orientation** | **Flexural Modulus (MPa)*** **[95% CI]** | **Relative Performance Modulus (%)** | | **Flexural Strength (MPa)*** **[95% CI]** | **Relative Performance Strength (%)** | |
|---|---|---|---|---|---|---|---|---|
| *PLA* | 50 [*n = 5*] | Side | ***803.8 ± 53.8 [753.6, 853.6]*** | **47.3** | *40.6* | ***46.2 ± 0.87 [45.5, 47.0]*** | **89.9** | *84.4* |
| | 50 [*n = 5*] | Top | ***710.9 ± 5.4 [706.1, 715.6]*** | **41.8** | *35.9* | ***43.3 ± 1.8 [41.7, 44.9]*** | **97.0** | *79.0* |
| | 80 [*n = 5*] | Side | **1068.9 ± 18.9 [1052.3, 1085.5]** | **62.9** | *54.0* | ***57.1 ± 0.88 [56.3, 57.9]*** | **64.0** | *95.8* |
| | 80 [*n = 5*] | Top | **1013.6 ± 64.1 [957.4, 1069.7]** | **59.7** | *51.2* | ***59.6 ± 1.5 [58.3, 61.0]*** | **57.1** | *91.2* |
| *HXA-PMMA* | 80 [*n = 5*] | Side | **1156.2 ± 78.9 [1087.0, 1225.4]** | **68.1** | *58.4* | ***39.5 ± 6.5 [33.8, 45.3]*** | **94.2** | *72.2* |
| | 80 [*n = 5*] | Top | **1068.3 ± 80.7 [988.8, 1147.7]** | **62.9** | *54.0* | ***45.5 ± 2.3 [43.5, 47.5]*** | **91.6** | *83.1* |
| *Bone-Like PLA* | 50 [*n = 5*] | Side | 943.2 ± 70.2 [881.7, 1004.8] | **55.5** | *47.6* | ***43.6 ± 8.3 [36.3, 50.9]*** | **96.3** | *79.5* |
| | 50 [*n = 5*] | Top | 644.0 ± 37.0 [611.6, 676.5] | **37.9** | *32.5* | ***38.8 ± 9.9 [30.1, 47.4]*** | **92.3** | *70.8* |
| | 80 [*n = 5*] | Side | ***1337.2 ± 27.2 [1313.4, 1361.0]*** | **78.7** | *67.5* | *56.9 ± 3.6 [53.7, 60.1]* | **64.5** | *96.2* |
| | 80 [*n = 5*] | Top | **1034.1 ± 150.4 [902.3, 1165.9]** | **60.9** | *52.2* | ***48.5 ± 3.4 [45.5, 51.4]*** | **84.5** | *88.5* |
| **Human Bone (Lee et al.) [13]** | -- | -- | **1699 ± 712** | **CRP Modulus (%)** | | **42 ± 14** | **CRP Strength (%)** | |
| | | | | **58.1** | | | **66.7** | |
| *Human Bone (Ondruschka et al.) [47]* | -- | -- | *1979.7 ± 815.1* | *CRP Modulus (%)* | | *54.8 ± 18.9* | *CRP Strength (%)* | |
| | | | | *58.8* | | | *65.5* | |

***Bolded** values indicate properties that fall within the deviation ranges of cranial bone properties in Lee et al; *Italicized* values indicate properties that fall within the deviation ranges of cranial bone properties in Ondruschka et al.

#### *4.3.1.1 — Case One: Observed Performances of Shelled Simulants*

Table 4.5 shows that all listed materials fall within the standard deviations of at least one study regarding natural bone. However, while the selected optimal specimens perform well in one criterion, they often need improvement in another. Notable performances include PLA and Bone-like PLA at 80% infill with the side-printed orientation. Consideration can also be given to PLA and Bone-like PLA at 50% infill with side-print orientation and HXA-PMMA at 50% and 80% infill with side-print orientation for their accurate representation of flexural strength.

The numerical performances of biofidelic simulants also portrayed similar failure mechanisms relative to skull bone. Zhai et al. [81] observed the flexural performance of skull specimens under quasi-static, intermediate, and high strain rates. Compared to the stress-strain behaviors in this study, native skull bone displayed a quasi-elastic stress-strain behavior: an initial non-linear toe region, followed by linear elasticity, and a creep stress reduction after its ultimate point, culminating in a drastic drop in stress. Some simulants developed in this study showed similar characteristics. Bone-simulating PLA resembled all three stages of the human bone's "toe-elastic-creep regime." For standard PLA, only specimens printed in the top direction showed the toe region, but all samples exhibited bone-like characteristics after the linear elastic range. The stress-strain behavior of HXA-PMMA initially showed accuracy in performance, with a highly simulative toe and linear regime within the strain range. However, it was followed by a drastically brittle response before reaching a creep regime and an expected strength point similar to native cranial bone.

#### *4.3.1.2 — Case Two: Observed Performances of Exposed Cortical-Trabecular Simulants*

Comparing the material performances of the exposed cortical-trabecular specimens in Case Two, flexural moduli and strength reductions were generally observed compared to the shelled samples in the first case study. As a result, selecting materials to fall within the deviations of the native bone properties in Lee et al. [47] and Ondruschka et al. [13], particularly in flexural modulus, was more rigorous. However, the reduction in flexural strength in second-case specimens was favorable for their biofidelic performance, as the previous case study sample set generally exceeded the behavior of native bone in strength performances. The most notable parameterized specimens tested were Bone-like PLA at 80% infill density and HXA-PMMA at 80% infill density, in both

side and top-printed raster orientations (*Table 4.6*). Both materials excelled in their relative performances for moduli and strength across comparative native studies.

Observing the stress-strain flow behavior of the second case specimens (*Figure 4.7*), the "toe-elastic-creep" regimes became more apparent, particularly for PLA and its variant. HXA-PMMA also showed some elasticity before its eventual brittle fracture in this manufacturing configuration. Notably, the mean stress-strain curve of the native bone specimens tested under the same 0.01 $s^{-1}$ strain rate in the Zhai et al. [94] study closely resembled the Bone-like PLA 80% Side Printed and PLA 80% Top Printed specimens. However, the tested loading method in the mentioned study observed bending tangential to the specimen curvature, while this study observed radial bending. It should also be noted that no explicit value for modulus and ultimate strength was given in the survey for incorporation into the modulus and strength comparisons in this research.

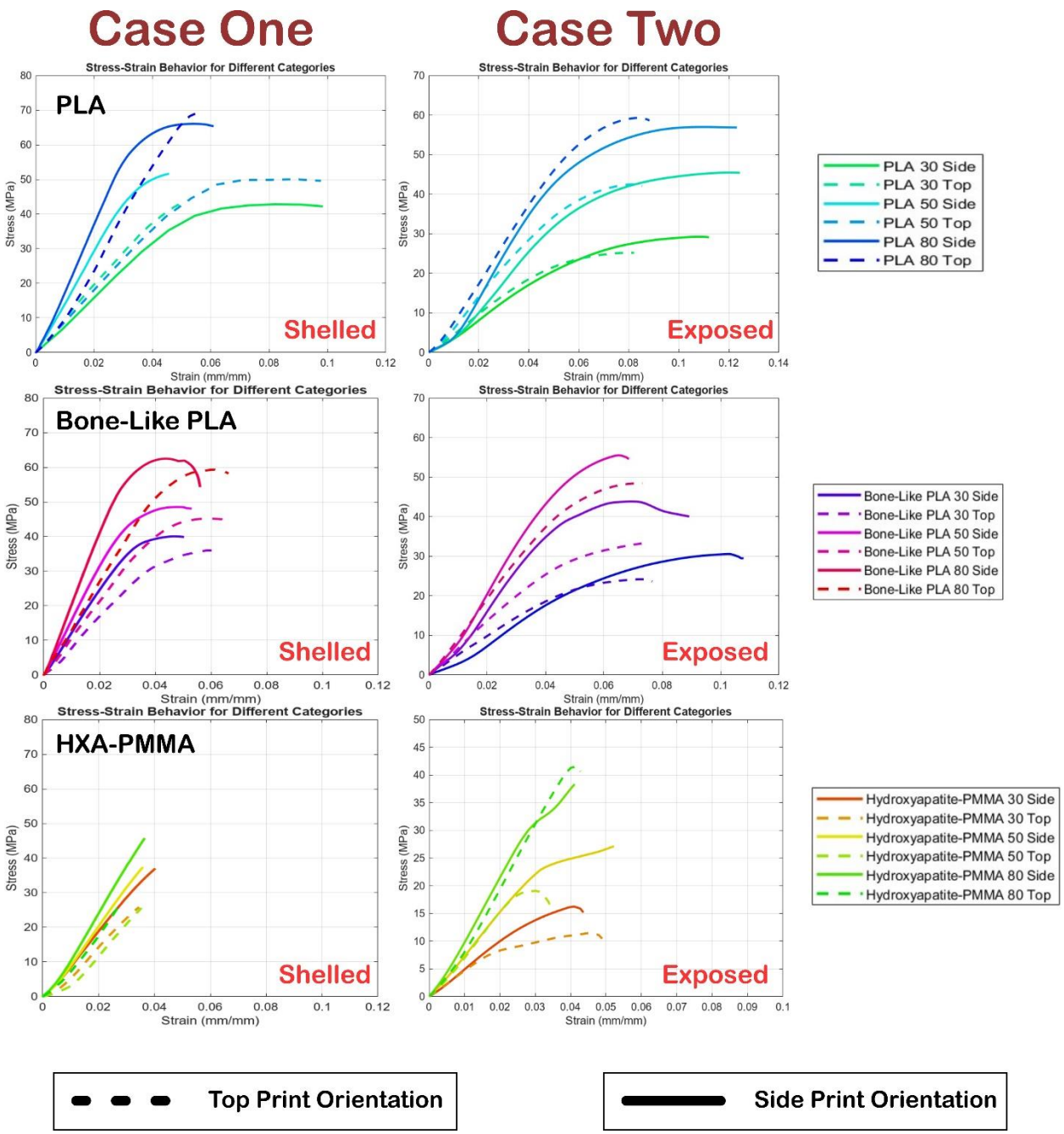


*Figure 4.7 — Mean Stress-Strain Curves of Bone-Simulant Materials (Quasi-Elastic Regimes)*

## *4.3.2 — Statistical Correlations Between Printing Parameters and Material Performance*

### *4.3.2.1 — Linear Regression Correlations of Flexural Modulus and Strength Under the Influence of Infill Density*

The first notable correlation observed was that increasing the infill density of the printed samples yields a proportional increase in flexural modulus and strength performance. This is most prominently seen in the first-case correlations for the flexural strength of PLA and Bone-like PLA samples in the side print orientation, with $R^2$ values remaining greater than 0.87 (*Figure 4.8*). Secondly, it was observed that printing orientation affected material performance, such that the side print orientations yielded improved properties in modulus and strength compared to the top-printed alternative specimens.

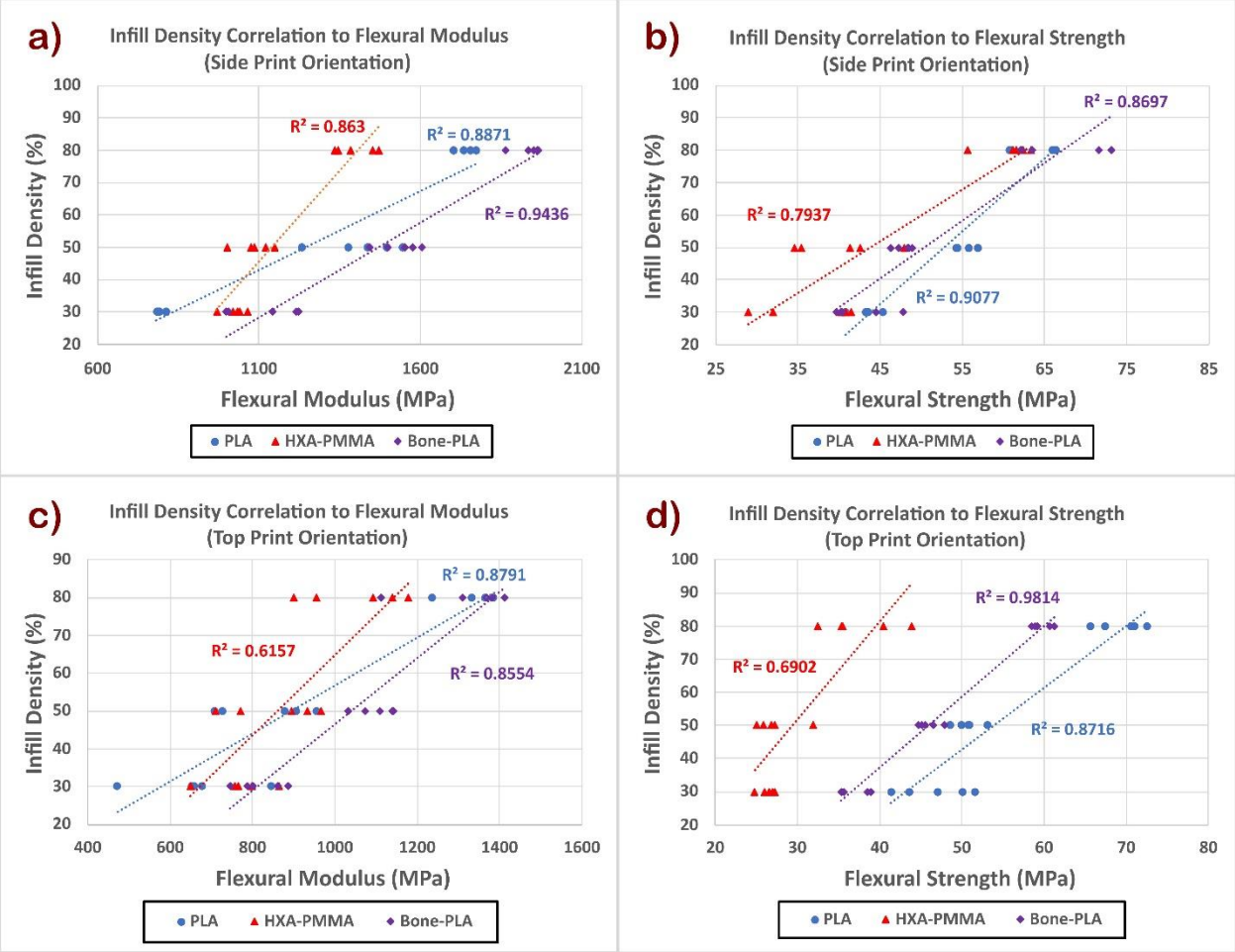

*Figure 4.8 — Case One: Linear Correlations Between Infill Density and Material Performance of Bone Simulants: (a) Side Print Orientation Flexural Modulus, (b) Side Print Orientation Flexural Strength; (c) Top Print Orientation Flexural Modulus, (d) Top Print Orientation Flexural Strength*

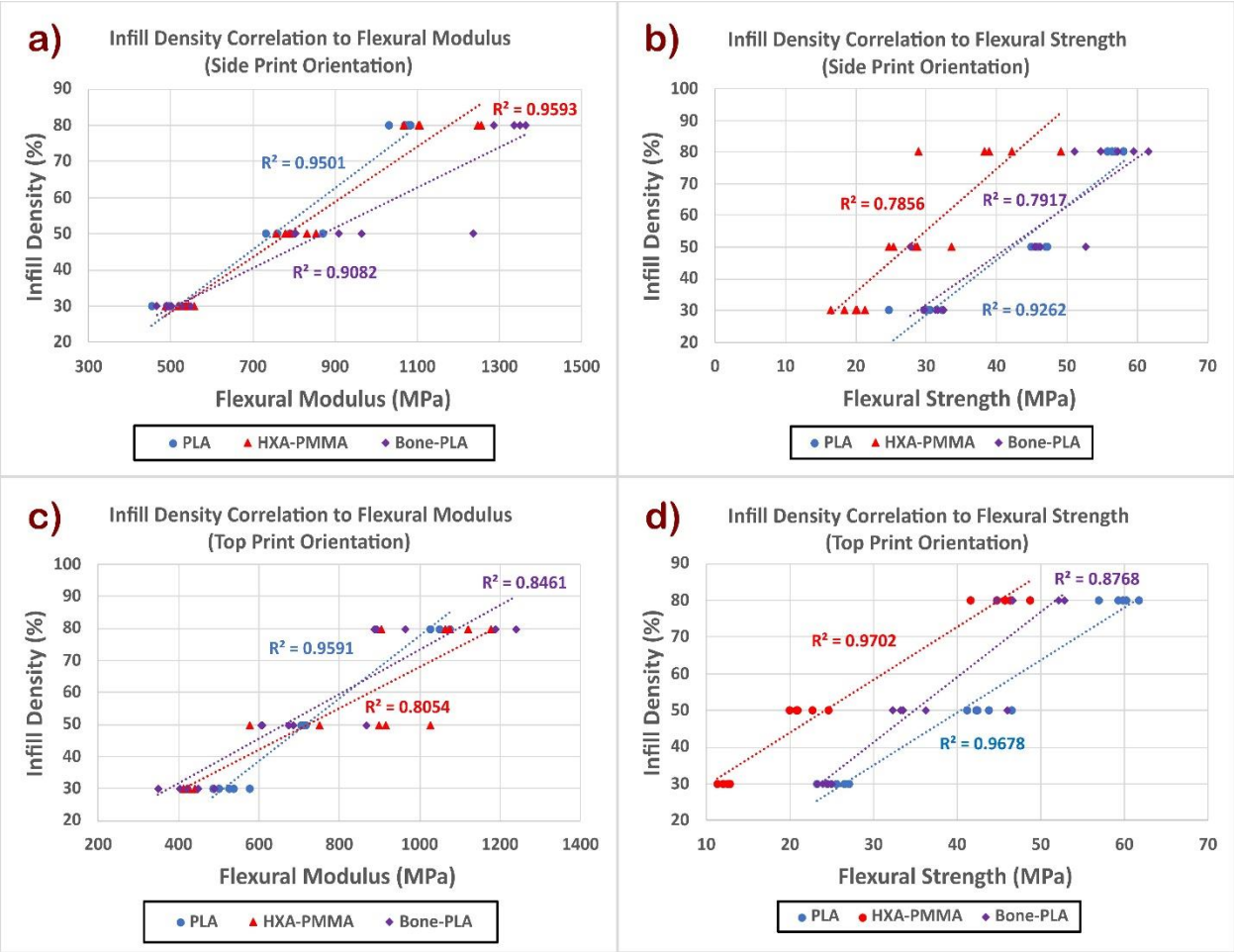


*Figure 4.9 — Case Two: Linear Correlations Between Infill Density and Material Performance of Bone Simulants: (a) Side Print Orientation Flexural Modulus, (b) Side Print Orientation Flexural Strength; (c) Top Print Orientation Flexural Modulus, (d) Top Print Orientation Flexural Strength*

Of the tested materials, Bone-like PLA and PLA displayed the closest correlations across all parameters in the first case study, with $R^2$ values ranging between 0.86 to 0.98. This may be due to the consistent quasi-ductile fractures throughout all parameters of PLA and its variant. The materials that experienced brittle fracture, most notably PLA at high infill densities and HXA-PMMA, showed reduced correlation among parameters between side and top printed modulus. Simultaneously, HXA-PMMA, which experienced the least correlation, showed brittle fracture across all given infill and print orientation parameters.

For the second case study, linear fitment is considerably reduced for PLA and Bone-like PLA specimens while correlations remain the same. HXA-PMMA specimens observed an increase in correlation for these parameters, serving as the material with the closest correlations, observing $R^2$ values no lower than 0.92 across the board. Once again, the correlation between material performance to infill density and raster direction could pertain to the method of material failure for the printed simulants. All materials observed brittle fracture following an initial elastic regime for this testing sequence. Furthermore, the failure process varied among specimens. The most notable failure methods were initial opening at the bending specimens' bottom apex and delamination of the outer cortical table from the trabecular region. This contrasts with the shelled specimens in the first case study, where all specimens strictly observed the first failure mode. In the second case study, materials in the side print orientation experienced either delamination of the cortical tables, an opening fracture at the bottom apex, or a combination of the two. In contrast, materials in the top print orientation experienced strictly opening fractures at the bottom apex.

#### *4.3.2.2 — Two-Way and Three-Way ANOVA Analysis of Statistical Significances of Adjusting Parameters*

The effects of infill density, print orientation, and printing method (Case One and Case Two) on material modulus and strength were further analyzed using a Three-Way Analysis of Variance (ANOVA) Test, aggregating data from all simulant materials tested ($n = 180$). The null hypothesis ($H_0$) posits that these parameters yield no significant effect on the mechanical performance of the printed simulants (i.e., modulus and strength). The alpha ($\alpha$) value was set at 0.05, where p-values $\leq 0.05$ reject the null hypothesis, indicating that these material conditions have a statistically significant effect on modulus and strength. Two-way ANOVA results for the impact of infill density and printing orientation, and their interaction, are found in Tables 4.7 and 4.8 for Case One moduli and strengths and Tables 4.9 and 4.10 for Case Two moduli and strengths. Additionally, to observe the influence of varying manufacturing methods between Case One and Case Two specimens, a Three-Way ANOVA was conducted to consider the significance between both printing methods, found in Table 4.11 for moduli and Table 4.12 for strengths.

*Table 4.7 — Case One: Two-Way ANOVA Test for Printing Parameter Influences on Flexural Modulus*

| Material | Source of Variance | Sum of Squares | Degrees of Freedom | Mean Square | F-Value | p-Value |
|---|---|---|---|---|---|---|
| ***Influence on Modulus*** | | | | | | |
| HXA-PMMA *[n = 30: 5 per Variance]* | *Orientation* | 3.8647e+05 | 1 | 3.8647e+05 | **65.1963** | **p < 0.001** |
| | *Infill* | 4.0137e+05 | 2 | 2.0068e+05 | **33.8548** | **p < 0.001** |
| | *Orientation and Infill Interaction* | 2.5930e+04 | 2 | 1.2965e+04 | 2.1872 | 0.1549 |
| | *Error* | 7.1133e+04 | | | | |
| | *Total* | 8.8489e+05 | | | | |
| PLA *[n = 30: 5 per Variance]* | *Orientation* | 2.5348e+05 | 1 | 2.5348e+05 | **63.5860** | **p < 0.001** |
| | *Infill* | 1.3117e+06 | 2 | 6.5585e+05 | **164.5223** | **p < 0.001** |
| | *Orientation and Infill Interaction* | 4.2020e+05 | 2 | 2.1010e+05 | 52.7038 | **p < 0.001** |
| | *Error* | 4.7837e+04 | | | | |
| | *Total* | 2.0332e+06 | | | | |
| Bone-Like PLA *[n = 30: 5 per Variance]* | *Orientation* | 1.0206e+06 | 1 | 1.0206e+06 | **137.4451** | **p < 0.001** |
| | *Infill* | 1.0806e+06 | 2 | 5.4031e+05 | **72.7632** | **p < 0.001** |
| | *Orientation and Infill Interaction* | 5.1227e+04 | 2 | 2.5614e+04 | 3.4494 | 0.0655 |
| | *Error* | 8.9107e+04 | | | | |
| | *Total* | 2.2416e+06 | | | | |

*Table 4.8 — Case One: Two-Way ANOVA Test for Printing Parameter Influences on Flexural Strength*

| Material | Source of Variance | Sum of Squares | Degrees of Freedom | Mean Square | F-Value | p-Value |
|---|---|---|---|---|---|---|
| ***Influence on Strength*** | | | | | | |
| HXA-PMMA *[n = 30: 5 per Variance]* | *Orientation* | 1.3377e+03 | 1 | 1.3377e+03 | **197.1621** | **p < 0.001** |
| | *Infill* | 1.0674e+03 | 2 | 533.6892 | **78.6570** | **p < 0.001** |
| | *Orientation and Infill Interaction* | 61.4742 | 2 | 30.7371 | 4.5301 | **0.0342** |
| | *Error* | 81.4202 | | | | |
| | *Total* | 2.5480e+03 | | | | |
| PLA *[n = 30: 5 per Variance]* | *Orientation* | 55.4870 | 1 | 55.4870 | **15.2051** | **p < 0.001** |
| | *Infill* | 1.4954e+03 | 2 | 747.6852 | **204.8876** | **p < 0.001** |
| | *Orientation and Infill Interaction* | 0.0062 | 2 | 0.0031 | 0.0009 | 0.9991 |
| | *Error* | 43.7910 | | | | |
| | *Total* | 1.5947e+03 | | | | |
| Bone-Like PLA *[n = 30: 5 per Variance]* | *Orientation* | 45.5441 | 1 | 45.5441 | **38.6484** | **p < 0.001** |
| | *Infill* | 1.5849e+03 | 2 | 792.4456 | **672.4637** | **p < 0.001** |
| | *Orientation and Infill Interaction* | 0.2295 | 2 | 0.1147 | 0.0974 | 0.9079 |
| | *Error* | 14.1411 | | | | |
| | *Total* | 1.6448e+03 | | | | |

*Table 4.9 — Case Two: Two-Way ANOVA Test for Printing Parameter Influences on Flexural Modulus*

| Material | Source of Variance | Sum of Squares | Degrees of Freedom | Mean Square | F-Value | p-Value |
|---|---|---|---|---|---|---|
| ***Influence on Modulus*** | | | | | | |
| HXA-PMMA *[n = 30: 5 per Variance]* | *Orientation* | 21304.3 | 1 | 21304.3 | **2.52** | 0.1256 |
| | *Infill* | 2026060.7 | 2 | 1013030.3 | **119.79** | **p < 0.001** |
| | *Orientation and Infill Interaction* | 27295.3 | 2 | 13647.7 | 1.61 | 0.22 |
| | *Error* | 202964.8 | | | | |
| | *Total* | 2277625.1 | | | | |
| PLA *[n = 30: 5 per Variance]* | *Orientation* | 12749.1 | 1 | 12749.1 | **6.35** | **0.0188** |
| | *Infill* | 1398143.5 | 2 | 699071.7 | **348.15** | **p < 0.001** |
| | *Orientation and Infill Interaction* | 17990.7 | 2 | 8995.3 | 4.48 | **0.0222** |
| | *Error* | 48190.5 | | | | |
| | *Total* | 1477073.8 | | | | |
| Bone-Like PLA *[n = 30: 5 per Variance]* | *Orientation* | 344058 | 1 | 344058 | **27.13** | **p < 0.001** |
| | *Infill* | 2601524.6 | 2 | 1300762.3 | **102.56** | **p < 0.001** |
| | *Orientation and Infill Interaction* | 32766.5 | 2 | 32766.5 | 2.58 | 0.0964 |
| | *Error* | 304401.2 | | | | |
| | *Total* | 3315516.8 | | | | |

*Table 4.10 — Case Two: Two-Way ANOVA Test for Printing Parameter Influences on Flexural Strength*

| Material | Source of Variance | Sum of Squares | Degrees of Freedom | Mean Square | F-Value | p-Value |
|---|---|---|---|---|---|---|
| ***Influence on Strength*** | | | | | | |
| HXA-PMMA *[n = 30: 5 per Variance]* | *Orientation* | 45.45 | 1 | 45.45 | **3.41** | 0.0771 |
| | *Infill* | 3682.92 | 2 | 1841.46 | **138.23** | **p < 0.001** |
| | *Orientation and Infill Interaction* | 266.87 | 2 | 133.44 | 10.02 | **p < 0.001** |
| | *Error* | 319.73 | | | | |
| | *Total* | 4314.97 | | | | |
| PLA *[n = 30: 5 per Variance]* | *Orientation* | 17.38 | 1 | 17.38 | **5.39** | **0.0291** |
| | *Infill* | 4793.77 | 2 | 2396.88 | **742.98** | **p < 0.001** |
| | *Orientation and Infill Interaction* | 61.85 | 2 | 30.92 | 9.59 | **p < 0.001** |
| | *Error* | 77.42 | | | | |
| | *Total* | 4950.42 | | | | |
| Bone-Like PLA *[n = 30: 5 per Variance]* | *Orientation* | 329.401 | 1 | 329.401 | **8.17** | **0.0087** |
| | *Infill* | 3132.01 | 2 | 1566.004 | **38.82** | **p < 0.001** |
| | *Orientation and Infill Interaction* | 16.18 | 2 | 8.092 | 0.2 | 0.8196 |
| | *Error* | 968.1 | | | | |
| | *Total* | 4445.69 | | | | |

*Table 4.11 — Three-Way ANOVA: Influence of Infill, Raster Orientation, and Printing Method on Simulant Moduli*

| **Material** | **Source of Variance** | **Sum of Squares** | **Degrees of Freedom** | **Mean Square** | **F-Value** | **p-Value** |
|---|---|---|---|---|---|---|
| ***Influence on Modulus*** | | | | | | |
| All Materials *[n = 180]* | *Orientation* | 1.6220e+06 | 1 | 1.6220e+06 | **79.1810** | **p < 0.001** |
| | *Infill* | 7.5678e+06 | 2 | 3.7839e+06 | **184.7198** | **p < 0.001** |
| | *Printing Method* | 4.4064e+06 | 1 | 4.4064e+06 | **215.1091** | **p < 0.001** |
| | *Orientation and Infill Interaction* | 2.3159e+05 | 2 | 1.1580e+05 | 5.6528 | **0.0044** |
| | *Orientation and Printing Interaction* | 4.5665e+05 | 1 | 4.5665e+05 | 22.2924 | **p < 0.001** |
| | *Infill and Printing Interaction* | 8.8633e+04 | 2 | 4.4316e+04 | 2.1634 | 0.1189 |
| | *Error* | 2.7449e+06 | | | | |
| | *Total* | 1.7636e+07 | | | | |

*Table 4.12 — Three-Way ANOVA: Influence of Infill, Raster Orientation, and Printing Method on Simulant Strengths*

| Material | Source of Variance | Sum of Squares | Degrees of Freedom | Mean Square | F-Value | p-Value |
|---|---|---|---|---|---|---|
| ***Influence on Strength*** | | | | | | |
| All Materials *[n = 180]* | *Orientation* | 710.1657 | 1 | 710.1657 | **9.8016** | **0.0021** |
| | *Infill* | 1.3277e+04 | 2 | 6.6387e+03 | **91.6264** | **p < 0.001** |
| | *Printing Method* | 4.1771e+03 | 1 | 4.1771e+03 | **57.6517** | **p < 0.001** |
| | *Orientation and Infill Interaction* | 49.3125 | 2 | 24.6563 | 0.3403 | 0.7122 |
| | *Orientation and Printing Interaction* | 37.2129 | 1 | 37.2129 | 0.5136 | 0.4748 |
| | *Infill and Printing Interaction* | 331.1892 | 2 | 165.5946 | 2.2855 | 0.1057 |
| | *Error* | 9.7088e+03 | | | | |
| | *Total* | 3.0084e+04 | | | | |

Across both case studies, adjusting infill densities and print raster orientations correlated with the material performances of moduli and strength in all materials — except HXA-PMMA in Case Two — with statistical significance (p-value < 0.05). It was generally observed that infill density had the most significant influence on material performance, often generating a greater F-value compared to print orientation. However, some outliers — such as PLA and Bone-like PLA in Case One strength (*Table 4.8*) and HXA-PMMA in Case One modulus (*Table 4.7*) — showed more significant influences from print orientation than infill, yielding greater F-values.

When considering the variations among printing methods for both case studies across all materials, raster orientation, infill density, and printing methods yielded statistically significant correlations ($p\text{-value} < 0.05$). Among these parameters, the printing method showed the greatest significance in modulus ($F\text{-value} = 215.1$), followed by infill density ($F\text{-value} = 184.7$) and print raster orientation ($F\text{-value} = 79.2$). For strength, infill density was the most significant parameter ($F\text{-value} = 91.6$), followed by printing method ($F\text{-value} = 57.7$) and print orientation ($F\text{-value} = 9.8$).

### *4.3.3 — Digital Image Correlation (DIC) of Specimen Failure Mechanisms*

DIC imaging and processing were used during testing to capture the full-field distribution of strain and displacement. Figures 4.10 and 4.11 capture the strain induced on the respective samples before their fracture point. DIC imaging revealed the distribution of stress throughout the entire specimens in testing. The maximum stress observed in these images corresponds to the strains in their respective load curves. While studies typically distinguish natural bone complete image correlations in their methodology, no testing correlations for strain have been provided. However, the survey by Ondruschka et al. provides displacement correlations in testing [13]. Comparisons with the displacement correlations in this graph show similar behavior in three-point bending tests. The displacement range yielded within the same degree of magnitude (i.e., Peak displacement occurred at the center of the specimens, and magnitudes tapered outwards throughout their span). Magnitudes of displacement exceeded those of natural bone counterparts among simulant samples, possibly due to the increased performances regarding the strength of the simulant materials (*Table 4.5, Table 4.6*).

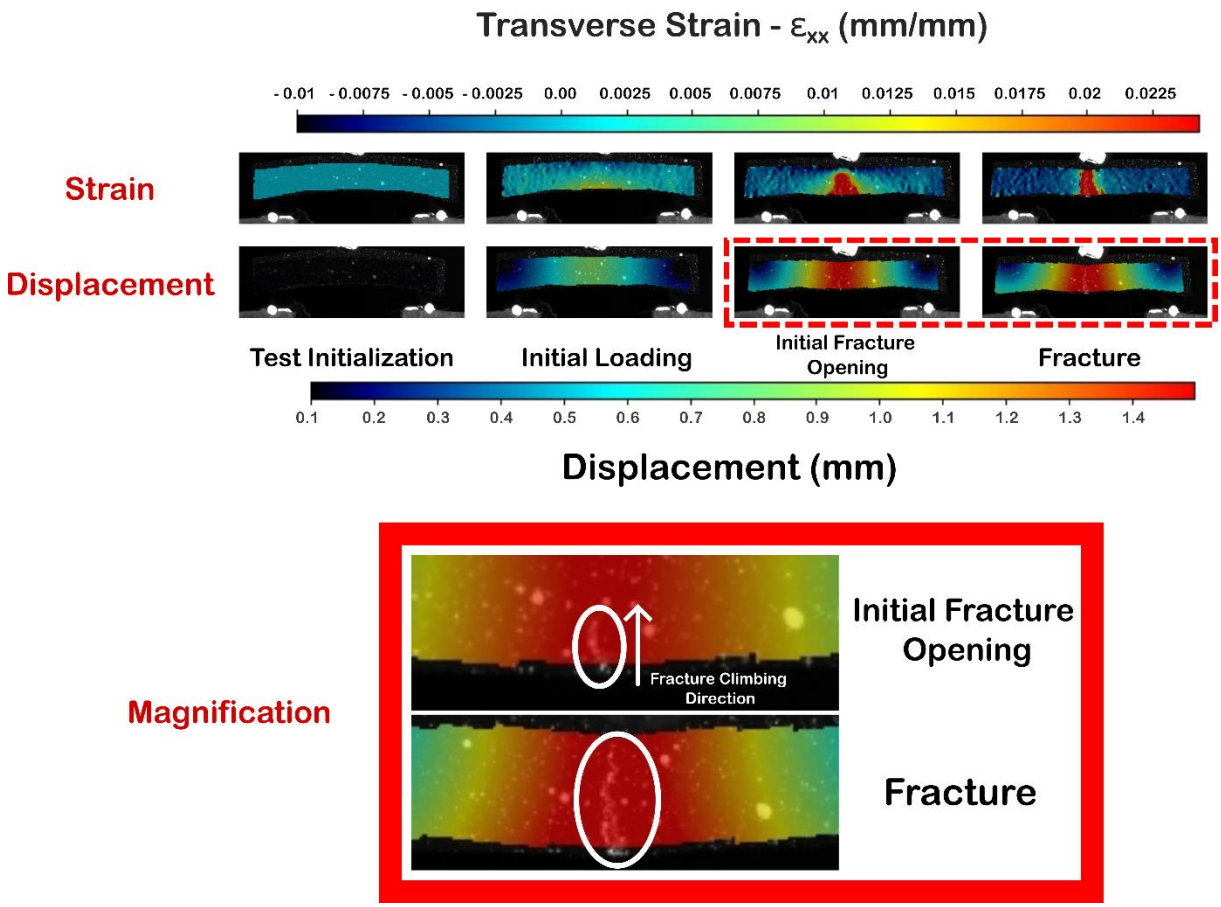


*Figure 4.10 — DIC Image Strain and Displacement Capturing of Bone-Like PLA at 80% Infill, Side Print Orientation: Various Loading Stages*

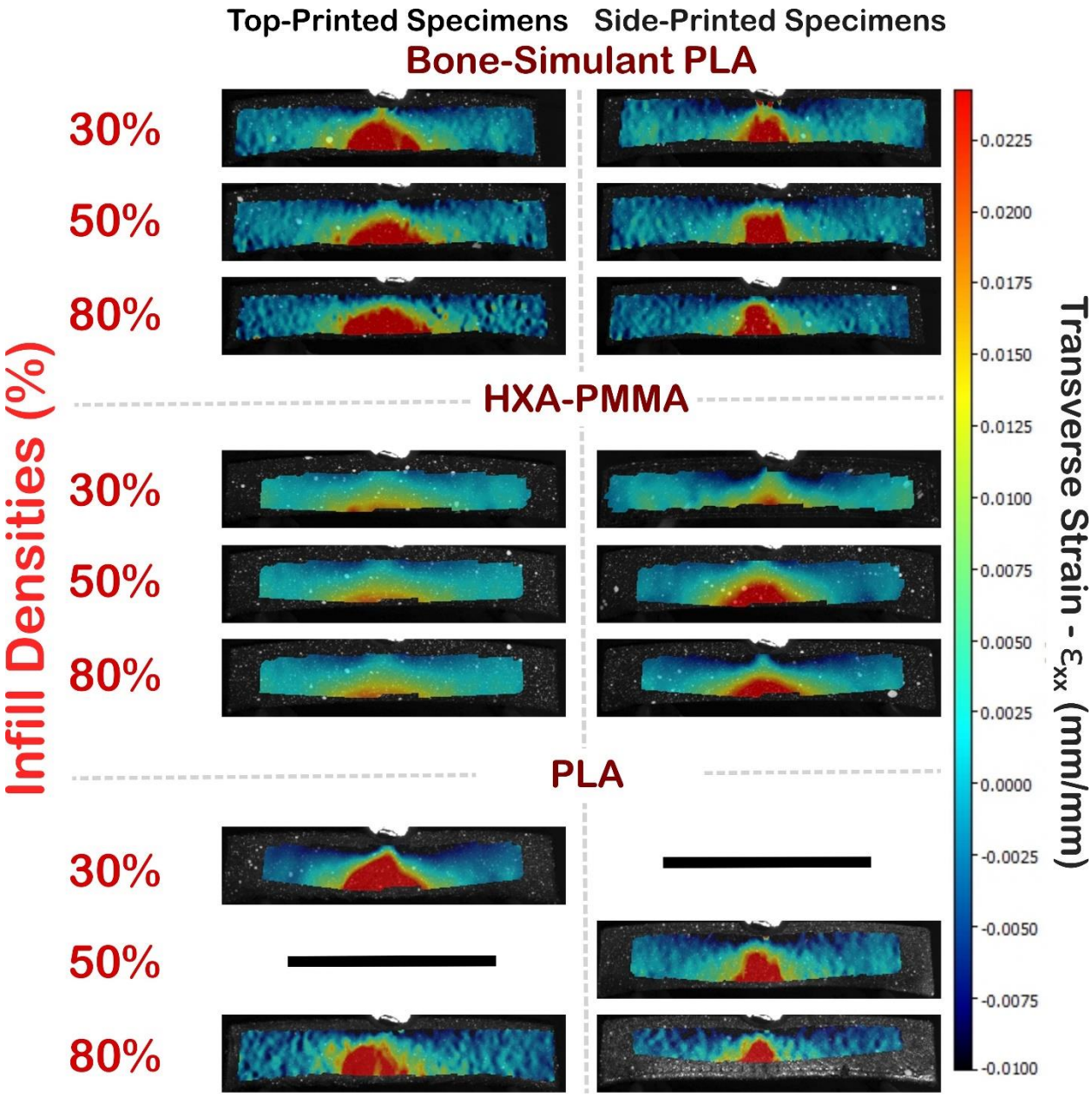


*Figure 4.11 — DIC: Crack Initiated Strain Field Behaviors of All Tested Simulants*

For all tested simulants in loading, initial peak stress was concentrated along the bottom apex of the specimens. Stresses concentrated at the bottom apex would continue to climb radially throughout the thickness of the samples and tangentially span to the width ends of the specimen. As loading continued, fracture opening began to form at the point of initial peak stress — the bottom apex of the sample — where the maximum recorded flexural strength occurred at the initial opening. Finally, the fracture would continue to propagate upwards through the sample's thickness,

correlating with the recorded creep regime of the stress-strain curve. Eventually, a complete fracture would be recorded, concluding the test sample run.

## 4.4 — Discussions

This research aims to provide a series of methods to characterize and select potential material candidates and manufacturing techniques to successfully create an artificial device that can accurately simulate the behavior of the human head under concussive impacts. This study repeated mechanical testing reported in previous studies involving the mechanical characterization of the human skull bone [5], [13], [46], [47], [81] using similarly behaving simulant materials. Additionally, simulant parameters were adjusted, and their effects on material performance and relative behavior were observed. Adjusted parameters aimed to recreate the structural characteristics of their native counterparts, such as the varying infill densities of additively manufactured simulant samples concerning the trabecular diploë regime of natural bone. Furthermore, a subsequent case study was developed to consider the influence of manufactured cortical tables on simulant structures and their respective material properties and flow characteristics. Observations of the defined testing results are categorized based on their respective methodologies below.

### *4.4.1 — Bone Simulant Characteristics from Three-Point Bending Tests*

The mechanical responses of the tested materials were assessed to observe their relative behavior compared to human cranial bone, as reported by Lee et al. and Ondruschka et al. [13], [47]. Other studies, such as by Zhai et al. [81], were also considered due to their incorporation of stress-strain curves of native skull bone in three-point bending tests. Furthermore, correlations between infill density, print orientation, and variations in printing methods concerning the mechanical performance of these specimens were assessed to ensure an optimal approach to developing a full-scale skull simulant through additive manufacturing. The selection of an optimal candidate is based on their relative performance compared to native specimens, their behavior in stress-strain and strain distributions, and added considerations for ease of additive manufacturing to ensure reliability and repeatability.

#### *4.4.1.1 — Flexural Performances Amongst Simulant Material Candidates*

4.4.1.1.1 — Case One: Shelled Simulant Material Performances

Observing Tables 4.5 and 4.6, the listed materials all fall within the standard deviations of either study regarding natural bone. However, all the selected optimal specimens perform well for one of the criteria while relatively lacking in others. Notable simulant performances include PLA and Bone-like PLA at 80% infill with the side-printed orientation. Considerations can also be made for PLA and Bone-like PLA at 50% infill with side-print orientation and HXA-PMMA at 50% and 80% infill with side-print orientation for their accurate representation of flexural strength. However, the stress-strain behavior of HXA-PMMA displays a drastically brittle response to loading, which may not represent the behavior of natural bone, considering the quasi-elasticity provided by the trabecular diploë region of cranial bone [44]–[46]. Additionally, recorded values regarding its flexural behavior yielded some inconsistencies across all parameters, and Figure 4.8 shows its wide variation across adjustments of infill density. Moreover, across Two-Way ANOVA analysis, HXA-PMMA displayed the largest influence of error in correlation, as seen in Tables 4.7 and 4.8. Despite its uses in biomedical applications and notable relative mean performance magnitudes, HXA-PMMA cannot be considered a sole artificial substitution for natural cranial bone in bulk mechanical properties.

Overall, distinct differences in performance were observed among the tested materials. For each given group of parameters, the general increase in material performance (moduli and strength) follows this order: HXA-PMMA, Bone-like PLA, and PLA (*Figures 4.6 to 4.9*). Material stress-strain behavior in bending follows the trend that all HXA-PMMA samples experience a brittle fracture, as displayed by their 'r'-shaped stress-strain trend, all Bone-like PLA samples experience a quasi-ductile deformation before fracture, while PLA samples are ductile when printed in the side orientation and brittle in the top orientation. For all materials, an increase in the observation of brittle fracture can be expected to be proportional to the increase in infill density. When comparing the stress-strain behaviors to native cortical bone, Zhai et al. comprehensively observed frontal lobe skull samples in flexion across quasi-static, intermediate, and high strain rates. It was observed that natural bone displayed a quasi-ductile failure mechanism akin to the PLA variant simulants among similar loading modes [79]. Comparing these performances to the simulants tested in this study, Bone-like PLA displayed the closest resemblance to these loading curves.

4.4.1.1.2 — Case Two: Exposed Cortical-Cancellous Simulant Material Performances

After establishing the performances of relevant material candidates as solid-printed structures by adjusting the print orientation and infill density, the second case extends the simulation of native cranial bone to include inner and outer cortical tables and an exposed cancellous region. The goal of this case study was to enhance the structure of these simulant candidates further to mimic the nature of native bone specimens, particularly in the context of extracting the frontal lobe for flexural mechanical characterization [13], [47], [81]. Cortical thickness ratios were maintained to ensure repeatability, according to Boruah et al. [46], with average total sample thicknesses and widths aligned with the native bone measurements in Lee et al. [47] and Ondruschka et al. [13]. Additionally, the thickness of the trabecular region was kept consistent with the values defined by Lee et al. [47] and Ondruschka et al. [13].

Characterizations using these printing methods identified overall reductions in modulus and strength across all materials and printing conditions, as shown in Figure 4.7 and Tables 4.5 and 4.6. Materials with higher infill densities, specifically those with 80% infill density, adhered more closely to reported skull bone values. However, all materials displayed moduli properties below those of native bone, contrary to previous case studies where some higher infill specimens exceeded native bone properties. Still, some simulants were successful in achieving modulus values within the deviations of natural bone. Reduced flexural strength values were advantageous, as most selected materials showed relative performance values within the deviations of native bone studies. Bone-variant PLA (80% infill, side-print orientation) and HXA-PMMA (80% infill, side-print orientation) showed the closest relative performances to native studies.

The reduction in properties could be attributed to changes in the stress-strain flow performance of the materials (*Figure 4.7*). In the second case study, all materials displayed a "toe-linear-creep" quasi-elastic regime similar to native bone. In contrast, the first case study showed a linear trend throughout the elastic portion of stress-strain until eventual creep and failure. Although the linear portion of the stress-strain curves was used to calculate material moduli, the presence of the toe regime could influence the materials' elasticity. The stress-strain behavior in the second case study followed the flow characteristics of native bone more closely, as observed by Zhai et al. [95]. Bone-variant PLA (80% infill, side-print orientation) provides the closest resemblance to quasi-

static flow curves. Elastic toe regions have also been noted in other uniaxial loading modes, such as compression [94].

The introduction of a considerable toe regime and the reduction in material properties between both case studies suggest the influence of the solid shell in the first case study and the exposed trabecular region in the second. The solid shell likely supported stress distribution substantially, increasing modulus and strength, while the exposed specimens in the second case study distributed stress strictly through the cortical and trabecular tables, reducing performance but yielding a biofidelic quasi-elastic behavior. The performance of the second case specimens underscores the importance of the cancellous region in bone, highlighting its dampening effects when native bone is loaded [13], [43], [47], [48], [80], [81]. Therefore, future characterization and manufacturing studies of artificial materials simulating osseous structures, especially skull bone, should consider these structures. Additionally, second-case specimens yielded properties closer to native bone at the highest infill density studied (80%). Histological, MRI, and Micro-CT microscopy investigations have shown average macroscale trabecular pore diameters of ~102 μm [95]–[97]. The artificial trabecular regions developed using the gyroid infill path had average diameters of ~669 μm, falling within the larger recorded pore thicknesses of native studies. Future studies may explore infill densities between 80–90% to achieve closer properties of simulant modulus to native bone.

#### *4.4.1.2 — Correlations of Infill Density and Print Orientation Regarding Flexural Performance*

It was observed that the top-print orientation resulted in a decrease in performance across the board. All materials—except for PLA in strength in both cases—experienced reductions in modulus and strength. This effect could be attributed to the anisotropic nature of additive manufacturing, where the printing direction relative to the direction of loading significantly influences the material performance of an additively manufactured object [86], [92]. This observation contrasts with the conclusions found in a similar test by Mantecón et al., where top-oriented samples for PLA displayed marginally greater performance values while flexural moduli remained consistent for both orientations [15]. This discrepancy could be due to the difference in printing parameters between the two studies. In the Mantecón et al. study, specimen thickness and print orientation were varied with a consistent infill density of 100%, whereas this study considered

changes in infill density and print orientation while maintaining consistent specimen thickness within deviation (*Table 4.2*). Additionally, the effect of printing orientation on the deposition of the infill pattern could influence the results, as the infill pattern is dictated by the direction of material deposition from the printer nozzle head (*Figure 4.2*). It is suggested that future studies consider the direction of material deposition if additive-manufactured infill density is a parameter in future cranial bone simulant characterization.

#### *4.4.1.3 — Simulant Failure Mechanisms from Digital Image Correlation (DIC) Observations*

A notable observation in this study is the analysis of fracture mechanics and failure mechanisms of the bone simulants compared to native skull bone (*Figures 4.10 and 4.11*). In the three-point bending tests, specimens consistently fractured in or around the apex of the sample curvature across all tested simulants. However, variations in fracture opening directions were observed depending on the material and print direction of the samples, with infill densities not affecting the variation of fracture directions. Variability in fracture direction was often associated with wider peak strain regimes, commonly correlated with samples exhibiting more brittle responses. The most notable sample set displaying this feature was the Hydroxyapatite-PMMA (HXA-PMMA) variations, which showed comparatively violent brittle responses in bending tests.

The fracture behavior of the materials was consistent with expectations for cranial fractures. In simulated recreations of flexural tests on cranial specimens, Wu et al. [80] observed similar fracture lines along the bottom apex of the mounted bending test specimens. It was further shown that fractures would occur between the interfacing layers of the bone's outer cortical and inner trabecular (diploë) regions. While second-case specimens were not investigated in DIC due to the inability to provide clear speckles for correlation, delamination between the interfacing inner and outer cortical tables and the trabecular regions was a commonly observed failure mechanism. Similar observations were noted in the first case-tested simulants, where outer shell filament-dense print layers often fractured from the inner infill layers after loading. These separations from interfacing layers were more common among reduced infill density and brittle samples (i.e., HXA-PMMA and top-printed specimens) and could indicate relatively weaker adhesion among layers in this regime.

Moreover, skull specimen flexural tests showed variations in the fracture direction of cranial fractures, often correlated with the pattern of trabecular pores in the tested diploë regions. This points to the consistency of fracture directions found in the simulant samples, where infill densities were altered, but pore sizes in the infill were consistent and followed a regular pattern, unlike the random assortment of trabecular pore sizes seen in actual skull bone [13], [47], [80], [81]. Advancements in anthropomorphic biofidelity should consider random pore and infill patterns, and this method should be explored in future studies.

#### *4.4.1.4 — Development of a Full-Scale Additive-Manufactured Biofidelic Skull Phantom*

This section outlines the creation of a life-sized skull phantom based on the methodologies defined in this study. The skull model was sourced from the National Institute of Health (NIH) 3D Model database (NIH 3D National Institute of Health; Bethesda, Maryland), which provided patient-specific MRI scans of the skull and brain. To ensure accuracy, the model's dimensions were adjusted according to the GHBMC M50 specifications [93]. Suture lines were designed to facilitate the incorporation of a brain phantom, effectively separating the skull calvarium from the rest of the skull. The skull was manufactured using the Bambu Carbon X1 printer with SimuBone Bone-like PLA at 80% infill, following the printing parameters detailed in Table 4.1.

*Table 4.13 — Skull Bone Simulant Measurements Compared to Native and GHBMC Skull Measurements*

| **Skull Phantom Characteristics** | |
|---|---|
| *Breadth (cm) [93]* | 15.0 |
| *Length (cm) [93]* | 19.5 |
| *Circumference (cm) [93]* | 56 |
| *Skull Mass (g) [with SimuBone$^{TM}$ PLA]* | 1003.6 |
| *Density (g/cc) [with SimuBone$^{TM}$ PLA]* | 1.34 |
| **Native Skull Characteristics (GHBMC M50) [93]** | |
| *Average Head Mass (Includes Brain, CSF, and Soft Tissues) (g)* | 4400 |
| *Average Density (g/cc) [106]* | 2.1 (Cortical), 1 (Diploë) |

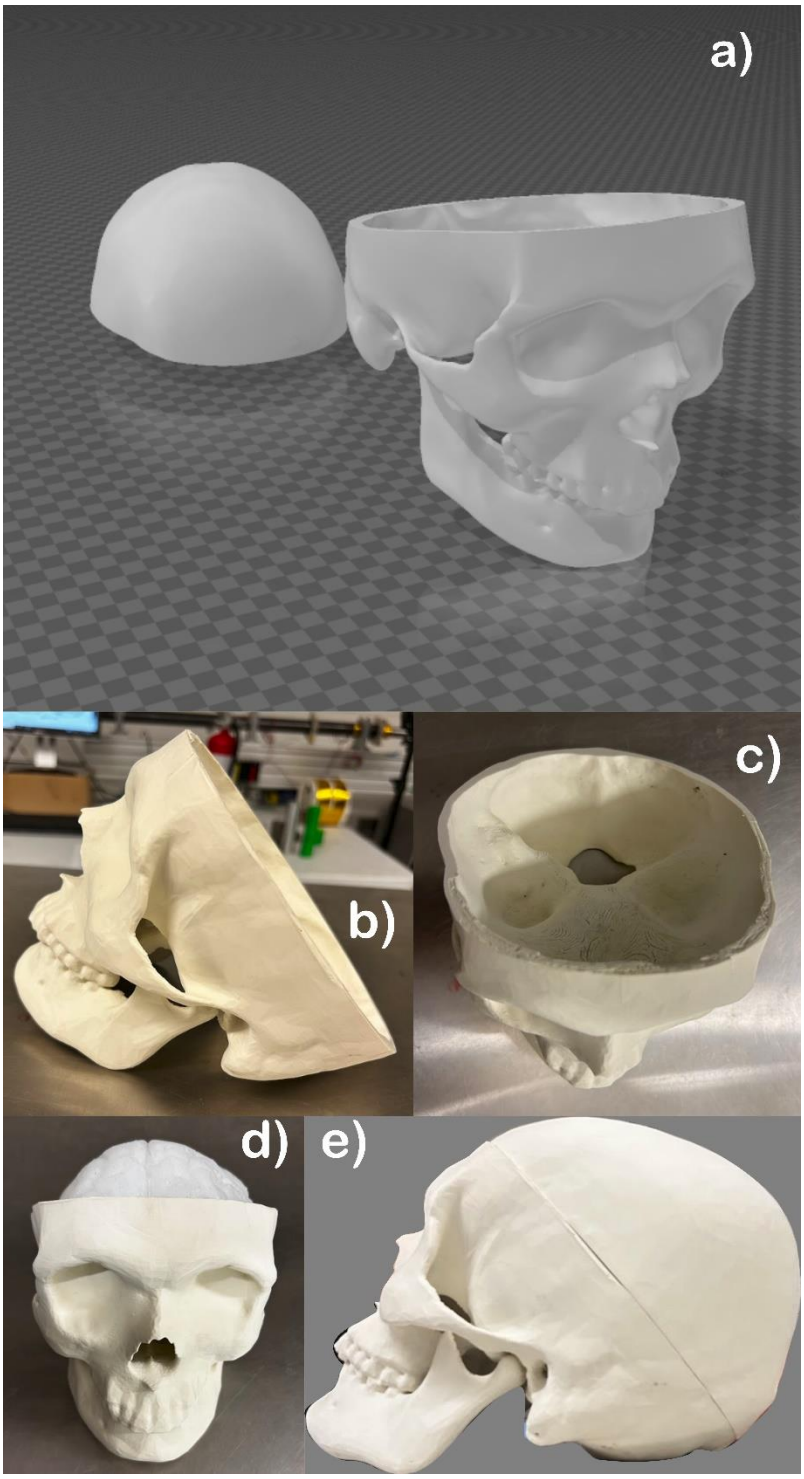


*Figure 4.12 — Developed Skull Phantom: a) STL File of Skull Model, b) Sagittal Plane of Skull Model, c) Top View Skull Model with Cranial Cavity, d) Coupled Biofidelic Brain and Skull Model, e) Encased Head Model with Skull Cap*

## 4.5 — Future Works and Conclusions

This study aimed to identify synthetic materials that mimic critical structures in the human head, particularly the skull. Our findings suggest that PLA, along with its bone-simulating variant, closely resembles the native properties of these structures. Adjustments in print orientation and infill density further enhance the elasticity properties, with increased infill density and tangential (side) print orientation showing improvements in flexural modulus and strength. Considering the established flexural performances of skull bone in strength, modulus, and loading curves, the bone-simulant variant of PLA exhibited optimal results when printed at a side orientation with at least 50% infill density, correlating with the minimum trabecular pore densities found in the skull bone [13], [46], [47], [80], [81].

Future advancements could improve the biofidelity of simulant materials through enhanced material selection, manufacturing methods, and composition adjustments. Composite materials tailored to simulate specific regions of cortical and diploë layers in human bone could be explored, along with testing composite materials in bending to comprehensively simulate skull bone behavior [50]. Utilizing composite materials through additive manufacturing warrants attention, with careful considerations in material adhesion parameters and the use of capable FFF printers, such as dual-extrusion models. Exploring alternative additive manufacturing techniques, such as STL resin printing, and incorporating bone-like additives like hydroxyapatite, can also be intriguing areas for study, as these methods have been applied in other forms of three-dimensional printing for biomedical engineering [11], [14], [18], [98].

Another parameter to consider in additive-manufactured biofidelic bone simulants is the adjustment of outer wall thickness along with infill densities. Further correlations may be found in adjusting flexural strength and modulus while maintaining an infill density that more closely resembles the trabecular bone volumes in native structures [13], [46], [47]. In the experiments conducted in the second case study, inner and outer cortical thickness, their cortical thickness fraction, and trabecular region thickness remained consistent to ensure repeatable parameters. While these thicknesses aimed to reflect mean measurements found in native bone, they vary depending on the region and could result in variations in mechanical properties found in literature [13], [43], [46], [47], [49]. Lee et al. [47] and Ondruschka et al. [13] have observed statistically

significant material properties correlating with variations in total material thicknesses. Consequently, the design of the infill pattern can be further investigated in future studies, as this study considered a homogeneous pattern that does not fully represent the random porous pattern of trabecular bone [46], [47]. Despite this, similar behaviors were observed compared to their native counterparts.

A limitation in this study to consider is the method of comparison to native critical human head structures, as the widely reported properties of human skull samples in literature were observed and compared [13], [47]. This is partly due to challenges in procuring and sampling structures for characterization, involving considerations and regulations towards sourcing, storage, time, and biosafety. Instead, this study recreated predetermined experiments involving testing sampling methodology and equipment while adhering to material standards to ensure repeatability. Great care was taken to ensure experiments were as true to their initial methodologies as possible, yielding similar and notable results compared to related tests.

This study finds additional limitation in the methodology of simulant constructions representing the $50^{th}$ Percentile Male Skull. Other representative models, such as the $5^{th}$ Percentile Female exist [93], and characterizations of the respective simulants can introduce further comparisons and significance towards their relative performance to female skulls. Studies have observed characteristic comparisons between native male and female skulls, though minimal statistical significance was found between the influence of sex on material performances [99], [100]. Despite this, the difference in both skull models display geometrical and structural differences [93], [100], which have shown significant statistical influence regarding material property on the human skull [13], [43], [47], [99], [100]. Analysis of characteristics comparing simulants representing both models could provide an avenue for distinguishing traumatic impact thresholds between sexes, and it is highly recommended that these aspects be considered in expanded study.

Future iterations of this study should expand upon the simulation of critical structures within the human head, such as the soft periosteum tissues surrounding the skull bone and the meningeal complex of soft tissue regions between the skull and brain in the cranial cavity, composed of the dura mater and the pia-arachnoid complex. Concussive symptoms have been shown to correlate with damage to these regions [101]–[105]. Studies characterizing human bone samples in three-

point bending have shown that the presence of soft tissues surrounding the bare bone improves the moduli and strength performances of the skull samples significantly [13], [47]. Zwirner et al. have conducted tests of human dura mater in tension to determine elastic modulus and tensile strength [104]. While native characterizations have been made, few to no studies have proposed simulant materials for these critical regions of the skull-brain [51], [52].

The benefit of FFF lies in its ease of reproduction and accessibility to commonly available materials. This study aimed to characterize the performances of these accessible materials and optimize their production parameters for biofidelity relative to the human skull. Further considerations under this method highlight the potential to contribute to a more accurate and effective simulation of human bone and anatomical head structures. This context allows for accurate representation of head impact kinematics and a better understanding of intracranial components and kinematic signatures in concussive impact events.

# *Chapter 5 — Conclusions, Limitations, and Future Work*

## 5.1 — Conclusions and Limitations

This thesis aimed to develop biofidelic head models—specifically the skull and brain—by selecting simulant materials that replicate the mechanical, geometrical, and structural properties of native human tissues. The literature review highlighted inconsistencies in the kinematic results produced by current Anthropomorphic Test Devices (ATDs) and their limited ability to validate Finite Element Models (FEMs). A key finding was the need for head models with enhanced anthropomorphic accuracy to improve FEM validation.

Simulants for the brain require further research, particularly in representing mechanical responses to oscillating strains. Skull simulants, though promising, need better representation of the cortical-cancellous structure to capture the native bone's quasi-elastic response. The lack of studies on meningeal properties was also noted, underscoring gaps in the biomechanical accuracy of current phantom models.

Chapter 3 examined brain simulants, revealing that while no material perfectly mimics all brain characteristics, Shore 00-10 Silicone showed promise, especially for concussive impacts. However, limitations in testing equipment restricted full replication of brain behavior at intermediate strain rates. The Shore 00-10 Silicone emerged as the most viable candidate for manufacturing brain phantoms, although adjustments in crosslinking concentration could improve biofidelity for specific impacts.

Chapter 4 focused on the mechanical simulation of the human skull using additive-manufactured specimens. SimuBone$^{TM}$, the bone-variant PLA at 80% infill density best replicated the skull's flexural properties. However, the trabecular bone structure's role in dampening was highlighted, with suggestions for refining infill densities and outer wall thickness to improve simulation accuracy. The study also identified the need for future exploration of composite materials and advanced additive manufacturing techniques to enhance skull biofidelity.

Overall, while challenges remain in fully replicating brain and skull behaviors, this thesis made significant progress in constructing biofidelic phantoms. Future work should focus on improving material properties, testing methods, and manufacturing techniques to create more accurate models for head injury biomechanics.

## 5.2 — Future Works

This thesis aimed to address key research gaps by developing biofidelic phantoms for critical components of the human head, such as the skull and brain, with a focus on improving current ATD head forms. However, several areas remain for further research, which can be explored in future work.

A notable area for future exploration is the representation of the meninges as a biofidelic phantom. While this research prioritized the skull and brain, previous studies have modeled the pia-arachnoid complex (PIA) and dura mater using geometric representations, such as nonwoven polyester sheets bonded to silicone [1], [2] and FFF-printed thermoplastic polyurethane (TPU) [3]. However, further investigation is needed to develop material simulants for these structures, similar to the methods used in this thesis. Other biofidelic aspects of the head, such as the scalp and CSF, call for further investigation in their phantom representations. Such aspects have been considered and properly characterized in previous iterations of biofidelic head models [1], [2].

The biofidelity of both brain and skull simulants can also be enhanced. The study in Chapter 3 treated brain tissue as a homogeneous structure, but literature highlights the importance of regional dependencies, such as differences between grey and white matter and various functional regions (See Section 2.4.1.1). Future work could involve creating brain phantoms with multiple elastomer compositions to represent these regions, necessitating further analysis of their mechanical characteristics, either from existing literature or by procuring native brain specimens.

In Chapter 4, skull simulant biofidelity was improved by introducing cortical-cancellous tables in AM material specimens. The design of the trabecular regions aimed to mimic porous structures but maintained a homogeneous infill pattern. Future research could explore heterogeneous trabecular infill patterns to better replicate native bone structures and improve failure mechanisms. Additionally, varying cortical thicknesses, which significantly impact material properties in native

skulls (See Section 2.4.2.1.3), were not considered in this study. Future studies should investigate how these thickness variations affect the mechanical behavior of skull simulants.

The current full-scale phantoms were designed to represent the Global Human Body Consortium's Male 50th Percentile Model. Expanding this research to include other models, such as the 5th Percentile Female, could provide insights into how geometric and structural differences influence material properties and impact thresholds. While studies have shown minimal statistical significance in material performance differences between male and female skulls, the geometric and structural differences suggest further investigation is warranted.

Continued work on this biofidelic head model should aim to embed sensors like accelerometers and gyroscopes into these components for laboratory-based head impact testing. The ultimate goal is to compare the kinematic signatures of this model with those of common ATD head forms when validated in an FEM model.

In conclusion, this thesis explored methods to enhance ATD head forms using accessible materials and manufacturing techniques. The research successfully identified material candidates for the skull and brain that can be constructed into full-sized phantoms, with the potential to improve the understanding of concussion mechanisms and the role of material properties in native structures under injurious loading conditions in head impact scenarios.

# *Bibliography*

## Chapter 1 References

[1] W. Torregrossa et al., ‘Behavioral and Psychiatric Symptoms in Patients with Severe Traumatic Brain Injury: A Comprehensive Overview’, *Biomedicines*, vol. 11, no. 5, p. 1449, May 2023 [Online]. Available: 10.3390/biomedicines11051449.

[2] J. K. Yue and H. Deng, ‘Traumatic Brain Injury: Contemporary Challenges and the Path to Progress’, *Journal of Clinical Medicine*, vol. 12, no. 9, p. 3283, Jan. 2023 [Online]. Available: 10.3390/jcm12093283.

[3] G. Critchley et al., ‘Epidemiology of Head Injury’, in *Traumatic Brain Injury*, 2nd ed., P. C. Whitfield, J. Welbourne, E. Thomas, F. Summers, M. Whyte, and P. J. Hutchinson, Eds. Cambridge University Press, 2020, pp. 1–11[Online]. Availablehttps://www.cambridge.org/core/product/identifier/9781108355247%23CN-bp-1/type/book_part[Accessed: 17April2024].

[4] S. Uysal, ‘Traumatic Brain Injury’, in *Functional Neuroanatomy and Clinical Neuroscience: Foundations for Understanding Disorders of Cognition and Behavior*, S. Uysal, Ed. Oxford University Press, 2023, p. 0[Online]. Availablehttps://doi.org/10.1093/oso/9780190943608.003.0020[Accessed: 17April2024].

[5] C. Wei et al., ‘Therapy of traumatic brain injury by modern agents and traditional Chinese medicine’, *Chinese Medicine*, vol. 18, no. 1, p. 25, Mar. 2023 [Online]. Available: 10.1186/s13020-023-00731-x.

[6] D. B. MacManus and M. Ghajari, ‘Material properties of human brain tissue suitable for modelling traumatic brain injury’, *Brain Multiphysics*, vol. 3, p. 100059, 2022 [Online]. Available: 10.1016/j.brain.2022.100059.

[7] L. White et al., ‘Scoring Systems for Trauma and Head Injury’, in *Traumatic Brain Injury*, 2nd ed., P. C. Whitfield, J. Welbourne, E. Thomas, F. Summers, M. Whyte, and P. J. Hutchinson, Eds. Cambridge University Press, 2020, pp. 57–64[Online].

Availablehttps://www.cambridge.org/core/product/identifier/9781108355247%23CN-bp-6/type/book_part[Accessed: 17April2024].

[8] T. B. Hoshizaki et al., ‘The development of a threshold curve for the understanding of concussion in sport’, *Trauma*, vol. 19, no. 3, pp. 196–206, Jul. 2017 [Online]. Available: 10.1177/1460408616676503.

[9] A. Post and T. Blaine Hoshizaki, ‘Rotational Acceleration, Brain Tissue Strain, and the Relationship to Concussion’, *Journal of Biomechanical Engineering*, vol. 137, no. 3, p. 030801, Mar. 2015 [Online]. Available: 10.1115/1.4028983.

[10] C. As et al., ‘Self-reported concussions in Canada: A cross-sectional study’, *Health reports*, vol. 34, no. 6, Jun. 2023[Online]. Availablehttps://pubmed.ncbi.nlm.nih.gov/37342962/[Accessed: 12August2024].

[11] K. L. O’Connor et al., ‘Head-Impact–Measurement Devices: A Systematic Review’, *Journal of Athletic Training*, vol. 52, no. 3, pp. 206–227, Mar. 2017 [Online]. Available: 10.4085/1062-6050.52.2.05.

[12] T. Wang et al., ‘Head Impact Sensor Triggering Bias Introduced by Linear Acceleration Thresholding’, *Ann Biomed Eng*, vol. 49, no. 12, pp. 3189–3199, Dec. 2021 [Online]. Available: 10.1007/s10439-021-02868-y.

[13] J. Newman et al., ‘A NEW BIOMECHANICAL ASSESSMENT OF MILD TRAUMATIC BRAIN INJURY PART 1 - METHODOLOGY’, 1999.

[14] D. Koncan et al., ‘Comparison of two anthropomorphic test devices using brain motion’, *Proceedings of the Institution of Mechanical Engineers, Part P: Journal of Sports Engineering and Technology*, vol. 232, no. 4, pp. 305–314, Dec. 2018 [Online]. Available: 10.1177/1754337117751741.

[15] B. R. Cobb et al., ‘Comparative analysis of helmeted impact response of Hybrid III and National Operating Committee on Standards for Athletic Equipment headforms’, *Proceedings of the Institution of Mechanical Engineers, Part P: Journal of Sports Engineering and Technology*, vol. 230, no. 1, pp. 50–60, Mar. 2016 [Online]. Available: 10.1177/1754337115599133.

[16] D. M. Haid, ‘Towards concussion prevention in ice hockey: mechanical metamaterial liners and helmet assessment’, PhD, Sheffield Hallam University, 2024[Online]. Availablehttps://shura.shu.ac.uk/33603/[Accessed: 14May2024].

[17] E. Takhounts et al., ‘Kinematic Rotational Brain Injury Criterion (BRIC)’, 2011[Online]. Availablehttps://www.semanticscholar.org/paper/Kinematic-Rotational-Brain-Injury-Criterion-(BRIC)-Takhounts-Hasija/0691a97a56a2197f2d3fbaf5f5cb4ba786349e03[Accessed: 14May2024].

[18] E. G. Takhounts et al., ‘Development of Brain Injury Criteria (BrIC)’, presented at the 57th Stapp Car Crash Conference, 2013, pp. 2013-22–0010[Online]. Availablehttps://www.sae.org/content/2013-22-0010/[Accessed: 8July2023].

[19] M. Franklyn and P. V. S. Lee, Eds., *Military Injury Biomechanics: The Cause and Prevention of Impact Injuries*, 1st ed. Boca Raton: CRC Press, 2017 [Online]. Available: 10.4324/9781315151731.

[20] T. Seeburrun et al., ‘Assessment of brain response in operators subject to recoil force from firing long-range rifles’, *Front. Bioeng. Biotechnol.*, vol. 12, Feb. 2024[Online]. Availabletse[Accessed: 11August2024].

[21] K. M. Tse et al., ‘The Skull and Brain: Computer Models for the Head and Its Protection’, in *Military Injury Biomechanics: The Cause and Prevention of Impact Injuries*, 1st ed., 2017, pp. 175–220 [Online]. Available: 10.4324/9781315151731-10.

[22] M. Navarro-Lozoya et al., ‘Development of phantom material that resembles compression properties of human brain tissue for training models’, *Materialia*, vol. 8, p. 100438, Dec. 2019 [Online]. Available: 10.1016/j.mtla.2019.100438.

[23] D. Singh et al., ‘Comparison of porcine brain mechanical properties to potential tissue simulant materials in quasi-static and sinusoidal compression’, *Journal of Biomechanics*, vol. 92, pp. 84–91, Jul. 2019 [Online]. Available: 10.1016/j.jbiomech.2019.05.033.

[24] L. Falland-Cheung et al., ‘Elastic behavior of brain simulants in comparison to porcine brain at different loading velocities’, *Journal of the Mechanical Behavior of Biomedical Materials*, vol. 77, pp. 609–615, Jan. 2018 [Online]. Available: 10.1016/j.jmbbm.2017.10.026.

[25] A. E. Forte et al., ‘On the characterization of the heterogeneous mechanical response of human brain tissue’, *Biomech Model Mechanobiol*, vol. 16, no. 3, pp. 907–920, Jun. 2017 [Online]. Available: 10.1007/s10237-016-0860-8.

[26] W. Li et al., ‘Dynamic mechanical characterization and viscoelastic modeling of bovine brain tissue’, *Journal of the Mechanical Behavior of Biomedical Materials*, vol. 114, p. 104204, Feb. 2021 [Online]. Available: 10.1016/j.jmbbm.2020.104204.

[27] W. Li et al., ‘Frequency dependent viscoelastic properties of porcine brain tissue’, *Journal of the Mechanical Behavior of Biomedical Materials*, vol. 102, p. 103460, Feb. 2020 [Online]. Available: 10.1016/j.jmbbm.2019.103460.

[28] S. Nicolle et al., ‘Shear Properties of Brain Tissue over a Frequency Range Relevant for Automotive Impact Situations: New Experimental Results’, *Stapp Car Crash J*, vol. 48, pp. 239–258, Nov. 2004 [Online]. Available: 10.4271/2004-22-0011.

[29] L. Bilston et al., ‘Large strain behaviour of brain tissue in shear: Some experimental data and differential constitutive model’, *Biorheology*, vol. 38, pp. 335–45, Feb. 2001.

[30] K. Adanty et al., ‘The effect of morphometric and geometric indices of the human calvarium on mechanical response’, *Clinical Biomechanics*, vol. 107, p. 106012, Jul. 2023 [Online]. Available: 10.1016/j.clinbiomech.2023.106012.

[31] K. Adanty et al., ‘The Mechanical Characterization and Comparison of Male and Female Calvaria Under Four-Point Bending Impacts’, *Journal of Biomechanical Engineering*, vol. 145, no. 5, p. 051009, May 2023 [Online]. Available: 10.1115/1.4056459.

[32] Q. Wu et al., ‘Theoretical prediction model and failure mechanism map of human skull porous structures with quasi-static bending performance’, *International Journal of Mechanical Sciences*, vol. 200, p. 106431, Jun. 2021 [Online]. Available: 10.1016/j.ijmecsci.2021.106431.

[33] X. Zhai et al., ‘The effects of loading-direction and strain-rate on the mechanical behaviors of human frontal skull bone’, *Journal of the Mechanical Behavior of Biomedical Materials*, vol. 103, p. 103597, Mar. 2020 [Online]. Available: 10.1016/j.jmbbm.2019.103597.

[34] B. Ondruschka et al., ‘A biomechanical comparison between human calvarial bone and a skull simulant considering the role of attached periosteum and dura mater’, *Int J Legal Med*, vol. 133, no. 5, pp. 1603–1610, Sep. 2019 [Online]. Available: 10.1007/s00414-019-02102-4.

[35] J. H. C. Lee et al., ‘An Investigation on the Correlation between the Mechanical Properties of Human Skull Bone, Its Geometry, Microarchitectural Properties, and Water Content’, *Journal of Healthcare Engineering*, vol. 2019, pp. 1–8, May 2019 [Online]. Available: 10.1155/2019/6515797.

## Chapter 2 References

[1] G. Critchley et al., ‘Epidemiology of Head Injury’, in *Traumatic Brain Injury*, 2nd ed., P. C. Whitfield, J. Welbourne, E. Thomas, F. Summers, M. Whyte, and P. J. Hutchinson, Eds. Cambridge University Press, 2020, pp. 1–11[Online]. Availablehttps://www.cambridge.org/core/product/identifier/9781108355247%23CN-bp-1/type/book_part[Accessed: 17April2024].

[2] T. B. Hoshizaki et al., ‘The development of a threshold curve for the understanding of concussion in sport’, *Trauma*, vol. 19, no. 3, pp. 196–206, Jul. 2017 [Online]. Available: 10.1177/1460408616676503.

[3] A. Post and T. Blaine Hoshizaki, ‘Rotational Acceleration, Brain Tissue Strain, and the Relationship to Concussion’, *Journal of Biomechanical Engineering*, vol. 137, no. 3, p. 030801, Mar. 2015 [Online]. Available: 10.1115/1.4028983.

[4] J. Faber et al., ‘Tissue-Scale Biomechanical Testing of Brain Tissue for the Calibration of Nonlinear Material Models’, *Current Protocols*, vol. 2, no. 4, Apr. 2022[Online]. Availablehttps://onlinelibrary.wiley.com/doi/10.1002/cpz1.381[Accessed: 19May2023].

[5] K. L. O’Connor et al., ‘Head-Impact–Measurement Devices: A Systematic Review’, *Journal of Athletic Training*, vol. 52, no. 3, pp. 206–227, Mar. 2017 [Online]. Available: 10.4085/1062-6050.52.2.05.

[6] L. White et al., ‘Scoring Systems for Trauma and Head Injury’, in *Traumatic Brain Injury*, 2nd ed., P. C. Whitfield, J. Welbourne, E. Thomas, F. Summers, M. Whyte, and P. J. Hutchinson, Eds. Cambridge University Press, 2020, pp. 57–64[Online].

Availablehttps://www.cambridge.org/core/product/identifier/9781108355247%23CN-bp-6/type/book_part[Accessed: 17April2024].

[7] C. E. Gaudet, ‘Immediate Post-Concussion and Cognitive Testing (ImPACT): Effects of Data Integration Strategies on Classification Accuracy’, *Journal of Head Trauma Rehabilitation*, vol. 37, no. 5, pp. E319–E326, Sep. 2022 [Online]. Available: 10.1097/HTR.0000000000000740.

[8] K. Bian and H. Mao, ‘Mechanisms and variances of rotation-induced brain injury: a parametric investigation between head kinematics and brain strain’, *Biomech Model Mechanobiol*, vol. 19, no. 6, pp. 2323–2341, Dec. 2020 [Online]. Available: 10.1007/s10237-020-01341-4.

[9] Y. Bouattour et al., ‘A Minireview on Brain Models Simulating Geometrical, Physical, and Biochemical Properties of the Human Brain’, *Front. Bioeng. Biotechnol.*, vol. 10, p. 818201, Mar. 2022 [Online]. Available: 10.3389/fbioe.2022.818201.

[10] S. Budday et al., ‘Fifty Shades of Brain: A Review on the Mechanical Testing and Modeling of Brain Tissue’, *Arch Computat Methods Eng*, vol. 27, no. 4, pp. 1187–1230, Sep. 2020 [Online]. Available: 10.1007/s11831-019-09352-w.

[11] N. Petrone et al., ‘Feasibility of using a novel instrumented human head surrogate to measure helmet, head and brain kinematics and intracranial pressure during multidirectional impact tests’, *Journal of Science and Medicine in Sport*, vol. 22, pp. S78–S84, Aug. 2019 [Online]. Available: 10.1016/j.jsams.2019.05.015.

[12] N. Petrone et al., ‘A Novel Instrumented Human Head Surrogate for the Impact Evaluation of Helmets’, in *The 12th Conference of the International Sports Engineering Association*, 2018, p. 269[Online]. Availablehttps://www.mdpi.com/2504-3900/2/6/269[Accessed: 5March2023].

[13] K. Laksari et al., ‘Resonance of human brain under head acceleration’, *J. R. Soc. Interface.*, vol. 12, no. 108, p. 20150331, Jul. 2015 [Online]. Available: 10.1098/rsif.2015.0331.

[14] J. G. Beckwith et al., ‘Estimated Brain Tissue Response Following Impacts Associated With and Without Diagnosed Concussion’, *Ann Biomed Eng*, vol. 46, no. 6, pp. 819–830, Jun. 2018 [Online]. Available: 10.1007/s10439-018-1999-5.

[15] B. S. Elkin et al., ‘Brain tissue strains vary with head impact location: A possible explanation for increased concussion risk in struck versus striking football players’, *Clinical*

*Biomechanics*, vol. 64, pp. 49–57, Apr. 2019 [Online]. Available: 10.1016/j.clinbiomech.2018.03.021.

[16] T. Wang et al., 'Head Impact Sensor Triggering Bias Introduced by Linear Acceleration Thresholding', *Ann Biomed Eng*, vol. 49, no. 12, pp. 3189–3199, Dec. 2021 [Online]. Available: 10.1007/s10439-021-02868-y.

[17] D. Koncan et al., 'Comparison of two anthropomorphic test devices using brain motion', *Proceedings of the Institution of Mechanical Engineers, Part P: Journal of Sports Engineering and Technology*, vol. 232, no. 4, pp. 305–314, Dec. 2018 [Online]. Available: 10.1177/1754337117751741.

[18] J. Newman et al., 'A NEW BIOMECHANICAL ASSESSMENT OF MILD TRAUMATIC BRAIN INJURY PART 1 - METHODOLOGY', 1999.

[19] B. R. Cobb et al., 'Comparative analysis of helmeted impact response of Hybrid III and National Operating Committee on Standards for Athletic Equipment headforms', *Proceedings of the Institution of Mechanical Engineers, Part P: Journal of Sports Engineering and Technology*, vol. 230, no. 1, pp. 50–60, Mar. 2016 [Online]. Available: 10.1177/1754337115599133.

[20] D. M. Haid, 'Towards concussion prevention in ice hockey: mechanical metamaterial liners and helmet assessment', PhD, Sheffield Hallam University, 2024[Online]. Availablehttps://shura.shu.ac.uk/33603/[Accessed: 14May2024].

[21] A. MacAlister and V. Tech, 'Surrogate Head Forms for the Evaluation of Head Injury Risk', 2013.

[22] E. Kennedy et al., 'The Development and Validation of a Biofidelic Synthetic Eye for the Facial and Ocular Countermeasure Safety (Focus) Headform', Sep. 2007.

[23] M. Kendall et al., 'Comparison between Hybrid III and Hodgson–WSU headforms by linear and angular dynamic impact response', *Proceedings of the Institution of Mechanical Engineers, Part P: Journal of Sports Engineering and Technology*, vol. 226, no. 3–4, pp. 260–265, 2012 [Online]. Available: 10.1177/1754337112436901.

[24] E. Takhounts et al., 'Kinematic Rotational Brain Injury Criterion (BRIC)', 2011[Online]. Availablehttps://www.semanticscholar.org/paper/Kinematic-Rotational-Brain-Injury-Criterion-

(BRIC)-Takhounts-Hasija/0691a97a56a2197f2d3fbaf5f5cb4ba786349e03[Accessed: 14May2024].

[25] E. G. Takhounts et al., ‘Development of Brain Injury Criteria (BrIC)’, presented at the 57th Stapp Car Crash Conference, 2013, pp. 2013-22–0010[Online]. Availablehttps://www.sae.org/content/2013-22-0010/[Accessed: 8July2023].

[26] F. Wang et al., ‘Evaluation of Head Injury Criteria for Injury Prediction Effectiveness: Computational Reconstruction of Real-World Vulnerable Road User Impact Accidents’, *Front. Bioeng. Biotechnol.*, vol. 9, p. 677982, Jun. 2021 [Online]. Available: 10.3389/fbioe.2021.677982.

[27] K. Sano et al., ‘Correlative studies of dynamics and pathology in whip-lash and head injuries’, *Scand J Rehabil Med*, vol. 4, no. 2, pp. 47–54, 1972.

[28] M. Franklyn and P. V. S. Lee, Eds., *Military Injury Biomechanics: The Cause and Prevention of Impact Injuries*, 1st ed. Boca Raton: CRC Press, 2017 [Online]. Available: 10.4324/9781315151731.

[29] T. Seeburrun et al., ‘Assessment of brain response in operators subject to recoil force from firing long-range rifles’, *Front. Bioeng. Biotechnol.*, vol. 12, Feb. 2024[Online]. Availabletse[Accessed: 11August2024].

[30] K. M. Tse et al., ‘The Skull and Brain: Computer Models for the Head and Its Protection’, in *Military Injury Biomechanics: The Cause and Prevention of Impact Injuries*, 1st ed., 2017, pp. 175–220 [Online]. Available: 10.4324/9781315151731-10.

[31] F. S. Gayzik et al., ‘Development of a Full Body CAD Dataset for Computational Modeling: A Multi-modality Approach’, *Ann Biomed Eng*, vol. 39, no. 10, pp. 2568–2583, Oct. 2011 [Online]. Available: 10.1007/s10439-011-0359-5.

[32] E. G. Takhounts et al., ‘On the Development of the SIMon Finite Element Head Model’, *Stapp Car Crash Journal*, vol. 47, pp. 107–133, Oct. 2003.

[33] D. B. MacManus and M. Ghajari, ‘Material properties of human brain tissue suitable for modelling traumatic brain injury’, *Brain Multiphysics*, vol. 3, p. 100059, 2022 [Online]. Available: 10.1016/j.brain.2022.100059.

[34] M. Hosseini-Farid et al., ‘The Strain Rates in the Brain, Brainstem, Dura, and Skull under Dynamic Loadings’, *MCA*, vol. 25, no. 2, p. 21, Apr. 2020 [Online]. Available: 10.3390/mca25020021.

[35] M. C. Dewan et al., ‘Estimating the global incidence of traumatic brain injury’, *Journal of Neurosurgery*, vol. 130, no. 4, pp. 1080–1097, Apr. 2019 [Online]. Available: 10.3171/2017.10.JNS17352.

[36] A. E. Forte et al., ‘A composite hydrogel for brain tissue phantoms’, *Materials & Design*, vol. 112, pp. 227–238, Dec. 2016 [Online]. Available: 10.1016/j.matdes.2016.09.063.

[37] A. Wermer et al., ‘Materials Characterization of Cranial Simulants for Blast-Induced Traumatic Brain Injury’, *Military Medicine*, vol. 185, no. Supplement_1, pp. 205–213, Jan. 2020 [Online]. Available: 10.1093/milmed/usz228.

[38] Y. Wang et al., ‘Development of a Photo-Crosslinking, Biodegradable GelMA/PEGDA Hydrogel for Guided Bone Regeneration Materials’, *Materials*, vol. 11, no. 8, p. 1345, Aug. 2018 [Online]. Available: 10.3390/ma11081345.

[39] K. Yue et al., ‘Synthesis, properties, and biomedical applications of gelatin methacryloyl (GelMA) hydrogels’, *Biomaterials*, vol. 73, pp. 254–271, Dec. 2015 [Online]. Available: 10.1016/j.biomaterials.2015.08.045.

[40] A. Tejo-Otero et al., ‘Soft-Tissue-Mimicking Using Hydrogels for the Development of Phantoms’, *Gels*, vol. 8, no. 1, p. 40, Jan. 2022 [Online]. Available: 10.3390/gels8010040.

[41] T. Distler et al., ‘Alginate-based hydrogels show the same complex mechanical behavior as brain tissue’, *Journal of the Mechanical Behavior of Biomedical Materials*, vol. 111, p. 103979, Nov. 2020 [Online]. Available: 10.1016/j.jmbbm.2020.103979.

[42] D. Singh et al., ‘Comparison of porcine brain mechanical properties to potential tissue simulant materials in quasi-static and sinusoidal compression’, *Journal of Biomechanics*, vol. 92, pp. 84–91, Jul. 2019 [Online]. Available: 10.1016/j.jbiomech.2019.05.033.

[43] M. Navarro-Lozoya et al., ‘Development of phantom material that resembles compression properties of human brain tissue for training models’, *Materialia*, vol. 8, p. 100438, Dec. 2019 [Online]. Available: 10.1016/j.mtla.2019.100438.

[44] L. Falland-Cheung et al., ‘Elastic behavior of brain simulants in comparison to porcine brain at different loading velocities’, *Journal of the Mechanical Behavior of Biomedical Materials*, vol. 77, pp. 609–615, Jan. 2018 [Online]. Available: 10.1016/j.jmbbm.2017.10.026.

[45] A. Chanda et al., ‘Biofidelic human brain tissue surrogates’, *Mechanics of Advanced Materials and Structures*, vol. 25, no. 15–16, pp. 1335–1341, Dec. 2018 [Online]. Available: 10.1080/15376494.2016.1143749.

[46] A. E. Forte et al., ‘On the characterization of the heterogeneous mechanical response of human brain tissue’, *Biomech Model Mechanobiol*, vol. 16, no. 3, pp. 907–920, Jun. 2017 [Online]. Available: 10.1007/s10237-016-0860-8.

[47] W. Li et al., ‘Dynamic mechanical characterization and viscoelastic modeling of bovine brain tissue’, *Journal of the Mechanical Behavior of Biomedical Materials*, vol. 114, p. 104204, Feb. 2021 [Online]. Available: 10.1016/j.jmbbm.2020.104204.

[48] S. Budday et al., ‘Mechanical characterization of human brain tissue’, *Acta Biomaterialia*, vol. 48, pp. 319–340, Jan. 2017 [Online]. Available: 10.1016/j.actbio.2016.10.036.

[49] M. T. Shaw and W. J. MacKnight, *Introduction to Polymer Viscoelasticity*, 1st ed. Wiley, 2005[Online]. Availablehttps://onlinelibrary.wiley.com/doi/book/10.1002/0471741833[Accessed: 27March2024].

[50] X. Jin et al., ‘A comprehensive experimental study on material properties of human brain tissue’, *Journal of Biomechanics*, vol. 46, no. 16, pp. 2795–2801, Nov. 2013 [Online]. Available: 10.1016/j.jbiomech.2013.09.001.

[51] B. Rashid et al., ‘Mechanical characterization of brain tissue in compression at dynamic strain rates’, *Journal of the Mechanical Behavior of Biomedical Materials*, vol. 10, pp. 23–38, Jun. 2012 [Online]. Available: 10.1016/j.jmbbm.2012.01.022.

[52] B. Rashid et al., ‘Mechanical characterization of brain tissue in tension at dynamic strain rates’, *Journal of the Mechanical Behavior of Biomedical Materials*, vol. 33, pp. 43–54, May 2014 [Online]. Available: 10.1016/j.jmbbm.2012.07.015.

[53] F. Eskandari et al., ‘Tension Strain-Softening and Compression Strain-Stiffening Behavior of Brain White Matter’, *Ann Biomed Eng*, vol. 49, no. 1, pp. 276–286, Jan. 2021 [Online]. Available: 10.1007/s10439-020-02541-w.

[54] C. S. von Bartheld et al., ‘The search for true numbers of neurons and glial cells in the human brain: A review of 150 years of cell counting: Quantifying neurons and glia in human brain’, *J. Comp. Neurol.*, vol. 524, no. 18, pp. 3865–3895, Dec. 2016 [Online]. Available: 10.1002/cne.24040.

[55] S. Budday et al., ‘Mechanical properties of gray and white matter brain tissue by indentation’, *Journal of the Mechanical Behavior of Biomedical Materials*, vol. 46, pp. 318–330, Jun. 2015 [Online]. Available: 10.1016/j.jmbbm.2015.02.024.

[56] X. Li et al., ‘An anatomically detailed and personalizable head injury model: Significance of brain and white matter tract morphological variability on strain’, *Biomech Model Mechanobiol*, vol. 20, no. 2, pp. 403–431, Apr. 2021 [Online]. Available: 10.1007/s10237-020-01391-8.

[57] W. Li et al., ‘Investigation of the Compressive Viscoelastic Properties of Brain Tissue Under Time and Frequency Dependent Loading Conditions’, *Ann Biomed Eng*, vol. 49, no. 12, pp. 3737–3747, Dec. 2021 [Online]. Available: 10.1007/s10439-021-02866-0.

[58] S. Budday et al., ‘Rheological characterization of human brain tissue’, *Acta Biomaterialia*, vol. 60, pp. 315–329, Sep. 2017 [Online]. Available: 10.1016/j.actbio.2017.06.024.

[59] A. F. Christ et al., ‘Mechanical difference between white and gray matter in the rat cerebellum measured by scanning force microscopy’, *Journal of Biomechanics*, vol. 43, no. 15, pp. 2986–2992, Nov. 2010 [Online]. Available: 10.1016/j.jbiomech.2010.07.002.

[60] A. S. Mijailovic et al., ‘Localized characterization of brain tissue mechanical properties by needle induced cavitation rheology and volume controlled cavity expansion’, *Journal of the Mechanical Behavior of Biomedical Materials*, vol. 114, p. 104168, Feb. 2021 [Online]. Available: 10.1016/j.jmbbm.2020.104168.

[61] A. Menichetti et al., ‘Regional characterization of the dynamic mechanical properties of human brain tissue by microindentation’, *International Journal of Engineering Science*, vol. 155, p. 103355, Oct. 2020 [Online]. Available: 10.1016/j.ijengsci.2020.103355.

[62] D. B. MacManus et al., ‘Mechanical characterisation of brain tissue up to 35% strain at 1, 10, and 100/s using a custom-built micro-indentation apparatus’, *Journal of the Mechanical Behavior of Biomedical Materials*, vol. 87, pp. 256–266, Nov. 2018 [Online]. Available: 10.1016/j.jmbbm.2018.07.025.

[63] J. A. W. van Dommelen et al., ‘Mechanical Properties of Brain Tissue: Characterisation and Constitutive Modelling’, in *Mechanosensitivity of the Nervous System*, vol. 2, A. Kamkim and I. Kiseleva, Eds. Dordrecht: Springer Netherlands, 2009, pp. 249–279[Online]. Availablehttp://link.springer.com/10.1007/978-1-4020-8716-5_12[Accessed: 3February2023].

[64] B. Mota and S. Herculano-Houzel, ‘All brains are made of this: a fundamental building block of brain matter with matching neuronal and glial masses’, *Front. Neuroanat.*, vol. 8, Nov. 2014[Online].
Availablehttp://journal.frontiersin.org/article/10.3389/fnana.2014.00127/abstract[Accessed: 25March2024].

[65] E. C. Kugler et al., ‘The “Neuro-Glial-Vascular” Unit: The Role of Glia in Neurovascular Unit Formation and Dysfunction’, *Front Cell Dev Biol*, vol. 9, p. 732820, Sep. 2021 [Online]. Available: 10.3389/fcell.2021.732820.

[66] A. Soles et al., ‘Extracellular Matrix Regulation in Physiology and in Brain Disease’, *IJMS*, vol. 24, no. 8, p. 7049, Apr. 2023 [Online]. Available: 10.3390/ijms24087049.

[67] H. Ahmadzadeh et al., ‘Viscoelasticity of Tau Proteins Leads to Strain Rate-Dependent Breaking of Microtubules during Axonal Stretch Injury: Predictions from a Mathematical Model’, *Biophysical Journal*, vol. 106, no. 5, pp. 1123–1133, Mar. 2014 [Online]. Available: 10.1016/j.bpj.2014.01.024.

[68] D. K. Cullen et al., ‘Strain rate-dependent induction of reactive astrogliosis and cell death in three-dimensional neuronal–astrocytic co-cultures’, *Brain Research*, vol. 1158, pp. 103–115, Jul. 2007 [Online]. Available: 10.1016/j.brainres.2007.04.070.

[69] N. Reiter et al., ‘Insights into the Microstructural Origin of Brain Viscoelasticity’, *J Elast*, vol. 145, no. 1, pp. 99–116, Aug. 2021 [Online]. Available: 10.1007/s10659-021-09814-y.

[70] A. Franck, ‘Viscoelasticity and dynamic mechanical testing’.

[71] W. Li et al., ‘Frequency dependent viscoelastic properties of porcine brain tissue’, *Journal of the Mechanical Behavior of Biomedical Materials*, vol. 102, p. 103460, Feb. 2020 [Online]. Available: 10.1016/j.jmbbm.2019.103460.

[72] W. Li et al., ‘Investigation of the Compressive Viscoelastic Properties of Brain Tissue Under Time and Frequency Dependent Loading Conditions’, *Ann Biomed Eng*, vol. 49, no. 12, pp. 3737–3747, Dec. 2021 [Online]. Available: 10.1007/s10439-021-02866-0.

[73] F. Boudjema et al., ‘Dynamical properties of the brain tissue under oscillatory shear stresses at large strain range’, *J. Phys.: Conf. Ser.*, vol. 790, p. 012002, Jan. 2017 [Online]. Available: 10.1088/1742-6596/790/1/012002.

[74] S. Nicolle et al., ‘Shear Properties of Brain Tissue over a Frequency Range Relevant for Automotive Impact Situations: New Experimental Results’, *Stapp Car Crash J*, vol. 48, pp. 239–258, Nov. 2004 [Online]. Available: 10.4271/2004-22-0011.

[75] L. E. Bilston, ‘Brain Tissue Mechanical Properties’, in *Biomechanics of the Brain*, K. Miller, Ed. Cham: Springer International Publishing, 2019, pp. 71–95[Online]. Availablehttp://link.springer.com/10.1007/978-3-030-04996-6_4[Accessed: 24November2022].

[76] I. Sack et al., ‘The impact of aging and gender on brain viscoelasticity’, *Neuroimage*, vol. 46, no. 3, pp. 652–657, Jul. 2009 [Online]. Available: 10.1016/j.neuroimage.2009.02.040.

[77] T. Takamura et al., ‘Influence of Age on Global and Regional Brain Stiffness in Young and Middle-Aged Adults’, *Journal of Magnetic Resonance Imaging*, vol. 51, no. 3, pp. 727–733, 2020 [Online]. Available: 10.1002/jmri.26881.

[78] A. Arani et al., ‘Measuring the effects of aging and sex on regional brain stiffness with MR elastography in healthy older adults’, *NeuroImage*, vol. 111, pp. 59–64, May 2015 [Online]. Available: 10.1016/j.neuroimage.2015.02.016.

[79] A. D. Drozdov and J. deC. Christiansen, ‘Tension–compression asymmetry in the mechanical response of hydrogels’, *Journal of the Mechanical Behavior of Biomedical Materials*, vol. 110, p. 103851, Oct. 2020 [Online]. Available: 10.1016/j.jmbbm.2020.103851.

[80] H. N. Kim and N. Choi, ‘Consideration of the Mechanical Properties of Hydrogels for Brain Tissue Engineering and Brain-on-a-chip’, *BioChip J*, vol. 13, no. 1, pp. 8–19, Mar. 2019 [Online]. Available: 10.1007/s13206-018-3101-7.

[81] L. Zhang et al., ‘The mechanical behavior of brain surrogates manufactured from silicone elastomers’, *Journal of the Mechanical Behavior of Biomedical Materials*, vol. 95, pp. 180–190, Jul. 2019 [Online]. Available: 10.1016/j.jmbbm.2019.04.005.

[82] C. K. McGarry et al., ‘Tissue mimicking materials for imaging and therapy phantoms: a review’, *Phys. Med. Biol.*, vol. 65, pp. 26–30, Sep. 2020 [Online]. Available: 10.1088/1361-6560/abbd17.

[83] Kenry et al., ‘Viscoelastic Effects of Silicone Gels at the Micro- and Nanoscale’, *Procedia IUTAM*, vol. 12, pp. 20–30, Jan. 2015 [Online]. Available: 10.1016/j.piutam.2014.12.004.

[84] Z. Liao et al., ‘On the stress recovery behaviour of Ecoflex silicone rubbers’, *International Journal of Mechanical Sciences*, vol. 206, p. 106624, Sep. 2021 [Online]. Available: 10.1016/j.ijmecsci.2021.106624.

[85] D. J. Carr et al., ‘The use of gelatine in wound ballistics research’, *Int J Legal Med*, vol. 132, no. 6, pp. 1659–1664, Nov. 2018 [Online]. Available: 10.1007/s00414-018-1831-7.

[86] M. Czerner et al., ‘Deformation and fracture behavior of physical gelatin gel systems’, *Food Hydrocolloids*, vol. 60, pp. 299–307, Oct. 2016 [Online]. Available: 10.1016/j.foodhyd.2016.04.007.

[87] L. Falland-Cheung et al., ‘Anatomical head model to measure impact force transfer through the head layers and their displacement’, *Journal of Concussion*, vol. 2, p. 2059700218777829, Jan. 2018 [Online]. Available: 10.1177/2059700218777829.

[88] K. Cui and J. P. Gong, ‘Aggregated structures and their functionalities in hydrogels’, *Aggregate*, vol. 2, no. 2, p. e33, 2021 [Online]. Available: 10.1002/agt2.33.

[89] M. V. Dobrynin et al., ‘Cyclometalated Platinum(II) Complexes Simultaneously Catalyze the Cross-Linking of Polysiloxanes and Function as Luminophores’, *ACS Appl. Polym. Mater.*, vol. 3, no. 2, pp. 857–866, Feb. 2021 [Online]. Available: 10.1021/acsapm.0c01190.

[90] R. M. Islamova et al., ‘bis-Nitrile and bis-Dialkylcyanamide Platinum(II) Complexes as Efficient Catalysts for Hydrosilylation Cross-Linking of Siloxane Polymers’, *Molecules*, vol. 21, no. 3, p. 311, Mar. 2016 [Online]. Available: 10.3390/molecules21030311.

[91] A. Tamura et al., ‘Mechanical Characterization of Brain Tissue in High-Rate Compression’, *JBSE*, vol. 2, no. 3, pp. 115–126, 2007 [Online]. Available: 10.1299/jbse.2.115.

[92] K. Pogoda et al., ‘Compression stiffening of brain and its effect on mechanosensing by glioma cells’, *New J. Phys.*, vol. 16, no. 7, p. 075002, Jul. 2014 [Online]. Available: 10.1088/1367-2630/16/7/075002.

[93] J. Wang et al., ‘Mechanical behavior and constitutive equations of porcine brain tissue considering both solution environment effect and strain rate effect’, *Mechanics of Advanced Materials and Structures*, pp. 1–15, Jan. 2023 [Online]. Available: 10.1080/15376494.2022.2150917.

[94] J. Rajagopalan et al., ‘The Role of Mechanical Tension in Neurons’, *MRS Online Proceedings Library*, vol. 1274, no. 1, p. 106, Dec. 2010 [Online]. Available: 10.1557/PROC-1274-QQ01-06.

[95] J. Zwirner et al., ‘Mechanical Properties of Human Dura Mater in Tension – An Analysis at an Age Range of 2 to 94 Years’, *Sci Rep*, vol. 9, no. 1, p. 16655, Nov. 2019 [Online]. Available: 10.1038/s41598-019-52836-9.

[96] B. Rashid et al., ‘Mechanical characterization of brain tissue in simple shear at dynamic strain rates’, 2020[Online]. Availablehttps://arxiv.org/abs/2009.01383[Accessed: 2November2023].

[97] L. Bilston et al., ‘Large strain behaviour of brain tissue in shear: Some experimental data and differential constitutive model’, *Biorheology*, vol. 38, pp. 335–45, Feb. 2001.

[98] E. Nicolas et al., ‘Biomechanical characterization of ex vivo human brain using ultrasound shear wave spectroscopy’, *Ultrasonics*, vol. 84, pp. 119–125, Mar. 2018 [Online]. Available: 10.1016/j.ultras.2017.10.009.

[99] C. Wex et al., ‘Isotropic incompressible hyperelastic models for modelling the mechanical behaviour of biological tissues: a review’, *Biomedical Engineering / Biomedizinische Technik*, vol. 60, no. 6, pp. 577–592, Dec. 2015 [Online]. Available: 10.1515/bmt-2014-0146.

[100] R. W. Ogden et al., ‘Fitting hyperelastic models to experimental data’, *Computational Mechanics*, vol. 34, no. 6, pp. 484–502, Nov. 2004 [Online]. Available: 10.1007/s00466-004-0593-y.

[101] A. Anssari-Benam, ‘Comparative modelling results between a separable and a non-separable form of principal stretches–based strain energy functions for a variety of isotropic incompressible soft solids: Ogden model compared with a parent model’, *Mech Soft Mater*, vol. 5, no. 1, p. 2, Dec. 2023 [Online]. Available: 10.1007/s42558-023-00050-z.

[102] S. Budday et al., ‘Towards microstructure-informed material models for human brain tissue’, *Acta Biomaterialia*, vol. 104, pp. 53–65, Mar. 2020 [Online]. Available: 10.1016/j.actbio.2019.12.030.

[103] D. De Kegel et al., ‘Biomechanical characterization of human dura mater’, *Journal of the Mechanical Behavior of Biomedical Materials*, vol. 79, pp. 122–134, Mar. 2018 [Online]. Available: 10.1016/j.jmbbm.2017.12.023.

[104] O. Chaudhuri et al., ‘Effects of extracellular matrix viscoelasticity on cellular behaviour’, *Nature*, vol. 584, no. 7822, pp. 535–546, Aug. 2020 [Online]. Available: 10.1038/s41586-020-2612-2.

[105] X. Jin et al., ‘Constitutive Modeling of Pia–Arachnoid Complex’, *Ann Biomed Eng*, vol. 42, no. 4, pp. 812–821, Apr. 2014 [Online]. Available: 10.1007/s10439-013-0948-6.

[106] Y. Lev and K. Y. Volokh, ‘On Cavitation in Rubberlike Materials’, *Journal of Applied Mechanics*, vol. 83, no. 4, p. 044501, Apr. 2016 [Online]. Available: 10.1115/1.4032377.

[107] S. Arutyunov et al., ‘Microbial Adhesion to Dental Polymers for Conventional, Computer-Aided Subtractive and Additive Manufacturing: A Comparative In Vitro Study’, *JFB*, vol. 13, no. 2, p. 42, Apr. 2022 [Online]. Available: 10.3390/jfb13020042.

[108] C. Wei et al., ‘Therapy of traumatic brain injury by modern agents and traditional Chinese medicine’, *Chinese Medicine*, vol. 18, no. 1, p. 25, Mar. 2023 [Online]. Available: 10.1186/s13020-023-00731-x.

[109] H. Mao et al., ‘Development of a Finite Element Human Head Model Partially Validated With Thirty Five Experimental Cases’, *Journal of Biomechanical Engineering*, vol. 135, no. 11, p. 111002, Nov. 2013 [Online]. Available: 10.1115/1.4025101.

[110] K. M. Guskiewicz and J. P. Mihalik, ‘Biomechanics of Sport Concussion: Quest for the Elusive Injury Threshold’, *Exercise and Sport Sciences Reviews*, vol. 39, no. 1, pp. 4–11, Jan. 2011 [Online]. Available: 10.1097/JES.0b013e318201f53e.

[111] L. Bartolini et al., ‘Comparison of frequency and strain-rate domain mechanical characterization’, *Sci Rep*, vol. 8, no. 1, p. 13697, Sep. 2018 [Online]. Available: 10.1038/s41598-018-31737-3.

[112] M. Verdet et al., ‘Mechanical Performance of Polyurethane and Epoxy Adhesives in Connections with Glued-in Rods at Elevated Temperatures’, *BioResources*, vol. 11, no. 4, pp. 8200–8214, Aug. 2016 [Online]. Available: 10.15376/biores.11.4.8200-8214.

[113] M. A. Meyers and K. K. Chawla, *Mechanical Behavior of Materials*, 2nd ed. Cambridge University Press, 2008[Online]. Availablehttps://www.cambridge.org/core/product/identifier/9780511810947/type/book[Accessed: 4August2024].

[114] J. A. Motherway et al., ‘The mechanical properties of cranial bone: The effect of loading rate and cranial sampling position’, *Journal of Biomechanics*, vol. 42, no. 13, pp. 2129–2135, Sep. 2009 [Online]. Available: 10.1016/j.jbiomech.2009.05.030.

[115] J. H. McElhaney et al., ‘Mechanical properties of cranial bone’, *Journal of Biomechanics*, vol. 3, no. 5, pp. 495–511, Oct. 1970 [Online]. Available: 10.1016/0021-9290(70)90059-X.

[116] J. H. C. Lee et al., ‘An Investigation on the Correlation between the Mechanical Properties of Human Skull Bone, Its Geometry, Microarchitectural Properties, and Water Content’, *Journal of Healthcare Engineering*, vol. 2019, pp. 1–8, May 2019 [Online]. Available: 10.1155/2019/6515797.

[117] Q. Wu et al., ‘Theoretical prediction model and failure mechanism map of human skull porous structures with quasi-static bending performance’, *International Journal of Mechanical Sciences*, vol. 200, p. 106431, Jun. 2021 [Online]. Available: 10.1016/j.ijmecsci.2021.106431.

[118] L. E. Murr, ‘Open-cellular metal implant design and fabrication for biomechanical compatibility with bone using electron beam melting’, *Journal of the Mechanical Behavior of Biomedical Materials*, vol. 76, pp. 164–177, Dec. 2017 [Online]. Available: 10.1016/j.jmbbm.2017.02.019.

[119] B. Ondruschka et al., ‘A biomechanical comparison between human calvarial bone and a skull simulant considering the role of attached periosteum and dura mater’, *Int J Legal Med*, vol. 133, no. 5, pp. 1603–1610, Sep. 2019 [Online]. Available: 10.1007/s00414-019-02102-4.

[120] K. Adanty et al., ‘The effect of morphometric and geometric indices of the human calvarium on mechanical response’, *Clinical Biomechanics*, vol. 107, p. 106012, Jul. 2023 [Online]. Available: 10.1016/j.clinbiomech.2023.106012.

[121] K. Adanty et al., ‘The Mechanical Characterization and Comparison of Male and Female Calvaria Under Four-Point Bending Impacts’, *Journal of Biomechanical Engineering*, vol. 145, no. 5, p. 051009, May 2023 [Online]. Available: 10.1115/1.4056459.

[122] X. Zhai et al., ‘The effects of loading-direction and strain-rate on the mechanical behaviors of human frontal skull bone’, *Journal of the Mechanical Behavior of Biomedical Materials*, vol. 103, p. 103597, Mar. 2020 [Online]. Available: 10.1016/j.jmbbm.2019.103597.

[123] J. Zwirner et al., ‘The dynamic impact behavior of the human neurocranium’, *Sci Rep*, vol. 11, no. 1, p. 11331, May 2021 [Online]. Available: 10.1038/s41598-021-90322-3.

[124] S. Bandyopadhyay-Ghosh, ‘Bone as a collagen-hydroxyapatite composite and its repair’, *Trends in Biomaterials and Artificial Organs*, vol. 22, no. 2, pp. 112–121, Aug. 2008.

[125] B. M. Thomson, ‘BONE*’, in *Encyclopedia of Human Nutrition (Second Edition)*, B. Caballero, Ed. Oxford: Elsevier, 1998, pp. 220–225[Online]. Availablehttps://www.sciencedirect.com/science/article/pii/B0122266943000296[Accessed: 18July2024].

[126] V. Šromová et al., ‘A Brief Review of Bone Cell Function and Importance’, *Cells*, vol. 12, no. 21, p. 2576, Jan. 2023 [Online]. Available: 10.3390/cells12212576.

[127] J. DJ. Black and B. J. Tadros, ‘Bone structure: from cortical to calcium’, *Orthopaedics and Trauma*, vol. 34, no. 3, pp. 113–119, Jun. 2020 [Online]. Available: 10.1016/j.mporth.2020.03.002.

[128] ‘Chapter 6 . Bone Tissue and the Skeletal System’, in *Anatomy and Physiology*, 2nd ed., OpenStax, 2022[Online]. Availablehttps://openstax.org/details/books/anatomy-and-physiology-2e?Book%20details.

[129] A. F. Dalley et al., *Moore’s clinically oriented anatomy*, Ninth edition, Revised reprint. Philadelphia: Wolters Kluwer, 2024.

[130] S. Boruah et al., ‘Variation of bone layer thicknesses and trabecular volume fraction in the adult male human calvarium’, *Bone*, vol. 77, pp. 120–134, Aug. 2015 [Online]. Available: 10.1016/j.bone.2015.04.031.

[131] S. Boruah et al., ‘Influence of bone microstructure on the mechanical properties of skull cortical bone – A combined experimental and computational approach’, *Journal of the Mechanical Behavior of Biomedical Materials*, vol. 65, pp. 688–704, Jan. 2017 [Online]. Available: 10.1016/j.jmbbm.2016.09.041.

[132] S. Boruah et al., ‘Response of Human Skull Bone to Dynamic Compressive Loading’, 2013.

[133] T. Matys et al., ‘Anatomy of the Calvaria and Skull Base’, *Neuroimaging Clinics of North America*, vol. 32, no. 3, pp. 447–462, Aug. 2022 [Online]. Available: 10.1016/j.nic.2022.04.011.

[134] S. L. Alexander et al., ‘Multiscale response of the human skull to quasi-static compression’, *Journal of the Mechanical Behavior of Biomedical Materials*, vol. 102, p. 103492, Feb. 2020 [Online]. Available: 10.1016/j.jmbbm.2019.103492.

[135] S. L. Alexander et al., ‘Microstructural Dependence of the Compressive Mechanical Response of Human Skull’, 2018.

[136] A. D. Brown et al., ‘The mechanical response of commercially available bone simulants for quasi-static and dynamic loading’, *Journal of the Mechanical Behavior of Biomedical Materials*, vol. 90, pp. 404–416, Feb. 2019 [Online]. Available: 10.1016/j.jmbbm.2018.10.032.

[137] A. D. Brown et al., ‘Shear behavior of human skull bones’, *Journal of the Mechanical Behavior of Biomedical Materials*, vol. 116, p. 104343, Apr. 2021 [Online]. Available: 10.1016/j.jmbbm.2021.104343.

[138] C. A. Gunnarsson et al., ‘Bending Response of Human Skull-Beams as a Function of Loading Rate and Loading-Tip Geometry’.

[139] E. e. Sigmund et al., ‘High-resolution MRI of internal field diffusion-weighting in trabecular bone’, *NMR in Biomedicine*, vol. 22, no. 4, pp. 436–448, 2009 [Online]. Available: 10.1002/nbm.1354.

[140] M. C. Wurnig et al., ‘Characterization of trabecular bone density with ultra-short echo-time MRI at 1.5, 3.0 and 7.0 T – comparison with micro-computed tomography’, *NMR in Biomedicine*, vol. 27, no. 10, pp. 1159–1166, 2014 [Online]. Available: 10.1002/nbm.3169.

[141] C. S. Rajapakse et al., ‘Volumetric Cortical Bone Porosity Assessment with MR Imaging: Validation and Clinical Feasibility’, *Radiology*, vol. 276, no. 2, pp. 526–535, Aug. 2015 [Online]. Available: 10.1148/radiol.15141850.

[142] I. O. Smith et al., ‘Confocal laser scanning microscopy as a tool for imaging cancellous bone’, *J Biomed Mater Res*, vol. 79B, no. 1, pp. 185–192, Oct. 2006 [Online]. Available: 10.1002/jbm.b.30529.

[143] L. Falland-Cheung et al., ‘Investigation of the elastic modulus, tensile and flexural strength of five skull simulant materials for impact testing of a forensic skin/skull/brain model’, *Journal of the Mechanical Behavior of Biomedical Materials*, vol. 68, pp. 303–307, Apr. 2017 [Online]. Available: 10.1016/j.jmbbm.2017.02.023.

[144] R. Mantecón et al., ‘Additive Manufacturing and Mechanical Characterization of PLA-Based Skull Surrogates’, *Polymers*, vol. 15, no. 1, p. 58, Dec. 2022 [Online]. Available: 10.3390/polym15010058.

[145] B. J. Henwood and G. Appleby-Thomas, ‘The suitability of Synbone® as a tissue analogue in ballistic impacts’, *J Mater Sci*, vol. 55, no. 7, pp. 3022–3033, Mar. 2020 [Online]. Available: 10.1007/s10853-019-04231-y.

[146] A. E. Jakus et al., ‘Hyperelastic “bone”: A highly versatile, growth factor–free, osteoregenerative, scalable, and surgically friendly biomaterial’, *Sci. Transl. Med.*, vol. 8, no. 358, Sep. 2016[Online]. Availablehttps://www.science.org/doi/10.1126/scitranslmed.aaf7704[Accessed: 29March2023].

[147] C. Niezrecki et al., ‘Digital Image Correlation Techniques for NDE and SHM’, in *Handbook of Advanced Non-Destructive Evaluation*, N. Ida and N. Meyendorf, Eds. Cham: Springer International Publishing, 2018, pp. 1–46[Online]. Availablehttps://doi.org/10.1007/978-3-319-30050-4_47-1[Accessed: 29July2024].

[148] G. W. Melenka and J. P. Carey, ‘Evaluation of Fiber Reinforced Cement Using Digital Image Correlation’, *PLOS ONE*, vol. 10, no. 6, p. e0128644, Jun. 2015 [Online]. Available: 10.1371/journal.pone.0128644.

[149] C. Franck et al., ‘Three-dimensional Full-field Measurements of Large Deformations in Soft Materials Using Confocal Microscopy and Digital Volume Correlation’, *Exp Mech*, vol. 47, no. 3, pp. 427–438, Jun. 2007 [Online]. Available: 10.1007/s11340-007-9037-9.

[150] M. Sutton et al., ‘Application of an optimized digital correlation method to planar deformation analysis’, *Image and Vision Computing*, vol. 4, no. 3, pp. 143–150, Aug. 1986 [Online]. Available: 10.1016/0262-8856(86)90057-0.

[151] M. Luo, ‘Displacement/strain measurements using an optical microscope and digital image correlation’, *Opt. Eng*, vol. 45, no. 3, p. 033605, Mar. 2006 [Online]. Available: 10.1117/1.2182108.

[152] H. Schreier et al., *Image Correlation for Shape, Motion and Deformation Measurements: Basic Concepts,Theory and Applications*. Boston, MA: Springer US, 2009[Online]. Availablehttps://link.springer.com/10.1007/978-0-387-78747-3[Accessed: 2August2024].

[153] Z. Sun et al., ‘Measuring Microscopic Deformations with Digital Image Correlation’, *Optics and Lasers in Engineering*, vol. 27, no. 4, pp. 409–428, Jul. 1997 [Online]. Available: 10.1016/S0143-8166(96)00041-3.

[154] International Digital Image Correlation Society et al., ‘A Good Practices Guide for Digital Image Correlation’, International Digital Image Correlation Society, Oct. 2018[Online]. Availablehttp://idics.org/guide/[Accessed: 2August2024].

[155] B. Pan et al., ‘Two-dimensional digital image correlation for in-plane displacement and strain measurement: a review’, *Meas. Sci. Technol.*, vol. 20, no. 6, p. 062001, Jun. 2009 [Online]. Available: 10.1088/0957-0233/20/6/062001.

[156] P. Sztefek et al., ‘Using digital image correlation to determine bone surface strains during loading and after adaptation of the mouse tibia’, *Journal of Biomechanics*, vol. 43, no. 4, pp. 599–605, Mar. 2010 [Online]. Available: 10.1016/j.jbiomech.2009.10.042.

[157] L. F. Monaheng et al., ‘Validation through digital image correlation of finite element analysis used in the design of a Ti6Al4V mandibular implant’, 2018.

[158] B. Lal et al., ‘A novel economically viable solution for 3D printing-assisted cranioplast fabrication’, *British Journal of Neurosurgery*, vol. 34, no. 3, pp. 280–283, May 2020 [Online]. Available: 10.1080/02688697.2020.1726289.

[159] Y. Han et al., ‘Three-Dimensional Printing of Hydroxyapatite Composites for Biomedical Application’, *Crystals*, vol. 11, no. 4, p. 353, Mar. 2021 [Online]. Available: 10.3390/cryst11040353.

[160] S. Zhang, *Hydroxyapatite Coatings for Biomedical Applications*, 1st ed. Boca Raton: CRC Press, 2013[Online]. Availablehttps://www.taylorfrancis.com/books/9780429111389[Accessed: 29August2023].

[161] L. Gu et al., ‘The influence of heterogeneous meninges on the brain mechanics under primary blast loading’, *Composites Part B: Engineering*, vol. 43, no. 8, pp. 3160–3166, Dec. 2012 [Online]. Available: 10.1016/j.compositesb.2012.04.014.

[162] D. R. Walsh et al., ‘Mechanical Properties of the Cranial Meninges: A Systematic Review’, *Journal of Neurotrauma*, vol. 38, no. 13, pp. 1748–1761, Jul. 2021 [Online]. Available: 10.1089/neu.2020.7288.

[163] D. R. Walsh et al., ‘Mechanical characterisation of the human dura mater, falx cerebri and superior sagittal sinus’, *Acta Biomaterialia*, vol. 134, pp. 388–400, Oct. 2021 [Online]. Available: 10.1016/j.actbio.2021.07.043.

[164] D. R. Walsh et al., ‘Regional mechanical and biochemical properties of the porcine cortical meninges’, *Acta Biomaterialia*, vol. 80, pp. 237–246, Oct. 2018 [Online]. Available: 10.1016/j.actbio.2018.09.004.

[165] X. Jin et al., ‘Biomechanical response of the bovine pia-arachnoid complex to tensile loading at varying strain-rates’, *Stapp Car Crash J*, vol. 50, pp. 637–649, Nov. 2006 [Online]. Available: 10.4271/2006-22-0025.

[166] N. Benko et al., ‘Mechanical characterization of the human pia-arachnoid complex’, *Journal of the Mechanical Behavior of Biomedical Materials*, vol. 120, p. 104579, Aug. 2021 [Online]. Available: 10.1016/j.jmbbm.2021.104579.

[167] M. S. Sacks et al., ‘Local mechanical anisotropy in human cranial dura mater allografts’, *J Biomech Eng*, vol. 120, no. 4, pp. 541–544, Aug. 1998 [Online]. Available: 10.1115/1.2798027.

[168] D. Chauvet et al., ‘Histological and biomechanical study of dura mater applied to the technique of dura splitting decompression in Chiari type I malformation’, *Neurosurg Rev*, vol. 33, no. 3, pp. 287–294; discussion 295, Jul. 2010 [Online]. Available: 10.1007/s10143-010-0261-x.

[169] A. J. Golman et al., ‘Hierarchical Model Validation of the Falx Cerebri and Tentorium Cerebelli’, 2014[Online]. Availablehttps://www.semanticscholar.org/paper/Hierarchical-Model-Validation-of-the-Falx-Cerebri-Golman-Wickwire/ec30feab4fbf006df243aba0ad75b00b7dc5797f[Accessed: 2August2024].

[170] A. Singh et al., ‘Investigation of role of falx and tentorium on brain simulant strain under impact loading’, *Journal of Biomechanics*, vol. 144, p. 111347, Nov. 2022 [Online]. Available: 10.1016/j.jbiomech.2022.111347.

[171] C. J. Freitas et al., ‘Dynamic Response Due to Behind Helmet Blunt Trauma Measured with a Human Head Surrogate’, *Int. J. Med. Sci.*, vol. 11, no. 5, pp. 409–425, 2014 [Online]. Available: 10.7150/ijms.8079.

[172] B. Stone et al., ‘A destructible headform for the assessment of sports impacts’, *Proceedings of the Institution of Mechanical Engineers, Part P: Journal of Sports Engineering and Technology*, vol. 237, no. 1, pp. 7–18, Mar. 2023 [Online]. Available: 10.1177/17543371211055905.

[173] A. Singh et al., ‘Measurement of brain simulant strains in head surrogate under impact loading’, *Biomech Model Mechanobiol*, vol. 20, no. 6, pp. 2319–2334, Dec. 2021 [Online]. Available: 10.1007/s10237-021-01509-6.

[174] A. Singh et al., ‘Biomechanical Response of Head Surrogate With and Without the Helmet’, *Journal of Biomechanical Engineering*, vol. 146, no. 031001, Jan. 2024[Online]. Availablehttps://doi.org/10.1115/1.4062968[Accessed: 13February2024].

[175] M. Hanna et al., ‘A Method for Evaluating Brain Deformation Under Sagittal Blunt Impacts Using a Half-Skull Human-Scale Surrogate’, *Journal of Biomechanical Engineering*, vol. 145, no. 6, p. 061001, Jun. 2023 [Online]. Available: 10.1115/1.4056547.

[176] P. Mahoney et al., ‘Ballistic impacts on an anatomically correct synthetic skull with a surrogate skin/soft tissue layer’, *Int J Legal Med*, vol. 132, no. 2, pp. 519–530, Mar. 2018 [Online]. Available: 10.1007/s00414-017-1737-9.

[177] A. K. Knutsen et al., ‘Characterization of material properties and deformation in the ANGUS phantom during mild head impacts using MRI’, *Journal of the Mechanical Behavior of Biomedical Materials*, vol. 138, p. 105586, Feb. 2023 [Online]. Available: 10.1016/j.jmbbm.2022.105586.

## Chapter 3 References

[1] W. Zhao et al., ‘Material properties of the brain in injury-relevant conditions – Experiments and computational modeling’, *J. Mech. Behav. Biomed. Mater.*, vol. 80, pp. 222–234, Apr. 2018 [Online]. Available: 10.1016/j.jmbbm.2018.02.005.

[2] R. E. Woodrow et al., ‘Acute thalamic connectivity precedes chronic post-concussive symptoms in mild traumatic brain injury’, *Brain*, p. awad056, Feb. 2023 [Online]. Available: 10.1093/brain/awad056.

[3] M. C. Dewan et al., ‘Estimating the global incidence of traumatic brain injury’, *J. Neurosurg.*, vol. 130, no. 4, pp. 1080–1097, Apr. 2019 [Online]. Available: 10.3171/2017.10.JNS17352.

[4] S. Premi et al., ‘Mechanical threshold for concussion based on computation of axonal strain using a finite element rat brain model’, *Brain Multiphysics*, vol. 2, p. 100032, 2021 [Online]. Available: 10.1016/j.brain.2021.100032.

[5] D. B. MacManus and M. Ghajari, ‘Material properties of human brain tissue suitable for modelling traumatic brain injury’, *Brain Multiphysics*, vol. 3, p. 100059, 2022 [Online]. Available: 10.1016/j.brain.2022.100059.

[6] T. B. Hoshizaki et al., ‘The development of a threshold curve for the understanding of concussion in sport’, *Trauma*, vol. 19, no. 3, pp. 196–206, Jul. 2017 [Online]. Available: 10.1177/1460408616676503.

[7] A. Post and T. Blaine Hoshizaki, ‘Rotational Acceleration, Brain Tissue Strain, and the Relationship to Concussion’, *J. Biomech. Eng.*, vol. 137, no. 3, p. 030801, Mar. 2015 [Online]. Available: 10.1115/1.4028983.

[8] M. Hosseini-Farid et al., ‘The Strain Rates in the Brain, Brainstem, Dura, and Skull under Dynamic Loadings’, *Math. Comput. Appl.*, vol. 25, no. 2, p. 21, Apr. 2020 [Online]. Available: 10.3390/mca25020021.

[9] B. S. Elkin et al., ‘Brain tissue strains vary with head impact location: A possible explanation for increased concussion risk in struck versus striking football players’, *Clin. Biomech.*, vol. 64, pp. 49–57, Apr. 2019 [Online]. Available: 10.1016/j.clinbiomech.2018.03.021.

[10] J. G. Beckwith et al., ‘Estimated Brain Tissue Response Following Impacts Associated With and Without Diagnosed Concussion’, *Ann. Biomed. Eng.*, vol. 46, no. 6, pp. 819–830, Jun. 2018 [Online]. Available: 10.1007/s10439-018-1999-5.

[11] K. Bian and H. Mao, ‘Mechanisms and variances of rotation-induced brain injury: a parametric investigation between head kinematics and brain strain’, *Biomech. Model. Mechanobiol.*, vol. 19, no. 6, pp. 2323–2341, Dec. 2020 [Online]. Available: 10.1007/s10237-020-01341-4.

[12] A. E. Forte et al., ‘A composite hydrogel for brain tissue phantoms’, *Mater. Des.*, vol. 112, pp. 227–238, Dec. 2016 [Online]. Available: 10.1016/j.matdes.2016.09.063.

[13] A. Chanda et al., ‘Biofidelic human brain tissue surrogates’, *Mech. Adv. Mater. Struct.*, vol. 25, no. 15–16, pp. 1335–1341, Dec. 2018 [Online]. Available: 10.1080/15376494.2016.1143749.

[14] D. Singh et al., ‘Comparison of porcine brain mechanical properties to potential tissue simulant materials in quasi-static and sinusoidal compression’, *J. Biomech.*, vol. 92, pp. 84–91, Jul. 2019 [Online]. Available: 10.1016/j.jbiomech.2019.05.033.

[15] M. Navarro-Lozoya et al., ‘Development of phantom material that resembles compression properties of human brain tissue for training models’, *Materialia*, vol. 8, p. 100438, Dec. 2019 [Online]. Available: 10.1016/j.mtla.2019.100438.

[16] L. Falland-Cheung et al., ‘Elastic behavior of brain simulants in comparison to porcine brain at different loading velocities’, *J. Mech. Behav. Biomed. Mater.*, vol. 77, pp. 609–615, Jan. 2018 [Online]. Available: 10.1016/j.jmbbm.2017.10.026.

[17] S. M. H. Ahmadzadeh and D. W. Hukins, ‘Feasibility of using mixtures of silicone elastomers and silicone oils to model the mechanical behaviour of biological tissues’, *Proc. Inst. Mech. Eng. [H]*, vol. 228, no. 7, pp. 730–734, Jul. 2014 [Online]. Available: 10.1177/0954411914540138.

[18] A. E. Forte et al., ‘On the characterization of the heterogeneous mechanical response of human brain tissue’, *Biomech. Model. Mechanobiol.*, vol. 16, no. 3, pp. 907–920, Jun. 2017 [Online]. Available: 10.1007/s10237-016-0860-8.

[19] A. Tejo-Otero et al., ‘Soft-Tissue-Mimicking Using Hydrogels for the Development of Phantoms’, *Gels*, vol. 8, no. 1, p. 40, Jan. 2022 [Online]. Available: 10.3390/gels8010040.

[20] L. Zhang et al., ‘The mechanical behavior of brain surrogates manufactured from silicone elastomers’, *J. Mech. Behav. Biomed. Mater.*, vol. 95, pp. 180–190, Jul. 2019 [Online]. Available: 10.1016/j.jmbbm.2019.04.005.

[21] C. K. McGarry et al., ‘Tissue mimicking materials for imaging and therapy phantoms: a review’, *Phys. Med. Biol.*, Sep. 2020[Online]. Availablehttps://iopscience.iop.org/article/10.1088/1361-6560/abbd17[Accessed: 2May2023].

[22] B. Zhang et al., ‘3D printed bone tissue regenerative PLA/HA scaffolds with comprehensive performance optimizations’, *Mater. Des.*, vol. 201, p. 109490, Mar. 2021 [Online]. Available: 10.1016/j.matdes.2021.109490.

[23] B. Ondruschka et al., ‘A biomechanical comparison between human calvarial bone and a skull simulant considering the role of attached periosteum and dura mater’, *Int. J. Legal Med.*, vol. 133, no. 5, pp. 1603–1610, Sep. 2019 [Online]. Available: 10.1007/s00414-019-02102-4.

[24] B. Lal et al., ‘A novel economically viable solution for 3D printing-assisted cranioplast fabrication’, *Br. J. Neurosurg.*, vol. 34, no. 3, pp. 280–283, May 2020 [Online]. Available: 10.1080/02688697.2020.1726289.

[25] R. Mantecón et al., ‘Additive Manufacturing and Mechanical Characterization of PLA-Based Skull Surrogates’, *Polymers*, vol. 15, no. 1, p. 58, Dec. 2022 [Online]. Available: 10.3390/polym15010058.

[26] B. P. Mahammod et al., ‘Investigation of Physico-mechanical Behavior, Permeability and Wall Shear Stress of Porous HA/PMMA Composite Bone Scaffold’, *Arab. J. Sci. Eng.*, vol. 45, no. 7, pp. 5505–5515, Jul. 2020 [Online]. Available: 10.1007/s13369-020-04467-w.

[27] L. Falland-Cheung et al., ‘Investigation of the elastic modulus, tensile and flexural strength of five skull simulant materials for impact testing of a forensic skin/skull/brain model’, *J. Mech. Behav. Biomed. Mater.*, vol. 68, pp. 303–307, Apr. 2017 [Online]. Available: 10.1016/j.jmbbm.2017.02.023.

[28] B. J. Henwood and G. Appleby-Thomas, ‘The suitability of Synbone® as a tissue analogue in ballistic impacts’, *J. Mater. Sci.*, vol. 55, no. 7, pp. 3022–3033, Mar. 2020 [Online]. Available: 10.1007/s10853-019-04231-y.

[29] Y. Han et al., ‘Three-Dimensional Printing of Hydroxyapatite Composites for Biomedical Application’, *Crystals*, vol. 11, no. 4, p. 353, Mar. 2021 [Online]. Available: 10.3390/cryst11040353.

[30] A. D. Drozdov and J. deC. Christiansen, ‘Tension–compression asymmetry in the mechanical response of hydrogels’, *J. Mech. Behav. Biomed. Mater.*, vol. 110, p. 103851, Oct. 2020 [Online]. Available: 10.1016/j.jmbbm.2020.103851.

[31] T. Distler et al., ‘Alginate-based hydrogels show the same complex mechanical behavior as brain tissue’, *J. Mech. Behav. Biomed. Mater.*, vol. 111, p. 103979, Nov. 2020 [Online]. Available: 10.1016/j.jmbbm.2020.103979.

[32] N. Petrone et al., ‘Feasibility of using a novel instrumented human head surrogate to measure helmet, head and brain kinematics and intracranial pressure during multidirectional impact tests’, *J. Sci. Med. Sport*, vol. 22, pp. S78–S84, Aug. 2019 [Online]. Available: 10.1016/j.jsams.2019.05.015.

[33] N. Petrone et al., ‘A Novel Instrumented Human Head Surrogate for the Impact Evaluation of Helmets’, in *The 12th Conference of the International Sports Engineering Association*, 2018, p. 269[Online]. Availablehttps://www.mdpi.com/2504-3900/2/6/269[Accessed: 5March2023].

[34] C. J. Freitas et al., ‘Dynamic Response Due to Behind Helmet Blunt Trauma Measured with a Human Head Surrogate’, *Int. J. Med. Sci.*, vol. 11, no. 5, pp. 409–425, 2014 [Online]. Available: 10.7150/ijms.8079.

[35] D. Koncan et al., ‘Comparison of two anthropomorphic test devices using brain motion’, *Proc. Inst. Mech. Eng. Part P J. Sports Eng. Technol.*, vol. 232, no. 4, pp. 305–314, Dec. 2018 [Online]. Available: 10.1177/1754337117751741.

[36] K. Laksari et al., ‘Resonance of human brain under head acceleration’, *J. R. Soc. Interface*, vol. 12, no. 108, p. 20150331, Jul. 2015 [Online]. Available: 10.1098/rsif.2015.0331.

[37] E. G. Takhounts et al., ‘Development of Brain Injury Criteria (BrIC)’, presented at the 57th Stapp Car Crash Conference, 2013, pp. 2013-22–0010[Online]. Availablehttps://www.sae.org/content/2013-22-0010/[Accessed: 8July2023].

[38] F. S. Gayzik et al., ‘Development of a Full Body CAD Dataset for Computational Modeling: A Multi-modality Approach’, *Ann. Biomed. Eng.*, vol. 39, no. 10, pp. 2568–2583, Oct. 2011 [Online]. Available: 10.1007/s10439-011-0359-5.

[39] B. R. Cobb et al., ‘Comparative analysis of helmeted impact response of Hybrid III and National Operating Committee on Standards for Athletic Equipment headforms’, *Proc. Inst. Mech. Eng. Part P J. Sports Eng. Technol.*, vol. 230, no. 1, pp. 50–60, Mar. 2016 [Online]. Available: 10.1177/1754337115599133.

[40] *PlatSil® Gel-OO20*, Polytek Development Corp. [Online]. Available: https://polytek.com/products/platsil-gel-oo20. [Accessed: 11 Dec. 2023].

[41] S. Budday et al., ‘Mechanical characterization of human brain tissue’, *Acta Biomater.*, vol. 48, pp. 319–340, Jan. 2017 [Online]. Available: 10.1016/j.actbio.2016.10.036.

[42] S. Budday et al., ‘Fifty Shades of Brain: A Review on the Mechanical Testing and Modeling of Brain Tissue’, *Arch. Comput. Methods Eng.*, vol. 27, no. 4, pp. 1187–1230, Sep. 2020 [Online]. Available: 10.1007/s11831-019-09352-w.

[43] S. Budday et al., ‘Rheological characterization of human brain tissue’, *Acta Biomater.*, vol. 60, pp. 315–329, Sep. 2017 [Online]. Available: 10.1016/j.actbio.2017.06.024.

[44] S. Budday et al., ‘Mechanical properties of gray and white matter brain tissue by indentation’, *J. Mech. Behav. Biomed. Mater.*, vol. 46, pp. 318–330, Jun. 2015 [Online]. Available: 10.1016/j.jmbbm.2015.02.024.

[45] W. Li et al., ‘Dynamic mechanical characterization and viscoelastic modeling of bovine brain tissue’, *J. Mech. Behav. Biomed. Mater.*, vol. 114, p. 104204, Feb. 2021 [Online]. Available: 10.1016/j.jmbbm.2020.104204.

[46] J. A. W. van Dommelen et al., ‘Mechanical Properties of Brain Tissue: Characterisation and Constitutive Modelling’, in *Mechanosensitivity of the Nervous System*, A. Kamkim and I. Kiseleva, Eds. Dordrecht: Springer Netherlands, 2009, pp. 249–279[Online]. Availablehttp://link.springer.com/10.1007/978-1-4020-8716-5_12[Accessed: 3February2023].

[47] F. Eskandari et al., ‘Tension Strain-Softening and Compression Strain-Stiffening Behavior of Brain White Matter’, *Ann. Biomed. Eng.*, vol. 49, no. 1, pp. 276–286, Jan. 2021 [Online]. Available: 10.1007/s10439-020-02541-w.

[48] C. S. von Bartheld et al., ‘The search for true numbers of neurons and glial cells in the human brain: A review of 150 years of cell counting: Quantifying neurons and glia in human brain’, *J. Comp. Neurol.*, vol. 524, no. 18, pp. 3865–3895, Dec. 2016 [Online]. Available: 10.1002/cne.24040.

[49] Y. Bouattour et al., ‘A Minireview on Brain Models Simulating Geometrical, Physical, and Biochemical Properties of the Human Brain’, *Front. Bioeng. Biotechnol.*, vol. 10, p. 818201, Mar. 2022 [Online]. Available: 10.3389/fbioe.2022.818201.

[50] A. Singh et al., ‘Measurement of brain simulant strains in head surrogate under impact loading’, *Biomech. Model. Mechanobiol.*, vol. 20, no. 6, pp. 2319–2334, Dec. 2021 [Online]. Available: 10.1007/s10237-021-01509-6.

[51] W. Peeters et al., ‘Epidemiology of traumatic brain injury in Europe’, *Acta Neurochir. (Wien)*, vol. 157, no. 10, pp. 1683–1696, Oct. 2015 [Online]. Available: 10.1007/s00701-015-2512-7.

[52] A. Wermer et al., ‘Materials Characterization of Cranial Simulants for Blast-Induced Traumatic Brain Injury’, *Mil. Med.*, vol. 185, no. Supplement_1, pp. 205–213, Jan. 2020 [Online]. Available: 10.1093/milmed/usz228.

[53] A. S. Mijailovic et al., ‘Localized characterization of brain tissue mechanical properties by needle induced cavitation rheology and volume controlled cavity expansion’, *J. Mech. Behav. Biomed. Mater.*, vol. 114, p. 104168, Feb. 2021 [Online]. Available: 10.1016/j.jmbbm.2020.104168.

[54] A. Menichetti et al., ‘Regional characterization of the dynamic mechanical properties of human brain tissue by microindentation’, *Int. J. Eng. Sci.*, vol. 155, p. 103355, Oct. 2020 [Online]. Available: 10.1016/j.ijengsci.2020.103355.

[55] D. B. MacManus et al., ‘Mechanical characterisation of brain tissue up to 35% strain at 1, 10, and 100/s using a custom-built micro-indentation apparatus’, *J. Mech. Behav. Biomed. Mater.*, vol. 87, pp. 256–266, Nov. 2018 [Online]. Available: 10.1016/j.jmbbm.2018.07.025.

[56] H. N. Kim and N. Choi, ‘Consideration of the Mechanical Properties of Hydrogels for Brain Tissue Engineering and Brain-on-a-chip’, *BioChip J.*, vol. 13, no. 1, pp. 8–19, Mar. 2019 [Online]. Available: 10.1007/s13206-018-3101-7.

[57] J. Wang et al., ‘Mechanical behavior and constitutive equations of porcine brain tissue considering both solution environment effect and strain rate effect’, *Mech. Adv. Mater. Struct.*, pp. 1–15, Jan. 2023 [Online]. Available: 10.1080/15376494.2022.2150917.

[58] W. Li et al., ‘Frequency dependent viscoelastic properties of porcine brain tissue’, *J. Mech. Behav. Biomed. Mater.*, vol. 102, p. 103460, Feb. 2020 [Online]. Available: 10.1016/j.jmbbm.2019.103460.

[59] W. Li et al., ‘Investigation of the Compressive Viscoelastic Properties of Brain Tissue Under Time and Frequency Dependent Loading Conditions’, *Ann. Biomed. Eng.*, vol. 49, no. 12, pp. 3737–3747, Dec. 2021 [Online]. Available: 10.1007/s10439-021-02866-0.

[60] D11 Committee, ‘Test Methods for Rubber Properties in Compression’, ASTM International[Online]. Availablehttp://www.astm.org/cgi-bin/resolver.cgi?D575-91R18[Accessed: 17April2023].

[61] F. Boudjema et al., ‘Dynamical properties of the brain tissue under oscillatory shear stresses at large strain range’, *J. Phys. Conf. Ser.*, vol. 790, p. 012002, Jan. 2017 [Online]. Available: 10.1088/1742-6596/790/1/012002.

[62] S. Nicolle et al., ‘Shear Properties of Brain Tissue over a Frequency Range Relevant for Automotive Impact Situations: New Experimental Results’, *Stapp Car Crash J.*, vol. 48, pp. 239–258, Nov. 2004 [Online]. Available: 10.4271/2004-22-0011.

[63] S. Budday et al., ‘Viscoelastic parameter identification of human brain tissue’, *J. Mech. Behav. Biomed. Mater.*, vol. 74, pp. 463–476, Oct. 2017 [Online]. Available: 10.1016/j.jmbbm.2017.07.014.

[64] G. Z. Voyiadjis and A. Samadi-Dooki, ‘Hyperelastic modeling of the human brain tissue: Effects of no-slip boundary condition and compressibility on the uniaxial deformation’, *J. Mech. Behav. Biomed. Mater.*, vol. 83, pp. 63–78, Jul. 2018 [Online]. Available: 10.1016/j.jmbbm.2018.04.011.

[65] A. Tamura et al., ‘Mechanical Characterization of Brain Tissue in High-Rate Compression’, *J. Biomech. Sci. Eng.*, vol. 2, no. 3, pp. 115–126, 2007 [Online]. Available: 10.1299/jbse.2.115.

[66] S. Chatelin, ‘Improvement of Traumatic Brain Injury understanding in case of Head Trauma: Heterogeneity and anisotropy inclusion using medical imaging’, 2010 [Online]. Available: 10.13140/2.1.3771.6481.

[67] L. Bilston et al., ‘Large strain behaviour of brain tissue in shear: Some experimental data and differential constitutive model’, *Biorheology*, vol. 38, pp. 335–45, Feb. 2001.

[68] L. E. Bilston, ‘Brain Tissue Mechanical Properties’, in *Biomechanics of the Brain*, K. Miller, Ed. New York, NY: Springer, 2011, pp. 69–89[Online]. Availablehttps://doi.org/10.1007/978-1-4419-9997-9_4[Accessed: 20March2024].

[69] X. Jin et al., ‘A comprehensive experimental study on material properties of human brain tissue’, *J. Biomech.*, vol. 46, no. 16, pp. 2795–2801, Nov. 2013 [Online]. Available: 10.1016/j.jbiomech.2013.09.001.

[70] B. Rashid et al., ‘Mechanical characterization of brain tissue in compression at dynamic strain rates’, *J. Mech. Behav. Biomed. Mater.*, vol. 10, pp. 23–38, Jun. 2012 [Online]. Available: 10.1016/j.jmbbm.2012.01.022.

[71] A. Anssari-Benam, ‘Comparative modelling results between a separable and a non-separable form of principal stretches–based strain energy functions for a variety of isotropic incompressible soft solids: Ogden model compared with a parent model’, *Mech. Soft Mater.*, vol. 5, no. 1, p. 2, Dec. 2023 [Online]. Available: 10.1007/s42558-023-00050-z.

[72] F. Pervin and W. W. Chen, ‘Dynamic mechanical response of bovine gray matter and white matter brain tissues under compression’, *J. Biomech.*, vol. 42, no. 6, pp. 731–735, Apr. 2009 [Online]. Available: 10.1016/j.jbiomech.2009.01.023.

[73] F. Pervin and W. W. Chen, ‘Mechanically Similar Gel Simulants for Brain Tissues’, in *Dynamic Behavior of Materials, Volume 1*, New York, NY, 2011, pp. 9–13 [Online]. Available: 10.1007/978-1-4419-8228-5_3.

[74] M. S. Lazarjan et al., ‘Experimental investigation of the mechanical properties of brain simulants used for cranial gunshot simulation’, *Forensic Sci. Int.*, vol. 239, pp. 73–78, Jun. 2014 [Online]. Available: 10.1016/j.forsciint.2014.03.022.

[75] K. Yue et al., ‘Synthesis, properties, and biomedical applications of gelatin methacryloyl (GelMA) hydrogels’, *Biomaterials*, vol. 73, pp. 254–271, Dec. 2015 [Online]. Available: 10.1016/j.biomaterials.2015.08.045.

[76] K. Cui and J. P. Gong, ‘Aggregated structures and their functionalities in hydrogels’, *Aggregate*, vol. 2, no. 2, p. e33, 2021 [Online]. Available: 10.1002/agt2.33.

[77] L. Lu et al., ‘The Formation Mechanism of Hydrogels’, *Curr. Stem Cell Res. Ther.*, vol. 13, no. 7, pp. 490–496.

[78] Z. Liao et al., ‘On the stress recovery behaviour of Ecoflex silicone rubbers’, *Int. J. Mech. Sci.*, vol. 206, p. 106624, Sep. 2021 [Online]. Available: 10.1016/j.ijmecsci.2021.106624.

[79] S. H. Lee et al., ‘Acoustic metamaterial with negative modulus’, *J. Phys. Condens. Matter*, vol. 21, no. 17, p. 175704, Apr. 2009 [Online]. Available: 10.1088/0953-8984/21/17/175704.

[80] B. Sharma and C. Sun, ‘Acoustic metamaterial with negative modulus and a double negative structure’, 2015[Online]. Availablehttps://arxiv.org/abs/1501.02833[Accessed: 11March2024].

[81] R. Zhou et al., *Validation of the GHBMC Small Female Head Model and Development of Crash Induced Injury Tolerance for Head Injury Prediction*. 2017.

[82] D. Lyu et al., ‘Development and Validation of a New Anisotropic Visco-Hyperelastic Human Head Finite Element Model Capable of Predicting Multiple Brain Injuries’, Front.Bioeng.Biotechnol.,vol.10,Mar.2022[Online].Availablehttps://www.frontiersin.org/journals/bioengineering-andbiotechnology/articles/10.3389/fbioe.2022.831595/full.

[83] B. Pakkenberg and H. J. Gundersen, 'Neocortical neuron number in humans: effect of sex and age', *J Comp Neurol*, vol. 384, no. 2, pp. 312–320, Jul. 1997.

[84] E. Courchesne et al., 'Normal brain development and aging: quantitative analysis at in vivo MR imaging in healthy volunteers', *Radiology*, vol. 216, no. 3, pp. 672–682, Sep. 2000 [Online]. Available: 10.1148/radiology.216.3.r00au37672.

[85] J. S. Allen et al., 'Normal neuroanatomical variation in the human brain: an MRI-volumetric study', *Am J Phys Anthropol*, vol. 118, no. 4, pp. 341–358, Aug. 2002 [Online]. Available: 10.1002/ajpa.10092.

[86] K. P. Cosgrove et al., 'Evolving Knowledge of Sex Differences in Brain Structure, Function, and Chemistry', *Biological Psychiatry*, vol. 62, no. 8, pp. 847–855, Oct. 2007 [Online]. Available: 10.1016/j.biopsych.2007.03.001.

## Chapter 4 References

[1] A. E. Forte et al., 'On the characterization of the heterogeneous mechanical response of human brain tissue', *Biomech Model Mechanobiol*, vol. 16, no. 3, pp. 907–920, Jun. 2017 [Online]. Available: 10.1007/s10237-016-0860-8.

[2] A. Chanda et al., 'Biofidelic human brain tissue surrogates', *Mechanics of Advanced Materials and Structures*, vol. 25, no. 15–16, pp. 1335–1341, Dec. 2018 [Online]. Available: 10.1080/15376494.2016.1143749.

[3] D. Singh et al., 'Comparison of porcine brain mechanical properties to potential tissue simulant materials in quasi-static and sinusoidal compression', *Journal of Biomechanics*, vol. 92, pp. 84–91, Jul. 2019 [Online]. Available: 10.1016/j.jbiomech.2019.05.033.

[4] M. Navarro-Lozoya et al., 'Development of phantom material that resembles compression properties of human brain tissue for training models', *Materialia*, vol. 8, p. 100438, Dec. 2019 [Online]. Available: 10.1016/j.mtla.2019.100438.

[5] L. Falland-Cheung et al., 'Investigation of the elastic modulus, tensile and flexural strength of five skull simulant materials for impact testing of a forensic skin/skull/brain model', *Journal of*

*the Mechanical Behavior of Biomedical Materials*, vol. 68, pp. 303–307, Apr. 2017 [Online]. Available: 10.1016/j.jmbbm.2017.02.023.

[6] L. Falland-Cheung et al., 'Elastic behavior of brain simulants in comparison to porcine brain at different loading velocities', *Journal of the Mechanical Behavior of Biomedical Materials*, vol. 77, pp. 609–615, Jan. 2018 [Online]. Available: 10.1016/j.jmbbm.2017.10.026.

[7] S. M. H. Ahmadzadeh and D. W. Hukins, 'Feasibility of using mixtures of silicone elastomers and silicone oils to model the mechanical behaviour of biological tissues', *Proc Inst Mech Eng H*, vol. 228, no. 7, pp. 730–734, Jul. 2014 [Online]. Available: 10.1177/0954411914540138.

[8] A. E. Forte et al., 'A composite hydrogel for brain tissue phantoms', *Materials & Design*, vol. 112, pp. 227–238, Dec. 2016 [Online]. Available: 10.1016/j.matdes.2016.09.063.

[9] A. Tejo-Otero et al., 'Soft-Tissue-Mimicking Using Hydrogels for the Development of Phantoms', *Gels*, vol. 8, no. 1, p. 40, Jan. 2022 [Online]. Available: 10.3390/gels8010040.

[10] L. Zhang et al., 'The mechanical behavior of brain surrogates manufactured from silicone elastomers', *Journal of the Mechanical Behavior of Biomedical Materials*, vol. 95, pp. 180–190, Jul. 2019 [Online]. Available: 10.1016/j.jmbbm.2019.04.005.

[11] B. Zhang et al., '3D printed bone tissue regenerative PLA/HA scaffolds with comprehensive performance optimizations', *Materials & Design*, vol. 201, p. 109490, Mar. 2021 [Online]. Available: 10.1016/j.matdes.2021.109490.

[12] C. K. McGarry et al., 'Tissue mimicking materials for imaging and therapy phantoms: a review', *Phys. Med. Biol.*, Sep. 2020[Online]. Availablehttps://iopscience.iop.org/article/10.1088/1361-6560/abbd17[Accessed: 2May2023].

[13] B. Ondruschka et al., 'A biomechanical comparison between human calvarial bone and a skull simulant considering the role of attached periosteum and dura mater', *Int J Legal Med*, vol. 133, no. 5, pp. 1603–1610, Sep. 2019 [Online]. Available: 10.1007/s00414-019-02102-4.

[14] B. Lal et al., 'A novel economically viable solution for 3D printing-assisted cranioplast fabrication', *British Journal of Neurosurgery*, vol. 34, no. 3, pp. 280–283, May 2020 [Online]. Available: 10.1080/02688697.2020.1726289.

[15] R. Mantecón et al., ‘Additive Manufacturing and Mechanical Characterization of PLA-Based Skull Surrogates’, *Polymers*, vol. 15, no. 1, p. 58, Dec. 2022 [Online]. Available: 10.3390/polym15010058.

[16] B. P. Mahammod et al., ‘Investigation of Physico-mechanical Behavior, Permeability and Wall Shear Stress of Porous HA/PMMA Composite Bone Scaffold’, *Arab J Sci Eng*, vol. 45, no. 7, pp. 5505–5515, Jul. 2020 [Online]. Available: 10.1007/s13369-020-04467-w.

[17] B. J. Henwood and G. Appleby-Thomas, ‘The suitability of Synbone® as a tissue analogue in ballistic impacts’, *J Mater Sci*, vol. 55, no. 7, pp. 3022–3033, Mar. 2020 [Online]. Available: 10.1007/s10853-019-04231-y.

[18] Y. Han et al., ‘Three-Dimensional Printing of Hydroxyapatite Composites for Biomedical Application’, *Crystals*, vol. 11, no. 4, p. 353, Mar. 2021 [Online]. Available: 10.3390/cryst11040353.

[19] A. D. Drozdov and J. deC. Christiansen, ‘Tension–compression asymmetry in the mechanical response of hydrogels’, *Journal of the Mechanical Behavior of Biomedical Materials*, vol. 110, p. 103851, Oct. 2020 [Online]. Available: 10.1016/j.jmbbm.2020.103851.

[20] T. Distler et al., ‘Alginate-based hydrogels show the same complex mechanical behavior as brain tissue’, *Journal of the Mechanical Behavior of Biomedical Materials*, vol. 111, p. 103979, Nov. 2020 [Online]. Available: 10.1016/j.jmbbm.2020.103979.

[21] S. Budday et al., ‘Mechanical characterization of human brain tissue’, *Acta Biomaterialia*, vol. 48, pp. 319–340, Jan. 2017 [Online]. Available: 10.1016/j.actbio.2016.10.036.

[22] S. Budday et al., ‘Viscoelastic parameter identification of human brain tissue’, *Journal of the Mechanical Behavior of Biomedical Materials*, vol. 74, pp. 463–476, Oct. 2017 [Online]. Available: 10.1016/j.jmbbm.2017.07.014.

[23] S. Budday et al., ‘Fifty Shades of Brain: A Review on the Mechanical Testing and Modeling of Brain Tissue’, *Arch Computat Methods Eng*, vol. 27, no. 4, pp. 1187–1230, Sep. 2020 [Online]. Available: 10.1007/s11831-019-09352-w.

[24] S. Budday et al., ‘Rheological characterization of human brain tissue’, *Acta Biomaterialia*, vol. 60, pp. 315–329, Sep. 2017 [Online]. Available: 10.1016/j.actbio.2017.06.024.

[25] S. Budday et al., ‘Mechanical properties of gray and white matter brain tissue by indentation’, *Journal of the Mechanical Behavior of Biomedical Materials*, vol. 46, pp. 318–330, Jun. 2015 [Online]. Available: 10.1016/j.jmbbm.2015.02.024.

[26] S. Budday et al., ‘Towards microstructure-informed material models for human brain tissue’, *Acta Biomaterialia*, vol. 104, pp. 53–65, Mar. 2020 [Online]. Available: 10.1016/j.actbio.2019.12.030.

[27] S. Nicolle et al., ‘Shear Properties of Brain Tissue over a Frequency Range Relevant for Automotive Impact Situations: New Experimental Results’, *Stapp Car Crash J*, vol. 48, pp. 239–258, Nov. 2004 [Online]. Available: 10.4271/2004-22-0011.

[28] S. Chatelin, ‘Improvement of Traumatic Brain Injury understanding in case of Head Trauma: Heterogeneity and anisotropy inclusion using medical imaging’, 2010 [Online]. Available: 10.13140/2.1.3771.6481.

[29] B. Rashid et al., ‘Mechanical characterization of brain tissue in compression at dynamic strain rates’, *Journal of the Mechanical Behavior of Biomedical Materials*, vol. 10, pp. 23–38, Jun. 2012 [Online]. Available: 10.1016/j.jmbbm.2012.01.022.

[30] F. Boudjema et al., ‘Dynamical properties of the brain tissue under oscillatory shear stresses at large strain range’, *J. Phys.: Conf. Ser.*, vol. 790, p. 012002, Jan. 2017 [Online]. Available: 10.1088/1742-6596/790/1/012002.

[31] W. Li et al., ‘Dynamic mechanical characterization and viscoelastic modeling of bovine brain tissue’, *Journal of the Mechanical Behavior of Biomedical Materials*, vol. 114, p. 104204, Feb. 2021 [Online]. Available: 10.1016/j.jmbbm.2020.104204.

[32] W. Li et al., ‘Investigation of the Compressive Viscoelastic Properties of Brain Tissue Under Time and Frequency Dependent Loading Conditions’, *Ann Biomed Eng*, vol. 49, no. 12, pp. 3737–3747, Dec. 2021 [Online]. Available: 10.1007/s10439-021-02866-0.

[33] F. Pervin and W. W. Chen, ‘Dynamic mechanical response of bovine gray matter and white matter brain tissues under compression’, *Journal of Biomechanics*, vol. 42, no. 6, pp. 731–735, Apr. 2009 [Online]. Available: 10.1016/j.jbiomech.2009.01.023.

[34] D. B. MacManus and M. Ghajari, ‘Material properties of human brain tissue suitable for modelling traumatic brain injury’, *Brain Multiphysics*, vol. 3, p. 100059, 2022 [Online]. Available: 10.1016/j.brain.2022.100059.

[35] W. Zhao et al., ‘Material properties of the brain in injury-relevant conditions – Experiments and computational modeling’, *Journal of the Mechanical Behavior of Biomedical Materials*, vol. 80, pp. 222–234, Apr. 2018 [Online]. Available: 10.1016/j.jmbbm.2018.02.005.

[36] J. A. W. van Dommelen et al., ‘Mechanical Properties of Brain Tissue: Characterisation and Constitutive Modelling’, in *Mechanosensitivity of the Nervous System*, A. Kamkim and I. Kiseleva, Eds. Dordrecht: Springer Netherlands, 2009, pp. 249–279[Online]. Availablehttp://link.springer.com/10.1007/978-1-4020-8716-5_12[Accessed: 3February2023].

[37] E. Comellas et al., ‘Modeling the porous and viscous responses of human brain tissue behavior’, *Computer Methods in Applied Mechanics and Engineering*, vol. 369, p. 113128, Sep. 2020 [Online]. Available: 10.1016/j.cma.2020.113128.

[38] D. B. MacManus et al., ‘Region and species dependent mechanical properties of adolescent and young adult brain tissue’, *Sci Rep*, vol. 7, no. 1, p. 13729, Dec. 2017 [Online]. Available: 10.1038/s41598-017-13727-z.

[39] F. Eskandari et al., ‘Tension Strain-Softening and Compression Strain-Stiffening Behavior of Brain White Matter’, *Ann Biomed Eng*, vol. 49, no. 1, pp. 276–286, Jan. 2021 [Online]. Available: 10.1007/s10439-020-02541-w.

[40] C. S. von Bartheld et al., ‘The search for true numbers of neurons and glial cells in the human brain: A review of 150 years of cell counting: Quantifying neurons and glia in human brain’, *J. Comp. Neurol.*, vol. 524, no. 18, pp. 3865–3895, Dec. 2016 [Online]. Available: 10.1002/cne.24040.

[41] J. Faber et al., ‘Tissue-Scale Biomechanical Testing of Brain Tissue for the Calibration of Nonlinear Material Models’, *Current Protocols*, vol. 2, no. 4, Apr. 2022[Online]. Availablehttps://onlinelibrary.wiley.com/doi/10.1002/cpz1.381[Accessed: 19May2023].

[42] A. K. McCarty et al., ‘Viscoelastic properties of shock wave exposed brain tissue subjected to unconfined compression experiments’, *Journal of the Mechanical Behavior of Biomedical Materials*, vol. 100, p. 103380, Dec. 2019 [Online]. Available: 10.1016/j.jmbbm.2019.103380.

[43] J. A. Motherway et al., ‘The mechanical properties of cranial bone: The effect of loading rate and cranial sampling position’, *Journal of Biomechanics*, vol. 42, no. 13, pp. 2129–2135, Sep. 2009 [Online]. Available: 10.1016/j.jbiomech.2009.05.030.

[44] S. M. Ott, ‘Cortical or Trabecular Bone: What’s the Difference?’, *Am J Nephrol*, vol. 47, no. 6, pp. 373–375, 2018 [Online]. Available: 10.1159/000489672.

[45] E. Kohtanen et al., ‘Vibration-based elastic parameter identification of the diploë and cortical tables in dry cranial bones’, *Journal of the Mechanical Behavior of Biomedical Materials*, vol. 123, p. 104747, Nov. 2021 [Online]. Available: 10.1016/j.jmbbm.2021.104747.

[46] S. Boruah et al., ‘Variation of bone layer thicknesses and trabecular volume fraction in the adult male human calvarium’, *Bone*, vol. 77, pp. 120–134, Aug. 2015 [Online]. Available: 10.1016/j.bone.2015.04.031.

[47] J. H. C. Lee et al., ‘An Investigation on the Correlation between the Mechanical Properties of Human Skull Bone, Its Geometry, Microarchitectural Properties, and Water Content’, *Journal of Healthcare Engineering*, vol. 2019, pp. 1–8, May 2019 [Online]. Available: 10.1155/2019/6515797.

[48] S. Boruah et al., ‘Influence of bone microstructure on the mechanical properties of skull cortical bone – A combined experimental and computational approach’, *Journal of the Mechanical Behavior of Biomedical Materials*, vol. 65, pp. 688–704, Jan. 2017 [Online]. Available: 10.1016/j.jmbbm.2016.09.041.

[49] J. H. McElhaney et al., ‘Mechanical properties of cranial bone’, *Journal of Biomechanics*, vol. 3, no. 5, pp. 495–511, Oct. 1970 [Online]. Available: 10.1016/0021-9290(70)90059-X.

[50] A. D. Brown et al., ‘The mechanical response of commercially available bone simulants for quasi-static and dynamic loading’, *Journal of the Mechanical Behavior of Biomedical Materials*, vol. 90, pp. 404–416, Feb. 2019 [Online]. Available: 10.1016/j.jmbbm.2018.10.032.

[51] N. Petrone et al., ‘Feasibility of using a novel instrumented human head surrogate to measure helmet, head and brain kinematics and intracranial pressure during multidirectional impact tests’, *Journal of Science and Medicine in Sport*, vol. 22, pp. S78–S84, Aug. 2019 [Online]. Available: 10.1016/j.jsams.2019.05.015.

[52] N. Petrone et al., ‘A Novel Instrumented Human Head Surrogate for the Impact Evaluation of Helmets’, in *The 12th Conference of the International Sports Engineering Association*, 2018, p. 269[Online]. Availablehttps://www.mdpi.com/2504-3900/2/6/269[Accessed: 5March2023].

[53] Y. Bouattour et al., ‘A Minireview on Brain Models Simulating Geometrical, Physical, and Biochemical Properties of the Human Brain’, *Front. Bioeng. Biotechnol.*, vol. 10, p. 818201, Mar. 2022 [Online]. Available: 10.3389/fbioe.2022.818201.

[54] C. J. Freitas et al., ‘Dynamic Response Due to Behind Helmet Blunt Trauma Measured with a Human Head Surrogate’, *Int. J. Med. Sci.*, vol. 11, no. 5, pp. 409–425, 2014 [Online]. Available: 10.7150/ijms.8079.

[55] P. Mahoney et al., ‘Ballistic impacts on an anatomically correct synthetic skull with a surrogate skin/soft tissue layer’, *Int J Legal Med*, vol. 132, no. 2, pp. 519–530, Mar. 2018 [Online]. Available: 10.1007/s00414-017-1737-9.

[56] A. Singh et al., ‘Measurement of brain simulant strains in head surrogate under impact loading’, *Biomech Model Mechanobiol*, vol. 20, no. 6, pp. 2319–2334, Dec. 2021 [Online]. Available: 10.1007/s10237-021-01509-6.

[57] B. Stone et al., ‘A destructible headform for the assessment of sports impacts’, *Proceedings of the Institution of Mechanical Engineers, Part P: Journal of Sports Engineering and Technology*, vol. 237, no. 1, pp. 7–18, Mar. 2023 [Online]. Available: 10.1177/17543371211055905.

[58] S. Ganpule et al., ‘Mechanics of blast loading on the head models in the study of traumatic brain injury using experimental and computational approaches’, *Biomech Model Mechanobiol*, vol. 12, no. 3, pp. 511–531, Jun. 2013 [Online]. Available: 10.1007/s10237-012-0421-8.

[59] M. Jesunathadas et al., ‘Describing headform pose and impact location for blunt impact testing’, *Journal of Biomechanics*, vol. 109, p. 109923, Aug. 2020 [Online]. Available: 10.1016/j.jbiomech.2020.109923.

[60] D. Koncan et al., ‘Comparison of two anthropomorphic test devices using brain motion’, *Proceedings of the Institution of Mechanical Engineers, Part P: Journal of Sports Engineering and Technology*, vol. 232, no. 4, pp. 305–314, Dec. 2018 [Online]. Available: 10.1177/1754337117751741.

[61] R. E. Woodrow et al., ‘Acute thalamic connectivity precedes chronic post-concussive symptoms in mild traumatic brain injury’, *Brain*, p. awad056, Feb. 2023 [Online]. Available: 10.1093/brain/awad056.

[62] M. C. Dewan et al., ‘Estimating the global incidence of traumatic brain injury’, *Journal of Neurosurgery*, vol. 130, no. 4, pp. 1080–1097, Apr. 2019 [Online]. Available: 10.3171/2017.10.JNS17352.

[63] S. Premi et al., ‘Mechanical threshold for concussion based on computation of axonal strain using a finite element rat brain model’, *Brain Multiphysics*, vol. 2, p. 100032, 2021 [Online]. Available: 10.1016/j.brain.2021.100032.

[64] W. Peeters et al., ‘Epidemiology of traumatic brain injury in Europe’, *Acta Neurochir*, vol. 157, no. 10, pp. 1683–1696, Oct. 2015 [Online]. Available: 10.1007/s00701-015-2512-7.

[65] M. Ghajari et al., ‘Computational modelling of traumatic brain injury predicts the location of chronic traumatic encephalopathy pathology’, *Brain*, vol. 140, no. 2, pp. 333–343, Feb. 2017 [Online]. Available: 10.1093/brain/aww317.

[66] G. Critchley et al., ‘Epidemiology of Head Injury’, in *Traumatic Brain Injury*, 2nd ed., P. C. Whitfield, J. Welbourne, E. Thomas, F. Summers, M. Whyte, and P. J. Hutchinson, Eds. Cambridge University Press, 2020, pp. 1–11[Online]. Availablehttps://www.cambridge.org/core/product/identifier/9781108355247%23CN-bp-1/type/book_part[Accessed: 17April2024].

[67] A. Post and T. Blaine Hoshizaki, ‘Rotational Acceleration, Brain Tissue Strain, and the Relationship to Concussion’, *Journal of Biomechanical Engineering*, vol. 137, no. 3, p. 030801, Mar. 2015 [Online]. Available: 10.1115/1.4028983.

[68] T. B. Hoshizaki et al., ‘The development of a threshold curve for the understanding of concussion in sport’, *Trauma*, vol. 19, no. 3, pp. 196–206, Jul. 2017 [Online]. Available: 10.1177/1460408616676503.

[69] K. L. O’Connor et al., ‘Head-Impact–Measurement Devices: A Systematic Review’, *Journal of Athletic Training*, vol. 52, no. 3, pp. 206–227, Mar. 2017 [Online]. Available: 10.4085/1062-6050.52.2.05.

[70] L. White et al., ‘Scoring Systems for Trauma and Head Injury’, in *Traumatic Brain Injury*, 2nd ed., P. C. Whitfield, J. Welbourne, E. Thomas, F. Summers, M. Whyte, and P. J. Hutchinson, Eds. Cambridge University Press, 2020, pp. 57–64[Online]. Availablehttps://www.cambridge.org/core/product/identifier/9781108355247%23CN-bp-6/type/book_part[Accessed: 17April2024].

[71] C. E. Gaudet, ‘Immediate Post-Concussion and Cognitive Testing (ImPACT): Effects of Data Integration Strategies on Classification Accuracy’, *Journal of Head Trauma Rehabilitation*, vol. 37, no. 5, pp. E319–E326, Sep. 2022 [Online]. Available: 10.1097/HTR.0000000000000740.

[72] M. Hosseini-Farid et al., ‘The Strain Rates in the Brain, Brainstem, Dura, and Skull under Dynamic Loadings’, *MCA*, vol. 25, no. 2, p. 21, Apr. 2020 [Online]. Available: 10.3390/mca25020021.

[73] B. S. Elkin et al., ‘Brain tissue strains vary with head impact location: A possible explanation for increased concussion risk in struck versus striking football players’, *Clinical Biomechanics*, vol. 64, pp. 49–57, Apr. 2019 [Online]. Available: 10.1016/j.clinbiomech.2018.03.021.

[74] J. G. Beckwith et al., ‘Estimated Brain Tissue Response Following Impacts Associated With and Without Diagnosed Concussion’, *Ann Biomed Eng*, vol. 46, no. 6, pp. 819–830, Jun. 2018 [Online]. Available: 10.1007/s10439-018-1999-5.

[75] K. Bian and H. Mao, ‘Mechanisms and variances of rotation-induced brain injury: a parametric investigation between head kinematics and brain strain’, *Biomech Model Mechanobiol*, vol. 19, no. 6, pp. 2323–2341, Dec. 2020 [Online]. Available: 10.1007/s10237-020-01341-4.

[76] Y. Wang et al., ‘Development of a Photo-Crosslinking, Biodegradable GelMA/PEGDA Hydrogel for Guided Bone Regeneration Materials’, *Materials*, vol. 11, no. 8, p. 1345, Aug. 2018 [Online]. Available: 10.3390/ma11081345.

[77] B. R. Cobb et al., ‘Comparative analysis of helmeted impact response of Hybrid III and National Operating Committee on Standards for Athletic Equipment headforms’, *Proceedings of the Institution of Mechanical Engineers, Part P: Journal of Sports Engineering and Technology*, vol. 230, no. 1, pp. 50–60, Mar. 2016 [Online]. Available: 10.1177/1754337115599133.

[78] M. Hanna et al., ‘A Method for Evaluating Brain Deformation Under Sagittal Blunt Impacts Using a Half-Skull Human-Scale Surrogate’, *Journal of Biomechanical Engineering*, vol. 145, no. 6, p. 061001, Jun. 2023 [Online]. Available: 10.1115/1.4056547.

[79] L. Falland-Cheung et al., ‘Anatomical head model to measure impact force transfer through the head layers and their displacement’, *Journal of Concussion*, vol. 2, p. 2059700218777829, Jan. 2018 [Online]. Available: 10.1177/2059700218777829.

[80] Q. Wu et al., ‘Theoretical prediction model and failure mechanism map of human skull porous structures with quasi-static bending performance’, *International Journal of Mechanical Sciences*, vol. 200, p. 106431, Jun. 2021 [Online]. Available: 10.1016/j.ijmecsci.2021.106431.

[81] X. Zhai et al., ‘The effects of loading-direction and strain-rate on the mechanical behaviors of human frontal skull bone’, *Journal of the Mechanical Behavior of Biomedical Materials*, vol. 103, p. 103597, Mar. 2020 [Online]. Available: 10.1016/j.jmbbm.2019.103597.

[82] S. M. Pituru et al., ‘A Review on the Biocompatibility of PMMA-Based Dental Materials for Interim Prosthetic Restorations with a Glimpse into Their Modern Manufacturing Techniques’, *Materials*, vol. 13, no. 13, p. 2894, Jun. 2020 [Online]. Available: 10.3390/ma13132894.

[83] C. Polzin et al., ‘Characterization and evaluation of a PMMA-based 3D printing process’, *Rapid Prototyping Journal*, vol. 19, no. 1, pp. 37–43, Jan. 2013 [Online]. Available: 10.1108/13552541311292718.

[84] A. Ridwan-Pramana et al., ‘Finite element analysis of 6 large PMMA skull reconstructions: A multi-criteria evaluation approach’, *PLoS ONE*, vol. 12, no. 6, p. e0179325, Jun. 2017 [Online]. Available: 10.1371/journal.pone.0179325.

[85] P. K. Penumakala et al., ‘A critical review on the fused deposition modeling of thermoplastic polymer composites’, *Composites Part B: Engineering*, vol. 201, p. 108336, Nov. 2020 [Online]. Available: 10.1016/j.compositesb.2020.108336.

[86] J. M. Chacón et al., ‘Additive manufacturing of PLA structures using fused deposition modelling: Effect of process parameters on mechanical properties and their optimal selection’, *Materials & Design*, vol. 124, pp. 143–157, Jun. 2017 [Online]. Available: 10.1016/j.matdes.2017.03.065.

[87] M. Arora, ‘Polymethylmethacrylate bone cements and additives: A review of the literature’, *WJO*, vol. 4, no. 2, p. 67, 2013 [Online]. Available: 10.5312/wjo.v4.i2.67.

[88] D. P. Street et al., ‘Self-Complementary Multiple Hydrogen-Bonding Additives Enhance Thermomechanical Properties of 3D-Printed PMMA Structures’, *Macromolecules*, vol. 52, no. 15, pp. 5574–5582, Aug. 2019 [Online]. Available: 10.1021/acs.macromol.9b00546.

[89] G. W. Melenka et al., ‘Evaluation of dimensional accuracy and material properties of the MakerBot 3D desktop printer’, *Rapid Prototyping Journal*, vol. 21, no. 5, pp. 618–627, Aug. 2015 [Online]. Available: 10.1108/RPJ-09-2013-0093.

[90] J. Villacres et al., ‘Additive manufacturing of shape memory polymers: effects of print orientation and infill percentage on mechanical properties’, *RPJ*, vol. 24, no. 4, pp. 744–751, May 2018 [Online]. Available: 10.1108/RPJ-03-2017-0043.

[91] S. C. Daminabo et al., ‘Fused deposition modeling-based additive manufacturing (3D printing): techniques for polymer material systems’, *Materials Today Chemistry*, vol. 16, p. 100248, Jun. 2020 [Online]. Available: 10.1016/j.mtchem.2020.100248.

[92] H. Ramezani Dana et al., ‘Polymer additive manufacturing of ABS structure: Influence of printing direction on mechanical properties’, *Journal of Manufacturing Processes*, vol. 44, pp. 288–298, Aug. 2019 [Online]. Available: 10.1016/j.jmapro.2019.06.015.

[93] R. Zhou et al., *Validation of the GHBMC Small Female Head Model and Development of Crash Induced Injury Tolerance for Head Injury Prediction*. 2017.

[94] S. Boruah et al., ‘Response of Human Skull Bone to Dynamic Compressive Loading’, 2013.

[95] I. O. Smith et al., ‘Confocal laser scanning microscopy as a tool for imaging cancellous bone’, *Journal of Biomedical Materials Research Part B: Applied Biomaterials*, vol. 79B, no. 1, pp. 185–192, 2006 [Online]. Available: 10.1002/jbm.b.30529.

[96] C. S. Rajapakse et al., ‘Volumetric Cortical Bone Porosity Assessment with MR Imaging: Validation and Clinical Feasibility’, *Radiology*, vol. 276, no. 2, pp. 526–535, Aug. 2015 [Online]. Available: 10.1148/radiol.15141850.

[97] M. C. Wurnig et al., ‘Characterization of trabecular bone density with ultra-short echo-time MRI at 1.5, 3.0 and 7.0 T – comparison with micro-computed tomography’, *NMR in Biomedicine*, vol. 27, no. 10, pp. 1159–1166, 2014 [Online]. Available: 10.1002/nbm.3169.

[98] A. E. Jakus et al., ‘Hyperelastic “bone”: A highly versatile, growth factor–free, osteoregenerative, scalable, and surgically friendly biomaterial’, *Sci. Transl. Med.*, vol. 8, no. 358, Sep. 2016[Online]. Availablehttps://www.science.org/doi/10.1126/scitranslmed.aaf7704[Accessed: 29March2023].

[99] J. Zwirner et al., ‘The dynamic impact behavior of the human neurocranium’, *Sci Rep*, vol. 11, no. 1, p. 11331, May 2021 [Online]. Available: 10.1038/s41598-021-90322-3.

[100] K. Adanty et al., ‘The Mechanical Characterization and Comparison of Male and Female Calvaria Under Four-Point Bending Impacts’, *Journal of Biomechanical Engineering*, vol. 145, no. 5, p. 051009, May 2023 [Online]. Available: 10.1115/1.4056459.

[101] T. L. Roth et al., ‘Transcranial amelioration of inflammation and cell death after brain injury’, *Nature*, vol. 505, no. 7482, pp. 223–228, Jan. 2014 [Online]. Available: 10.1038/nature12808.

[102] D. R. Walsh et al., ‘Regional mechanical and biochemical properties of the porcine cortical meninges’, *Acta Biomaterialia*, vol. 80, pp. 237–246, Oct. 2018 [Online]. Available: 10.1016/j.actbio.2018.09.004.

[103] D. R. Walsh et al., ‘Mechanical Properties of the Cranial Meninges: A Systematic Review’, *Journal of Neurotrauma*, vol. 38, no. 13, pp. 1748–1761, Jul. 2021 [Online]. Available: 10.1089/neu.2020.7288.

[104] J. Zwirner et al., ‘Mechanical Properties of Human Dura Mater in Tension – An Analysis at an Age Range of 2 to 94 Years’, *Sci Rep*, vol. 9, no. 1, p. 16655, Nov. 2019 [Online]. Available: 10.1038/s41598-019-52836-9.

[105] D. R. Walsh et al., ‘Mechanical characterisation of the human dura mater, falx cerebri and superior sagittal sinus’, *Acta Biomaterialia*, vol. 134, pp. 388–400, Oct. 2021 [Online]. Available: 10.1016/j.actbio.2021.07.043.

[106] D. Lyu et al., ‘Development and Validation of a New Anisotropic Visco-Hyperelastic Human Head Finite Element Model Capable of Predicting Multiple Brain Injuries’, Front. Bioeng.Biotechnol.,vol.10,Mar.2022[Online].Availablehttps://www.frontiersin.org/journals/bioengineering-and-biotechnology/articles/10.3389/fbioe.2022.831595/full.

## Chapter 5 References

[1] N. Petrone et al., ‘Feasibility of using a novel instrumented human head surrogate to measure helmet, head and brain kinematics and intracranial pressure during multidirectional impact tests’, *Journal of Science and Medicine in Sport*, vol. 22, pp. S78–S84, Aug. 2019 [Online]. Available: 10.1016/j.jsams.2019.05.015.

[2] N. Petrone et al., ‘A Novel Instrumented Human Head Surrogate for the Impact Evaluation of Helmets’, in *The 12th Conference of the International Sports Engineering Association*, 2018, p. 269[Online]. Availablehttps://www.mdpi.com/2504-3900/2/6/269[Accessed: 5March2023].

[3] A. Singh et al., ‘Investigation of role of falx and tentorium on brain simulant strain under impact loading’, *Journal of Biomechanics*, vol. 144, p. 111347, Nov. 2022 [Online]. Available: 10.1016/j.jbiomech.2022.111347.

# *Appendix A — Additional Information for Brain Simulant Characterization*

The following Appendix A provides supplemental information towards the study found in Chapter 3 of this thesis. The material provided in this appendix will include additional data and figures to provide extended context to the results found in this work.

## Appendix A.1 — Quasi-Static Compression Tests

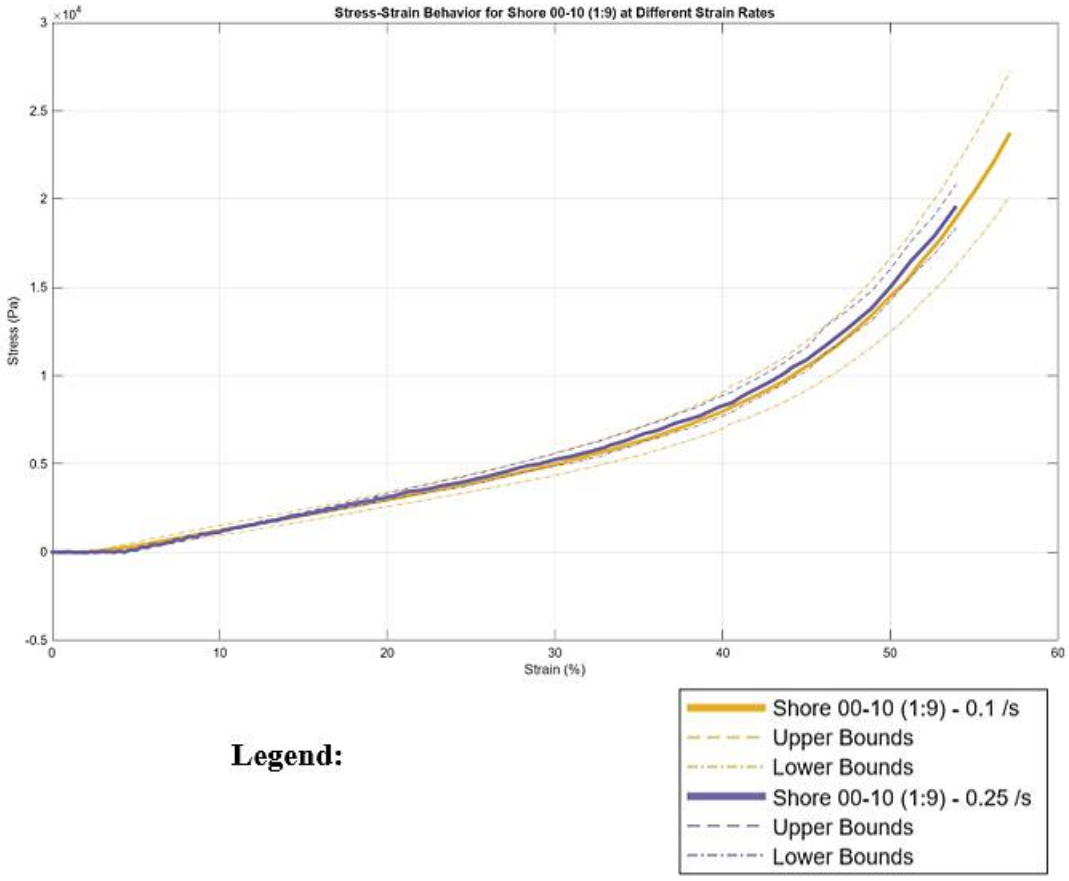


*Figure A1 — Alternating Strain Rate Performance of Shore 00-10 (1:9) at 0.1 $s^{-1}$ and 0.25 $s^{-1}$*

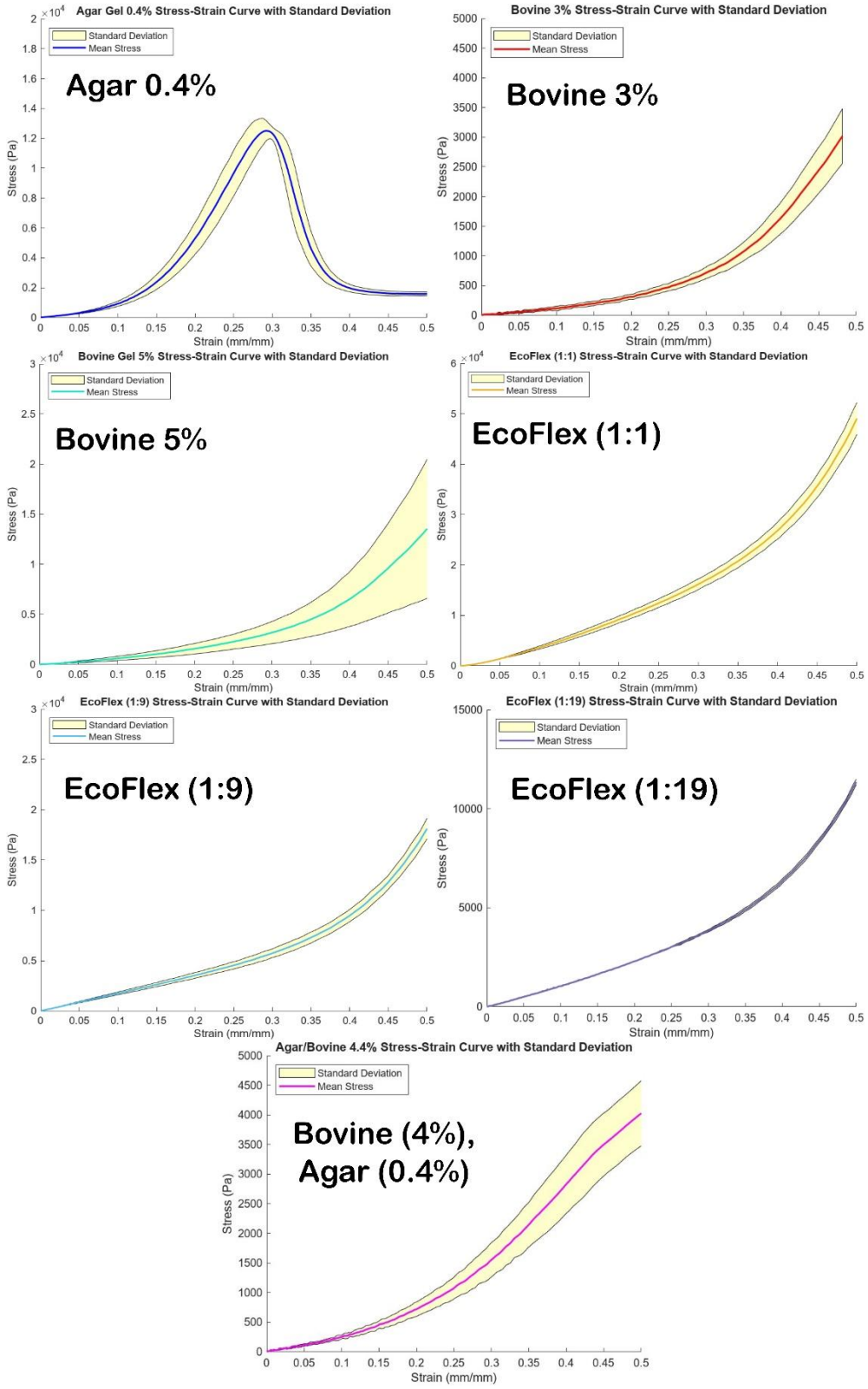


*Figure A2 — Standrd Deviated Mean Stress-Strain Curves*

## Appendix A.2 — Viscoelastic Frequency Sweep Tests

*Appendix A.2.1 — Shear Frequency Sweep*

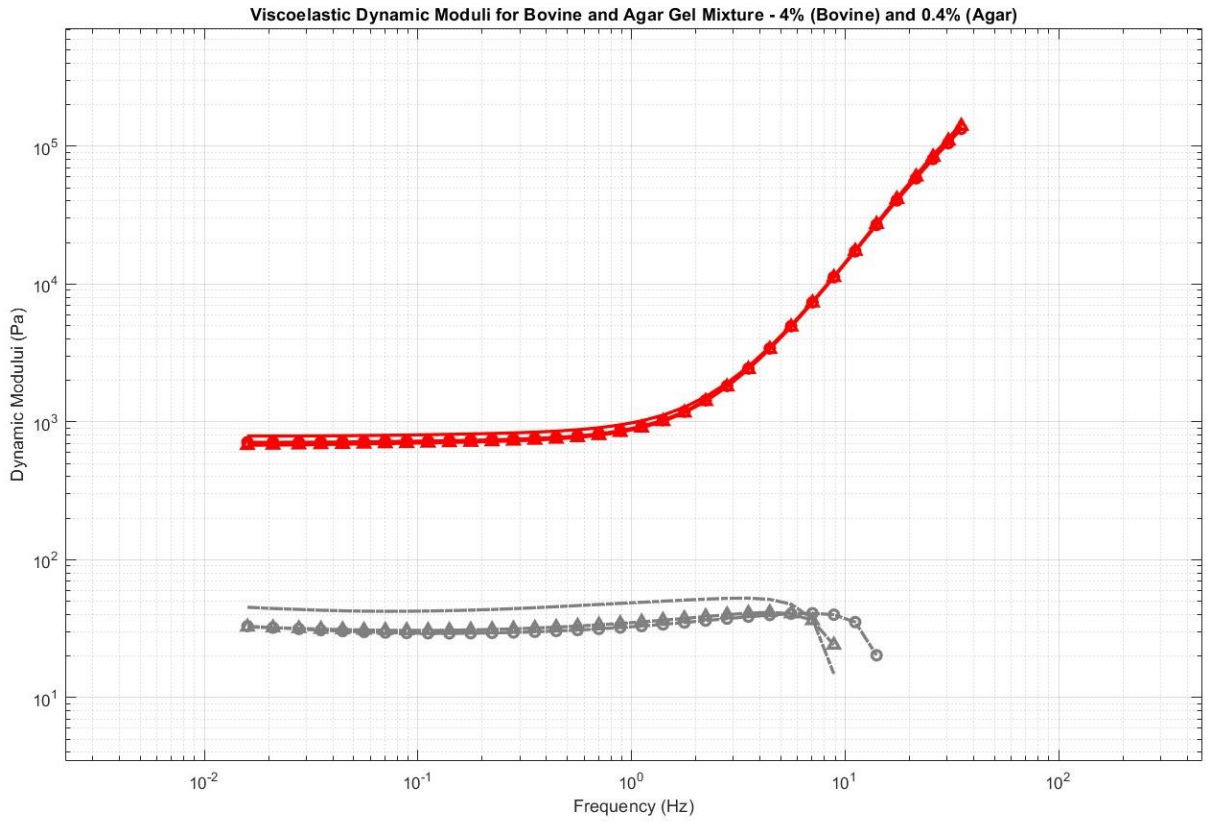


*Figure A3 — Storage and Loss Modulus Values in Shear for Bovine Gel at 3% Concentration*

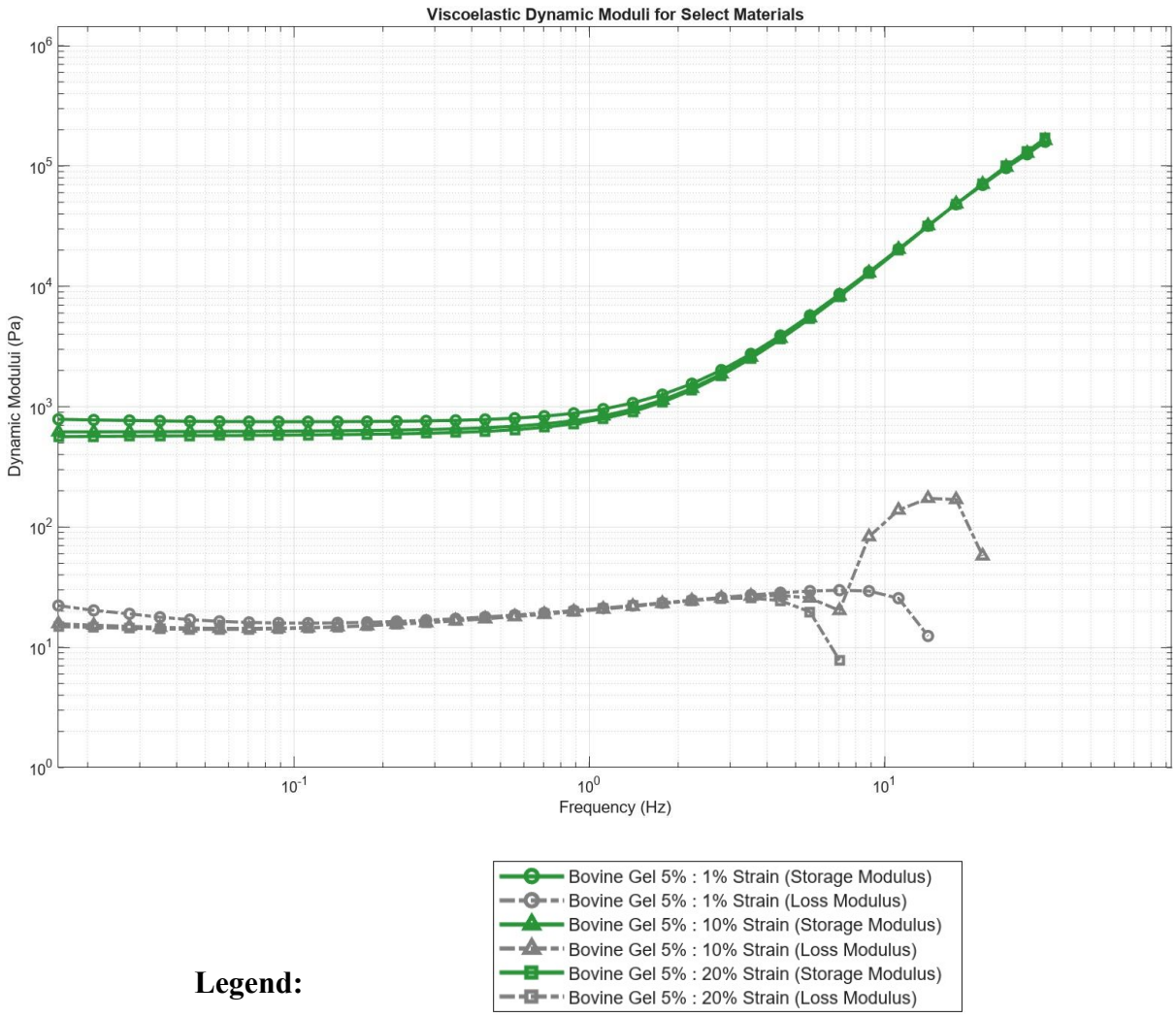


*Figure A4 — Storage and Loss Modulus Values in Shear for Bovine Gel at 3% Concentration*

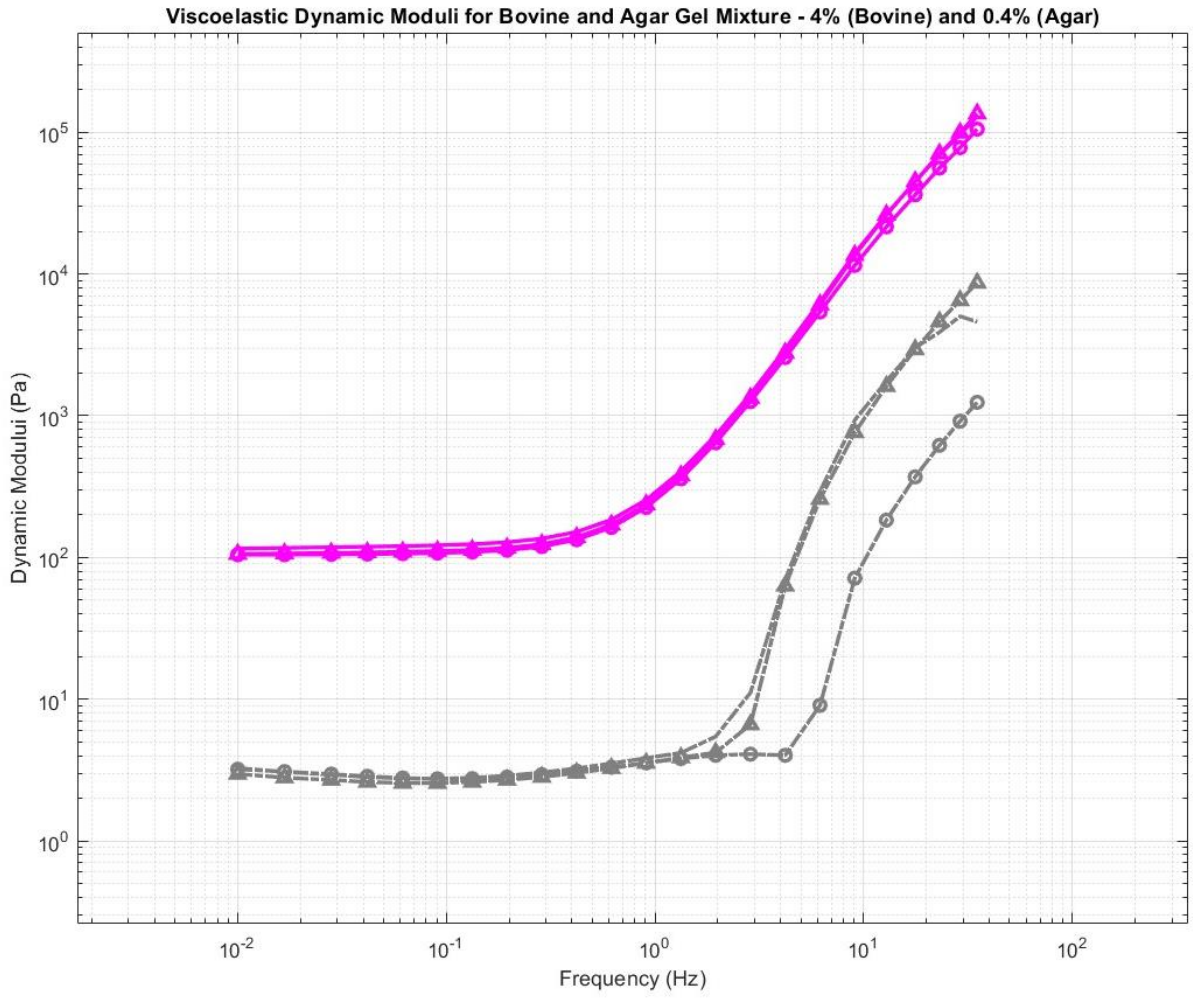


*Figure A5 — Storage and Loss Modulus Values in Shear for Bovine Gel, Agar Gel Mixture at 4% (Bovine), 0.4% (Agar) Concentrations*

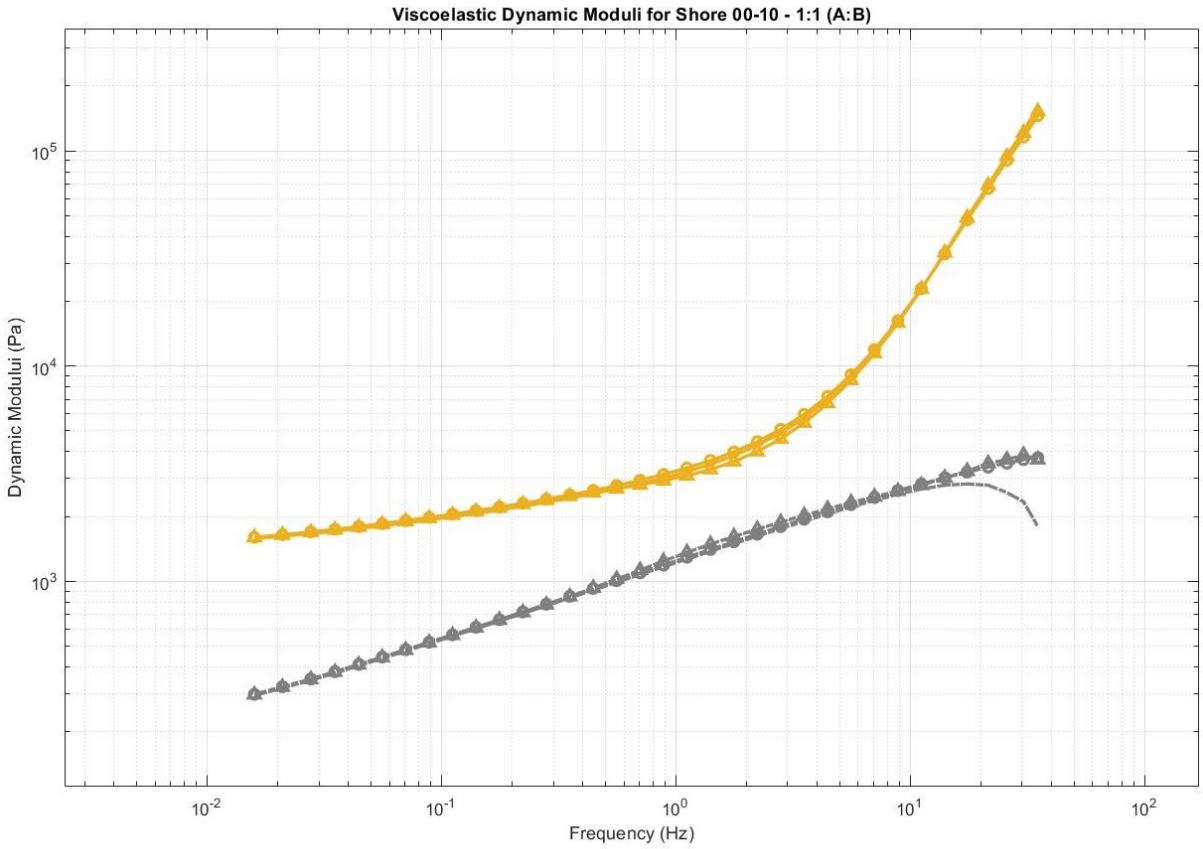


**Legend:**

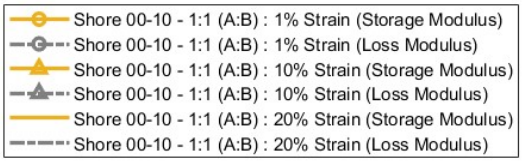


*Figure A6 — Storage and Loss Modulus Values in Shear for Shore 00-10 Silicone Elastomer at 1:1 (A:B) Concentration*

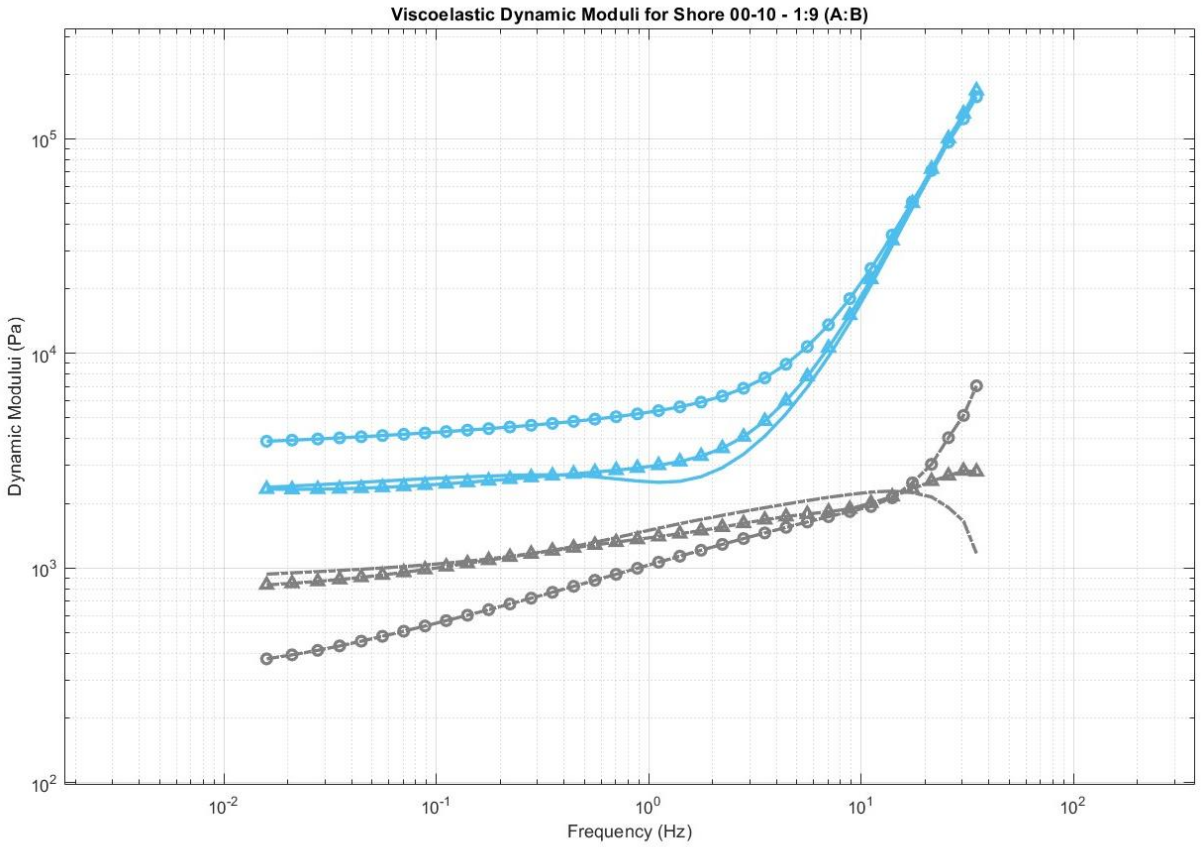


**Legend:**

- Shore 00-10 - 1:9 (A:B) : 1% Strain (Storage Modulus)
- Shore 00-10 - 1:9 (A:B) : 1% Strain (Loss Modulus)
- Shore 00-10 - 1:9 (A:B) : 10% Strain (Storage Modulus)
- Shore 00-10 - 1:9 (A:B) : 10% Strain (Loss Modulus)
- Shore 00-10 - 1:9 (A:B) : 20% Strain (Storage Modulus)
- Shore 00-10 - 1:9 (A:B) : 20% Strain (Loss Modulus)

*Figure A7 — Storage and Loss Modulus Values in Shear for Shore 00-10 Silicone Elastomer at 1:1 (A:B) Concentration*

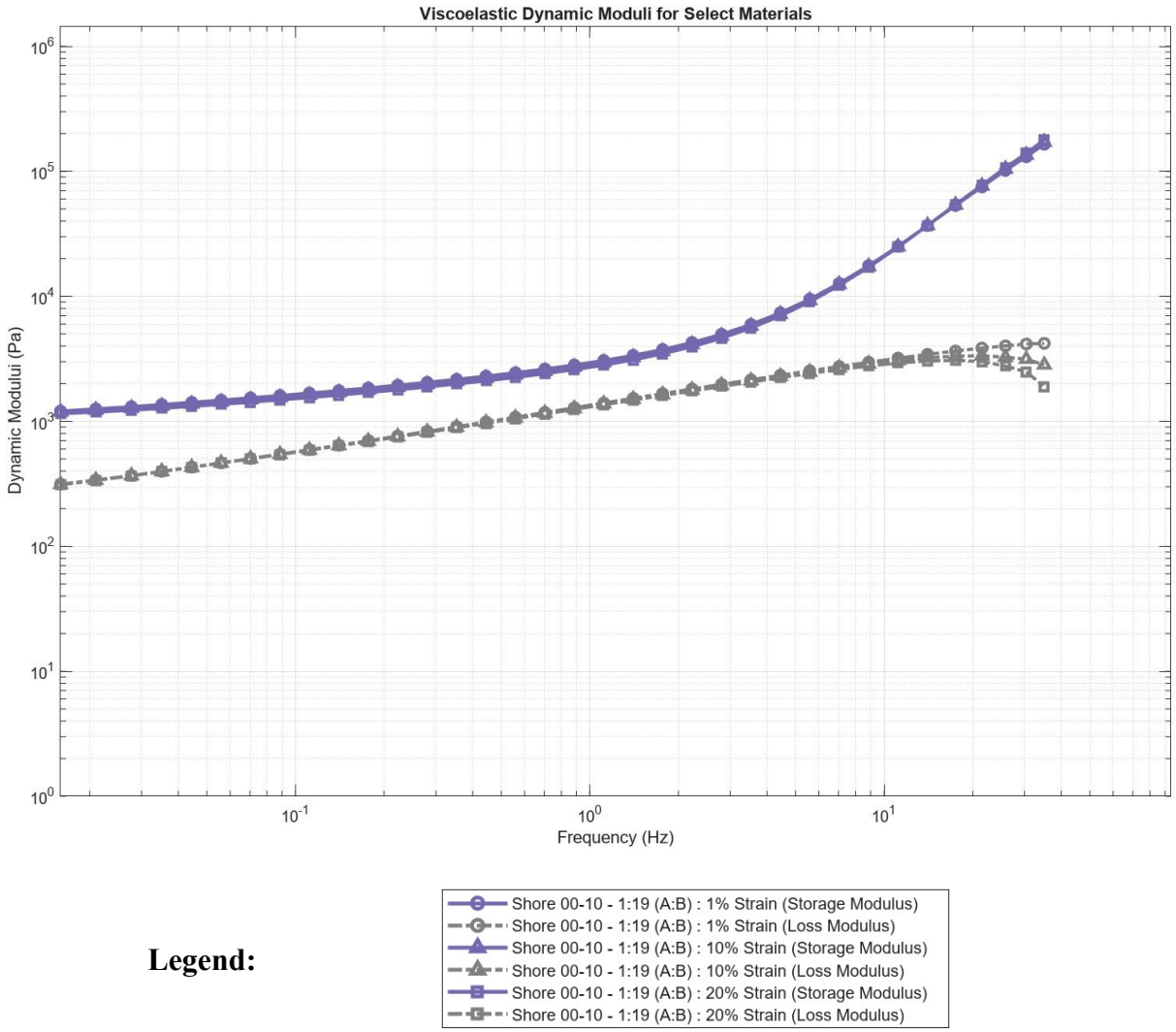


*Figure A8 — Storage and Loss Modulus Values in Shear for Shore 00-10 Silicone Elastomer at 1:19 (A:B) Concentration*

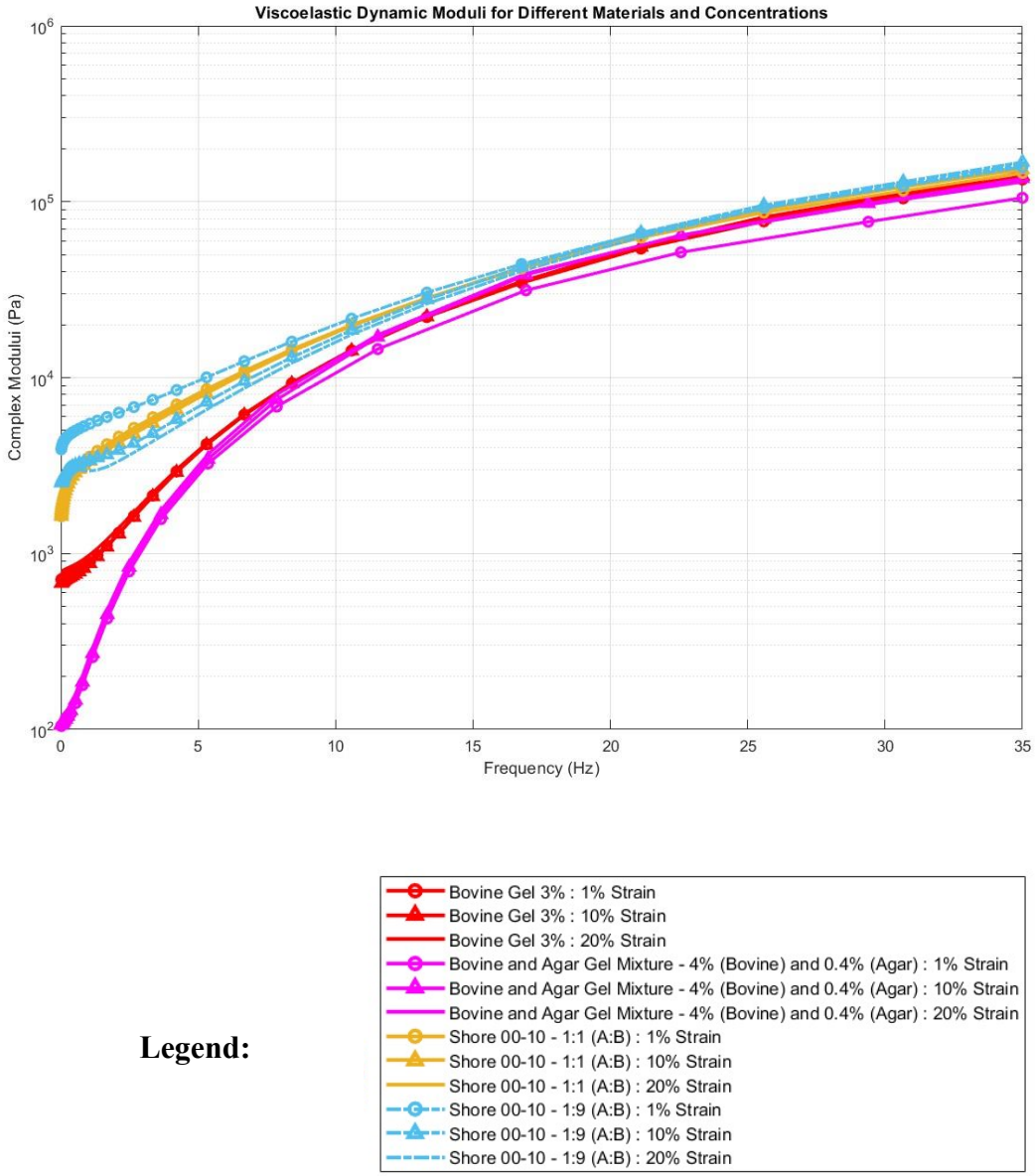


*Figure A9 — Complex Moduli of Tested Simulants in Shear Frequency Sweep*

*Table A14 — Tabulated Moduli Points for Frequency Sweep Tests in Shear (1% Strain)*

| Material | Frequency (Hz) | Moduli (Pa) | | | | | |
|---|---|---|---|---|---|---|---|
| | | Storage | S.D. (± Pa) | Loss | S.D. (± Pa) | Complex | S.D. (± Pa) |
| Shore 00-10 1:1 (50% A; 50% B) Mean Value | 0.5 | 4905.68 | 1392.85 | 869.67 | 200.88 | 4982.47 | 1406.26 |
| | 5 | 9202.09 | 1984.87 | 1633.37 | 409.61 | 9346.12 | 2025.81 |
| | 10 | 18846.00 | 2216.20 | 1929.12 | 527.10 | 18946.93 | 2257.51 |
| | 15 | 37435.30 | 2401.13 | 2142.24 | 599.26 | 37499.44 | 2430.58 |
| | 20 | 55227.37 | 2498.18 | 2244.06 | 636.66 | 55275.56 | 2521.22 |
| | 25 | 83237.77 | 2611.87 | 2329.86 | 675.69 | 83272.57 | 2628.86 |
| | 30 | 128803.33 | 3182.91 | 4632.81 | 3570.83 | 128933.67 | 3279.11 |
| | 35 | 156926.67 | 5501.19 | 7058.32 | 7129.17 | 157233.91 | 5863.68 |
| Shore 00-10 1:9 (10% A; 90% B) Mean Value | 0.5 | 2748.63 | 226.97 | 993.04 | 27.18 | 2922.94 | 223.04 |
| | 5 | 7629.04 | 277.56 | 2251.49 | 30.66 | 7954.49 | 274.68 |
| | 10 | 17158.80 | 309.01 | 2818.13 | 28.57 | 17388.70 | 309.22 |
| | 15 | 35096.23 | 343.80 | 3236.99 | 26.90 | 35245.19 | 344.45 |
| | 20 | 52137.13 | 370.40 | 3453.21 | 26.07 | 52251.36 | 370.86 |
| | 25 | 78884.35 | 374.44 | 3640.01 | 23.19 | 78968.29 | 374.75 |
| | 30 | 121110.00 | 422.44 | 3741.64 | 45.40 | 121167.80 | 423.46 |
| | 35 | 145692.50 | 459.77 | 3751.12 | 105.34 | 145740.80 | 462.18 |
| Shore 00-10 1:19 (5% A; 95% B) Mean Value | 0.5 | 2406.85 | 10.20 | 1061.51 | 16.31 | 2630.60 | 7.68 |
| | 5 | 7820.29 | 37.38 | 2507.87 | 28.82 | 8212.59 | 44.18 |
| | 10 | 18619.53 | 139.75 | 3180.79 | 35.07 | 18889.28 | 143.11 |
| | 15 | 38993.43 | 342.39 | 3681.12 | 40.22 | 39166.81 | 344.07 |
| | 20 | 58362.03 | 549.97 | 3939.85 | 44.14 | 58494.87 | 551.00 |
| | 25 | 88765.73 | 866.56 | 4163.49 | 52.28 | 88863.33 | 867.48 |
| | 30 | 136744.70 | 1422.83 | 4268.88 | 65.76 | 136811.30 | 1423.59 |
| | 35 | 164852.70 | 1606.18 | 4202.66 | 73.38 | 164906.20 | 1607.40 |
| Bovine Gel 4% and Agar Gel 0.4%, Mixed Mean Value | 0.5 | 775.34 | 310.23 | 30.67 | 14.77 | 775.95 | 310.63 |
| | 5 | 3558.30 | 343.32 | 41.17 | 19.24 | 3558.57 | 343.52 |
| | 10 | 11795.23 | 410.22 | 42.31 | 21.88 | 11795.32 | 410.30 |
| | 15 | 28351.58 | 591.74 | 33.33 | 23.56 | 28351.60 | 591.76 |
| | 20 | 44385.53 | 796.00 | 17.88 | 20.22 | 44385.53 | 795.98 |
| | 25 | 69742.70 | 1165.76 | -44.70 | 28.18 | 69742.72 | 1165.75 |
| | 30 | 109940.25 | 1765.45 | -212.88 | 41.88 | 109940.46 | 1765.43 |
| | 35 | 133751.25 | 2184.11 | -361.78 | 117.52 | 133751.79 | 2184.11 |
| Bovine Gel, 3% | 0.5 | 127.49 | 1.03 | 3.21 | 0.10 | 127.53 | 1.03 |
| | 5 | 1965.67 | 101.94 | 4.64 | 0.20 | 1965.67 | 101.94 |

| | | | | | | | |
|---|---|---|---|---|---|---|---|
| Mean Value | 10 | 8679.05 | 473.51 | 2.05 | 0.54 | 8679.05 | 473.51 |
| | 15 | 18515.40 | 1013.50 | 2.15 | 0.68 | 18515.40 | 1013.50 |
| | 20 | 39394.25 | 2052.65 | 133.95 | 83.83 | 39394.55 | 2052.92 |
| | 25 | | | | | | |
| | 30 | 86047.55 | 4895.45 | 1439.63 | 1542.07 | 86074.96 | 4868.10 |
| | 35 | 105242.90 | 6184.10 | 1242.66 | 1502.96 | 105262.10 | 6165.23 |
| Bovine Gel, 5% Mean Value | 0.5 | 784.953 | 138.42 | 18.36 | 3.12 | 785.1677 | 138.46 |
| | 5 | 4075.50 | 235.13 | 29.81 | 4.07 | 4075.61 | 235.15 |
| | 10 | 13905.80 | 523.71 | 31.93 | 4.32 | 13905.84 | 523.72 |
| | 15 | 33677.90 | 1107.54 | 25.77 | 4.84 | 33677.91 | 1107.55 |
| | 20 | 52846.95 | 1682.66 | 11.54 | 0.41 | 52846.95 | 1682.66 |
| | 25 | 83219.85 | 2586.23 | -43.91 | 3.86 | 83219.86 | 2586.24 |
| | 30 | 131284.00 | 4170.78 | -199.03 | 78.02 | 131284.20 | 4170.85 |
| | 35 | 159274.50 | 5022.28 | -326.05 | 170.22 | 159274.80 | 5022.44 |

*Table A15 — Tabulated Moduli Points for Frequency Sweep Tests in Shear (10% Strain)*

| **Material** | **Frequency (Hz)** | **Moduli (Pa)** | | | | | |
|---|---|---|---|---|---|---|---|
| | | **Storage** | **S.D. (± Pa)** | **Loss** | **S.D. (± Pa)** | **Complex** | **S.D. (± Pa)** |
| Shore 00-10 1:1 (50% A; 50% B) Mean Value | 0.5 | 2787.52 | 1268.41 | 1274.51 | 553.19 | 3162.73 | 1143.08 |
| | 5 | 6184.15 | 885.65 | 1884.05 | 691.29 | 6499.13 | 903.85 |
| | 10 | 15761.43 | 738.33 | 1771.66 | 650.18 | 15872.53 | 769.61 |
| | 15 | 34398.43 | 1613.16 | 2237.21 | 845.04 | 34480.50 | 1633.70 |
| | 20 | 54244.17 | 4303.92 | 2609.53 | 1245.81 | 54317.98 | 4344.18 |
| | 25 | 84579.63 | 7272.56 | 3586.41 | 2628.11 | 84686.86 | 7383.09 |
| | 30 | 136749.00 | 15810.92 | 2470.00 | 1561.10 | 136777.90 | 15831.08 |
| | 35 | 168003.30 | 19199.30 | 2809.65 | 2382.37 | 168039.50 | 19236.38 |
| Shore 00-10 1:9 (10% A; 90% B) Mean Value | 0.5 | 2713.96 | 224.98 | 986.85 | 27.15 | 2888.24 | 221.06 |
| | 5 | 7040.51 | 584.93 | 2330.11 | 196.90 | 7426.09 | 481.98 |
| | 10 | 16821.65 | 59.53 | 2751.45 | 35.92 | 17045.23 | 58.28 |
| | 15 | 35072.63 | 459.76 | 3044.35 | 105.99 | 35204.80 | 449.47 |
| | 20 | 52823.45 | 1033.57 | 3329.14 | 220.24 | 52928.48 | 1045.59 |
| | 25 | 82821.73 | 4896.36 | 3921.87 | 1319.93 | 82921.22 | 4960.53 |
| | 30 | 127846.80 | 7063.87 | 4865.63 | 3326.03 | 127973.70 | 7222.87 |
| | 35 | 152352.00 | 2200.91 | 3674.66 | 2001.79 | 152408.60 | 2261.97 |
| Shore 00-10 1:19 (5% A; 95% B) | 0.5 | 2320.04 | 27.14 | 1049.07 | 12.94 | 2546.29 | 20.98 |
| | 5 | 7623.20 | 10.93 | 2459.14 | 19.10 | 8010.04 | 15.95 |
| | 10 | 18286.53 | 114.98 | 3101.25 | 20.00 | 18547.65 | 116.18 |

| | | | | | | | |
|---|---|---|---|---|---|---|---|
| Mean Value | 15 | 38764.43 | 316.42 | 3489.38 | 21.33 | 38921.17 | 316.42 |
| | 20 | 58584.50 | 538.40 | 3605.94 | 25.03 | 58695.38 | 538.26 |
| | 25 | 90319.57 | 921.43 | 3551.90 | 42.54 | 90389.40 | 920.56 |
| | 30 | 140101.30 | 1283.09 | 3318.28 | 61.35 | 140140.60 | 1282.63 |
| | 35 | 171293.30 | 1776.20 | 2831.06 | 77.34 | 171316.80 | 1775.64 |
| Bovine Gel 4% and Agar Gel 0.4%, Mixed Mean Value | 0.5 | 756.67 | 299.4227 | 32.80798 | 13.94 | 757.38 | 299.74 |
| | 5 | 3523.54 | 331.6407 | 43.66433 | 18.20 | 3523.84 | 331.83 |
| | 10 | 11696.38 | 395.1362 | 34.41048 | 21.03 | 11696.44 | 395.19 |
| | 15 | 28422.95 | 601.2195 | -36.4519 | 21.69 | 28422.98 | 601.20 |
| | 20 | 44967.18 | 802.5949 | -145.707 | 21.81 | 44967.42 | 802.56 |
| | 25 | 71416.85 | 1336.702 | -383.731 | 71.04 | 71417.92 | 1336.74 |
| | 30 | 113593.30 | 1915.739 | -779.545 | 53.14 | 113595.90 | 1915.85 |
| | 35 | 139776.30 | 2307.089 | -1126.75 | 337.81 | 139781.20 | 2307.62 |
| Bovine Gel, 3% Mean Value | 0.5 | 108.26 | 1.0035 | 2.536585 | 0.19 | 108.29 | 1.00 |
| | 5 | 1956.32 | 100.04 | 5.37738 | 0.089 | 1956.33 | 100.04 |
| | 10 | 8609.06 | 457.12 | 44.9983 | 44.26 | 8609.30 | 456.88 |
| | 15 | 18654.85 | 804.15 | 501.7112 | 525.42 | 18669.62 | 789.39 |
| | 20 | 41477.50 | 1378.5 | 3310.465 | 588.34 | 41615.23 | 1327.14 |
| | 25 | | | | | | |
| | 30 | 94401.25 | 3610.55 | 9504.59 | 844.01 | 94886.14 | 3507.56 |
| | 35 | 117848.50 | 1900.5 | 11055.91 | 1852.30 | 118383.20 | 1718.93 |
| Bovine Gel, 5% Mean Value | 0.5 | 747.07 | 110.435 | 20.05545 | 3.42 | 747.34 | 110.49 |
| | 5 | 13778.55 | 486.3434 | 19.9835 | 4.17 | 13778.56 | 486.35 |
| | 10 | 13778.55 | 486.3434 | 19.9835 | 4.17 | 13778.56 | 486.35 |
| | 15 | 33802.65 | 1064.013 | -70.3954 | 7.45 | 33802.72 | 1064.02 |
| | 20 | 53517.40 | 3661.166 | -202.967 | 2750.63 | 53517.79 | 3782.72 |
| | 25 | 85011.05 | 2497.608 | -468.071 | 428.36 | 85012.35 | 2497.66 |
| | 30 | 135295.00 | 4132.643 | -955.456 | 645.76 | 135298.40 | 4133.96 |
| | 35 | 166756.00 | 5188.19 | -1584.55 | 816.1994 | 166763.5 | 5191.74 |

*Table A16 — Tabulated Moduli Points for Frequency Sweep Tests in Shear (20% Strain)*

| **Material** | **Frequency (Hz)** | **Moduli (Pa)** | | | | | |
|---|---|---|---|---|---|---|---|
| | | **Storage** | **S.D. (± Pa)** | **Loss** | **S.D. (± Pa)** | **Complex** | **S.D. (± Pa)** |
| Shore 00-10 1:1 (50% A; 50% B) | 0.5 | 3489.35 | 1293.83 | 1145.04 | 617.08 | 3714.31 | 1321.13 |
| | 5 | 6817.35 | 1915.43 | 1928.60 | 929.50 | 7161.89 | 1853.64 |
| | 10 | 16077.47 | 2204.07 | 2181.25 | 1033.51 | 16261.84 | 2172.89 |

| | | | | | | | |
|---|---|---|---|---|---|---|---|
| Mean Value | 15 | 34675.93 | 2187.95 | 2338.06 | 1117.28 | 34773.65 | 2171.46 |
| | 20 | 52660.87 | 2037.12 | 2371.06 | 1178.15 | 52727.82 | 2025.84 |
| | 25 | 81525.83 | 1376.72 | 2374.68 | 1280.97 | 81570.65 | 1365.97 |
| | 30 | 130264.00 | 699.86 | 4408.23 | 3910.22 | 130396.30 | 854.42 |
| | 35 | 163881.30 | 340.60 | 6476.37 | 7649.10 | 164187.50 | 352.95 |
| Shore 00-10 1:9 (10% A; 90% B) Mean Value | 0.5 | 2648.11 | 221.80 | 975.55 | 26.47 | 2822.54 | 217.64 |
| | 5 | 7384.21 | 270.10 | 2202.19 | 29.64 | 7705.76 | 267.17 |
| | 10 | 16799.33 | 299.56 | 2722.05 | 27.80 | 17018.45 | 299.77 |
| | 15 | 35042.78 | 332.51 | 2970.85 | 25.44 | 35168.48 | 333.10 |
| | 20 | 52837.95 | 792.50 | 3163.52 | 289.25 | 52933.11 | 808.96 |
| | 25 | 80389.40 | 690.51 | 2955.76 | 17.10 | 80443.72 | 690.19 |
| | 30 | 126509.00 | 668.44 | 2764.70 | 147.79 | 126539.30 | 670.79 |
| | 35 | 158258.80 | 989.57 | 1797.06 | 63.41 | 158269.00 | 989.19 |
| Shore 00-10 1:19 (5% A; 95% B) Mean Value | 0.5 | 2207.05 | 43.54 | 1035.11 | 12.02 | 2437.89 | 35.84 |
| | 5 | 7368.46 | 24.54 | 2398.75 | 7.90 | 7749.10 | 21.06 |
| | 10 | 17967.53 | 76.16 | 2986.75 | 3.13 | 18214.09 | 75.14 |
| | 15 | 38665.30 | 233.65 | 3262.76 | 6.90 | 38802.73 | 232.69 |
| | 20 | 58550.00 | 474.62 | 3305.39 | 13.62 | 58643.24 | 473.21 |
| | 25 | 90056.50 | 924.58 | 3259.10 | 66.93 | 90115.50 | 922.62 |
| | 30 | 143017.70 | 1349.63 | 2854.14 | 59.29 | 143046.20 | 1348.21 |
| | 35 | 178864.70 | 1966.27 | 1889.61 | 85.86 | 178874.70 | 1965.51 |
| Bovine Gel 4% and Agar Gel 0.4%, Mixed Mean Value | 0.5 | 862.093 | 265.60 | 46.52 | 11.81 | 863.35 | 265.85 |
| | 5 | 3633.33 | 298.11 | 54.16 | 13.99 | 3633.75 | 298.26 |
| | 10 | 11843.57 | 389.88 | 27.42 | 17.40 | 11843.61 | 389.90 |
| | 15 | 28890.90 | 639.26 | -101.57 | 23.31 | 28891.09 | 639.24 |
| | 20 | 45448.20 | 880.79 | -250.29 | 23.88 | 45448.90 | 880.77 |
| | 25 | 72005.67 | 1788.74 | -471.40 | 56.43 | 72007.23 | 1788.99 |
| | 30 | 116429.70 | 2256.33 | -903.11 | 71.99 | 116433.20 | 2256.80 |
| | 35 | 146675.00 | 2977.14 | -1889.94 | 76.73 | 146687.20 | 2977.80 |
| Bovine Gel, 3% Mean Value | 0.5 | 126.21 | 14.88 | 3.98 | 0.56 | 126.27 | 14.85 |
| | 5 | 1096.96 | 970.94 | 5.76 | 0.23 | 1097.02 | 970.89 |
| | 10 | 4616.01 | 4469.36 | 4.52 | 1.53 | 4616.08 | 4469.30 |
| | 15 | 9807.59 | 9641.11 | 15.81 | 9.49 | 9807.66 | 9641.06 |
| | 20 | 21506.43 | 21309.27 | 942.47 | 935.83 | 21527.07 | 21329.81 |
| | 25 | | | | | | |
| | 30 | 49895.69 | 49650.31 | 4515.70 | 4508.76 | 50099.85 | 49854.37 |
| | 35 | 59692.65 | 59371.35 | 4552.26 | 4544.99 | 59866.21 | 59544.82 |
| | 0.5 | 733.34 | 90.55 | 23.37 | 4.45 | 733.71 | 90.64 |

| | | | | | | | |
|---|---|---|---|---|---|---|---|
| Bovine Gel, 5% Mean Value | 5 | 4013.16 | 185.95 | 33.82 | 5.15 | 4013.30 | 185.98 |
| | 10 | 13840.30 | 479.94 | -0.39 | 3.62 | 13840.30 | 479.94 |
| | 15 | 34168.60 | 1055.42 | -155.55 | 9.57 | 34168.95 | 1055.45 |
| | 20 | 54032.80 | 1651.20 | -340.42 | 18.85 | 54033.87 | 1651.27 |
| | 25 | 86935.45 | 2996.44 | -718.59 | 179.21 | 86938.43 | 2997.53 |
| | 30 | 139579.50 | 4496.43 | -1363.34 | 178.91 | 139586.20 | 4497.80 |
| | 35 | 176269.50 | 5742.43 | -2301.32 | 130.75 | 176284.50 | 5743.46 |

## *Appendix A.2.2 — Compression Frequency Sweep*

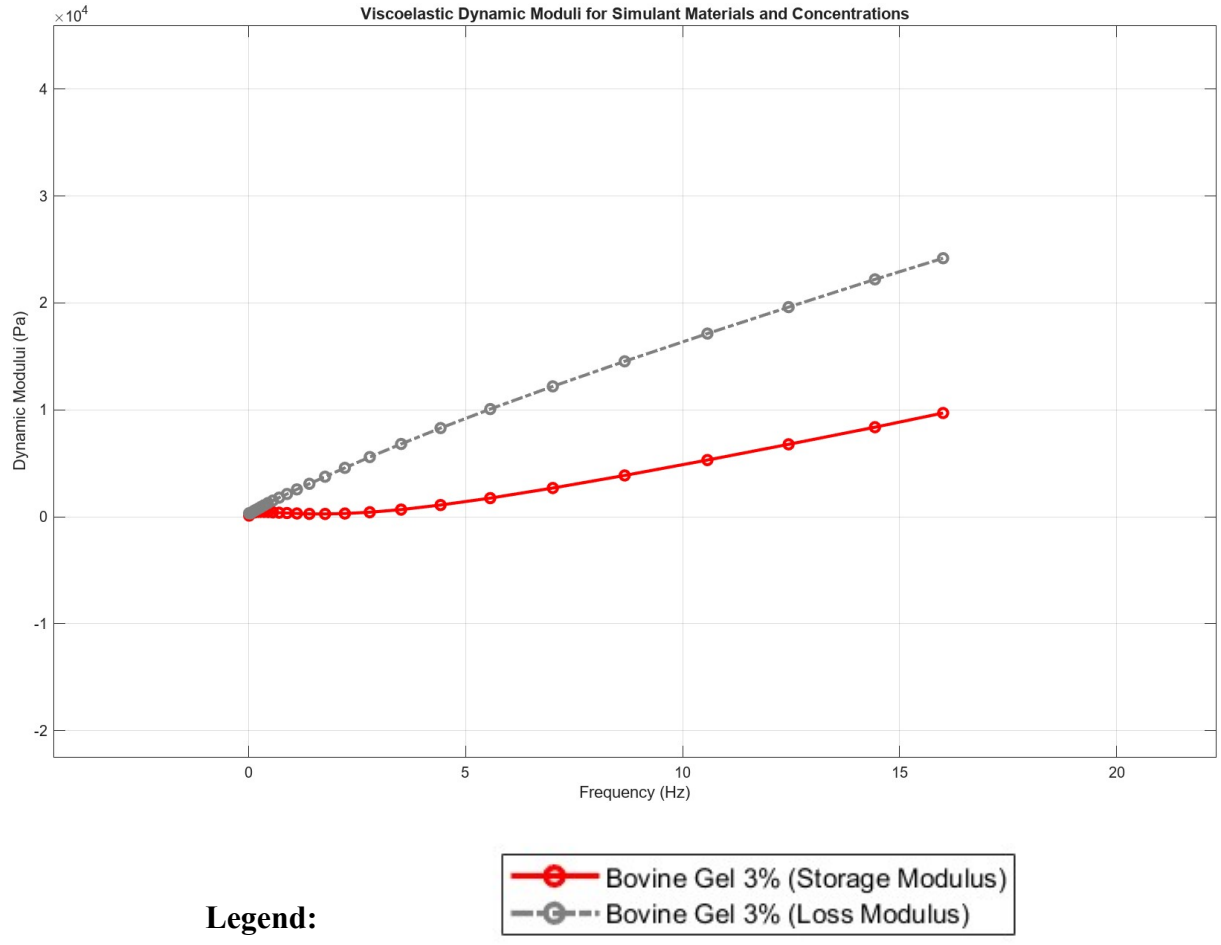


*Figure A10 — Storage and Loss Modulus Values in Compression for Bovine Gel at 3% Concentration*

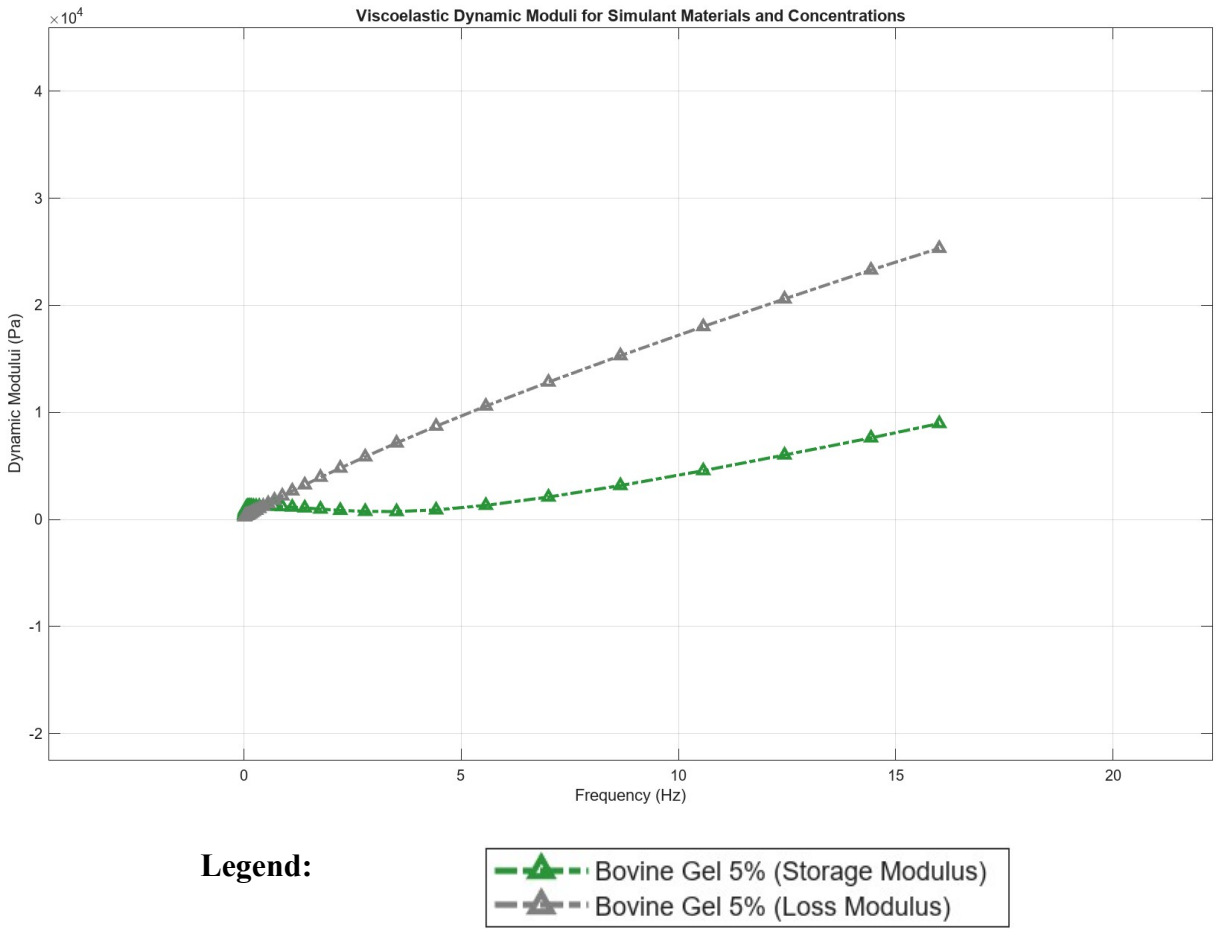


*Figure A11 — Storage and Loss Modulus Values in Compression for Bovine Gel at 5% Concentration*

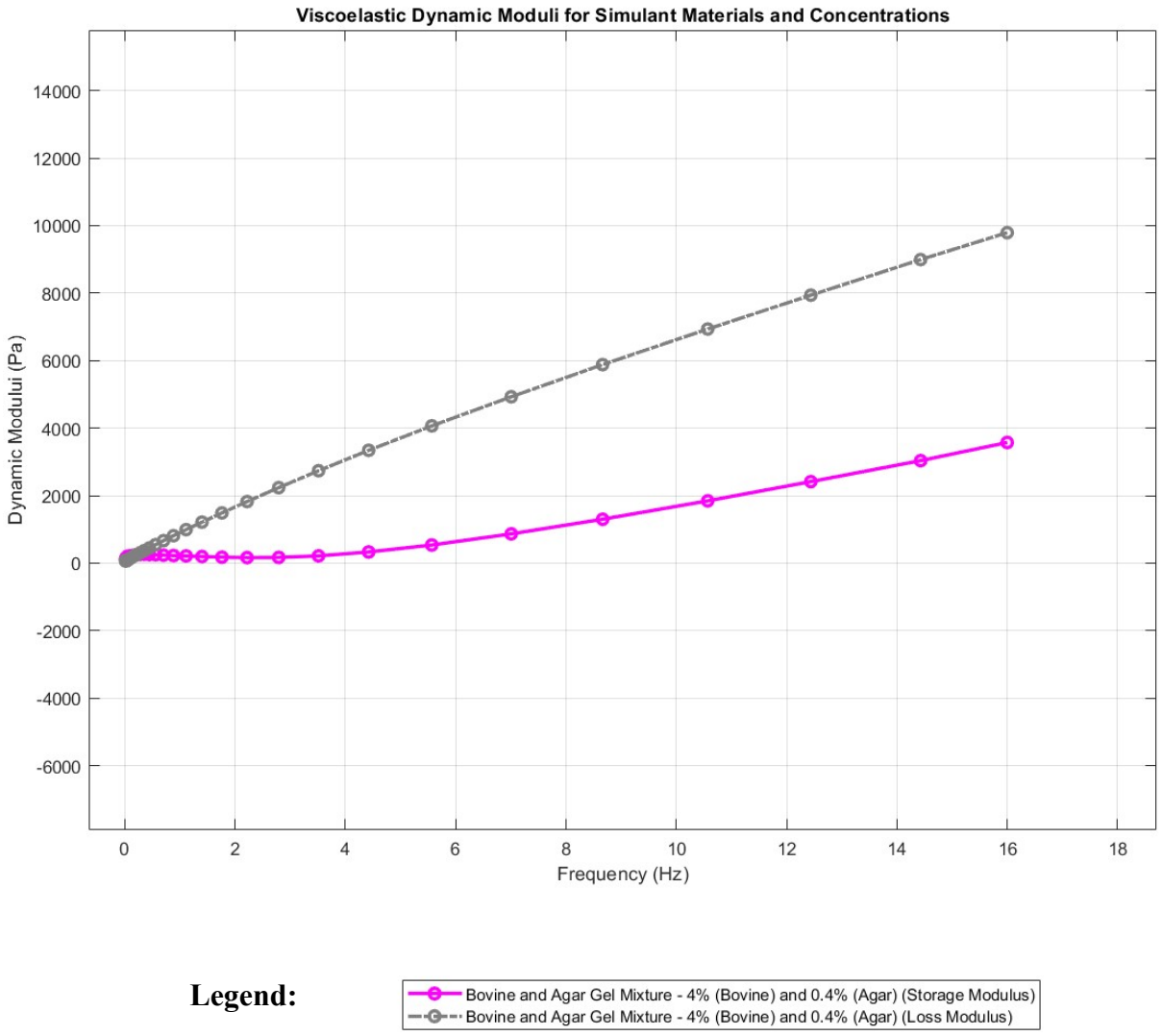


*Figure A12 — Storage and Loss Modulus Values in Compression for Bovine Gel, Agar Gel Mixture at 4% (Bovine), 0.4% (Agar) Concentrations*

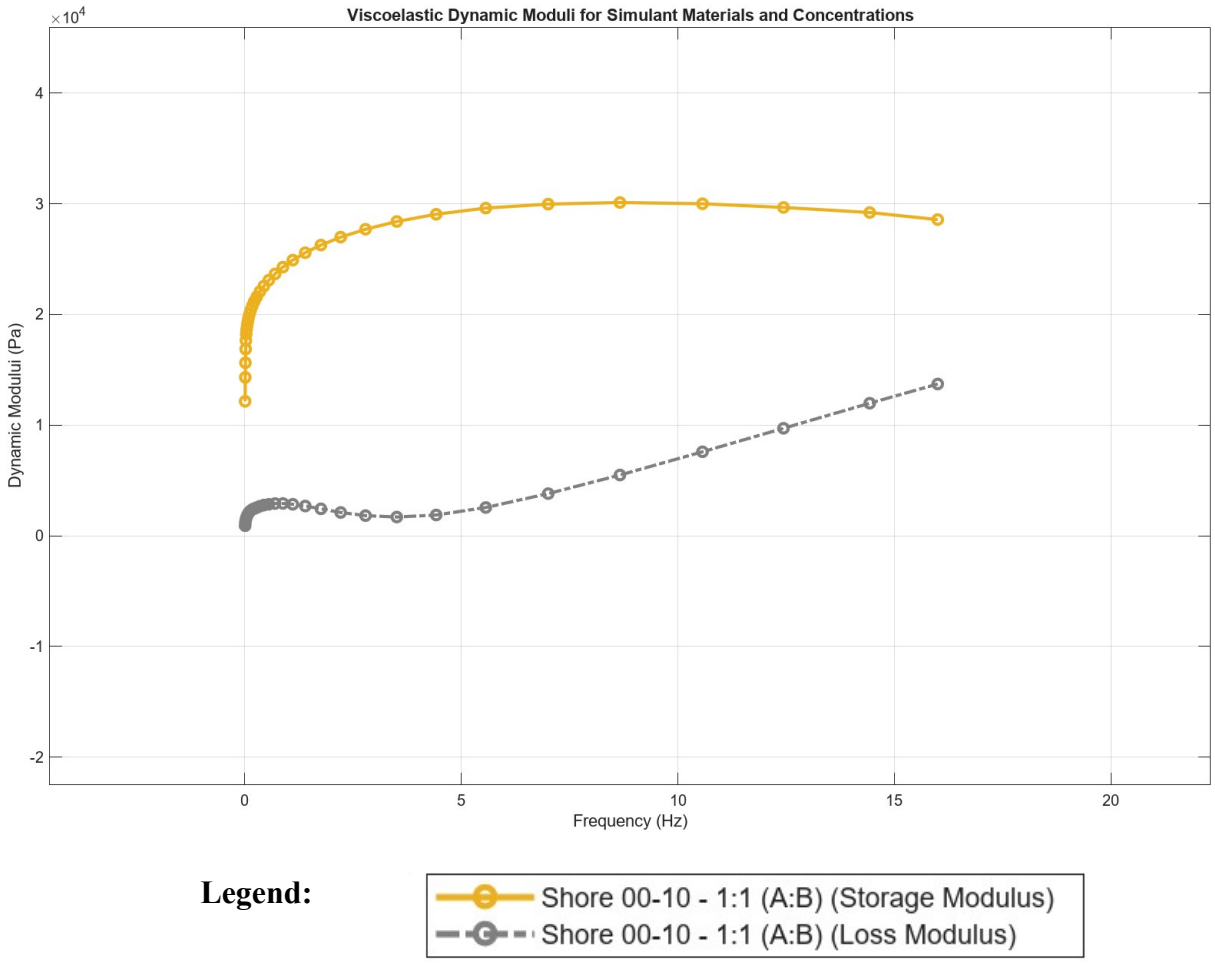


*Figure A13 — Storage and Loss Modulus Values in Compression for Shore 00-10 Silicone Elastomer at 1:1 (A:B) Concentration*

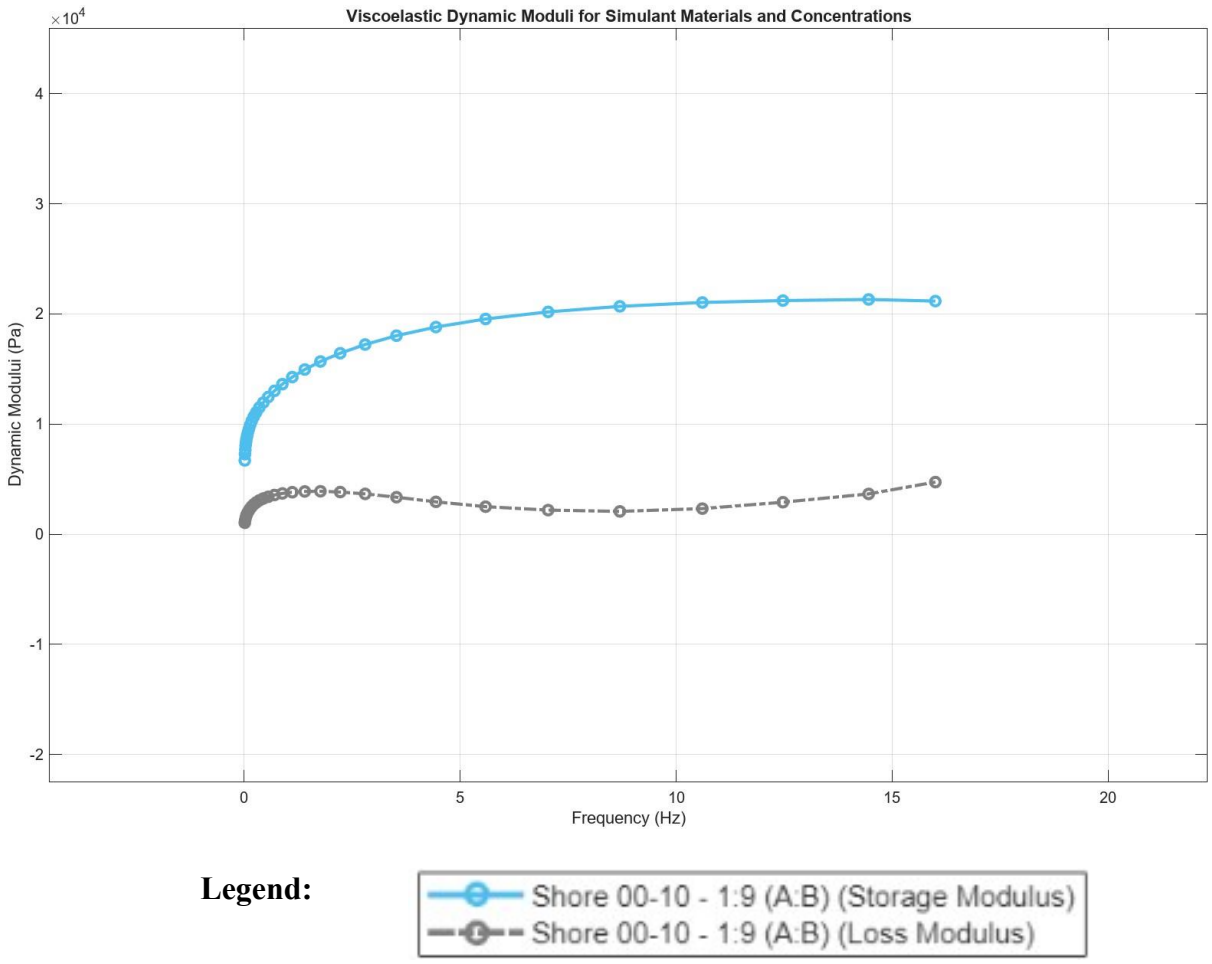


*Figure A14 — Storage and Loss Modulus Values in Compression for Shore 00-10 Silicone Elastomer at 1:9 (A:B) Concentration*

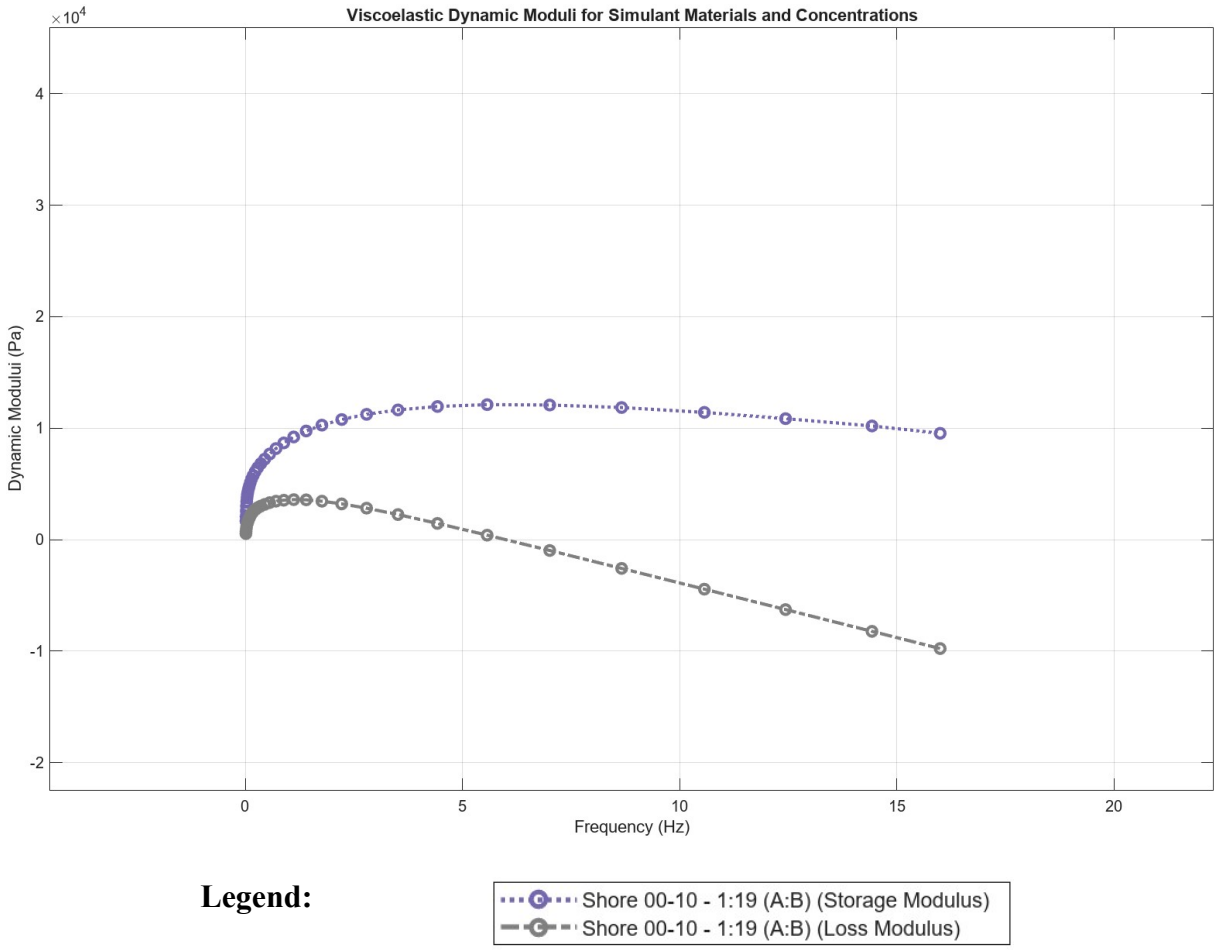


*Figure A15 — Storage and Loss Modulus Values in Compression for Shore 00-10 Silicone Elastomer at 1:19 (A:B) Concentration*

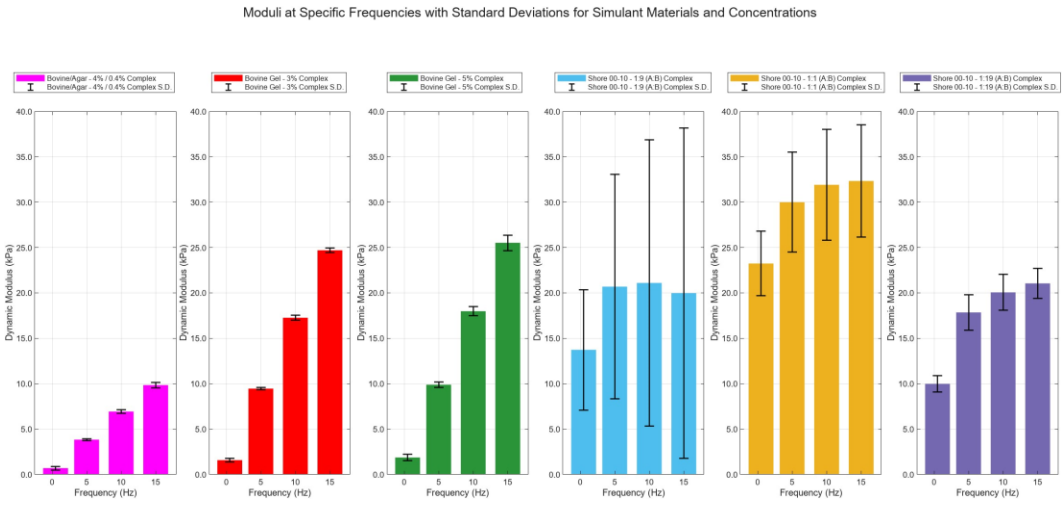


*Figure A16 — Complex Moduli at Specific Frequency Points for Compression*

*Table A17 — Tabulated Moduli Points for Frequency Sweep Tests in Compression*

| Material | Frequency (Hz) | Moduli (Pa) | | | | | |
|---|---|---|---|---|---|---|---|
| | | Storage | S.D. (± Pa) | Loss | S.D. (± Pa) | Complex | S.D. (± Pa) |
| Shore 00-10 1:1 (50% A; 50% B) Mean Value | 0.5 | 23074.00 | 3464.91 | 2821.10 | 853.82 | 23249.73 | 3543.24 |
| | 5 | 29881.83 | 5539.85 | -992.14 | 2423.25 | 30002.50 | 5506.19 |
| | 10 | 30838.00 | 6806.10 | -7040.19 | 3010.49 | 31917.07 | 6101.83 |
| | 15 | 28695.07 | 8021.38 | -13537.80 | 3246.46 | 32306.43 | 6152.59 |
| Shore 00-10 1:9 (10% A; 90% B) Mean Value | 0.5 | 12302.81 | 541.78 | 3296.82 | 1570.55 | 13754.39 | 6632.51 |
| | 5 | 19659.14 | 1061.78 | 2632.25 | 1521.25 | 20706.81 | 12393.39 |
| | 10 | 21477.29 | 1359.06 | -523.38 | 683.10 | 21094.24 | 15782.18 |
| | 15 | 21366.39 | 1572.64 | -4348.57 | 2500.61 | 19854.63 | 18752.36 |
| Shore 00-10 1:19 (10% A; 90% B) Mean Value | 0.5 | 9392.57 | 802.93 | 3402.25 | 388.54 | 9990.25 | 886.91 |
| | 5 | 17789.87 | 1900.19 | 1043.52 | 1286.09 | 17861.97 | 1945.17 |
| | 10 | 19533.83 | 2485.32 | -3868.04 | 1909.83 | 20061.50 | 1972.95 |
| | 15 | 18606.00 | 3097.22 | -9639.04 | 2225.86 | 21241.77 | 1557.92 |
| Bovine Gel 4% and Agar Gel 0.4%, Mixed Mean Value | 0.5 | 275.98 | 449.53 | -491.58 | 74.18 | 694.91 | 206.15 |
| | 5 | -322.71 | 428.73 | -3807.05 | 126.62 | 3845.47 | 100.03 |
| | 10 | -1579.94 | 416.96 | -6736.16 | 223.81 | 6932.45 | 192.63 |
| | 15 | -3506.84 | 372.13 | -9721.55 | 347.38 | 10342.60 | 310.12 |
| Bovine Gel, 3% Mean Value | 0.5 | 428.40 | 50.99 | -1545.94 | 161.68 | 1631.10 | 168.78 |
| | 5 | -1269.18 | 24.76 | -9452.33 | 22.34 | 9537.71 | 19.05 |
| | 10 | -4729.65 | 13.80 | -16751.60 | 28.75 | 17406.87 | 24.0 |
| | 15 | -9661.71 | 73.87 | -24184.90 | 17.20 | 26043.77 | 11.20 |
| Bovine Gel, 5% Mean Value | 0.5 | 1062.69 | 430.65 | -316.64 | 198.87 | 1110.97 | 441.34 |
| | 5 | 1518.32 | 624.70 | -1136.50 | 253.68 | 1924.24 | 359.37 |
| | 10 | -3705.77 | 429.33 | -17668.30 | 450.02 | 18055.55 | 496.09 |
| | 15 | -8654.04 | 639.22 | -25366.30 | 736.32 | 26805.40 | 874.18 |

# *Appendix B — Additional Information for Skull Simulant Characterization*

The following Appendix B provides supplemental information towards the study found in Chapter 4 of this thesis. The material provided in this appendix will include additional data and figures to provide extended context to the results found in this work. Further supplemental information, such as video capturing of DIC strain fields, can be found here: [DOI: 10.1016/j.jmbbm.2024.106680].

*Table B1 — Dimensional Parameters for Skull Simulant Specimens*

| **Material** | **Infill Density** [$n = 5$] **for each condition** | **Case One and Case Two** | | | **Case Two Only** | | **Curvature Radius (mm)** | **Length (mm)** |
|---|---|---|---|---|---|---|---|---|
| | | **Print Orientation** | **Thickness (mm)** | **Width (mm)** | **Outer Cortical Thickness (mm)** | **Inner Cortical Thickness (mm)** | | |
| **PLA** | 30 | Side | 7.817 ± 0.01 | 10.05 ± 0.01 | 2.34 ± 0.18 | 1.41 ± 0.22 | 89.13 [95] | 40 |
| | 50 | | 7.82 ± 0.01 | 10.02 ± 0.01 | 2.21 ± 0.06 | 1.31 ± 0.09 | | |
| | 80 | | 7.81 ± 0.02 | 10.10 ± 0.01 | 2.17 ± 0.04 | 1.30 ± 0.04 | | |
| | 30 | Top | 8.02 ± 0.01 | 9.98 ± 0.01 | 2.586 ± 0.03 | 1.58 ± 0.07 | | |
| | 50 | | 10.00 ± 0.02 | 8.00 | 2.00 ± 0.02 | 1.59 ± 0.06 | | |
| | 80 | | 8.06 ± 0.02 | 10.00 ± 0.02 | 2.43 ± 0.34 | 1.44 ± 0.26 | | |
| **HXA-PMMA** | 30 | Side | 7.88 ± 0.02 | 10.02 ± 0.06 | 1.98 ± 0.09 | 1.25 ± 0.11 | | |
| | 50 | | 7.88 ± 0.05 | 10.13 ± 0.02 | 1.87 ± 0.11 | 1.25 ± 0.05 | | |
| | 80 | | 7.91 ± 0.02 | 10.20 ± 0.02 | 1.90 ± 0.13 | 1.22 ± 0.10 | | |
| | 30 | Top | 8.39 ± 0.03 | 10.03 ± 0.01 | 1.92 ± 0.11 | 1.15 ± 0.08 | | |
| | 50 | | 8.45 ± 0.01 | 10.04 ± 0.01 | 2.44 ± 0.07 | 1.68 ± 0.14 | | |
| | 80 | | 8.47 ± 0.01 | 10.05 ± 0.03 | 2.44 ± 0.07 | 1.61 ± 0.08 | | |
| **Bone-Simulating PLA** | 30 | Side | 7.78 ± 0.01 | 9.99 ± 0.02 | 2.22 ± 0.03 | 1.49 ± 0.19 | | |
| | 50 | | 7.77 ± 0.01 | 9.99 ± 0.01 | 2.19 ± 0.03 | 2.34 ± 0.09 | | |
| | 80 | | 7.78 ± 0.01 | 10.00 ± 0.01 | 2.21 ± 0.05 | 1.38 ± 0.04 | | |
| | 30 | Top | 8.01 ± 0.01 | 10.04 ± 0.02 | 2.66 ± 0.01 | 1.67 ± 0.07 | | |
| | 50 | | 8.01 ± 0.01 | 10.05 ± 0.01 | 2.38 ± 0.29 | 1.62 ± 0.04 | | |
| | 80 | | 8.01 ± 0.03 | 10.05 ± 0.03 | 2.25 ± 0.23 | 1.48 ± 0.22 | | |

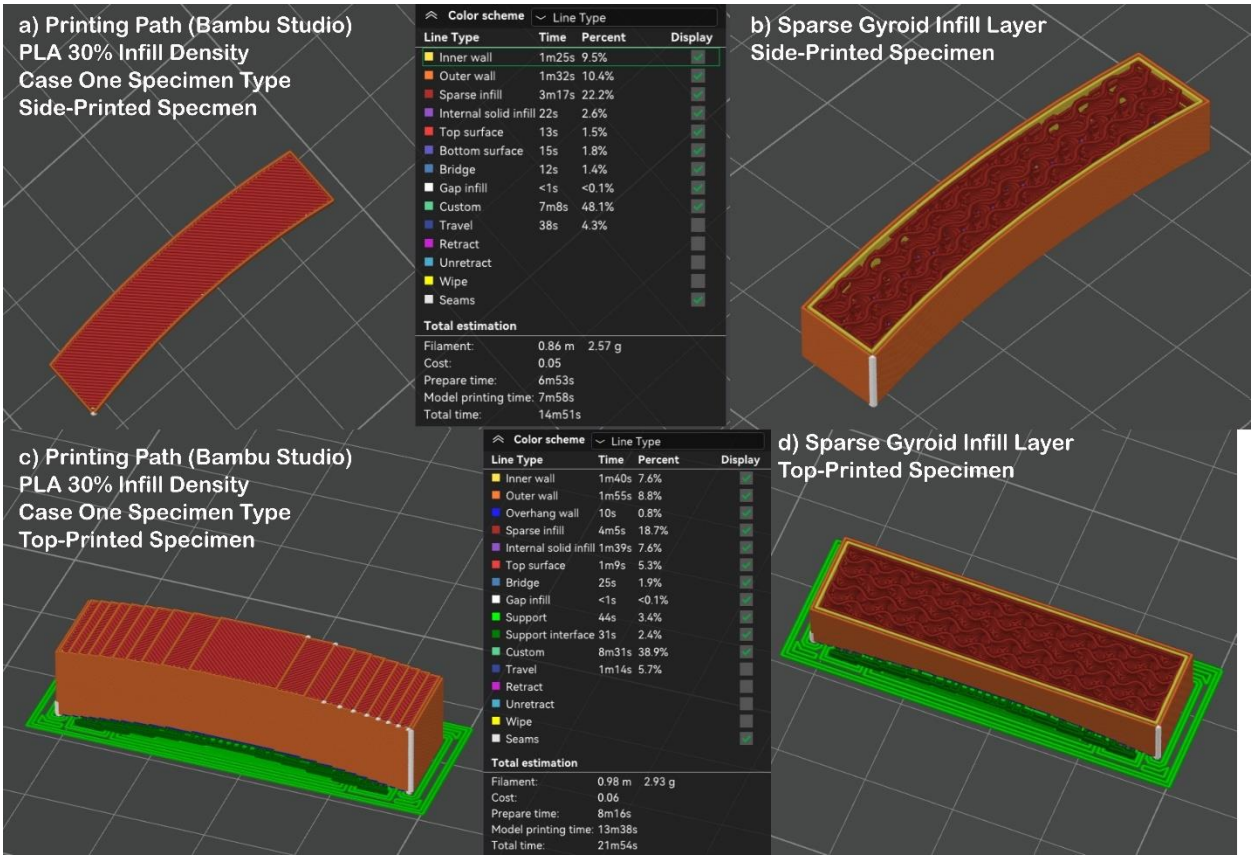


*Figure B1 — Print Path Slicing* for Case One Side and Top *Simulant Specimens*

*Table B2 — Case One: Mean Mechanical Performance of Bone Simulant Candidates (Shelled Candidates; n = 5 for Each Statistic)*

| ***Material*** | **Infill Density (%)** | **Raster Direction** | **Flexural Modulus (MPa)* [95% CI]** | **Relative Performance (%)** | | **Flexural Strength (MPa)* [95% CI]** | **Relative Performance (%)** | |
|---|---|---|---|---|---|---|---|---|
| *PLA* | 30 *[n = 5]* | Side | 791.1 ± 10.3 [782.1, 800.2] | 46.6 | 40.0 | ***43.2 ± 1.4 [42.0, 44.5]*** | **97.1** | *78.9* |
| | 30 *[n = 5]* | Top | 661.9 ± 118.2 [558.3, 765.5] | 38.9 | 33.4 | ***46.7 ± 3.8 [43.4, 50.1]*** | **88.7** | *85.3* |
| | 50 *[n = 5]* | Side | ***1415.8 ± 108.1 [1321.1, 1510.6]*** | **83.3** | *71.5* | ***55.6 ± 1.2 [54.6, 56.6]*** | **67.7** | *98.6* |
| | 50 *[n = 5]* | Top | 835.0 ± 99.7 [747.7, 922.4] | 49.1 | 42.2 | ***50.7 ± 1.5 [49.4, 52.0]*** | **79.3** | *92.5* |
| | 80 *[n = 5]* | Side | ***1732.1 ± 28.9 [1706.8, 1757.4]*** | **98.0** | *87.5* | *64.0 ± 2.6 [61.7, 66.3]* | 47.7 | *83.3* |
| | 80 *[n = 5]* | Top | ***1340.4 ± 55.3 [1291.9, 1388.8]*** | **78.9** | *67.7* | *69.4 ± 2.5 [67.2, 71.6]* | 34.7 | *73.3* |
| *HXA-PMMA* | 30 | Side | **1024.9 ± 32.3** | **60.3** | 51.8 | ***36.6 ± 5.1*** | **87.2** | *66.8* |

| | | | | | | | | |
|---|---|---|---|---|---|---|---|---|
| | *[n = 5]* | | **[996.6, 1053.2]** | | | ***[32.1, 41.1]*** | | |
| | 30 *[n = 5]* | Top | 767.5 ± 70.2 [706.2, 828.9] | 45.1 | 38.8 | **26.3 ± 0.9 [25.5, 27.1]** | 62.7 | 48.0 |
| | 50 *[n = 5]* | Side | **1085.1 ± 50.0 [1041.3, 1129.0]** | **63.9** | 54.8 | ***40.3 ± 4.9 [36.0, 44.6]*** | **95.9** | *73.5* |
| | 50 *[n = 5]* | Top | 855.3 ± 98.7 [768.8, 941.8] | 50.2 | 43.2 | 27.4 ± 2.4 [25.3, 29.5] | 65.3 | 50.0 |
| | 80 *[n = 5]* | Side | ***1397.4 ± 56.1 [1358.3, 1446.6]*** | **82.3** | *70.6* | *60.7 ± 2.7 [58.4, 63.1]* | 53.4 | *89.2* |
| | 80 *[n = 5]* | Top | **1054.4 ± 107.4 [960.2, 1148.5]** | **62.1** | 53.3 | ***37.6 ± 4.1 [34.0, 41.2]*** | **89.4** | *68.5* |
| *Bone-Like PLA* | 30 *[n = 5]* | Side | **1115.8 ± 98.1 [1029.9, 1201.8]** | **65.7** | 56.4 | ***42.4 ± 3.1 [39.7, 45.2]*** | **98.9** | *77.5* |
| | 30 *[n = 5]* | Top | 817.2 ± 51.8 [771,7, 862.4] | 48.1 | 41.3 | ***36.8 ± 1.6 [35.4, 38.2]*** | **87.6** | *67.2* |
| | 50 *[n = 5]* | Side | ***1534.3 ± 57.7 [1483.7, 1584.8]*** | **90.3** | *77.5* | ***47.8 ± 1.0 [47.0, 48.7]*** | **86.2** | *87.3* |
| | 50 *[n = 5]* | Top | **1099.7 ± 41.6 [1063.3, 1136.2]** | **64.7** | 55.6 | ***45.9 ± 1.1 [45.0, 46.9]*** | **90.6** | *83.8* |
| | 80 *[n = 5]* | Side | ***1935.1 ± 37.2 [1902.4, 1967.7]*** | **86.1** | *97.8* | *66.4 ± 4.8 [62.2, 70.6]* | 41.8 | *78.8* |
| | 80 *[n = 5]* | Top | ***1318.0 ± 108.2 [1223.2, 1412.8]*** | **77.6** | *66.6* | *59.7 ± 1.1 [58.8, 60.7]* | 57.8 | *91.0* |
| ***Human Bone (Lee et al.) [13]*** | -- | -- | **1699 ± 712** | **Deviation Relative Performance: Modulus (%)** | | **42 ± 14** | **Deviation Relative Performance: Modulus (%)** | |
| | | | | **58.1** | | | **66.7** | |
| *Human Bone (Ondruschka et al.) [47]* | -- | -- | *1979.7 ± 815.1* | **Deviation Relative Performance: Modulus (%)** | | *54.8 ± 18.9* | **Deviation Relative Performance: Modulus (%)** | |
| | | | | *58.8* | | | *65.5* | |

***Bolded** values indicate properties that fall within the deviation ranges of cranial bone properties in Lee et al; *Italicized* values indicate properties that fall within the deviation ranges of cranial bone properties in Ondruschka et al.

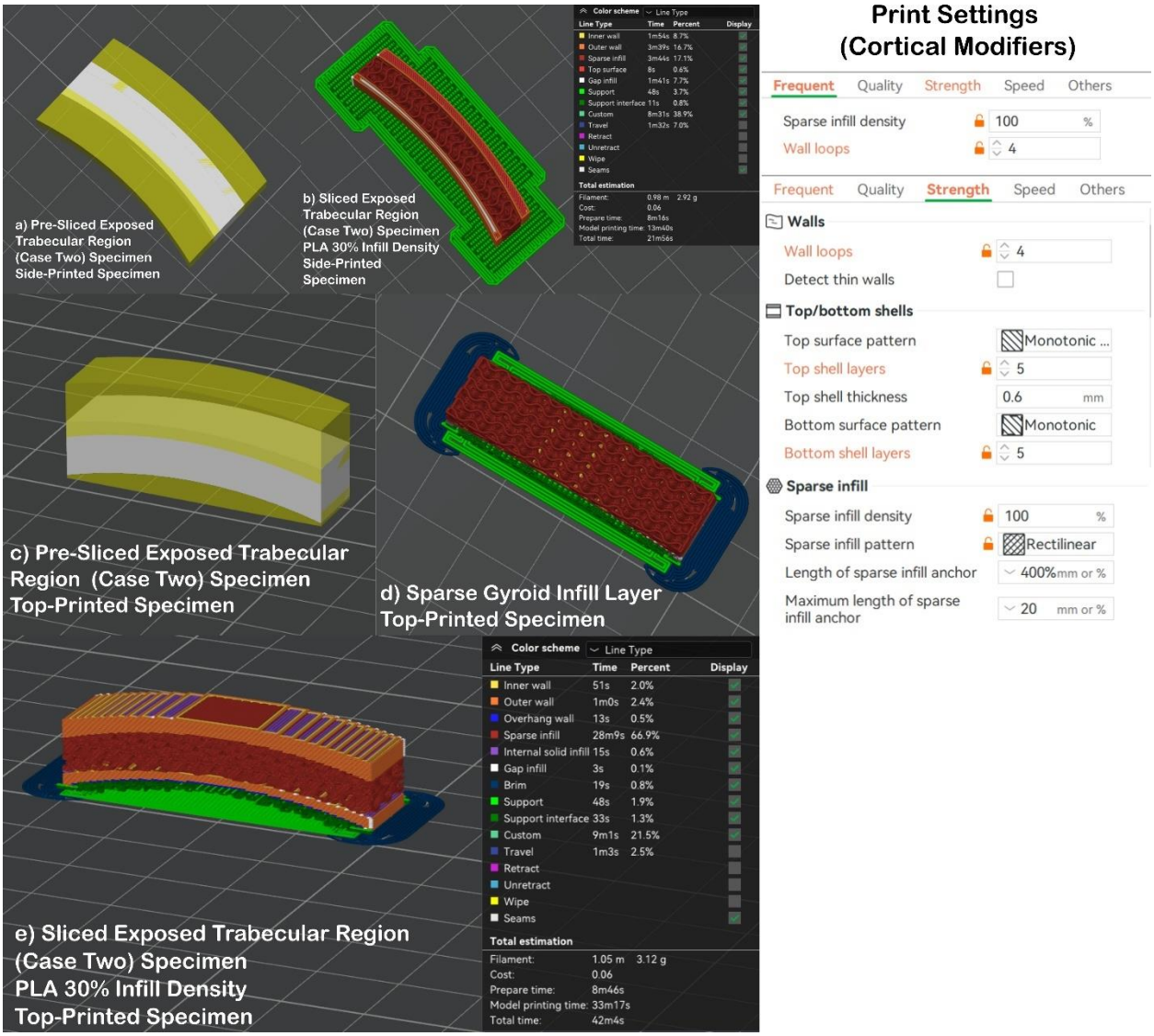


*Figure B2 — Print Path Slicing* for Case Two Side and Top *Simulant Specimens*

*Table B3 — Case Two: Mean Mechanical Performance of Select Bone Simulant Candidates (Exposed Candidates; n = 5 for Each Statistic)*

| ***Material*** | **Infill Density (%) *[Sample Size (n)]*** | **Print Orientation** | **Flexural Modulus (MPa)* [95% CI]** | **Relative Performance (%)** | | **Flexural Strength (MPa)* [95% CI]** | **Relative Performance (%)** | |
|---|---|---|---|---|---|---|---|---|
| *PLA* | 30 *[n = 5]* | Side | 500.64 ± 30.5 [473.9, 527.4] | 29.5 | 25.3 | ***29.5 ± 2.5 [27.3, 31.7]*** | **70.3** | 53.9 |
| | 30 *[n = 5]* | Top | 525.19 ± 31.3 [497.7, 562.6] | 30.9 | 26.5 | 25.4 ± 1.4 [24.2, 26.6] | 60.5 | 46.4 |
| | 50 | Side | 803.8 ± 56.8 | 47.3 | 40.6 | ***46.2 ± 0.9*** | **89.9** | *84.4* |

| | | | | | | | | |
|---|---|---|---|---|---|---|---|---|
| | *[n = 5]* | | [754.0, 853.6] | | | ***[45.5, 47.0]*** | | |
| | 50 *[n = 5]* | Top | 710.9 ± 5.4 [706.1, 715.6] | 41.8 | 35.9 | ***43.3 ± 1.8 [41.7, 44.9]*** | **97.0** | *79.0* |
| | 80 *[n = 5]* | Side | **1068.9 ± 18.9 [1052.3, 1085.5]** | **62.9** | 54.0 | *57.1 ± 0.9 [56.3, 57.9]* | 64.0 | *95.8* |
| | 80 *[n = 5]* | Top | **1013.6 ± 64.1 [957.4, 1069.7]** | **59.7** | 51.2 | *59.6 ± 1.5 [58.2, 61.0]* | 57.1 | *91.2* |
| *HXA-PMMA* | 30 *[n = 5]* | Side | 528.0 ± 24.0 [481.3, 532.5] | 45.9 | 26.7 | 19.3 ± 1.7 [17.8, 20.8] | 45.9 | 35.2 |
| | 30 *[n = 5]* | Top | 424.5 ± 9.2 [381.2, 462.6] | 29.4 | 21.4 | 12.3 ± 0.6 [11.9, 12.8] | 29.4 | 22.5 |
| | 50 *[n = 5]* | Side | **802.0 ± 35.5 [881.7, 1004.8]** | **67.2** | 40.5 | **28.2 ± 3.2 [25.5, 31.0]** | **67.2** | 51.5 |
| | 50 *[n = 5]* | Top | 833.6 ± 155.6 [611.5, 676.5] | 52.0 | 42.1 | 21.8 ± 1.6 [20.4, 23.3] | 52.0 | 39.9 |
| | 80 *[n = 5]* | Side | **1156.2 ± 78.9 [1313.4, 1361.0]** | **94.2** | 58.4 | ***39.5 ± 6.5 [33.8, 45.3]*** | **94.2** | *72.2* |
| | 80 *[n = 5]* | Top | **1068.3 ± 90.7 [902.3, 1165.9]** | **91.6** | 54.0 | ***45.5 ± 2.3 [43.5, 47.5]*** | **91.6** | *83.1* |
| *Bone-Like PLA* | 30 *[n = 5]* | Side | **506.9 ± 29.2 [507.0, 549.0]** | **73.9** | 25.6 | **31.1 ± 1.1 [30.1, 32.0]** | **73.9** | 56.7 |
| | 30 *[n = 5]* | Top | 421.9 ± 46.4 [416.4, 432.6] | 58.0 | 21.3 | 24.4 ± 0.7 [23.8, 24.9] | 58.0 | 44.4 |
| | 50 *[n = 5]* | Side | **943.2 ± 70.2 [770.9, 833.1]** | **96.3** | 47.7 | ***43.6 ± 8.3 [36.3, 50.9]*** | **96.3** | *79.5* |
| | 50 *[n = 5]* | Top | **644.0 ± 37.0 [687.2, 970.0]** | **92.3** | 32.5 | ***38.8 ± 9.9 [30.1, 47.4]*** | **92.3** | *70.8* |
| | 80 *[n = 5]* | Side | ***1337.2 ± 27.2 [1087.0, 1225.4]*** | **64.5** | *67.5* | *56.9 ± 3.6 [53.7, 60.1]* | 64.5 | *96.2* |
| | 80 *[n = 5]* | Top | **1034.1 ± 150.4 [988.8, 1147.7]** | **84.5** | 52.2 | ***58.5 ± 3.4 [45.6, 51.5]*** | **84.5** | *88.5* |
| ***Human Bone (Lee et al.) [13]*** | -- | -- | **1699 ± 712** | **Deviation Relative Performance: Modulus (%)** | | **42 ± 14** | **Deviation Relative Performance: Modulus (%)** | |
| | | | | **58.1** | | | **66.7** | |
| *Human Bone (Ondruschka et al.) [47]* | -- | -- | *1979.7 ± 815.1* | **Deviation Relative Performance: Modulus (%)** | | *54.8 ± 18.9* | **Deviation Relative Performance: Modulus (%)** | |
| | | | | *58.8* | | | *65.5* | |

***Bolded** values indicate properties that fall within the deviation ranges of cranial bone properties in Lee et al; *Italicized* values indicate properties that fall within the deviation ranges of cranial bone properties in Ondruschka et al.

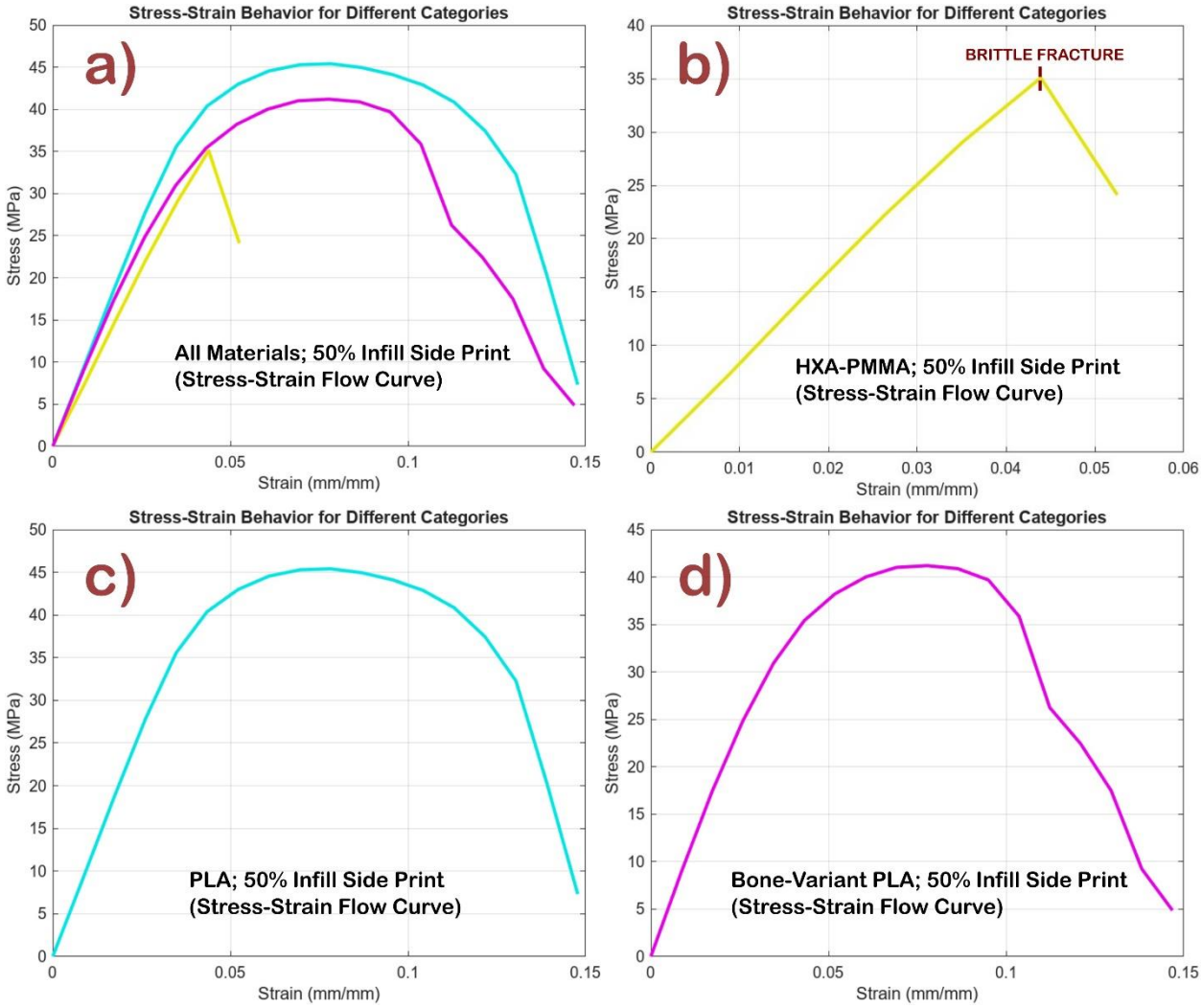


*Figure B3 — Case One: Stress-Strain Flow Curve Including Failure Regions for All Tested Materials at 50% Infill, Side Print Orientation: (a) All Materials, 50% Infill Density Side Print; (b) HXA-PMMA, 50% Infill Density Side Print; (c) PLA, 50% Infill Density Side Print; (d) Bone-Variant PLA, 50% Infill Density Side Print*

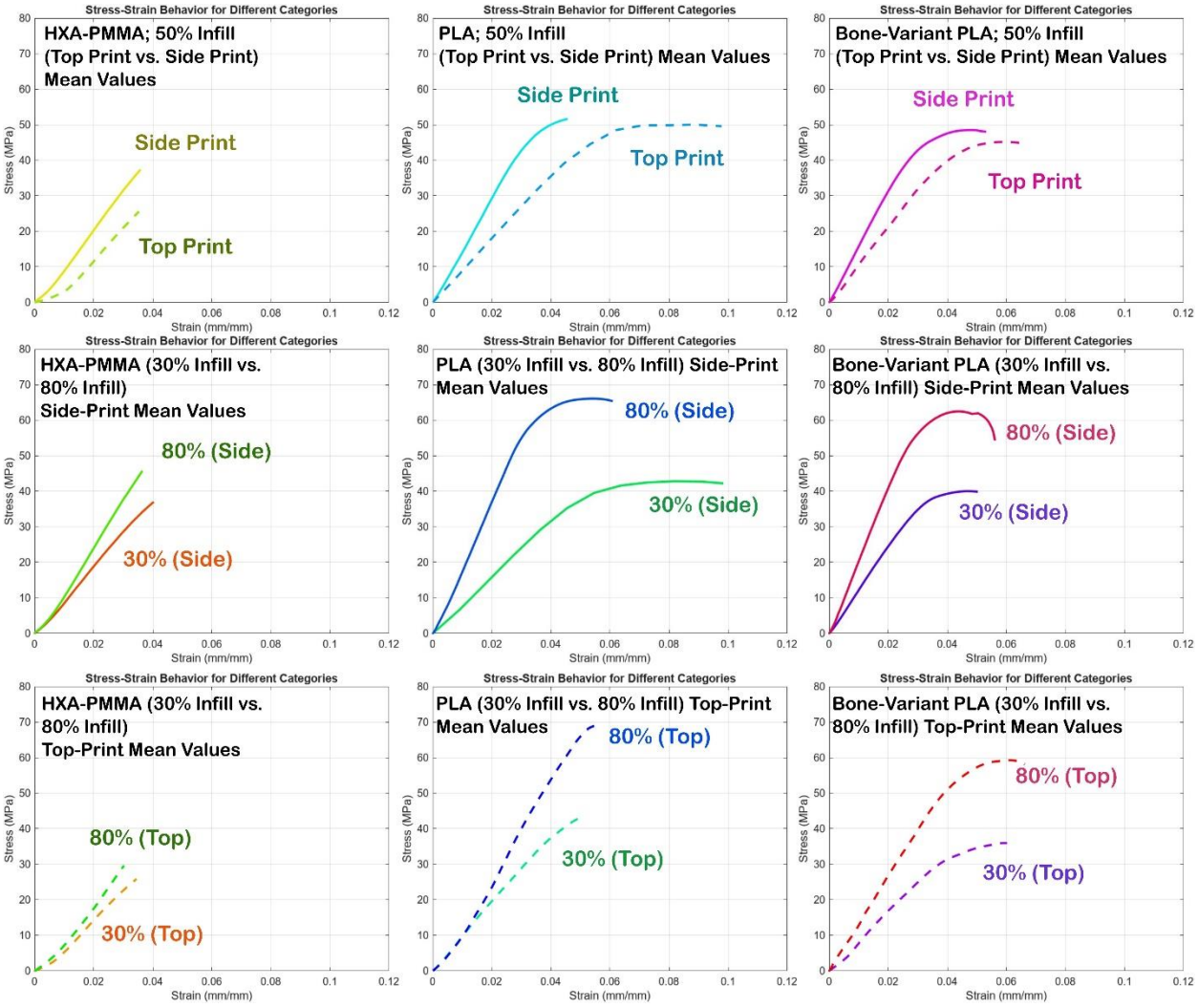


*Figure B4 — Case One: Parameter Adjustment Comparisons in Stress-Strain Behaviour of Bone Simulants*

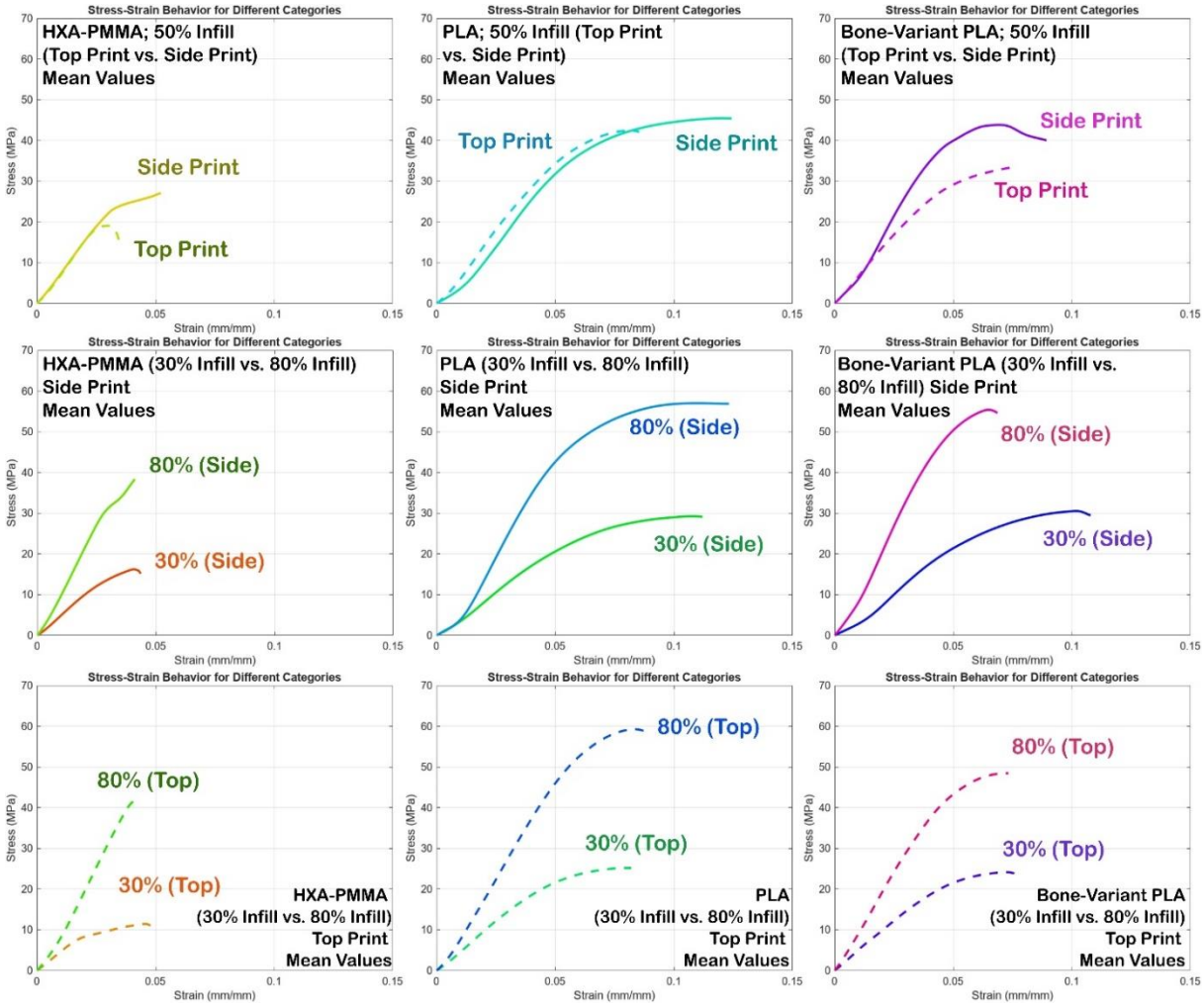


*Figure B5 — Case Two: Parameter Adjustment Comparisons in Stress-Strain Behaviour of Bone Simulants*

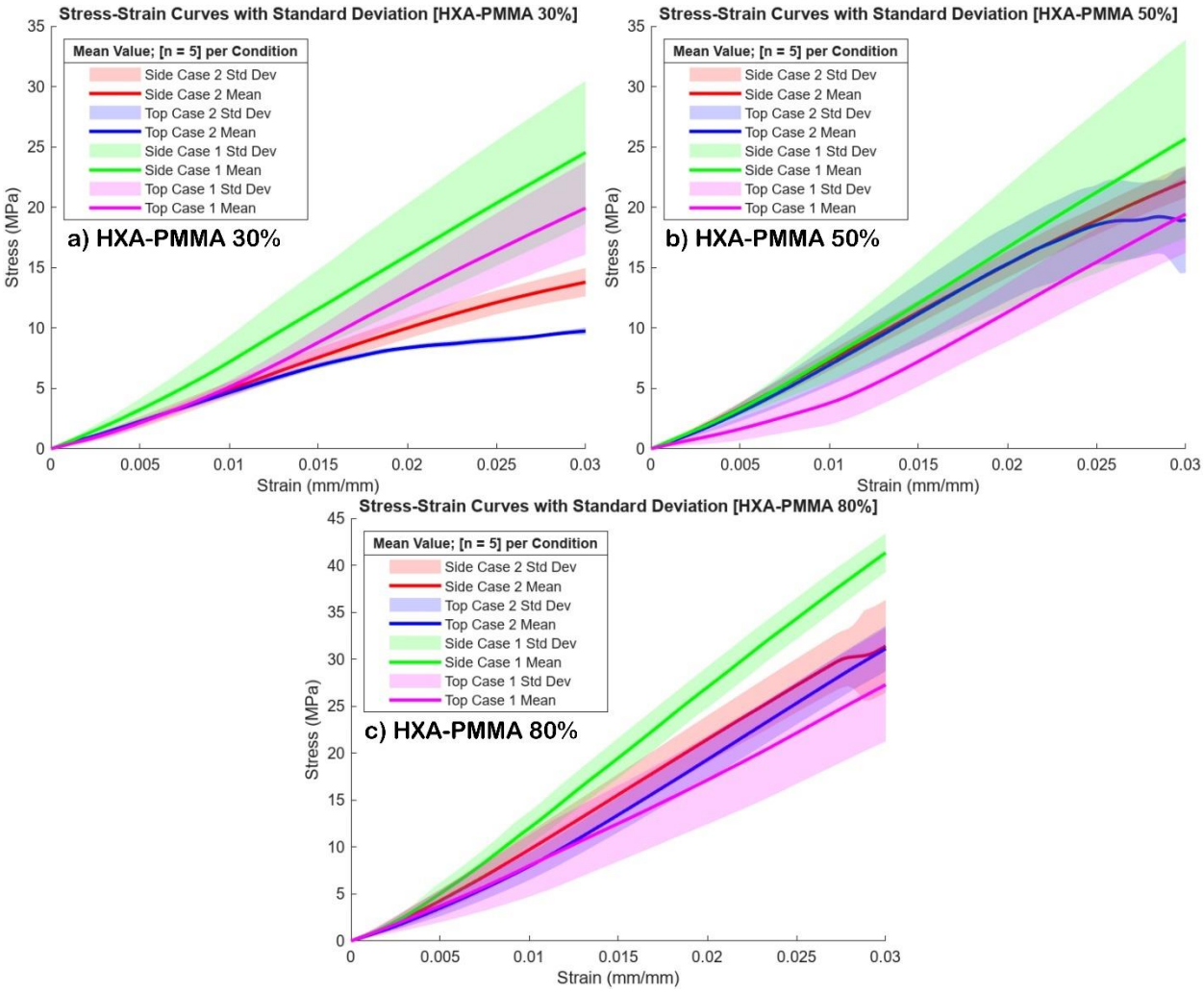


*Figure B6 — Mean Modulus Region Stress-Strain with Standard Deviations (HXA-PMMA)*

Drastic changes in standard deviations on relevant stress-strain signify points at which samples met failure.

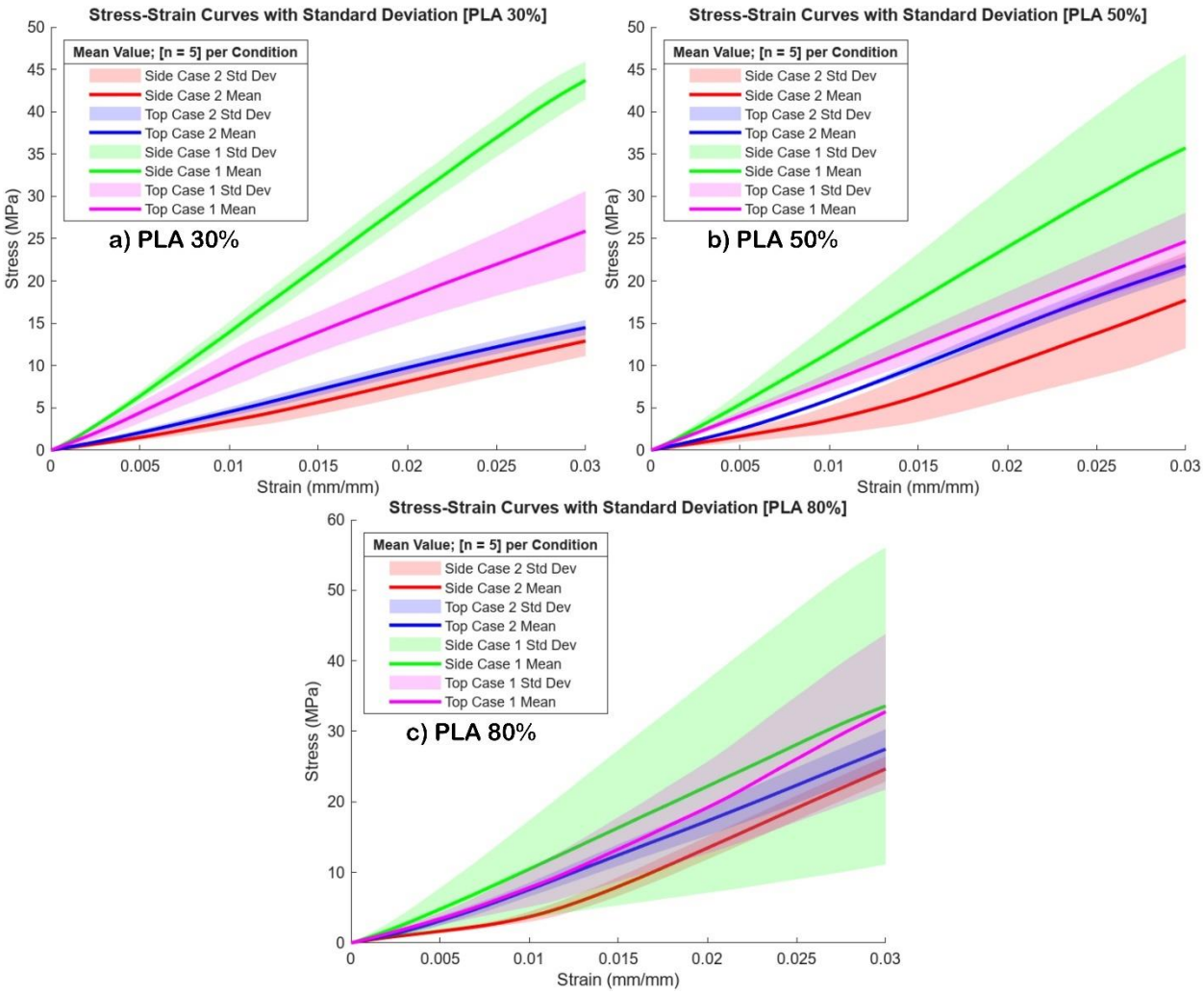


*Figure B7 — Mean Modulus Region Stress-Strain with Standard Deviations (PLA)*

Drastic changes in standard deviations on relevant stress-strain signify points at which samples met failure.

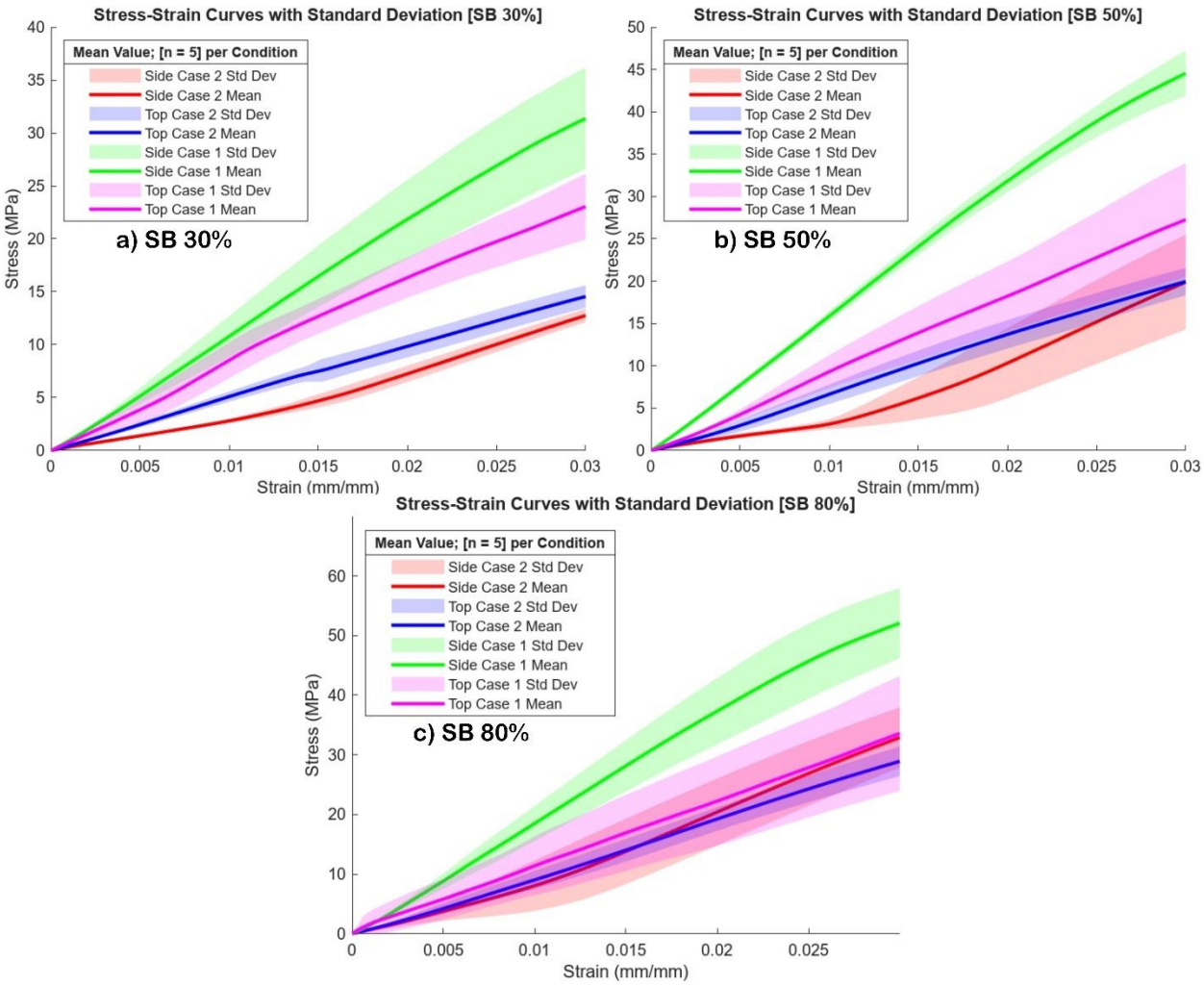


*Figure B8 — Mean Modulus Region Stress-Strain with Standard Deviations (Bone-PLA 30%)*

Drastic changes in standard deviations on relevant stress-strain signify points at which samples met failure.

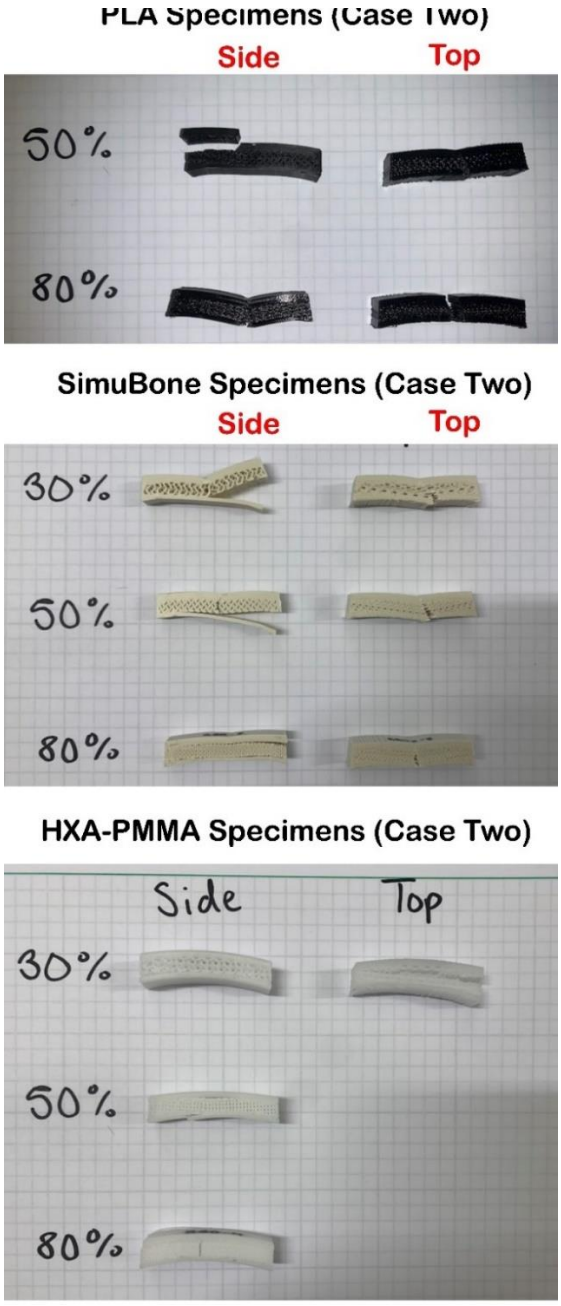


*HXA-PMMA 50% and 80% (Top) Samples are missing for fracture observations, as sample sets are no longer available

*Figure B9 — Case Two: Available Fractured Specimens Displaying Variation in Fracture Mechanisms*